Alaska Department of Transportation & Public Facilities

Research & Technology Transfer

Improved Permafrost Protection Using Air Convection and Ventilated Shoulder Cooling Systems – Final Project Report

Prepared by:
Douglas J. Goering, PhD, PE
Professor and Dean Emeritus
Institute of Northern Engineering
University of Alaska Fairbanks
ELIF Suite 240, 1764 Tanana Drive
Fairbanks, AK 99775-5910

Date: November 2022

Prepared for:
Alaska Department of Transportation and Public Facilities
Statewide Research Office
3132 Channel Drive
Juneau, AK 99801-7898

Publication Number: FHWA-AK-RD-4000(185)

Notice

This document is disseminated under the sponsorship of the U.S. Department of Transportation in the interest of information exchange. The U.S. Government assumes no liability for the use of the information contained in this document. The U.S. Government does not endorse products or manufacturers. Trademarks or manufacturers' names appear in this report only because they are considered essential to the objective of the document.

Quality Assurance Statement

The Federal Highway Administration (FHWA) provides high-quality information to serve Government, industry, and the public in a manner that promotes public understanding. Standards and policies are used to ensure and maximize the quality, objectivity, utility, and integrity of its information. FHWA periodically reviews quality issues and adjusts its programs and processes to ensure continuous quality improvement.

Author's Disclaimer

The contents of this report reflect the views of the author, who is responsible for the facts and the accuracy of the information presented herein. This document is disseminated under the sponsorship of the Alaska Department of Transportation and Public Facilities in the interest of information exchange. The University of Alaska, the U.S. Government, and any matching sponsors assume no liability for the contents or use thereof.

REPORT DOCUMENTATION PAGE

Form approved OMB No.

1. AGENCY USE ONLY (LEAVE BLANK)	2. REPORT DATE	3. REPORT TYPE AND DATES COVERED
FHWA-AK-RD-4000(185)	November 2022	Final Report, February 2019 – December 2022

4. TITLE AND SUBTITLE

Improved Permafrost Protection using Air Convection and Ventilated Shoulder Cooling Systems

Final Project Report

5. FUNDING NUMBERS

6. AUTHOR(S)

Douglas J. Goering, PhD, PE

7. PERFORMING ORGANIZATION NAME(S) AND ADDRESS(ES)

UAF Institute of Northern Engineering
ELIF Building Room 240, 1760 Tanana Drive
Fairbanks, AK 99775-5910

8. PERFORMING ORGANIZATION REPORT NUMBER

INE 22.02

9. SPONSORING/MONITORING AGENCY NAME(S) AND ADDRESS(ES)

State of Alaska, Alaska Dept. of Transportation and Public Facilities
Research and Technology Transfer
3132 Channel Drive
Juneau, AK 99801-7898

10. SPONSORING/MONITORING AGENCY REPORT NUMBER

FHWA-AK-RD-4000(185
HFHWY00126

11. SUPPLENMENTARY NOTES

12a. DISTRIBUTION / AVAILABILITY STATEMENT

No restrictions

12b. DISTRIBUTION CODE

13. ABSTRACT (Maximum 200 words)

This report focuses on the effectiveness of air convection embankments (ACE) and ventilated shoulder (VS) cooling systems designed to cool foundation soils and preserve permafrost beneath roadway embankments. The four main sections of the report include a literature review, an analysis of field data from the Thompson Drive Experimental Feature near Fairbanks, an analysis of data from the Alaska Highway Dot Lake Experimental Feature site, and a discussion of techniques for modeling ACE and VS structures using the GeoSlope Temp/W modeling package. Fifteen years (2005-2020) of data from the Thompson Drive site are analyzed using contour plots of average annual temperatures within the embankment and underlying foundation soils along with time series of temperature behavior at specific locations throughout the embankment test sections. Similarly, data from the Alaska Highway site is analyzed over a three-year period (June 2017 to May 2020) by examining average annual temperatures at an array of measurement points within the embankment test sections and underlying soils. In all cases the data indicates a strong overall cooling influence, particularly in the layers underlying the VS structures.

14- KEYWORDS :

Permafrost, Air Convection Embankment, Ventilated Shoulder

15. NUMBER OF PAGES
144

16. PRICE CODE

N/A

17. SECURITY CLASSIFICATION OF REPORT	18. SECURITY CLASSIFICATION OF THIS PAGE	19. SECURITY CLASSIFICATION OF ABSTRACT	20. LIMITATION OF ABSTRACT
Unclassified	Unclassified	Unclassified	N/A

NSN 7540-01-280-5500

STANDARD FORM 298 (Rev. 2-98)
Prescribed by ANSI Std. 239-18 298-102

SI* (MODERN METRIC) CONVERSION FACTORS

METRIC (SI*) CONVERSION FACTORS

APPROXIMATE CONVERSIONS TO SI UNITS

Symbol	When You Know	Multiply By	To Find	Symbol
		LENGTH		
in	inches	25.4		mm
ft	feet	0.3048		m
yd	yards	0.914		m
mi	Miles (statute)	1.61		km
		AREA		
in^2	square inches	645.2	millimeters squared	cm^2
ft^2	square feet	0.0929	meters squared	m^2
yd^2	square yards	0.836	meters squared	m^2
mi^2	square miles	2.59	kilometers squared	km^2
ac	acres	0.4046	hectares	ha
		MASS (weight)		
oz	Ounces (avdp)	28.35	grams	g
lb	Pounds (avdp)	0.454	kilograms	kg
T	Short tons (2000 lb)	0.907	megagrams	mg
		VOLUME		
fl oz	fluid ounces (US)	29.57	milliliters	mL
gal	Gallons (liq)	3.785	liters	liters
ft^3	cubic feet	0.0283	meters cubed	m^3
yd^3	cubic yards	0.765	meters cubed	m^3

Note: Volumes greater than 1000 L shall be shown in m^3

		TEMPERATURE (exact)		
°F	Fahrenheit temperature	5/9 (°F-32)	Celsius temperature	°C
		ILLUMINATION		
fc	Foot-candles	10.76	lux	lx
fl	foot-lamberts	3.426	candela/m^2	cd/cm^2
		FORCE and PRESSURE or STRESS		
lbf	pound-force	4.45	newtons	N
psi	pound-force per square inch	6.89	kilopascals	kPa

These factors conform to the requirement of FHWA Order 5190.1A *SI is the symbol for the International System of Measurements

APPROXIMATE CONVERSIONS FROM SI UNITS

Symbol	When You Know	Multiply By	To Find	Symbol
		LENGTH		
mm	millimeters	0.039	inches	in
m	meters	3.28	feet	ft
m	meters	1.09	yards	yd
km	kilometers	0.621	Miles (statute)	mi
		AREA		
mm^2	millimeters squared	0.0016	square inches	in^2
m^2	meters squared	10.764	square feet	ft^2
km^2	kilometers squared	0.39	square miles	mi^2
ha	hectares (10,000 m^2)	2.471	acres	ac
		MASS (weight)		
g	grams	0.0353	Ounces (avdp)	oz
kg	kilograms	2.205	Pounds (avdp)	lb
mg	megagrams (1000 kg)	1.103	short tons	T
		VOLUME		
mL	milliliters	0.034	fluid ounces (US)	fl oz
liters	liters	0.264	Gallons (liq)	gal
m^3	meters cubed	35.315	cubic feet	ft^3
m^3	meters cubed	1.308	cubic yards	yd^3
		TEMPERATURE (exact)		
°C	Celsius temperature	9/5 °C+32	Fahrenheit temperature	°F
		ILLUMINATION		
lx	lux	0.0929	foot-candles	fc
cd/cm^2	candela/m^2	0.2919	foot-lamberts	fl
		FORCE and PRESSURE or STRESS		
N	newtons	0.225	pound-force	lbf
kPa	kilopascals	0.145	pound-force per square inch	psi

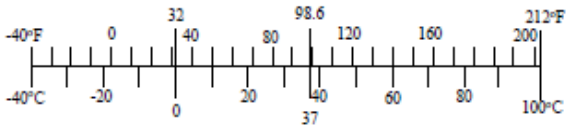

TABLE OF CONTENTS

LIST OF FIGURES

APPENDICIES

LIST OF TABLES

EXECUTIVE SUMMARY

This report focuses on the effectiveness of air convection embankments (ACE) and ventilated shoulder (VS) cooling systems designed to cool foundation soils and preserve permafrost beneath roadway embankments. These systems generally include one or more layers of highly porous, poorly graded rock aggregate that is permeable enough to allow the internal circulation of pore air and/or the intrusion of ambient air into the embankment in response to temperature gradients. The resulting air circulation is typically more vigorous during winter months, helping to enhance cooling of the embankment and foundation soils and increasing the thermal stability of any underlying permafrost layers.

The first section of the report includes a review of the recent ACE research, including papers focusing on experimental data, numerical simulation results, and material properties. The papers reviewed span contributions from North America, Europe, and China. Many of the recent papers from China focus on the Qinghai-Tibet Plateau and the Qinghai-Tibet Railway which was completed in the mid-2000's. Several recent projects in Canada are also reviewed.

The second part of the report examines the cooling performance and permafrost-preservation capabilities of ACE and VS embankment features using field data from Thompson Drive and the Alaska Highway Dot Lake test site. Data from Thompson Drive for the 15-year period stretching from 2005 to 2020 has been analyzed and results have been presented in terms of average annual temperature contours for three test sections. Contours include both the embankment structures and underlying foundation soils. These results show that all the cooling systems utilized in Thompson Drive (air convection layers, ventilated shoulders, and hair-pin thermosyphons) have effectively cooled the foundation soils and maintained frozen conditions beneath the embankment. For the Alaska Highway Dot Lake site, three years of data extending from June 1, 2016 to May 31, 2019 were analyzed. Each of the three test sections at the Alaska Highway site indicated a cooling effect over the three-year period, although foundation soils remained thawed at the end of data collection.

The third part of the report discusses numerical modeling of ACE and VS embankment structures. Two numerical modeling packages were utilized, the SoilVision SVHEAT package and the Geoslope TEMP/W package. Neither UAF nor AKDOT own a license for the SoilVisoin SVHEAT package but this package is known to be used by geotechnical engineering firms within the State and, as a result, it was determined that the package should be evaluated for use in modeling ACE and VS embankments. The first part of CHAPTER 4 describes the evaluation process and the conclusions that were arrived at. The second part of CHAPTER 4 describes a more extensive modeling effort based on the Geoslope Temp/W simulation package. The series of modeling simulations carried out with Temp/W were focused on two broad objectives. The first was to compare model output to the actual field measurements obtained from the Thompson Drive test site (focusing on test section #1). The second objective was to examine the impact of different ventilated shoulder boundary condition assumptions on the model output and the predicted effectiveness of cooling in the foundation soils.

Two general conclusions can be drawn from the information presented in this report. The first is that air convection layers, ventilated shoulders, and hairpin thermosyphons are all capable of providing a large cooling influence on foundation soils and, thus, can be used to prevent thaw of permafrost underlying roadway embankments. The second is that it is possible to model the behavior of these systems using numerical simulations, although the specifics of how a ventilated shoulder interacts with a surface snow

layer and the surrounding ambient air mass cannot be handled by current modeling packages, resulting in the need for simplifying assumptions which may reduce the accuracy of the numerical results.

Based on the conclusions above, it is recommended that AKDOT continue to consider these systems for use in future projects where there is a need to maintain the structural integrity of ice-rich permafrost layers underlying roadways.

CHAPTER 1. PROJECT OVERVIEW

This project report details a series of efforts aimed at better understanding the behavior and cooling effectiveness of air convection embankments (ACE) and ventilated shoulders (VS) that are utilized for permafrost preservation beneath roadway embankments. The three focus areas of the report include a review of recent literature related to ACE and VS performance, an analysis of field data from two test sites in interior Alaska, and a comparison between numerical modeling results and field data. The study has been supported by a three-year grant (2/2019 to 12/2022) from the Alaska Department of Transportation and Public Facilities.

CHAPTER 2 of the report details the findings of the literature review including papers that focused on experimental results, modeling studies, and material properties. While the papers discussed span contributions from China, North America, and Northern Europe, the majority of recent field data publications have addressed measurements made along the Qhinghai Tibet Railway (QTR). This rail line was completed in the mid-2000s and included several instrumented test sections that employed various ACE or VS configurations. Additionally, some field data from the Canadian section of the Alaska Highway is also reviewed.

Many of the modeling studies reviewed are also focused on various aspects of QTR performance, including modeling the influence of climate change and other factors influencing ACE or VS performance, such as sand-clogging of the ACE aggregate. Another series of modeling studies reviewed were aimed at developing design tools for ACE embankments.

Finally, a third sequence of publications focused on various aspects of ACE material characteristics, including the impact of particle-to-particle radiation, the appropriateness of using the Boussinesq approximation during modeling, and a number of studies aimed at determining the air permeability of ACE materials.

CHAPTER 3 of the report includes an extensive analysis of 15 years' worth of data from Thompson Drive and 3 years' worth of data from the Alaska Highway Dot Lake test site. Both of these projects include instrumented ACE and VS layers, although only the Thompson Drive embankment contains enough temperature measuring points within the embankment to actually contour temperature behavior throughout the annual cycle. For Thompson Drive, key temperature measurements are plotted over time and trends discussed. In addition, annual average temperatures are contoured for each of the Thompson Drive test sections over the 15-year measurement history. For the Alaska Highway Dot Lake site, annual average temperatures are calculated for each of the measurement points and plotted graphically.

CHAPTER 4 discusses a series of numerical modeling exercises that were carried out utilizing Soilvision SVHEAT and Geoslope Temp/W. The use of SVHEAT for ACE and VS modeling was investigated using an evaluation license that was obtained from Bentley Systems, Inc. SVHEAT has not been used in the past by either UAF or AKDOT personnel for simulating ACE and VS performance, but the evaluation exercise discussed in CHAPTER 4 indicated that it has some advantages over Temp/W. Unfortunately, license purchasing issues have precluded long-term use of SVHEAT. Following the SVHEAT evaluation, the Geoslope Temp/W modeling package was used to simulate data from the Thompson Drive site. A series of different simulations have been conducted aimed at better understanding the impact of boundary condition assumptions on the modeling results and comparisons with the field data.

CHAPTER 2. LITERATURE REVIEW

The literature regarding air convection embankments and crushed rock embankment structures dates back to the mid-1990s. Most of this work has focused on protecting railway or roadway embankments from the effects of permafrost thaw. There is a body of companion literature that has been focused on geological features, such as cooling of talus/scree slopes in mountainous regions and other types of geological "cold spots". While the literature related to those geological systems is of interest and generally supports the cooling effect of poorly sorted highly porous rock layers, that literature is not reviewed here.

This literature review was conducted by identifying the most relevant of the recent publications on air convection and crushed rock embankments using Google Scholar. Google Scholar is particularly effective at allowing an investigator to follow a particular thread of published literature by identifying subsequent papers that have reference a particular article. Using this tool, it is possible to track the most recent relevant papers by looking at newer publications that reference key publications from the past. Using this methodology, a list of 25 of the most recent papers (most published within the last four years) was developed and reviewed. The full reference list is given below.

In order to better organize the review, the reference papers were sorted into three categories. These included 1) papers reporting primarily on experimental results, 2) papers detailing modeling studies, and, 3) papers investigating the thermal and fluid flow characteristics of crushed rock and poorly graded aggregate. Six to eight papers in each of these categories have been reviewed below.

In addition to those papers that focus in the three areas identified above, there are also several recent review papers that focus on a comparison of adaptation/mitigation measures for thaw unstable permafrost foundation soils beneath engineered infrastructure. Dore et al. [7] provide a summary of methods (including air convection embankments (ACE)) that have been used in various experimental and operational installations in Alaska, Canada, and China to mitigate permafrost degradation. In addition to discussing several specific installations they also summarize the physical and climatic conditions that lead to geotechnical problems. They also include a discussion of climate change impacts. Kong et al. [8] describe the development of design tools that can be applied to ACE or other types of convective cooling systems. Their approach is based on a heat balance technique somewhat similar to the AKDOT design tool that was developed by McHattie and Goering in 2009.

2.1. Papers Focusing on Experimental Results

Many recent papers have reported on the results from large scale field experiments involving ACE embankments in either railway or roadway projects. One of the largest of these projects was the Qinghai-Tibet rail line (QTR) that was constructed during the mid-2000s. This large project involved the construction of a new rail line connecting Goldmud near the Gobi Desert in Western China with the Tibetan center of Lhasa. The new rail line traverses approximately 630 km of warm permafrost as it crosses the Tibetan Plateau from north to south. Several instrumented test sections that utilize a variety of crushed-rock embankment structures were included in the project. Many recent papers have reported on results from this rail project. One of the early papers by Ma et al. [24] reported on the types of crushed rock – ACE structures used in the QTR project (see Figure 2-1). While these three structures were used extensively along the line, configuration b. and c. may not be optimized to produce the best cooling performance due to the location of the horizontal ACE layer at the base of the

embankment. Another early paper by Zhizhong et al. [35] reports on results from a QTR test site at Bieluhe on the Tibetan Plateau. The two test sections there employed "crushed rock slope protection", essentially a ventilated shoulder, with particle gradations of 5-8 cm and 40-50 cm. Initial results showed that the larger material was more effective at cooling the embankment side slopes. In a separate more recent study, Luo et al. [23] examined a longer record of temperature trends beneath a section of the QTR project. Their results were for a section where both side slopes included a ventilated shoulder (similar to Figure 2-1 a.). They found that over an eleven-year period (2003 – 2014) significant cooling took place under the test section with the permafrost table moving up into the base of the embankment over time and deeper permafrost temperatures cooling. Based on these results they were able to confirm the effectiveness of the design in terms of preserving permafrost beneath the embankment. Similarly, Mu et al. [25] examined temperatures beneath several different test sections along the QTR line and found that the permafrost table aggraded under all of the test sections over a 13-year period. Figure 2-2 shows the results they obtained for five different test sections (labelled HX, FHS, WDL-2, WL, KXL-3), the details of which can be found in the paper. Finally, a third study on the long-term cooling effectiveness of the QTR ACE sections was recently completed by Zhao et al. [34]. In this paper a 13-year data set was examined for three test sections with configurations similar to those shown in Figure 2-1. They also found that each of the test sections was effective at reducing subgrade permafrost temperatures and decreasing the depth to the top of the permafrost table. Their results showed that temperatures beneath the ACE test sections were reduced by 0.45-2.20°C compared to conventional (non-ACE) sections.

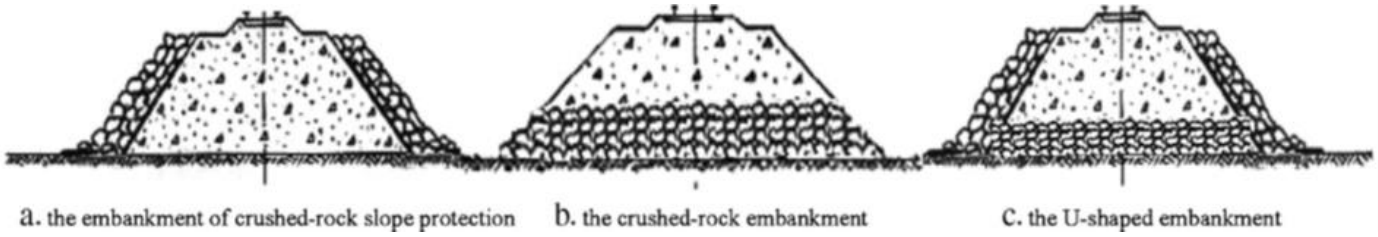

Figure 2-1 Crushed rock configurations used in the QTR project (Ma et al. [15])

Two other recent papers were focused on other aspects of the QTR ACE section performance. Liu et al. [22] examined the impact of including an impermeable cover over the upper surface of a ventilated shoulder. Their test section is shown in Figure 2-3. In this work the investigators focused on reducing side-slope heating during the warm season, enhancing forced convective cooling due to prevailing winds, and preventing the contamination of the ACE layer by wind-blown sand. Other papers have noted that fouling of ACE crushed rock layers by wind-blown sand has been a problem in several sections of the QTR project. In another recent experimental study, Pei et al. [27] used a laboratory-scale experiment to examine the impact of varying the thickness of a ventilated shoulder rock covering. For their conditions they were able to show that the optimal thickness of the crushed rock layer is close to 1.3 m.

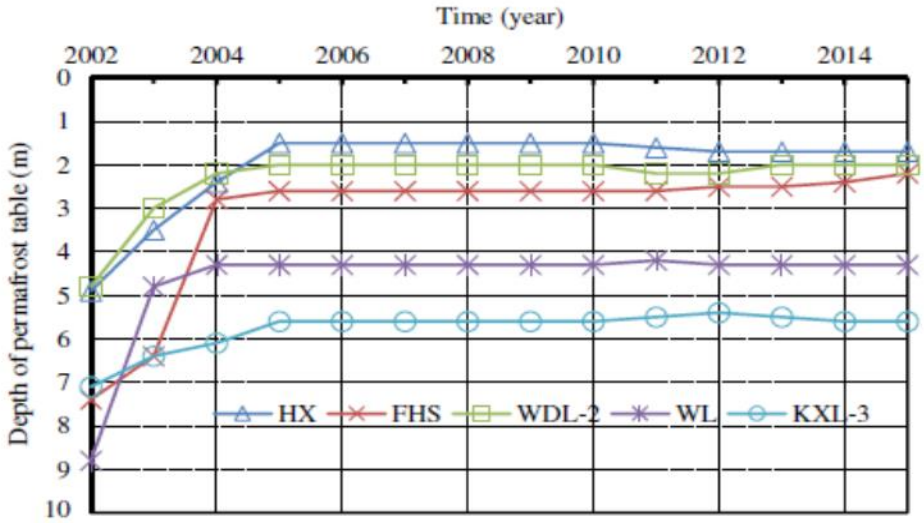

Figure 2-2 Variations in permafrost table depth over time beneath the centerline of five ACE monitoring sites (labelled HX, FHS, WDL-2, WL, and KXL-3), along the QTR. See Mu et al. [16] for details.

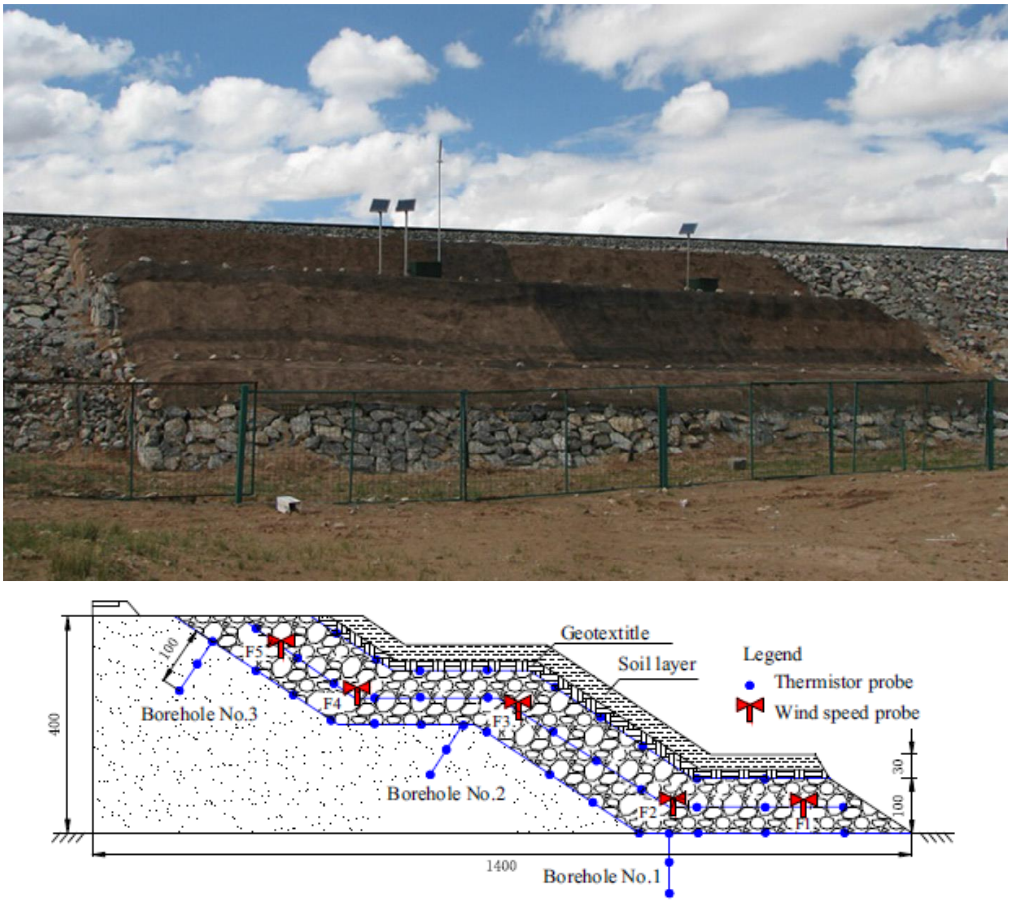

Figure 2-3 QTR test section with covered ventilated shoulder (Liu et al. [13])

In addition to the ACE test sections along the QTR project, there was an ACE test site developed at Beaver Creek in the Yukon Territory as part of a rebuilding project for the Alaska Highway. The test sites were established in 2008 and are described by Lepage et al. [20]. This paper describes difficulties associated with the re-construction project that led to significant thermal degradation of the foundation soils due to the need to excavate material from the pre-existing embankment structure. While there has been little reporting of the detailed thermal measurements from this collection of test sites, some of the data has been used to develop design tools in the recent paper by Kong et al. [17] and also used to support the modeling study of another paper by Kong et al. [16].

2.2. Papers Focusing on Modeling Studies

As for the experimental studies described above, there have been a number of numerical modeling studies published by various researchers from China, mostly focusing on aspects of the QTR railway project described above. Many of these researchers come from the State Key Laboratory of Frozen Soil Engineering in Lanzhou, China. It appears that this research group has developed its own 2D Finite Element Model that has been calibrated against experimental results and used in many of the studies described here. The recent studies of Chen et al. [4] and Yu et al. [33] focused on the detrimental impact of climate change and sand clogging of ACE structures along the QTR line. Their results showed that an ACE embankment should be able to resist climate warming for the next 20 years (assuming warming of 0.052 °C/year) so long as it is not impacted by clogging due to wind-blown sand. However, the results showed that gradual inundation of the ACE layer by sand will degrade the performance of the embankment to the point where the permafrost is no longer protected from thawing. Liu et al. [21] used a numerical model to investigate an ACE crushed rock layer that is designed for a wide expressway (see Figure 2-4). The results showed that the central vent opening facilitated additional forced convection due to wind effects and increased the cooling effectiveness over that of an ACE layer with no central vent.

In addition to the papers from the Chinese researchers, there have also been several recent North-American contributions to the ACE modeling literature. Jorgensen et al. [15] used a commercial CFD code (Fluent) to investigate the convective cooling in two proposed ACE geometries for application to the side slope of an embankment. Both geometries experimented with impermeable coverings over the side slope in order to limit warming during summer months. The authors noted that both the model and their laboratory tests, that were developed to support the modeling effort, are limited in terms of their ability to accurately predict performance of actual field installations. Darrow and Jensen [6] used Geoslope TEMP/W to model a field installation of an ACE embankment along the Taylor Highway near Lost Chicken, Alaska. The site was constructed in 2012 and included one instrumented section with a high-resolution (1 foot spacing) temperature acquisition cable stretched across the base of the ACE test section. TEMP/W modeling was completed with the assumption of closed boundaries at all surfaces and indicated generally colder temperatures than were measured in the field. More recently, Kong et al. [16] used SoilVision's SV Heat modeling package (conduction only, no air convection was included) to examine data from the Beaver Creek test site (described above). The goal of this work was to examine the heat balance at the base of a conventional (non-ACE) embankment and develop a design chart indicating the likelihood of permafrost degradation beneath the site. The numerical model was calibrated using measured data from the Beaver Creek site and a design chart was developed that indicated whether permafrost beneath the site would be stable or unstable based on embankment

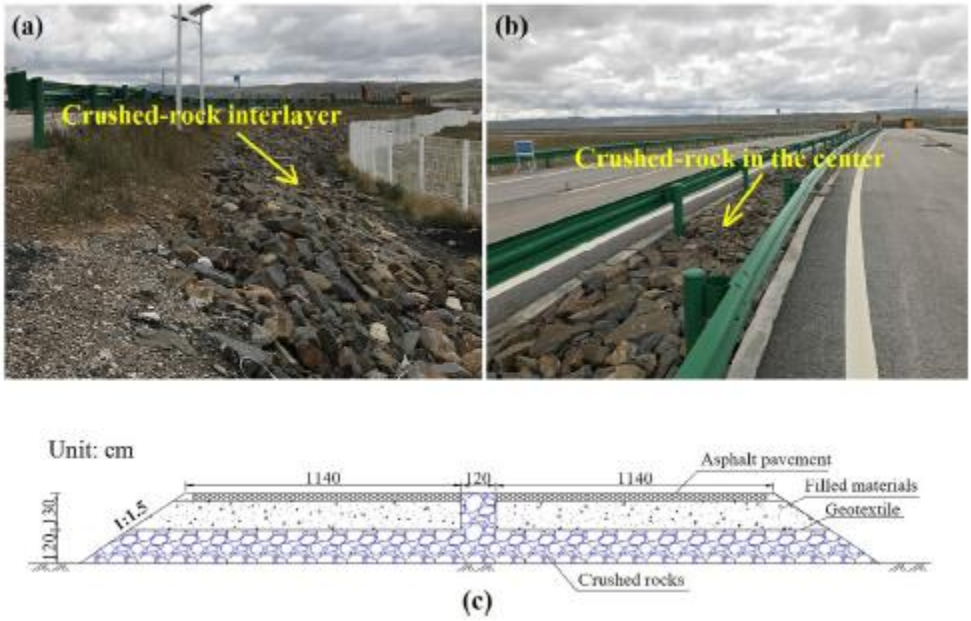

Figure 2-4 ACE layer with center vent designed for use in a wide expressway (Liu et al. [21])

thickness and thermal gradient at the embankment base. A similar technique was utilized in Kong et al. [17] to develop a design methodology for convective cooling systems (ACE layers and heat drains) that were also installed at the Beaver Creek test site.

2.3. Papers Focusing on Material Properties

In addition to the publications described above that focused on experimental or numerical investigations of ACE-type installations, a number of recent papers have investigated the thermal and hydraulic properties of crushed rock and open graded aggregate in order to support better modeling accuracy of these systems. Lebeau and Konrad [18] investigated the use of the Boussinesq approximation in the numerical modeling of ACE-type problems (their application involved a rockfill dam) and found that this approximation was an accurate way of handling the compressibility of air. In later work, Lebeau and Konrad [19], the same authors investigated the impact of non-Darcy flow and thermal radiation in convective embankment modeling. These authors compared their results for a railway embankment problem to results that I had published back in 2003 (my analysis assumed Darcy flow and had a simplified model of radiative transfer in the rock layer) and showed that there were differences once Non-Darcy flow and radiation were fully included in the model. However, differences were small and would likely become insignificant when comparing predictions to actual ACE performance in field installations. Never-the-less, the methodologies identified in this paper for incorporating radiation and Non-Darcy effects are quite useful. A companion paper from this group, Fillion et al. [8], provides more information about the impact of thermal radiation on the effective thermal conductivity of materials ranging from sand to rock-fill. In addition to their work on effective thermal conductivity, the same group, Cote et al. [5], has investigated the Intrinsic Permeability of the same materials. In this paper a 1x1x1 m heat transfer cell was used to experimentally determine the intrinsic permeability of rock-fill materials. The authors essentially used known heat transfer

correlations to back out the intrinsic permeability of the porous material based on heat transfer measurements in the test apparatus. This paper provides valuable details regarding the prediction of intrinsic permeability for aggregates in the size ranges that are typically used in ACE embankments. In a series of closely related papers, Rieksts et al. [29], [30], [31], and [32], used a similar 1x1x1 m test cell to investigate heat transfer in coarse open-graded materials. These four papers also focused on laboratory techniques for measuring the intrinsic permeability and effective thermal conductivity for crushed rock materials similar to those typically used in ACE embankments. Finally, Qin et al. [28] carried out lab scale experiments aimed at measuring the solar reflectance of different types of crushed rock layers. Their interest in this topic is related to the large solar input experienced by roads and railways located on the Tibetan Plateau. Measurements there have shown that solar input on the side of an ACE type embankment can have a large impact on overall thermal performance, particularly due to the high solar input experienced on the plateau.

CHAPTER 3. EXPERIMENTAL FEATURE TEST DATA

Field data from Thompson Drive and the Alaska Highway Dot Lake Experimental Feature test sites are examined in this chapter. Both of these projects include ACE and VS embankment features while Thompson Drive also includes 150 hair-pin thermosyphons. Generally, the field data has been evaluated by examining yearly average temperature trends. Such an approach eliminates the complexities associated with daily or monthly temperature variations, focusing instead on annual average temperature behavior which is most relevant for deep soil and permafrost temperatures. For the Thompson Drive test site, temperature data was collected and stored hourly starting in late 2004 and continuing to the present day (this report details Thompson Drive data through the end of 2020). For the AK Highway site, hourly temperatures were recorded from May of 2017 until June of 2020.

The experimental data presented here focuses primarily on the thermal performance of the test sections, but casual observations were also carried out regarding the structural stability of the embankment and driving surface. It is noteworthy that, since it's construction in 2004, Thompson Drive has not required any maintenance or repaving of any portion of the roadway surface. This is in contrast to a number of repaving operations on Geist Road which is located in the same general area. At the AK Highway site, there has been some settlement in the untreated sections of the highway that abut the experimental feature (Billings and Berggren [3]) but little maintenance has been required within the test sections themselves..

3.1. Thompson Drive Experimental Results

The Thompson Drive Project underwent conceptual design during 2001. Initial discussions regarding the inclusion of air convection embankment (ACE) and thermosyphon design features within the project began during the spring of 2001. Conversations between Billy Connor, Steve Saboundjian, Malcolm Pearson (AKDOT) and Doug Goering (UAF), resulted in an initial set of proposed test sections that included a combination of ACE and thermosyphon technology. An analysis plan was formulated during April and May of 2001 and analysis of the initial test section configurations was carried out in June and July. The results of this analysis and resulting recommendations can be found in Goering [11]. As a result of these analyses, some changes were made to the final configurations and an instrumentation plan was formulated, Goering [13].

In the following sections of this report, we first summarize the details of the Thompson Drive Project including the instrumentation system and the layout of the three test sections. Data is then presented for the each of the test sections in terms of yearly average temperature contour plots and time series plots showing how individual temperatures changed at selected locations. Also presented are time series plots showing air temperature and associated thermosyphon evaporator/condenser temperatures as well as thermosyphon evaporator/condenser heat flux values (the latter for test section #3 only).

3.1.1. Instrumentation

Figure 3-1 shows an overview of the project area with the Geist Road on the left and Tanana Loop and Tanana Drive on the right side of the figure. Thompson Drive begins at Geist Road and crosses through a previously wooded area to the north. The embankment has a relatively small height near Geist Road and gradually increases in height as it heads north towards the railroad tracks. The embankment height

reaches approximately 10 m at the location of the railroad tracks in order to join the overpass. Thus, the project encompasses embankments with heights ranging from less than a meter to approximately 10 m.

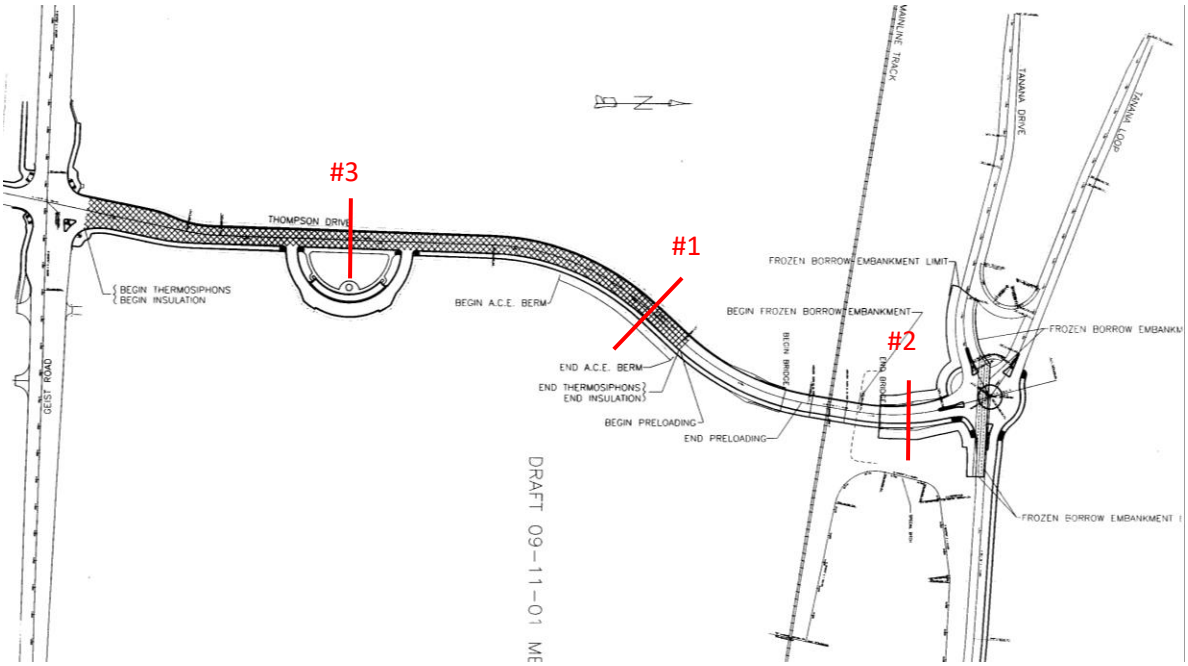

Figure 3-1 Thompson Drive test section locations

Due to the varying embankment height in different areas of the project, three types of passive cooling systems were proposed. See Goering [11] for a complete discussion and analysis of the proposed cooling systems. The first of the three consisted of an insulated roadway with an ACE side slope (VS) on the eastern side of the embankment and hairpin thermosyphons beneath the roadway. This system was utilized in the wooded area just south of the railroad tracks. The location corresponds to the area near test section #1 shown in Figure 3-1. In this area, the embankment height is approximately 4 m. The second system consists of an ACE core combined with ACE side slopes and is being utilized in the area north of the tracks (near test section #2 shown in Figure 3-1) where the embankment height is about 10 m. Finally, the third system consisted of hairpin thermosyphons alone. This system was used near Geist Road (near test section #3 shown in Figure 3-1) where the embankment height is very small. In this case, thermosyphons were utilized because the limited embankment height did not provide for enough vertical height to accommodate the needed ACE rock layer thickness for proper operation.

In order to acquire accurate information regarding the thermal performance of the three test section configurations, it was proposed that each cross section be instrumented with temperature sensors connected to data logging equipment. The original instrumentation plan can be reviewed in Goering [11]. The recommendations given there were incorporated into the design specifications, AKDOT [2]. Many of the detailed specifications for the instrumentation systems were very similar to those used for the ACE test section installed in the Parks Interchange Project, see AKDOT [1] for additional details. In particular, it was recommended that the temperature sensors consist of encapsulated/armored thermistors with a resistance of 16K Ohms at 0°C and 0.1°C accuracy. For the thermistor strings that are located in ACE material, the thermistor cables were shielded in schedule 80 PVC electrical conduit for protection against the ACE rock. Thermistor points were originally to be brought outside the PVC conduit and armored using aluminum rings (See AKDOT [2] for details). After consultation with the

instrumentation sub-contractor, an alteration to the original plan was allowed and instead of using aluminum rings, the thermistor cable was completely enclosed in the PVC conduit and sealed. Then vent holes were drilled in the PVC to allow communication with the pore air in the ACE rock. Finally, the PVC conduit was filled with silicone rubber blockages between the vented thermistors to avoid air transmission directly through the PVC shielding conduit.

Figure 3-2 shows one of the finished thermistor cables lying next to a prepared PVC shield pipe. During installation, the cables were laid out in position and then the conduit was drilled as shown in

Figure 3-2. After drilling, the cable was pulled into the proper position within the shielding tube and silicone was injected at the intermediate points to hold the cable in place and block air motion. For the thermistor strings run vertically into the foundation soil, unshielded cables were used inside a sealed PVC casing with the annulus filled with silicon oil.

Figure 3-2 Thermistor sensor wire and vented PVC armoring tube as used in ACE areas

Data acquisition equipment consists of Campbell CR10XT data loggers connected to AM416 multiplexers. Because of the distance separating the three test sections, three separate data logging stations were utilized. Each station is connected to AC power with 12 VDC backup, and contains one CR10XT data logger, and the appropriate number of multiplexers (see paragraphs below for details). AC power was unavailable for the first year of the project, so deep cycle 12 VDC batteries were used for the first year. Each of the three data acquisition stations are housed in permanent traffic controller electrical boxes (see Figure 3-3 for a photo of data acquisition station for test section #1).

The following paragraphs give a brief description of the instrumentation strings included at each test section. A photo showing test section #1, including the ventilated shoulder, is shown in Figure 3-4 while the thermistor sensor layout is shown in Figure 3-6. Note that in Figure 3-6 through Figure 3-8 the slope

Figure 3-3 Data logging station for test section #1

Figure 3-4 Photo Showing Test Section #1 and Ventilated Shoulder on Thompson Drive

angles are listed as A:B, meaning AV:BH (e.g. a slope of 1:2 indicates 1V:2H). A total of nine separate thermistor strings (strings A1-I1) are included in Figure 3-6. Strings D1 and E1 are located within the ACE ventilated shoulder layer and, thus, are shielded using vented PVC conduit. Strings H1 and I1 are fastened directly to the evaporator and condenser pipes of the thermosyphon. The remaining strings are of conventional construction and are installed vertically in sealed PVC wells with silicone oil. All instrumentation strings are run to the side of the embankment for connection to the data logging system. For this cross section, the nine thermistor strings contain a total of 62 thermistor sensors. Since each AM416 multiplexer is capable of switching up to 32 sensor lines, two multiplexers were installed at this test section. The table below lists the characteristics of each individual string.

Table 3-1 Thermistor String Characteristics for Test Section #1

String	Number of Sensors	Sensor Spacing	Construction
A1	8	2 m	Conventional
B1	8	2 m	Conventional
C1	8	2 m	Conventional
D1	6	2 m	Conventional
E1	6	2 m	Conventional
F1	5	2 m	Shielded
G1	5	2 m	Shielded
H1	4	3 m	Fasten to TS pipe
I1	4	3 m	Fasten to TS pipe

The suggested thermistor sensor layout for test section #2 is shown in Figure 3-7. A total of nine separate thermistor strings (strings A2-I2) are included in the diagram. Strings E2, F2, G2, H2, and I2 are located within the ACE layers and, thus, are shielded using vented PVC conduit. The remaining strings are of conventional construction and are installed vertically in sealed PVC wells with silicone oil. All instrumentation strings are run to the side of the embankment for connection to the data logging system. For this cross section, the nine thermistor strings contain a total of 95 thermistor sensors requiring a total of 3 AM416 multiplexers. Table 3-2 lists the characteristics of each individual string.

The thermistor sensor layout for test section #3 is shown in Figure 3-8. A total of five separate thermistor strings (strings A3-E3) are included in the diagram. For this test section there is no ACE material so none of the strings require shielding. Strings D3 and E3 are fastened directly to the evaporator and condenser pipes of the thermosyphon. The remaining strings are of conventional construction and are installed vertically in sealed PVC wells with silicone oil. All instrumentation strings are run to the side of the embankment for connection to the data logging system. For this cross section, the five thermistor strings contain a total of 31 thermistor sensors. However, during the formulation of the design plans, AKDOT personnel decided to add thermistor strings adjacent to section #3 in the

turnout area of the project, thus increasing the number of required AM416 multiplexers to two. Table 3-3 lists the characteristics of each individual thermistor string that was used beneath the roadway test section, see AKDOT [2] for additional information regarding the thermistor strings beneath the turnout area.

Table 3-2 Thermistor String Characteristics for Test Section #2

String	Number of Sensors	Sensor Spacing	Construction
A2	8	2 m	Conventional
B2	8	2 m	Conventional
C2	7	2 m	Conventional
D2	4	2 m	Conventional
E2	15	1 m	Shielded
F2	16	1 m	Shielded
G2	17	1 m	Shielded
H2	12	2 m	Shielded
I2	8	2 m	Shielded

Table 3-3 Thermistor String Characteristics for Test Section #3

String	Number of Sensors	Sensor Spacing	Construction
A3	7	2 m	Conventional
B3	7	2 m	Conventional
C3	7	2 m	Conventional
D3	4	3 m	Fasten to TS pipe
E3	4	3 m	Fasten to TS pipe

In addition to thermistor sensors, it was also decided to add heat flux sensors to the thermosyphon evaporator and condenser pipes in test section #3. Six Omega HFS-4 heat flux sensors were glued directly to the evaporator and condenser pipes at the positions shown by the blue dots in Figure 3-8. These sensors produce a nominal output voltage of 2 $\mu V/(W/m^2)$. The addition of these sensors required six additional data channels which were available on the second AM416 included in test section #3. Figure 3-5 shows a photograph of one of the heat flux sensors being attached to the evaporator tube using quick set epoxy. After attachment of the heat flux sensors, an additional layer of an

epoxy/carbon powder mix was placed over the top of the sensors to shield them from impact. Also, a thick layer of silicone rubber was placed over the lead wires to help avoid damage due to compaction around the thermosyphons. The carbon powder was added in an attempt to better match the thermal conductivity of the epoxy sensor coating with that of the surrounding bedding material. In addition, the heat flux sensors were fastened to the side of the thermosyphon tubes (as opposed to the top or the bottom) in an effort to average out any peripheral heat flux variation.

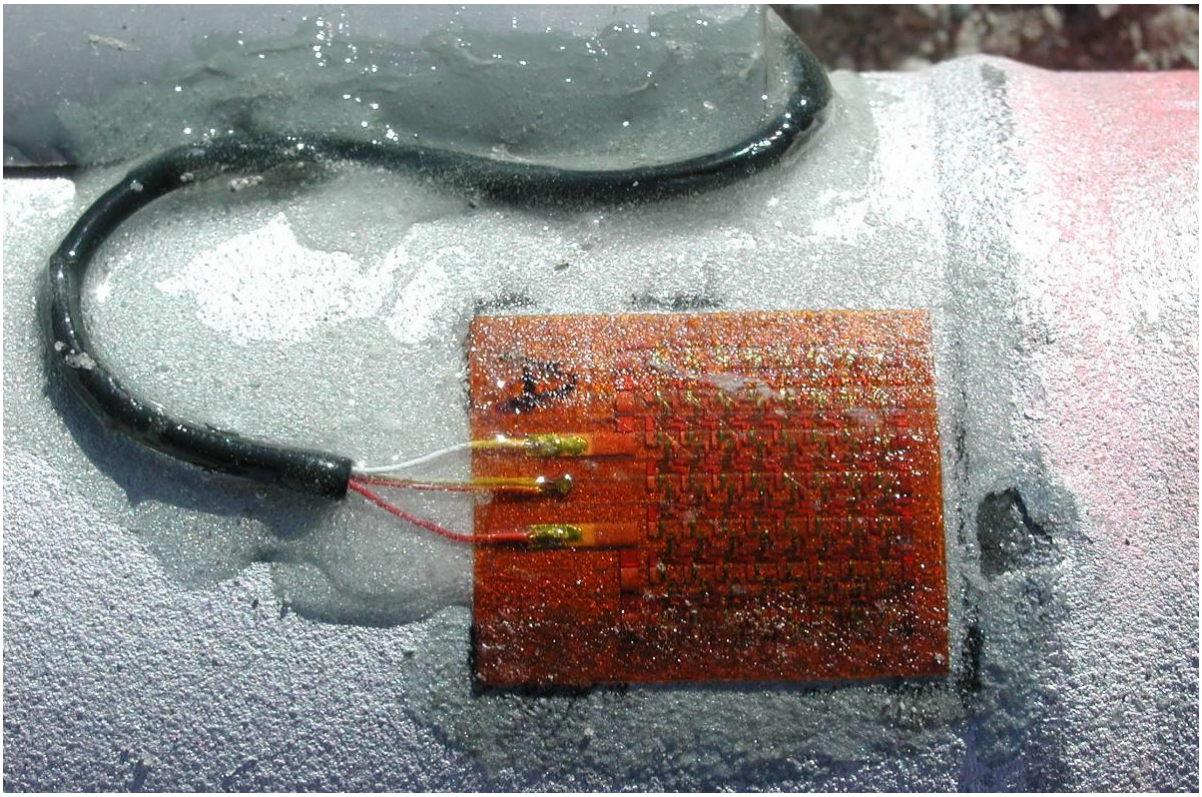

Figure 3-5 Installation of heat flux sensor on condenser tube

The data logging system described here has been used to collect data from each of the three test sections on a regular basis since late 2004. All thermistors are measured each 15 minutes with resistance values converted to hourly average temperatures and stored in an SM4 storage module. The storage modules were set in “ring” mode and programed to overwrite data once the module fills up. This results in a storage capacity of roughly 1.5 years (depending on the number of thermistor sensors at each test section), which necessitates annual data downloads (there are no external communication connections, so the storage modules must be downloaded manually on an annual basis using a laptop computer). Regular data downloads have taken place annually since the project was initiated in 2004.

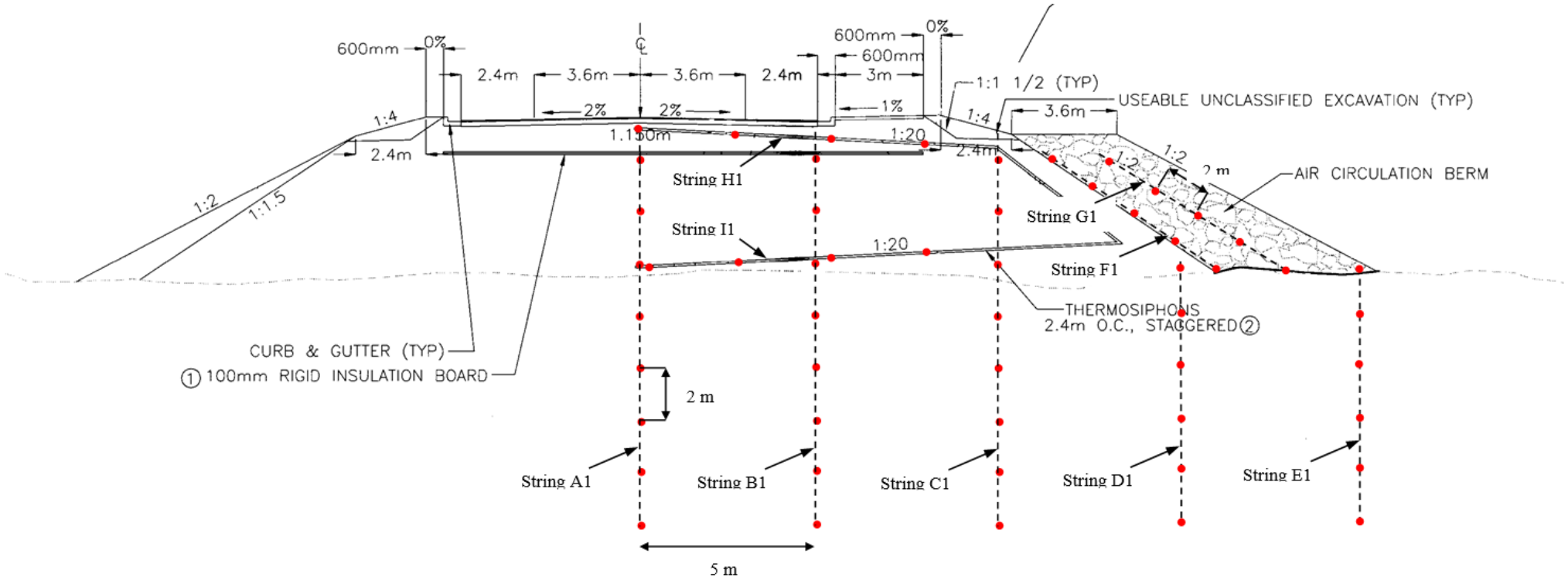

Figure 3-6 Instrumentation for test section #1 consisting of 9 thermistor strings with a total of 62 thermistor temperature sensors

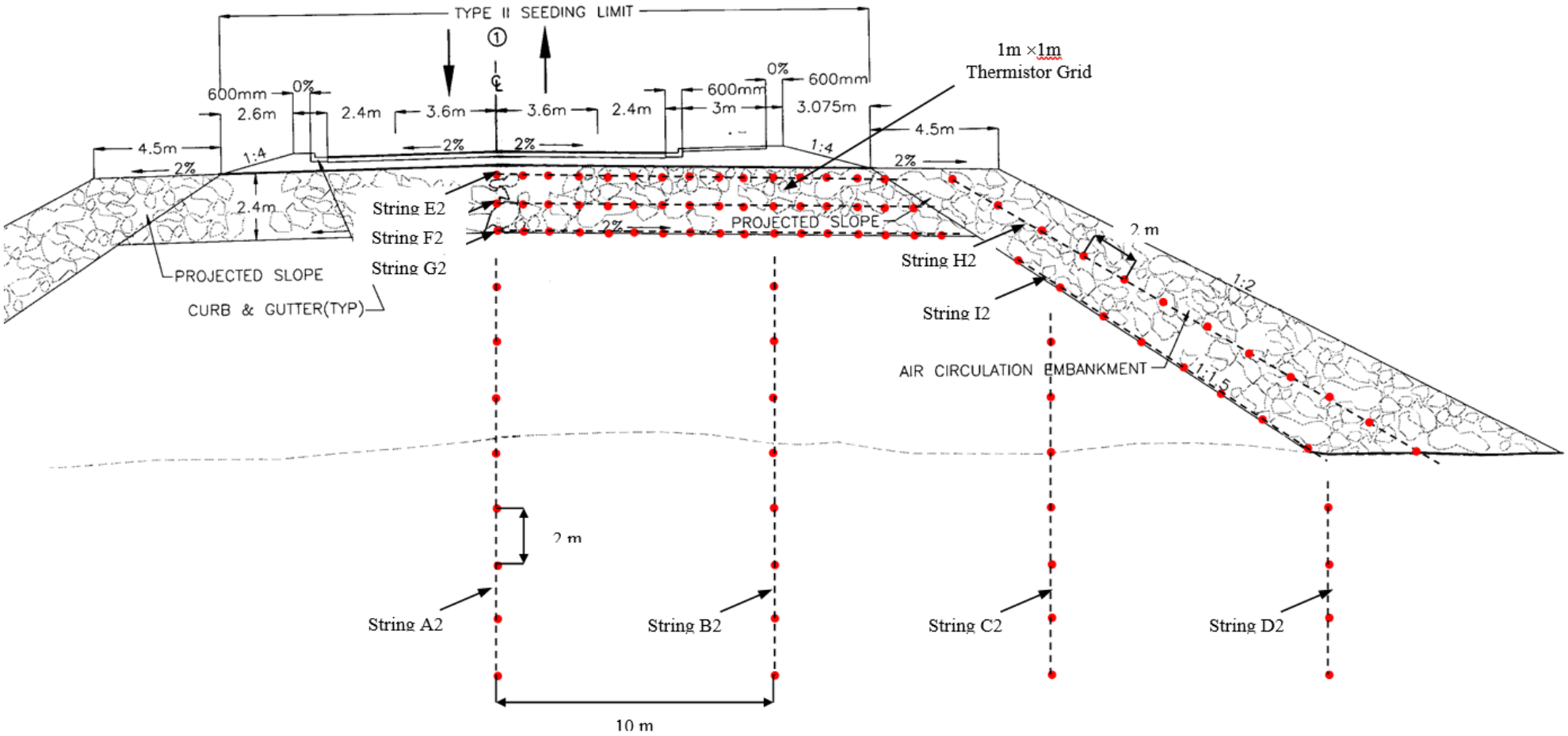

Figure 3-7 Instrumentation for test section #2 consisting of 9 thermistor strings with a total of 95 thermistor temperature sensors

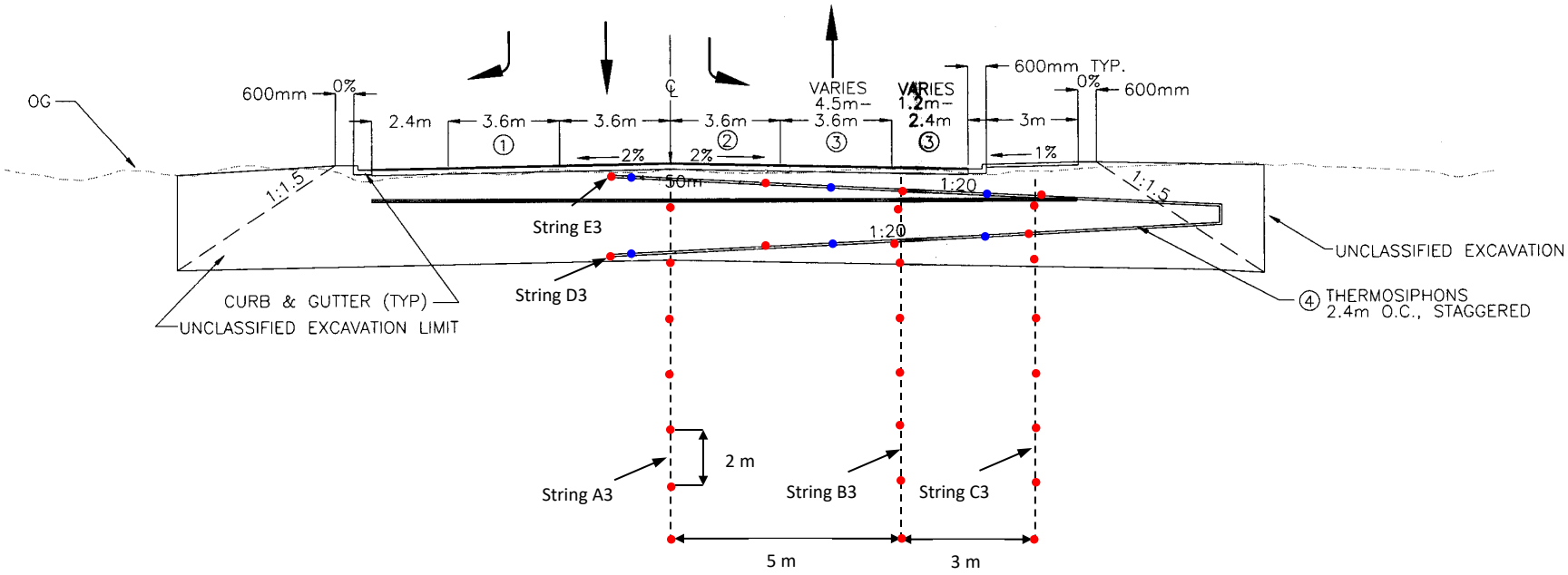

Figure 3-8 Instrumentation for test section #3 consisting of 5 thermistor strings with a total of 29 thermistor temperature sensors

3.1.2. Thompson Drive Air Temperatures

The data logging stations at each of the Thompson Drive test sections include an air temperature sensor that is located in a radiation shield fastened to the side of the data logger enclosure. The air temperature sensor for test section #1 can be seen attached to the side of the enclosure shown in

Figure 3-3. Air temperature data is collected on the same schedule as the rest of the embankment temperatures resulting in hourly temperature readings extending from late 2004 to the present time. While this temperature record includes the details of daily temperature fluctuations, it is the annually averaged value of air temperature that has an impact on deeper embankment and foundation soil temperatures.

The air temperatures collected from test section #1 were used to calculate mean annual air temperatures for the Thompson Drive project as shown in Table 3-4. Test section #1 was selected because the air temperature sensor at that station is fastened to the north side of the instrumentation enclosure, thus limiting the impact of solar heating on the measured values. In addition, test section #1 is midway through the project and at roughly the average project elevation. In addition to test section #1 temperatures, Table 3-4 also includes data obtained from NOAA for the Fairbanks airport and the annually averaged Pacific Decadal Oscillation (PDO) Index.

Table 3-4 Mean Annual Air Temperatures at Thompson Drive and the Fairbanks Airport

Year	Mean Annual Air Temp. Thompson Drive Test Section #1 (°C)	Mean Annual Air Temp. Thompson Drive Test Section #1 (°F)	Mean Annual Air Temp. Fairbanks Airport NOAA (°C)	Mean Annual Air Temp. Fairbanks Airport NOAA (°F)	Mean Annual PDO Index
2005	-0.42	31.2	-1.56	29.2	-0.19
2006	-2.13	28.2	-3.17	26.3	-0.35
2007	-1.05	30.1	-2.22	28.0	-0.70
2008	-2.69	27.2	-3.28	26.1	-1.66
2009	-1.40	29.5	-2.00	28.4	-1.03
2010	-1.00	30.2	-1.67	29.0	-1.06
2011	-1.35	29.6	-2.39	27.7	-1.81
2012	-3.04	26.5	-4.39	24.1	-1.73
2013	-1.11	30.0	-2.17	28.1	-1.17
2014	0.10	32.2	-0.61	30.9	0.55
2015	0.11	32.2	-1.11	30.0	0.92
2016	0.78	33.4	-0.21	31.6	0.67
2017	0.00	32.0	-1.39	29.5	-0.09
2018	0.29	32.5	-0.83	30.5	-0.36
2019	1.33	34.4	0.28	32.5	-0.15
2020	-1.77	28.8	-2.78	27.0	-1.14

Papeneau [26] discusses the connection between the PDO Index and weather patterns in Alaska and shows that there is a general tendency for winter temperatures in the Interior of Alaska to be warmer

during periods of relatively high PDO index values. This correlation can be seen clearly in Figure 3-9 which shows annual average values of Thompson Drive air temperature, Fairbanks airport air temperature, and PDO index. Fairbanks airport temperatures averaged -2.54°C (27.4°F) for the years 2005 through 2013, close to the long-term mean for Fairbanks air temperature. Average temperatures at Thompson Drive were generally about 1°C warmer than those reported at the airport, which is likely due to differences in elevation and the location of Thompson Drive at the base of College Hill. The years 2014 through 2019 corresponded to a period of relatively high PDO values and warm air temperatures. During those five years, air temperatures averaged -0.65°C at the airport and +0.44°C at Thompson Drive, substantially warmer than long-term average air temperatures for Fairbanks. In 2020 the PDO index dropped and air temperatures returned to values more in line with long-term average values for Fairbanks.

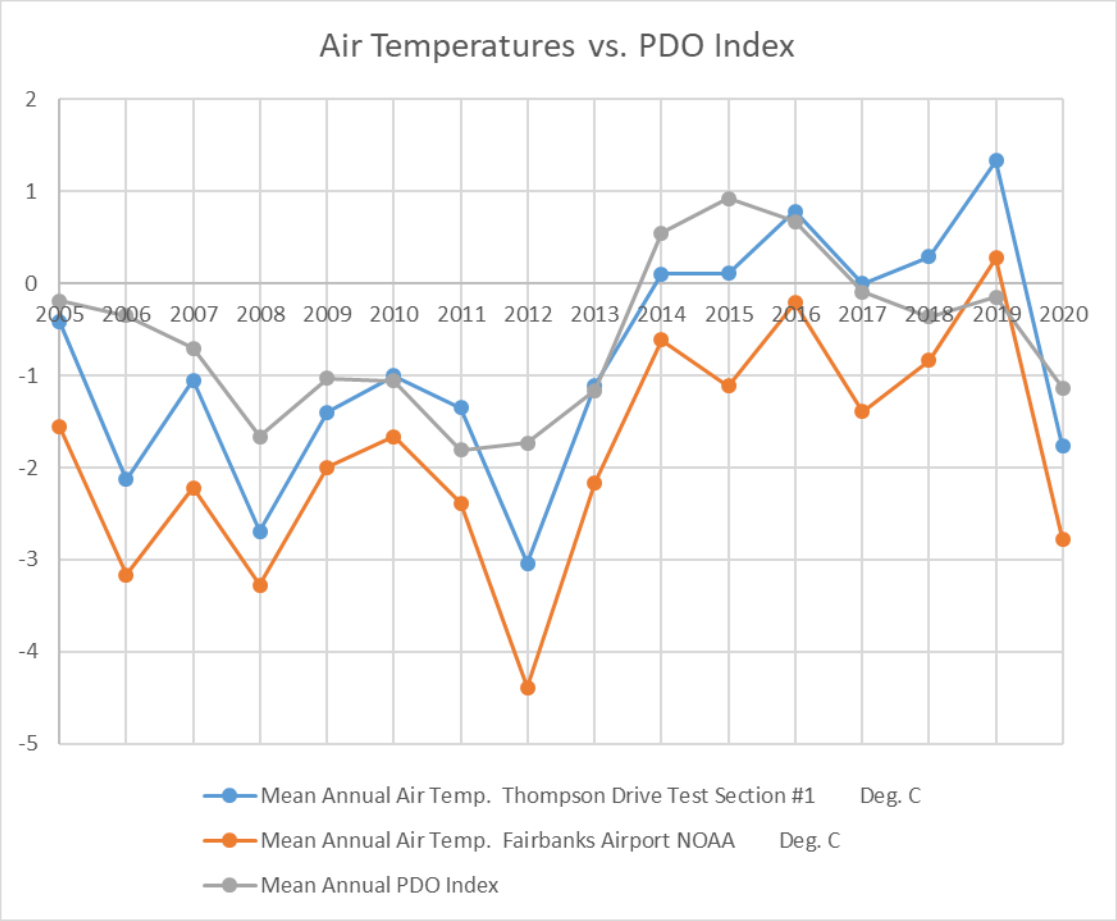

Figure 3-9 Thompson Drive and Fairbanks Airport Mean Annual Air Temperatures vs. PDO Index

An examination of the temperature profiles for Thompson Drive shows that the thermal performance of the ACE, VS, and thermosyphon installations were influenced significantly by the warmer ambient air temperatures experienced in the 2014-2019 time period**, however, it appears that sufficient cooling was maintained even during these warm years to avoid any thawing in the subsurface permafrost layers**.

Significant finding tending to indicate that the system can withstand some climate warming.

3.1.3. Mean Annual Temperature Profiles for Thompson Drive

Mean annual temperature contour plots are contained in APPENDIX A , APPENDIX B , and APPENDIX C , for test section #1, test section #2, and test section #3, respectively. In each case, the mean annual temperature values are calculated by simply averaging the individual hourly temperature measurements for the entire calendar year. For test section #1 and #2, the contour plots have been produced separately for the ACE/VS structures and the core of the embankment and foundation soil. This is due to the fact that the sharp differences in temperature behavior between the rock layers contained in the ACE/VS structures and the conventional materials contained in the embankment core and foundation did not allow the contouring routine to accurately depict the different contour characteristics. In each of the figures, the actual position of the temperature sensors is given by the '+' symbols. For test sections #1 and #3, mean annual temperature contours are provided for each calendar year spanning from 2005 to 2019. However, data logging problems at test section #2 did not allow for an accurate calculation of mean annual temperature for the years 2010, 2011, 2012, 2014, 2015, 2016, 2017, 2018, and 2019. The data logging problem at this site was traced to a bad connection on one of the AM416 multiplexers which was corrected during 2019, allowing the calculation of mean annual temperatures for test section #2 for the final year of this study (2020).

Prior to the generation of the contour plots contained in the appendices, the raw data files were examined carefully to identify erroneous data. Given the nature of the mechanical AM416 Multiplexers, periodic measurement or data registration errors were inevitable. However, this happened very infrequently (perhaps a few times per year) and typically only occurred for a single set of hourly measurements at a time. Data processing routines were developed in the Python programing language that identified problematic data in the raw temperature data files and marked bad data points. After identification, bad data was either replaced by interpolating between good values or removed entirely from the analysis. The only extensive data collection problems experience occurred at test section #2 (as noted above). In this case, a consistent problem with one of the AM416 multiplexer connections resulted in data loss for a significant portion of those years noted above, precluding the calculation of an accurate mean annual temperature. Still, as will be shown later, the remaining measurements provided a good indication of cooling effectiveness for test section #2.

3.1.4. Mean Annual Temperatures for Test Section #1

As shown in Figure 3-6, test section #1 consists of a conventional embankment with an embedded hairpin thermosyphon and a ventilated shoulder. The test section includes a total of 62 thermistor temperature sensors, 10 of which are contained in the ventilated shoulder layer. APPENDIX A includes mean annual temperature contours for test section #1 shown separately for the core of the embankment and ventilated shoulder. As a reminder, a photo of this test section (looking from the north) can be seen in Figure 3-4. The contour plots include the zone from the centerline of the embankment out to the edge of the VS toe. The base of the VS is located at the level of the original ground surface and the contour plots extend below original grade to a depth of 10 m. The position of the hairpin thermosyphon is indicated by the heavy dark line in the plots with the evaporator located roughly 4 m below the asphalt and the condenser placed above the insulation layer (light gray line in the plots) just below the driving surface.

Figure A-1 shows mean annual temperature profiles for the first year of operation (2005). Portion (a) of the figure shows temperatures in the VS rock layer, while (b) shows the temperatures in the core of the

embankment with the VS rock layer shaded. The figure shows that deeper foundation soil temperatures are in the range of 0 - -0.2°C, indicating very warm permafrost conditions. Soil cores taken during site investigations did indicate frozen material beneath the site, but clearly the permafrost layer is quite warm and likely susceptible to thawing under normal roadway embankment conditions (i.e. without any cooling measures). The figure indicates very little cooling influence during the first year of operation, although there is a notable cold zone forming just beneath the VS with a depression of mean annual temperatures of about 1°C at the lower left corner of the VS structure. Note that the thermosyphon evaporator does not appear to provide any cooling influence during this time frame, but that may be a result of the fact that the roadway was not maintained for the first part of 2005 since it had not yet opened for public use. As a result, snow was allowed to accumulate on the driving surface likely insulating the thermosyphon condenser from the cold winter air mass and, thus, reducing cooling capacity.

Figure A-1 (a) shows average temperature contours for the VS structure. Note that there is a dramatic shift in mean annual temperature values between the top (~+2.5°C) and bottom (~-4.0°C) of the shoulder layer. This is a direct result of the intrusion of cold winter air into the toe of the shoulder and upward convection through the rock. This pattern of winter air convection provides the maximum cooling effect in the lower reaches of the rock VS layer, resulting in very low mean annual temperatures. Table 3-4 shows that the mean annual air temperature for 2005 was -0.42°C, so the convective cooling effect was able to depress average annual temperature by about 3.5°C at the base of the VS toe.

Figure A-2 shows annual average temperature contours for calendar year 2006. For this year, a much more pronounced cooling effect is indicated in the temperature data. Unlike 2005, now it is easy to see the cooling influence of the hairpin thermosyphon with mean annual temperatures depressed by about 1°C in the region of the evaporator as compared to the surrounding temperatures. Also, the influence of the VS has grown with a significantly larger (and colder) zone of temperature depression beneath the side-slope. In this case, a temperature depression on the order of 2.5°C is indicated in the zone just beneath the shoulder. Temperature profiles within the rock layer of the VS are also somewhat colder than they were for 2005, as indicated in Figure A-2 (a).

For the years 2006 through 2013, annual air temperatures at Thompson Drive remained relatively cold, as shown in Figure 3-9. Mean annual temperature contours for test section #1 during this time period can be found in Figures Figure A-2 through Figure A-9. As shown in these figures, every year provided additional cooling in the foundation soils beneath the test section. Temperature depressions in the vicinity of the thermosyphon evaporator increased to roughly 2°C while temperature depressions beneath the VS side-slope increased to roughly 3°C. The zone of cooling produced by the VS and that produced by the thermosyphon have merged to a certain extent and effectively cooled the entire foundation base from the centerline out to the edge of the toe. During the same time, temperatures within the VS rock layer remained similar or slightly cooler than they were during 2005, with mean annual temperatures of -5 to -6°C at the base of the shoulder layer and +1 to +2°C in the upper portions of the shoulder.

Figures Figure A-1 through Figure A-9 have significant implications for cooling and thermal stability of the supporting permafrost layers beneath the embankment. Figure A-9 shows that the cooling influence from both the thermosyphon evaporator and VS structure have gradually propagated downward into the underlying foundation soils. While temperatures at the 30 m depth are only slightly colder than

indicated at the beginning of the project, the upper foundation soil layers have experienced significant cooling over this time period. As shown in Figure A-9, during 2013 the -1.0°C annual temperature contour extended to a depth of nearly 8 m below the VS and 4 m below the thermosyphon evaporator.

As shown in Figure 3-9, Fairbanks and the Thompson Drive site experience a string of relatively warm years during the 2014 to 2019 time period. As discussed in section 3.1.3, mean yearly air temperatures at Thompson Drive averaged +0.44°C, significantly above freezing, during this 6-year period. While these warm temperatures are likely to become more common in the future due to climate change, they still represented a significant departure from historical Fairbanks temperatures. Figures Figure A-10 through Figure A-15 show annual temperature contours for test section #1 during this time period, and do indicate that cooling of the foundation soils was negatively impacted by the warm air temperatures. Starting in 2014 the rate of foundation soil cooling and the temperature depressions caused by the thermosyphon and VS moderated significantly. As shown in Figure A-10, temperatures in the upper foundation soil layers were significantly warmer in 2014 than they had been in 2013. Figure A-12, Figure A-14, and Figure A-15, indicate that the thermosyphon was mostly ineffective at providing a significant cooling effect (i.e. negligible temperature depression) during calendar years 2016, 2018, and 2019. This is likely due to the fact that these are the three warmest years during this time frame with average annual air temperatures of +0.78°C, +0.29°C, and +1.33°C, respectively, at test section #1. While the temperature depression produced by the VS beneath the side-slope was also negatively impacted during these years, the data does show continued (albeit reduced) cooling beneath the shoulder. Contour plots for the VS structure also show generally warmer temperatures during these three years than were experience earlier with temperatures at the base of the rock layer of ~-2.5°C instead of -5 to -6°C as shown for earlier, colder years.

While still warmer than normal, 2014, 2015, and 2017 were not quite as extreme as the other three years with mean annual air temperatures of +0.10°C, +0.11°C, and 0.00°C, respectively. As shown in Figures Figure A-10, Figure A-11, and Figure A-13, both the thermosyphon and VS produced some cooling influence during these years, although cooling was not as effective as it had been during the 2005-2013 time frame. Each of these three years produced a noticeable cooling influence near the thermosyphon evaporator and beneath the VS structure.

Perhaps most important for the warm 2014-2019 period is the behavior of the deeper foundation soil temperatures beneath the embankment. While this string of warm years seemed to halt additional cooling of the foundation soil, there was very little evidence of actual warming. For instance, examining Figure A-9 shows that temperatures at a depth of roughly 8 m below original grade had been reduced from the initial values of ~-0.2°C to values of ~-0.6°C, while Figure A-15 shows that temperatures at this depth remain in the range of -0.4 to -0.6°C after the 6-year warm period. Air temperatures returned to somewhat more normal values in 2020 and cooling beneath the thermosyphon evaporator and VS structure resumed as shown in Figure A-16.

3.1.5. Mean Annual Temperatures for Test Section #2

As shown in Figure 3-7, test section #2 consists of a relatively high embankment (located just to the north of the railroad bridge) with a horizontal ACE layer and VS layers on each side of the embankment. This test section does not contain any thermosyphons. The horizontal ACE layer has a height of 2.4 m and extends all the way across the upper portion of the embankment beneath the driving surface.

Beneath the ACE layer is roughly 8 m of select material, resulting in a total embankment height of about 10 m. The test section includes a thermistor array with a total of 95 sensors, 48 of which are located in a 1 m x 1 m grid spanning the right half of the ACE layer and 20 of which are located in two separate thermistor strings placed in the righthand VS structure. Thermistor locations are indicated by red dots in Figure 3-7. In an effort to reduce warming of underlying foundation soils, this section of the project was completed during winter, see Figure 3-10.

Figure 3-10 Winter Construction of Test Section #2

As discussed in section 3.1.3, data problems with the instrumentation system did now allow for an accurate calculation of mean annual temperatures for test section #2 in years 2010-2012 and 2014-2019, thus contour plots for these years are not included in APPENDIX B . Generally, the data for this test section is harder to interpret than that for test section #1. In some cases there are data anomalies that can only be explained by water intrusion, which is a distinct possibility but hard to quantify. Some of these anomalies may also be a result of the winter construction effort which likely caused large variations of temperature and moisture content in the select material beneath the ACE layer, see Figure 3-10 which shows winter placement of the select material.

Figure B-1 shows mean annual temperature contours for test section #2 in 2005, the first full year of measurements. As for test section #1, this portion of the roadway was not maintained during the late winter and spring of 2005 due to the fact that the road had not yet been opened for public use. As a result, snow accumulated on the top of the embankment which likely reduced the cooling effectiveness of the horizontal ACE layer. This behavior is illustrated in Figure B-1 (a) which shows relatively warm mean annual temperatures in the horizontal ACE layer of +2 to +3°C. On the other hand, cooling in the VS can clearly be seen, with mean annual temperatures of ~-5°C in the lower portions of the side slope.

This is indicative of convection through the VS rock layer which is not significantly impacted from the presence of the snow layer.

Figure B-1 (b) shows the mean temperature profiles in the underlying select material and foundation soils and closely mimics what was seen for the initial temperatures beneath test section #1. Deep foundation soil temperatures are in the range of 0.0 to -0.2°C, just barely below freezing. Much of the select material that was placed above the original grade is thawed with temperatures ranging from 0.0 to +0.6°C, this is despite the winter construction shown in Figure 3-10.

Figure B-2 through Figure B-5 show development of the mean annual temperatures during the first four years after the project was completed and opened for public use. Generally, mean annual temperatures at the base of the horizontal ACE layer are in the range of -1°C or colder, and temperatures in the VS structure are ~-6 to -8°C in the lower portions of the side slope and slightly above freezing at the top. This series of figures shows a strong cooling influence propagating downward over time from the horizontal ACE layer and the base of the VS structure. Over this 4-year period, temperatures in the select material cooled from a thawed state as shown in Figure B-1 to a frozen state as shown in Figure B-5. Figure B-5 shows a very strong cooling influence beneath the horizontal ACE layer and at the base of the VS shoulder with mean annual temperatures of about -2.5°C beneath the ACE layer to as low as -3°C beneath the base of the VS. These low mean temperatures are having a strong cooling influence on the select material and foundation soils beneath the ACE/VS layers.

Numerical simulations that were conducted as part of the design process (Goering [11]) tended to indicate that closed circulation cells would occur in the ACE and VS layers during winter, however these possible details are not revealed in the mean annual temperature plots contained in APPENDIX B . However, examining instantaneous temperature isotherms can provide some insight regarding the type of pore air circulation that is likely occurring during winter.

Figure 3-11 shows instantaneous temperature contours for test section #2 on Jan. 15, 2020. The contours shown in the figure tend to indicate larger scale circulatory flow in the VS with more than a single entry point as indicated by the hypothesized air flow patterns shown in the shoulder region. Within the horizontal ACE layer it is harder to draw conclusions from the measured isotherm shapes but the data is consistent with the hypothesized cellular flow shown**. It is clear from the figure that the warmest portion of the air convection zone occurs in the upper reaches of the side slope. Given the relatively warm temperatures in this area, it is likely that pore air is exiting through the snow layer in this area and drawing air from both the horizontal ACE layer and the lower portions of the side slope, resulting in the temperature patterns observed. It is interesting that this is different behavior than that predicted in the original design simulations (Goering [11]), however that may be a result of inaccurate boundary conditions used during the simulation process. More discussion of this point is included in CHAPTER 4**.

Another feature of note, particularly in Figure B-2 through Figure B-4, and less so in Figure B-5, is the warm zone that develops beneath the shoulder region. Note that these figures indicate mean annual temperatures, not instantaneous temperature values, so it is possible that water infiltrating downward from the right edge of the pavement structure during summer collected in the lower portion of the select material layer and caused some warming to occur. These figures indicate that there is a bubble of thawed material that develops and then persists in this area for several years after construction,

eventually freezing back. This warm zone may also have persisted as a result of somewhat less effective cooling in this area.

Figure 3-11 shows predicted temperature isotherms from the numerical simulations that were conducted as part of the design process, Goering [11]. This simulation tends to indicate a warmer zone (indicated in red shading) in this portion of the embankment and, thus, less efficient cooling at that location

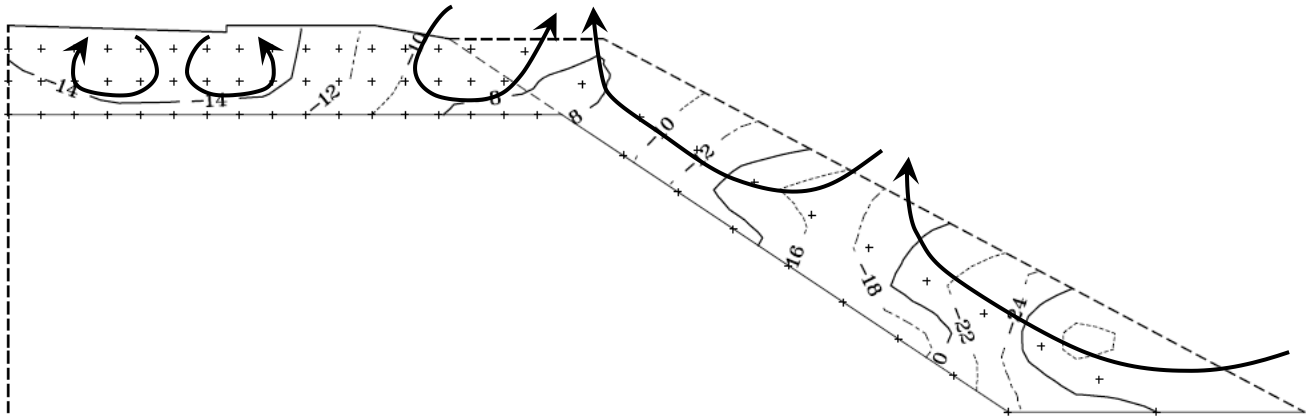

Figure 3-11 Temperature Contours for Test Section #2 on Jan. 15, 2020 With Possible Airflow Patterns

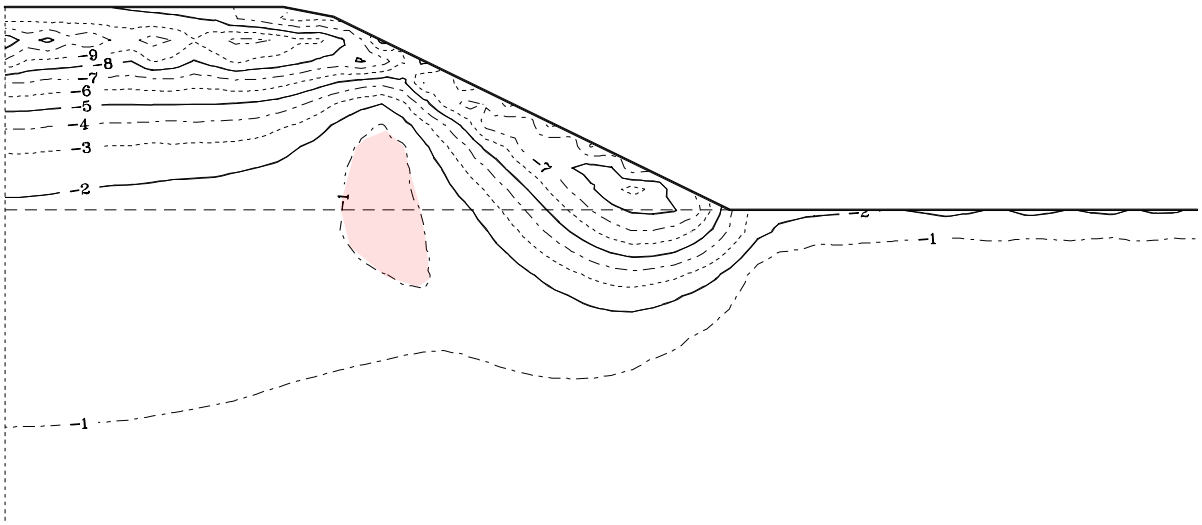

Figure 3-12 Calculated Temperature Isotherms for Test Section #2 for April, (Goering [11])

Figure B-6 and Figure B-7 show mean annual temperature contours for test section #2 for the years 2013 and 2020, respectively. Both figures show relatively cold temperatures in the select material beneath the horizontal ACE layer and the foundation soils. Temperatures are much colder than those after initial construction as shown in Figure B-1, indicating the effectiveness of the cooling influence of the ACE and VS layers. Note that 2013 followed the coldest year in the data record (see Table 3-4),

whereas 2020 followed a string of several warm years. The influence of this variable yearly annual temperature can be seen in the Figures Figure B-6 and Figure B-7. While both of these figures indicate temperatures much colder than the original foundation soil temperatures, 2013 is notably colder than 2020. Still, even in 2020, temperatures in the select and foundation soils remain substantially below 0°C, especially in the region beneath the shoulder.

3.1.6. Mean Annual Temperatures for Test Section #3

APPENDIX C shows mean annual temperature contours for test section #3. This test section contains hairpin thermosyphons but does not contain any ACE cooling features. As shown in Figure 3-8, the driving surface at this location in the project was essentially level with the original grade and did not provide any vertical height which is needed for convection to occur in ACE or VS layers. As a result, cooling for this test section is achieved using a hairpin thermosyphon that wraps around a layer of EPS insulation. The insulation layer is shown by the heavy black line in Figure 3-8, and is indicated by the gray shaded line in the APPENDIX C figures (in which the approximate thermosyphon position is indicated by the heavy black line).

Figure C-1 shows mean annual temperature contours for 2005, the first full year of measurement. As indicated above, the project had not opened for public use at this point, so a significant snow layer built up on the embankment in the spring of 2005, effectively insulating the thermosyphons and reducing their cooling impact. As a result, little cooling influence from the thermosyphon evaporator can be seen in Figure C-1. As for the other test sections, the data in this figure indicates that soils in this area of the project are also quite warm, ranging from 0.0 to -0.05°C, just barely below freezing.

Starting in 2006, Figure C-2 indicates that the thermosyphon is beginning to produce a cooling effect, with temperatures near the evaporator dropping to ~-0.35°C. Figures Figure C-3 to Figure C-14 illustrate the continued cooling which continues throughout the years. As illustrated in the yearly data, the cooling influence of the thermosyphon is not dramatic, but it is sufficient to provide a modest cooling influence beneath the insulation layer and has been able to provide the necessary cooling to keep the permafrost layer frozen beneath the embankment. At the base of the measurement zone, roughly 12 m beneath the driving surface, there is a moderate temperature reduction of ~0.1°C during the measurement period. This modest cooling effect did not seem to be diminished by the series of warm years experienced during the 2014 to 2019 time frame.

3.1.7. Time Series Data

In addition to the contours of mean annual temperatures provided in APPENDIX A , APPENDIX B , and APPENDIX C , selected temperature measurements were also analyzed as a continuous function of time. These time-series analyses give a more complete picture of annual temperature variations and long-term temperature trends at the selected measurement points, and can provide further insight into the cooling effect of the ACE, VS, and thermosyphon installations.

Figure 3-14 shows continuous temperature measurements for thermistors A1-6, B1-6, C1-6, D1-6, and E1-6 from 2005 through to the end of 2020. These temperature measurement points are located in test section #1 as shown in Figure 3-6. Note that the thermistor string sensors are numbered from the bottom of the string upwards, so the points A1-6 to D1-6 are located roughly at the elevation of the original grade beneath the embankment (essentially the sixth red dot up from the bottom on strings A1

to D1, as shown in Figure 3-6). The annual cycles of winter and summer temperatures can be seen clearly manifested in each of the five curves shown in Figure 3-14. All of the curves display a heavy bias toward below freezing temperatures with relatively short periods where they are above 0°C. The temperatures at points A1-6 and B1-6 see some winter influence from the thermosyphon cooling, while points D1-6 and E1-6 are more influenced by the ventilated shoulder. Point C1-6 is less influenced by either of these cooling systems and generally displays more stable temperature behavior throughout the year. The largest positive temperature departures are shown for temperature E1-6. This is because of the proximity of this point to the ground surface at the toe of the shoulder and, consequently, its relatively strong connection to summer air temperatures. The largest negative temperatures are experienced for temperature D1-6 as a result of its location right beneath the inner boundary of the ventilated shoulder. This is consistent with the mean annual temperature contour plots shown in APPENDIX A that indicate the strongest cooling influence from the VS centered at the location of D1-6. Temperature variations, both positive and negative, are more limited for points A1-6, B1-6, and C1-6 because of the embankment material and insulation layer covering these points. For these points, winter temperature extremes range from ~-2 to -4°C with summer extremes less than +1°C. The influence of warm winter temperatures can be seen clearly in the time series, especially for years 2014, 2016, 2017, 2018, and 2019, each of which show markedly warmer winter temperatures than the prior years (refer to Figure 3-9 for air temperature data for these years).

Figure 3-15 shows data for the same five thermistor strings as discussed above, except that these are the points at the bottom of the thermistor strings, 10 m below original grade. Note that the temperature variations over the 16-year time record at this depth are small, on the order of 0.5°C. Because of the small vertical scale used in this figure, the noise present in the temperature measurements is more apparent. Given that stated accuracy of the thermistor sensors is 0.1°C, the fluctuations shown in Figure 3-15 are not surprising. In addition, the absolute values of the readings in this figure cannot be trusted to more than about 0.1°C due to the same accuracy specification, thus it is probably better to focus on temperature trends rather than absolute values in this case. The data in the figure suggests that temperature D1-1 starts out thawed at about +0.2°C and then drops over time to about -0.5°C. Since this temperature behavior seems out of sync with the others that begin the time sequence colder, at about -0.2°C, it is possible that sensor D1-1 is reading high by 0.1°C (or perhaps a bit more). In any case, temperatures D1-1 and C1-1 experience the largest cooling trends over the 16-year period, both cooling by 0.5°C or more. These two temperature sensors are beneath the ventilated shoulder and are likely experiencing this relatively strong cooling due to the cooling influence of the winter shoulder convection. Temperature E1-1 experiences the next most significant cooling trend, dropping in temperature by about 0.3°C over the time period shown. Finally, temperatures A1-1 and B1-1 which are positioned closer to the embankment centerline, experience the least amount of cooling with temperature reductions of about 0.2°C during the 16-year time record. In all five cases the cooling trends mostly subside after 2015, probably due to the string of warm years that were experienced starting in 2014 (see Figure 3-9).

Figure 3-16 shows the temperature behavior for measurement points A2-8 and B2-8. As shown in Figure 3-7, these points are located about 2 m below the horizontal ACE layer in test section #2 (the top red dot in the figure for each thermistor string). Due to the data collection problems described in section 3.1.3, these temperature time series are not complete, but, rather, contain several sections of missing data, particularly in the years 2014 to 2019. Never-the-less, even with the missing data, the

overall behavior of the temperature at these two points is very well illustrated in the figure. Point A2-8 is located at the centerline and shows the largest annual temperature fluctuations of the two points. B2-8 is located at the same elevation and still beneath the horizontal ACE layer, but it is beneath the sidewalk where the thickness of the layer above the ACE rock (and likely the snow cover) is thicker. Thus, B2-8 shows significant annual temperature fluctuations, but they are smaller in amplitude compared to A2-8. The heavy bias towards freezing temperatures is clear in the figure. The temperature at A2-8 shows maximum summer values on the order of +6°C, whereas the minimum winter temperatures are close to -15°C, clearly indicating the strong freeze potential at this location. Likewise, for point B2-8, summer temperature maximums are on the order of +4°C while winter minimums are -6°C to -7°C. This strong cooling influence extends all the way through the 16-year measurement period with little apparent impact from the warm years (2014-2019). Finally, note that both temperature records exhibit significant temperature fluctuations during the winter season (especially for point A2-8). This is caused by the fluctuating nature of the convection that takes place in the horizontal ACE layer. During periods of particularly cold ambient temperatures, the intensity of air circulation in the ACE layer increases, thus increasing the rate of cooling in the underlying material. When winter air temperatures temporarily warm, convection ceases or is less intensive, resulting in reduced cooling beneath the ACE layer. Thus, the temperatures at points A2-8 and B2-8 are somewhat correlated with winter air temperature fluctuations.

Figure 3-17 shows the temperature time series for measurement points D2-1, D2-2, and D2-3, which are oriented vertically beneath the ventilated shoulder in test section #2 at depths of 8 m, 6 m and 4 m, respectively, below original grade (see Figure 3-7). Unfortunately, the thermistor sensor at point D2-4 was damaged and non-functional, so that point is not included in the figure. These three temperatures indicate how well the ventilated shoulder is able to cool the foundation soil immediately below the shoulder. The temperature at D2-3 initially increases and remains slightly above 0°C for much of the first year of measurement. This is likely due to disturbance of the soil column during construction and may also be related to water infiltration and drainage patterns after the embankment construction was completed. However, during the second year of measurements, the temperatures at D2-3 again drop below 0°C and then begin a period of strong cyclical yearly cooling in 2007 and beyond, eventually reaching a minimum value of -4.4°C during the winter of 2013. For 2014 to 2020 the rate of cooling at D2-3 moderates, likely due to the warmer yearly air temperatures experience during that time frame. The temperatures at D2-1 and D2-2 mimic the behavior of D2-3 with the exception that there is no thawing indicated during the 2005-2006 time frame and the amplitude of the yearly cyclical cooling is diminished for these points compared to D2-3 due to their increased depth. Careful inspection of Figure 3-17 also shows an increasing time lag in thermal response as depth increases from D2-3 to D2-1 which is also a function of increasing depth.

Figure 3-18 shows temperature time series for measurement points A2-5, B2-5, and C2-5 which are located close to the original ground surface in test section #2 as indicated by the dashed line in Figure 3-7. The temperature at measurement point C2-5 shows increasing temperature for the first four years of measurements before beginning to experience cooling. During this time frame the temperature at this point reaches a maximum value of about +0.2°C. As for the point D2-3 discussed above, this warming behavior at C2-5 is hypothesized to be related to water infiltration during the early years of the project. The location of point C2-5 is beneath the upper portion of the side-slope about four meters away from the edge of the seeded top soil at the surface. It is likely that any water from snowmelt or

summer precipitation would work its way downward into the select material of the embankment core at this location, thus providing a warming influence at the location of C2-5. After successive infiltration events, the select material at this location eventually becomes saturated and refreezes due to the cooling influence of the ventilated shoulder above. Once refreeze occurs in 2009 the temperature begins to experience a strong annual cooling cycle with temperatures eventually dropping as low as -2.1°C in 2013. After 2013 cooling at this point moderates due to warmer ambient air temperatures in the 2014-2019 time frame. At points A2-5 and B2-5 temperature variations are much smaller over the measurement period. Point B2-5 appears to experience a very mild increase in temperature (but no thawing) from the beginning of the temperature record until about 2012, after which it begins to cool. Point A2-5 experiences only cooling for the entire measurement record with an increase in cyclical cooling after 2011. Temperatures at A2-5 cool from their initial value of about -0.1°C to the range of ~-0.3°C to -0.5°C by about 2014 and then seem to settle into a regular range of annual oscillation without further cooling.

Figure 3-19 shows temperature time series for points A2-1, B2-1, C2-1, and D2-1, which are located roughly 8 m below the original grade and nearly 20 m below the elevation of the driving surface at the top of the embankment in test section #2. All four of the temperature series shown in the figure show temperature reductions over time, with the temperature at point D2-1 displaying the largest drop and point A2-1 only a minimal reduction. Point D2-1 is located 8 m beneath the inner corner of the ventilated shoulder and, thus, is strongly influenced by convective cooling in the shoulder ventilation layer. Note that the strong cooling influence takes some time to propagate downward to point D2-1, with strong cyclical cooling not becoming apparent until 2009, four years after construction. Points A2-1 and C2-1 show more muted behavior with only mild temperature depressions over the measurement period. On the other hand, point B2-1 appears to start in an initially thawed state and then begin to cool in about 2011, eventually cooling to about -0.6°C. This seemingly anomalous behavior may be a result of water movement, or, potentially a case of a mis-calibrated thermistor. While it is hard to know for certain what is happening at this point, examination of the temperatures at points directly above B2-1 (i.e. points B2-2, B2-3, and B2-4) shows that all of those points remain frozen during the entire data collection period, tending to lend evidence to the suggestion that B2-1 may be mis-calibrated or damaged in some way and producing erroneous temperature readings.

Figure 3-20 shows temperature time series for points A3-6, B3-6, and C3-6, which are located at the base of the unclassified excavation as shown in Figure 3-8. These measurement points lie less than a meter below the thermosyphon evaporator and roughly 2 m beneath the insulation sheet. As shown in the figure, the temperatures at all three measurement points were relatively warm the first winter and summer, with winter values of -0.2°C to -0.9°C for the three points, and summer values of just above 0°C to +1.5°C. These warm temperatures are due to the fact that the roadway was not maintained during the winter of 2005 and snow was allowed to accumulate on the driving surface, thus insulating the thermosyphon condenser. After 2005, however, there is a record of eight continuous years of fairly strong winter cooling with point A3-6 dropping into the range of -2°C to -3°C each winter. Points B3-6 and C3-6 were somewhat warmer in winter, but still generally in the range of -0.5°C to -2°C. During summer, only point B3-6 showed any significant thawing. Starting in 2014, however, the cooling potential of the thermosyphon was more limited due to generally warmer ambient temperatures during the winters of 2014-2019. Not only are winter temperatures of all three points warmer, starting in about 2016, all three points begin to show significant warming above 0°C during summer with

temperatures topping out in the range of +1°C to +2°C during the summer of 2019. Looking at the record as a whole, it is clear that the years between 2006 and 2016 indicate that the thermosyphon generated a fairly strong freeze potential beneath the insulation sheet. This resulted in cooling of the foundation soils as discussed in Section 3.1.6. However, for the later years cooling and foundation freezing potential is more limited due to the warmer ambient air temperatures and little additional cooling occurred in the foundation soils beneath this test section.

Figure 3-21 shows temperature time series for the points A3-1, B3-1, and C3-1 which are located about 13 m below the driving surface in test section #3 as shown in Figure 3-8. The data in this figure is somewhat difficult to interpret and it may be that some of the data, in particular, the data for B3-1 may be impacted by mis-calibration of the temperature measurement. For instance, other measurement points at similar depths beneath test section #3 indicate frozen conditions at the beginning of the project. Thus, the temperature values indicated by points A3-1 and C3-1, ranging from -0.1°C at the beginning of the measurement record to -0.11°C to -0.27°C at the end of the record are reasonable. Based on these and other observations, it is unlikely that the temperature at B3-1 is actually above 0°C, and thus may be in error in absolute terms. Despite that, the temperature trend displayed by the B3-1 measurement is probably accurate, indicated a cooling of ~0.13°C during the measurement period, similar to that observed at point A3-1. Note that the point C3-1 is further from the thermosyphon evaporator which provides most of its active cooling near the lower portion of its reach (near point A3-1), so it is reasonable that the rate of cooling at that point would be lower, as indicated in Figure 3-21.

As described in Section 3.1.1, and shown in Figure 3-8, the hairpin thermosyphon in test section #3 was instrumented with heat flux and surface temperature sensors. Three heat flux sensors were located on the evaporator and three on the condenser, with positions shown by the blue dots in Figure 3-8. Figure 3-22 shows a time record of the heat flux measurements for the first four years of the measurement period. Despite the efforts to protect the heat flux sensors from mechanical failure as described in Section 3.1.1, these sensors proved to be quite fragile and several of them failed within the first four years of measurements. Still, the data shown in Figure 3-22 is quite valuable and provides quite a bit of insight into the thermosyphon performance. Of the six heat flux sensor values shown in the figure, HF-A, HF-B, and HF-C are fastened to the evaporator (the lower portion of the hairpin), with HF-A located at the lowest elevation near the evaporator tip. HF-D, HF-E, and HF-F are fastened to the condenser with HF-D located near the upper tip of the condenser. The data in Figure 3-22 shows distinctly different heat flux behavior for winter as compared to summer as would be expected for thermosyphon operation. During winter the system is active with heat entering the evaporator (negative heat flux) and exiting out the condenser (positive values). During summer the system becomes inactive and heat flux values for both the evaporator and condenser collapse to near zero. Note that the heat flux values during the 2005 time frame were more modest than those seen in later years. This is a result of the lack of snow clearing on the roadway surface during the winter of 2005 which added insulation to the condenser heat flow path and reduced overall performance.

Examining the data in Figure 3-22 for the winter of 2005-2006, shows essentially mirror image behavior for HF-A and HF-D, both of which generate the largest heat flux values shown. This is interesting as it implies that the highest thermosyphon cooling capacity occurs near the evaporator tip and that the highest rate of heat rejection occurs at the upper tip of the condenser. Note also that the heat flux data is in close synchronization with ambient temperature fluctuations (air temperature values are shown in

Figure 3-23 for the same time period), with colder air temperatures resulting in enhanced heat flux values. Heat flux values further away from the evaporator or condenser tip (points HF-B and HF-C on the evaporator and points HF-E and HF-F on the condenser) are generally lower than those at the tip, although the heat flux appears to be somewhat more evenly spread along the condenser than it is along the evaporator. Unfortunately, HF-A became non-functional in August of 2006 after roughly two years of service and HF-B failed in June of 2007, thus the heat flux data for 2007 and beyond is limited.

Figure 3-23 shows thermosyphon evaporator and condenser temperatures for the first four years of the measurement time frame. In addition to the four temperature measurements on the evaporator (D3-1 to D3-4) and the four temperature measurements on the condenser (E3-1 to E3-4) the figure also includes a curve showing ambient air temperature over the time period. As was the case for the heat flux values described above, the evaporator and condenser temperatures show distinctly different behavior for summer periods as opposed to the behavior seen during winter. During winter all eight evaporator and condenser temperatures track fairly close to one another with maximum temperature differences of ~5°C for the entire group. During summer, the condenser temperatures (E3-1 to E3-4) track air temperature trends closely, although they are typically elevated above air temperatures by as much as 5°C to 10°C. This is a result of solar heating of the asphalt driving surface during summer and indicative of a large thawing N-factor at the pavement surface. On the other hand, evaporator temperatures (D3-1 to D3-4) remain relatively cool during summer and show a significant "zero curtain" during the thaw period in early summer. Even after the material around the evaporator thaws out, temperatures climb only modestly and remain ~20°C cooler than the condenser temperatures.

The data shown in Figure 3-23 is indicative of the behavior we would expect for proper thermosyphon operation. During winter the system "turns on" and the two-phase heat transfer consisting of evaporation/boiling of the working fluid in the evaporator and condensation of the working fluid in the condenser tends to drive the evaporator and condenser temperatures to the same values, as seen in Figure 3-23. During summer the evaporation-condensation process ceases since the liquid puddle in the evaporator is at a lower temperature than the condenser, and, thus, there is no active heat transfer mechanism to drive the evaporator and condenser temperatures to the same values. In terms of heat transfer, Figure 3-22 shows that the evaporator is performing properly by removing a substantial amount of heat from the surrounding material during winter but then becomes dormant during summer thus producing a net annual cooling effect which chills the lower portion of the embankment and underlying foundation soils.

Figure 3-25 contains the same evaporator and condenser temperature data as Figure 3-23 except that the time series extends from 2005 to 2020. This data is included to illustrate that the behavior of the hairpin thermosyphon is quite consistent over the entire 16-year measurement record. Each winter evaporator and condenser temperatures track together with a strong correlation to ambient air temperatures, and each summer the evaporator and condenser temperatures depart from one another with the evaporator remaining very cool compared to the condenser or ambient air temperatures. The figure does not seem to indicate any degradation in thermosyphon performance during the measurement period.

In addition to thermistor stings A, B, C, D, and E, as shown in Figure 3-8, test section #3 included two additional vertical thermistor strings (strings F and G) that were located further away from Thompson Drive. Figure 3-13 shows a plan view that illustrates the position of strings F and G compared to the

strings A, B, and C that are located in the roadway. As seen in the figure, string F is located in a grass-covered area roughly half way between Thompson Drive and the rounded parking area that was installed as part of the project. String G is installed beneath the center of the paved parking area as illustrated. String F contains six measurement points that are located at depths of 0.85 m, 2.85 m, 4.85 m, 6.85 m, 8.85 m, and 10.85 m beneath the grass surface. There is no insulation installed at the location of string F. String G contains seven measurement points located at depths of 1.1 m, 3.1 m, 5.1 m, 7.1 m, 9.1 m, 11.1 m, and 13.1 m beneath the paved surface. At the location of string G there is a 5 cm insulation layer installed just beneath the top sensor of string G that extends beneath the paved parking area and sidewalk. Sensor numbering is consistent with thermistor string numbering elsewhere in the project so that measurement point G3-1 is at the greatest depth (13.1 m) and G3-7 is located just above the insulation sheet at a depth of 1.1 m beneath the asphalt surface.

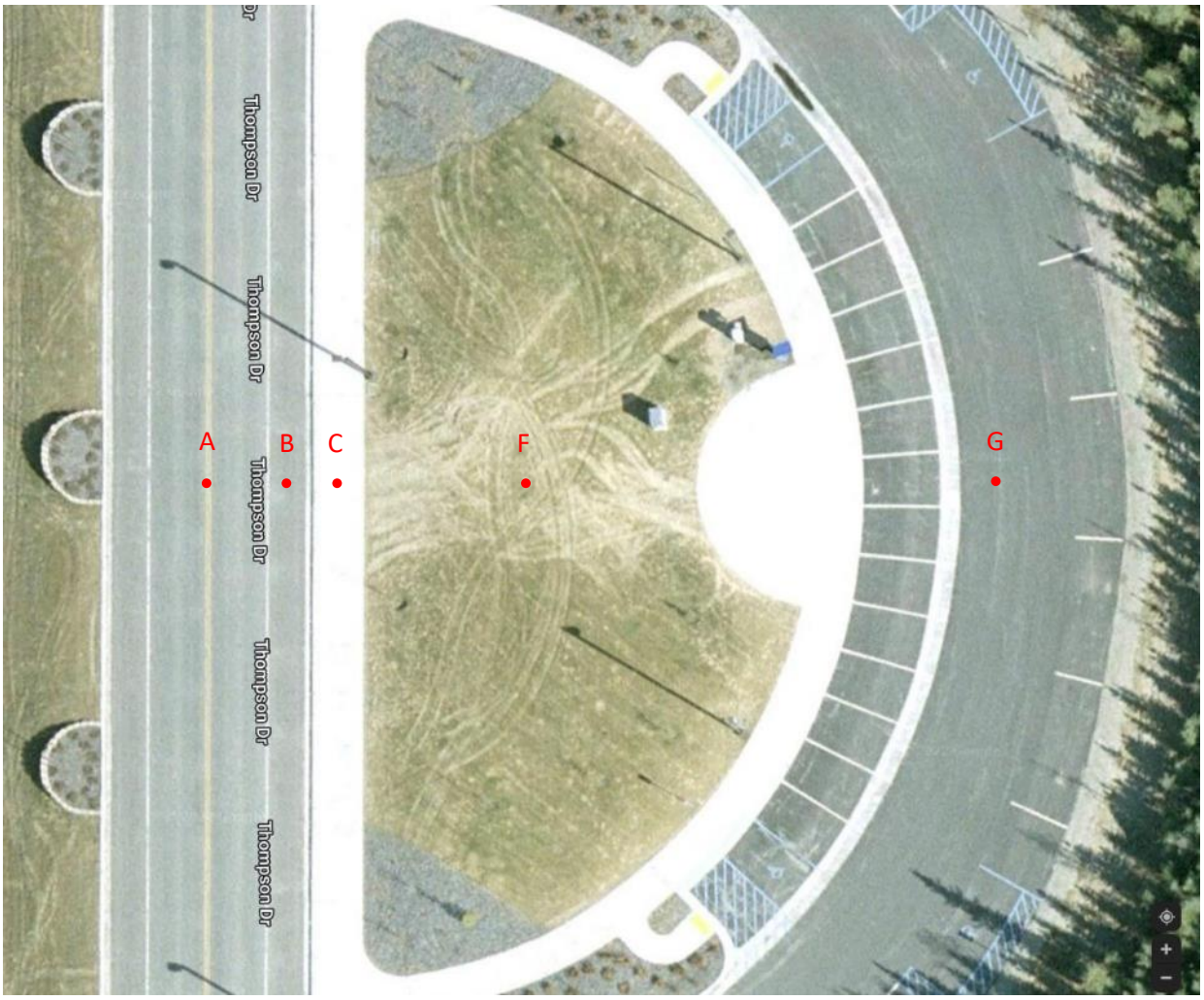

Figure 3-13 Plan View of Thermistor String Locations for Test Section #3

Figure 3-24 shows the temperature time series for the thermistors in sting F. As would be expected, point F3-6, which is closest to the grass surface, displays the greatest annual temperature variations but remains thawed during the entire measurement period. Note that this area is snow-covered during the winter which likely limits subsurface freezing. Winter low temperatures at F3-6 start out in the range of

+0.2°C but gradually increase throughout the measurement record to values of about +1.5°C in the year 2020. Summer high temperatures at this point also increase from ~+3°C to nearly +5°C during the measurement period. The rest of the measurement points (F3-1 to F3-5) start out in the frozen state with temperatures of about -0.2°C. However, by 2006 point F3-5 starts to display a warming trend and becomes completely thawed throughout the yearly cycle by about 2009. After 2009 the temperature at F3-5 continues to increase and falls in the range of +1.3°C to +2.6°C by the end of the measurement record. Starting in about 2012, point F3-4 also starts to show a warming trend and it to thaws completely by about 2015, eventually fluctuating between about +0.8°C and _1.2°C by the end of the measurement period. Towards the end of the measurement record, point F3-3 also begins to show some evidence of warming but points F3-1 and F3-2 hold steady at about -0.2°C for the entire timeline. The warming trend shown in Figure 3-24 is unmistakable and presumably it would only be a matter of time before the thaw progressed all the way down to the deepest measurement point. As of 2020 the thaw depth had reached a depth of about 6 m below the surface but there did not appear to be evidence of thaw settlement.

Figure 3-26 shows the temperature time record for measurement points G3-1, G3-2, G3-3, G3-4, G3-5, and G3-6. Note that all six of these points lie at a depth of 3.1 m or more below the paved surface, and all are below the 5 cm insulation layer (measurement point G3-7, which is above the insulation, is left out of this plot due to its large temperature variations). Comparing Figure 3-26 and Figure 3-24 shows that there is much less soil warming taking place beneath the insulated parking area as opposed to that beneath the grass-covered surface. This is likely due to the combination of snow clearing in winter and the helpful influence of the insulation layer. The data for point G3-6 shows that there is substantial annual freeze/thaw activity at the depth of 3.1 m, roughly 2 m below the insulation sheet. However, it is clear that even though annual re-freeze does occur, the temperatures at G3-6 are highly biased towards thawing with annual maximum temperatures on the order of +5°C and annual minimums on the order of -1°C. Initially, points G3-4 and G3-5 also tend to show annual temperature variations that include yearly freezing of the material although they are also highly biased toward thawing. However, after about 2017 neither of these points appear to be refreezing during the winter. Measurement points G3-1, G3-2, and G3-3 all maintain fairly constant temperatures of about -0.2°C for the entire measurement record with the exception that point G3-3 begins to show evidence of warming in 2019 and 2020. While the indications of soil warming for measurement string G are more muted than those for string F, Figure 3-26 does seem to show a gradual warming trend, particularly after 2016. If trends shown in the figure continue, it is likely that the entire soil column down to a depth of 13 m or deeper will eventually thaw. A reasonable conclusion would be that while snow clearing and an insulation layer have significantly reduced the potential at this location for permafrost thaw, given additional time, complete thawing is likely.

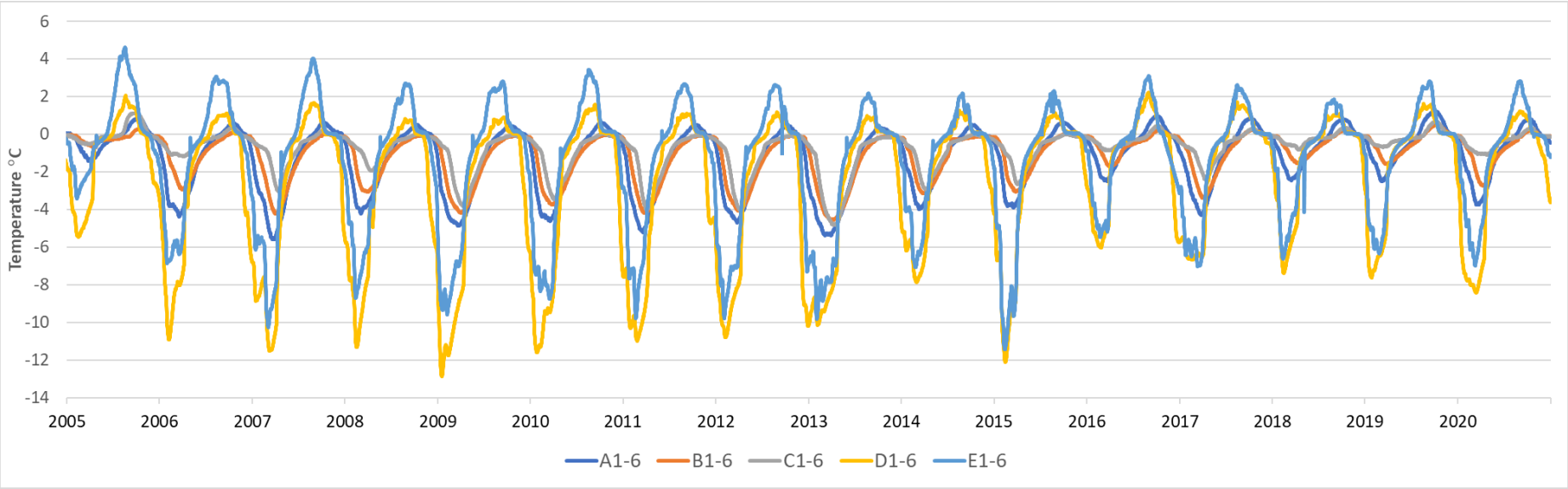

Figure 3-14 Temperature Time Series for Test Section #1 at Original Grade

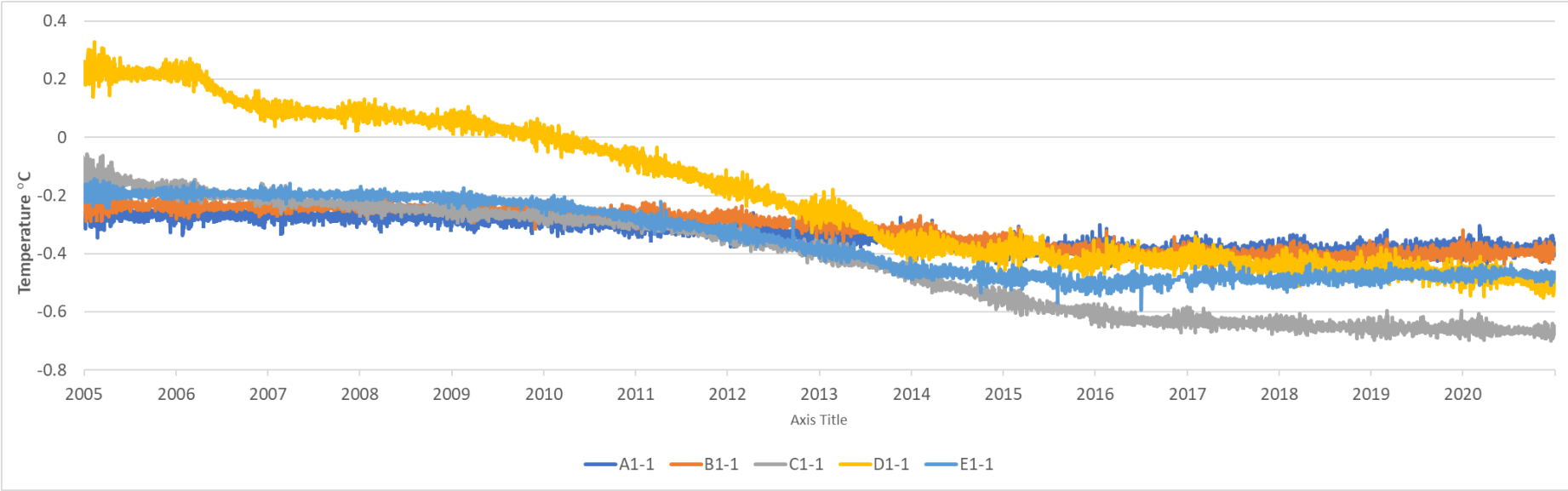

Figure 3-15 Temperature Time Series for Test Section #1 at 10 m Below Original Grade

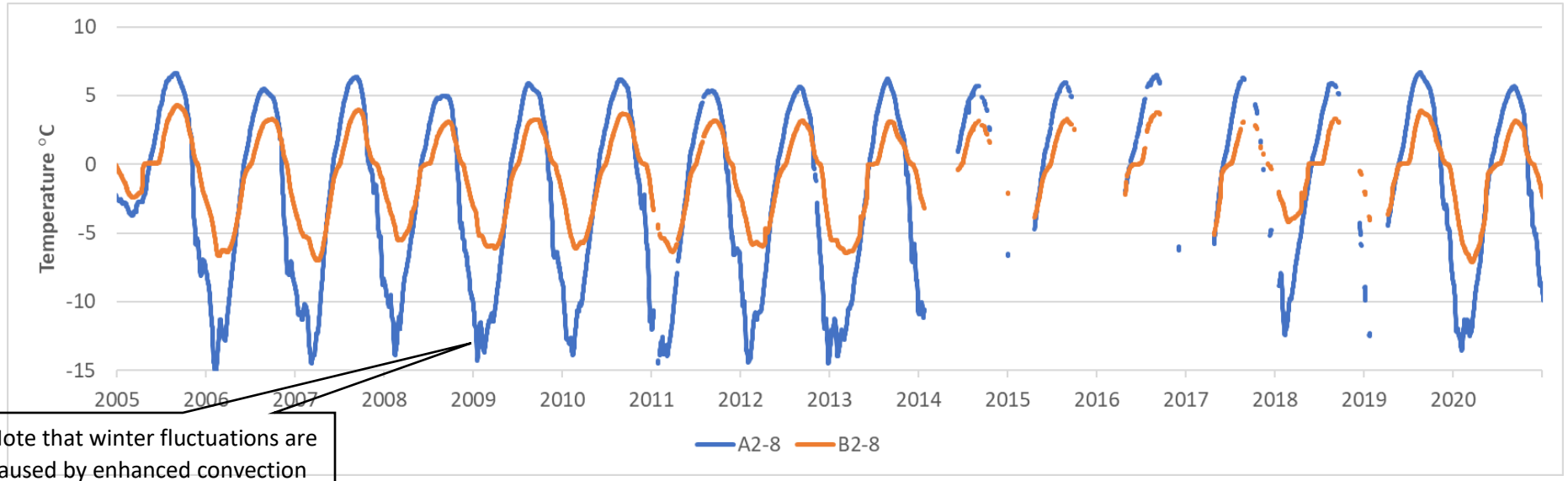

Note that winter fluctuations are caused by enhanced convection in the ACE layer as ambient temperatures fluctuate.

Figure 3-16 Temperature Time Series for Test Section #2 Below Horizontal ACE layer

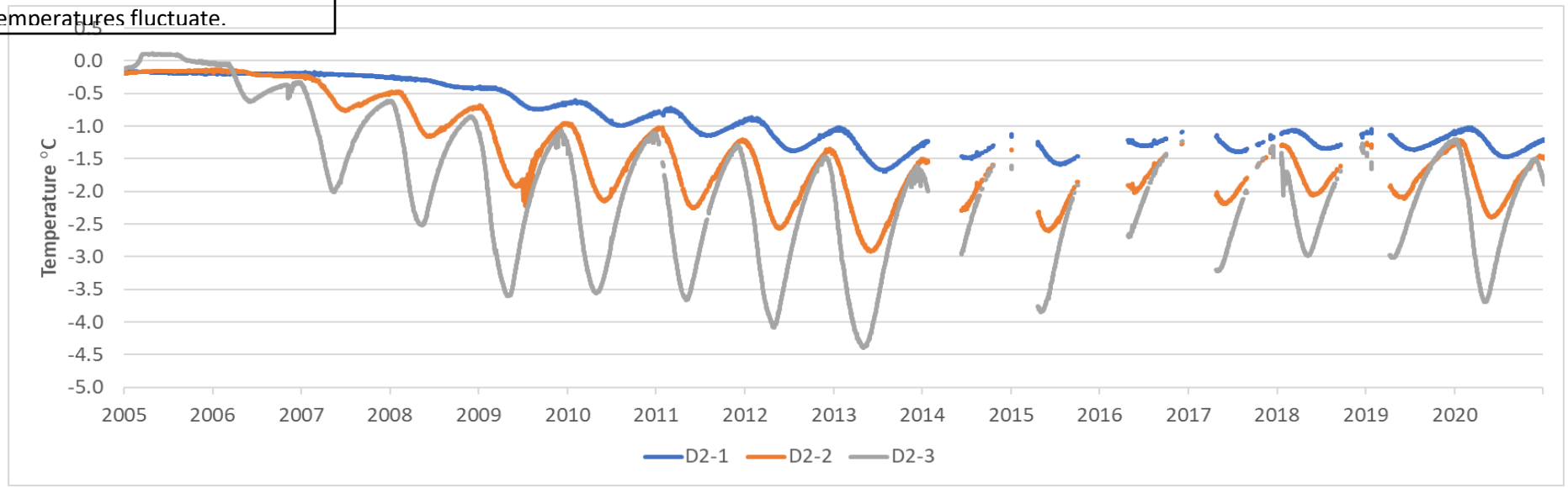

Figure 3-17 Temperature Time Series for Test Section #2 Below Ventilated Shoulder

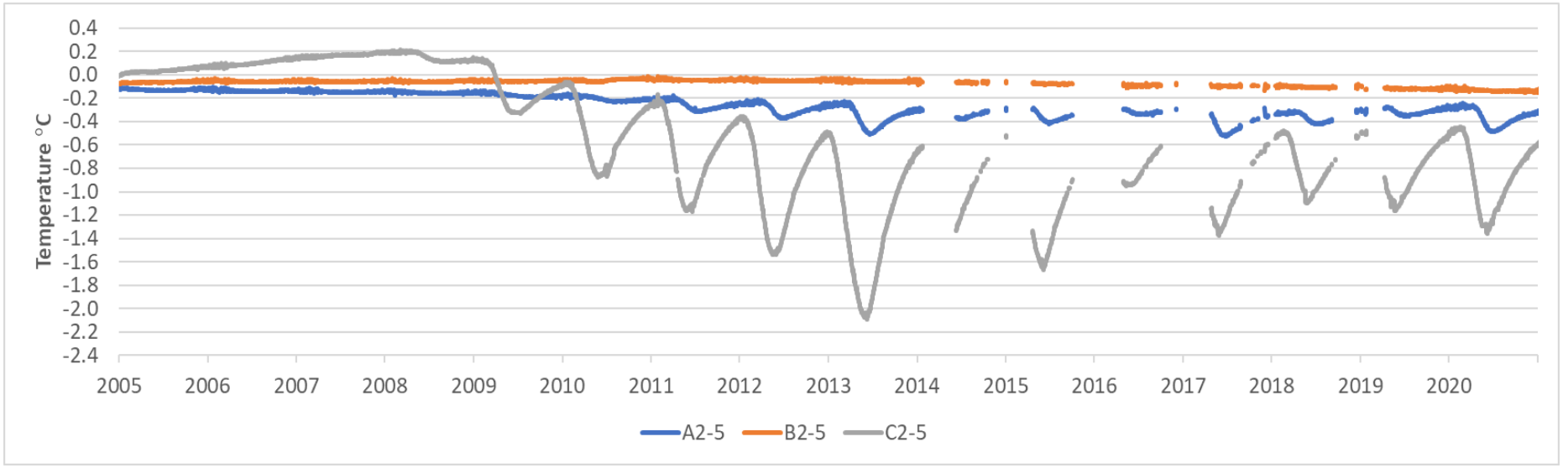

Figure 3-18 Temperature Time Series for Test Section #2 at Original Grade

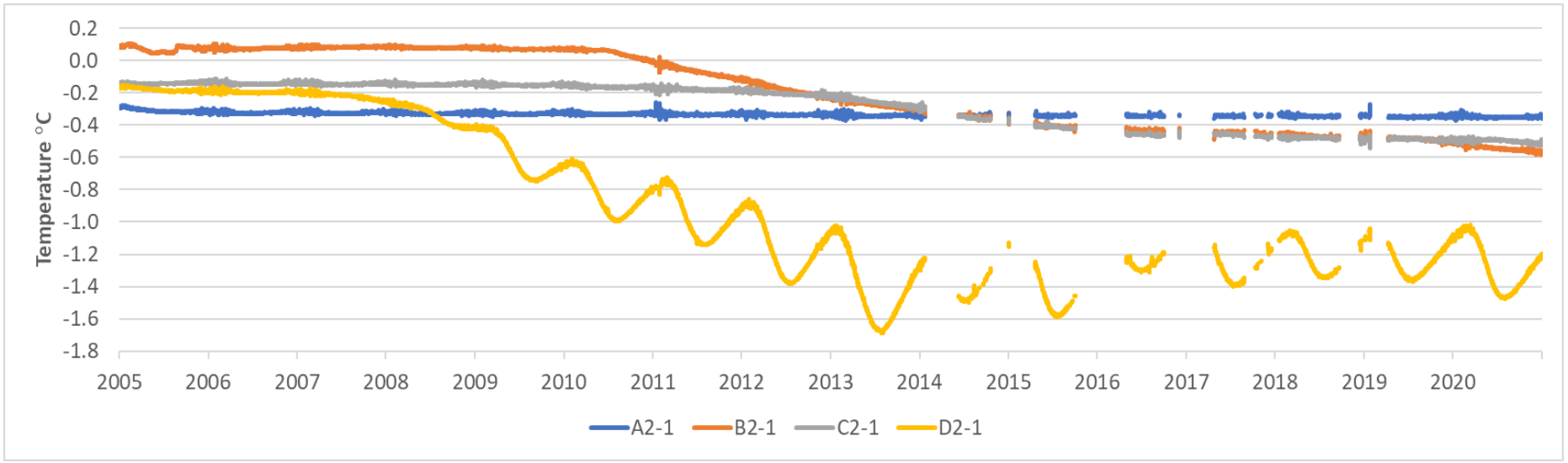

Figure 3-19 Temperature Time Series for Test Section #2 at 8 m Below Original Grade

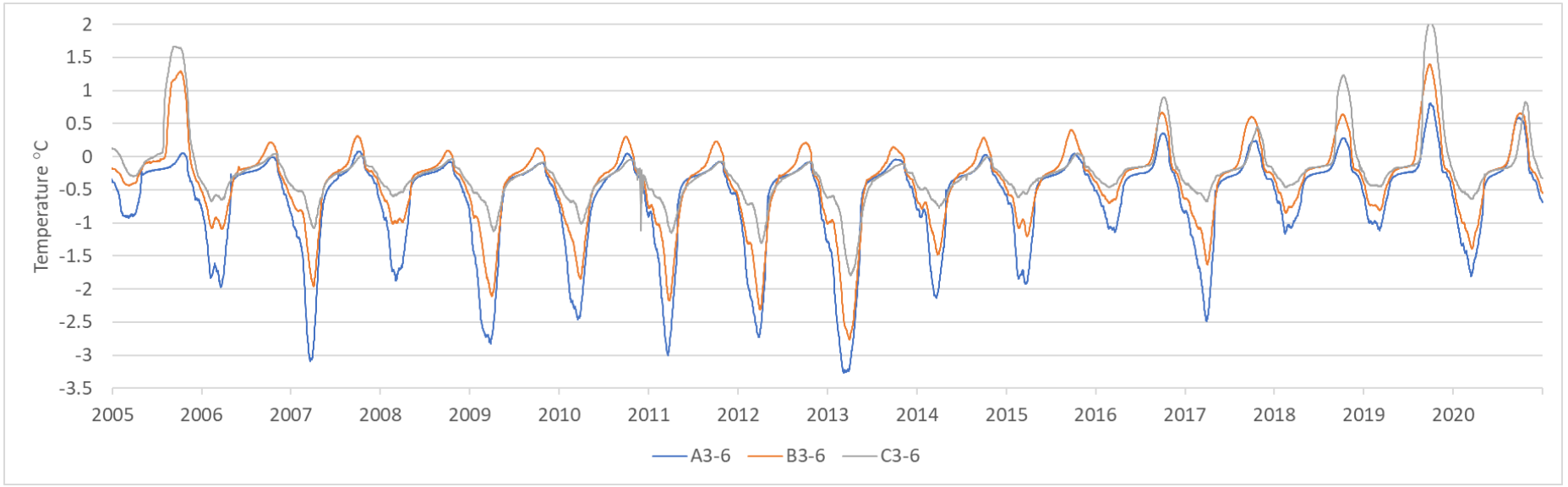

Figure 3-20 Temperature Time Series for Test Section #3 at Base of the Unclassified Excavation

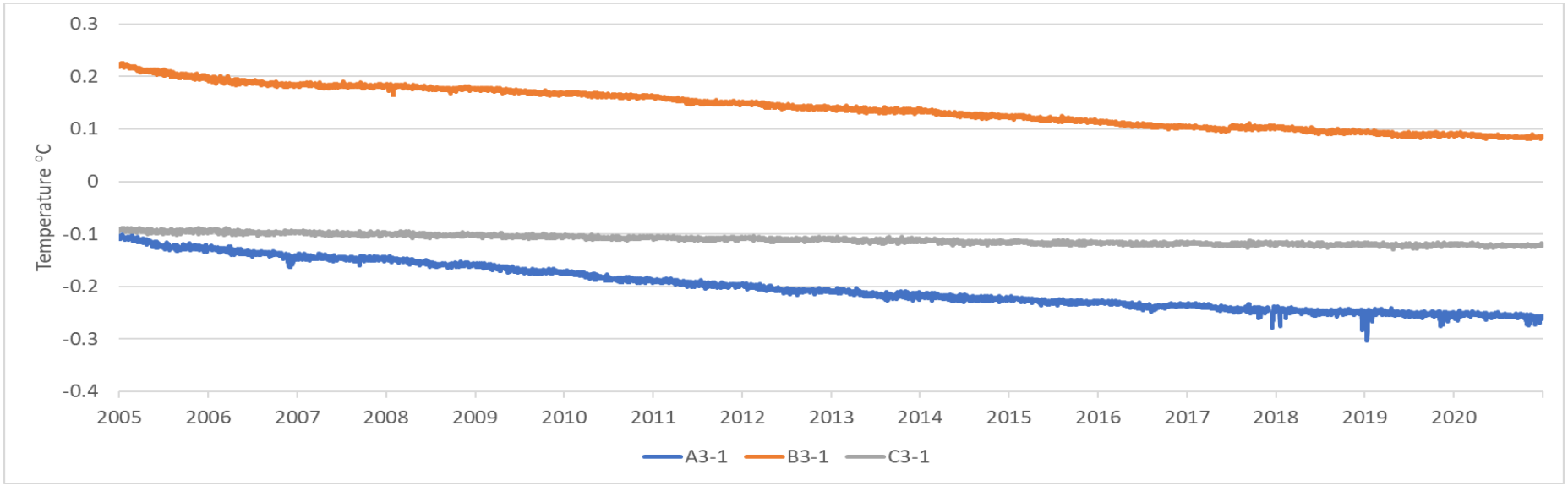

Figure 3-21 Temperature Time Series for Test Section #3 at 13 m Below Roadway Surface

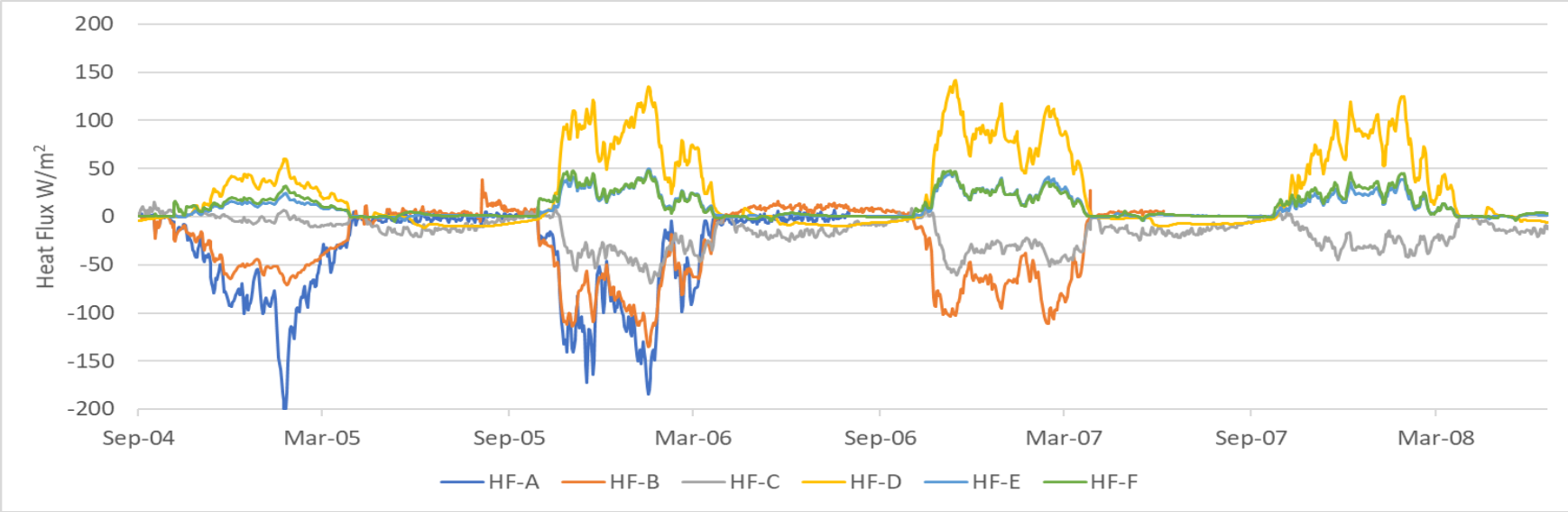

Figure 3-22 Thermosyphon Heat Flux Time Series for Test Section #3

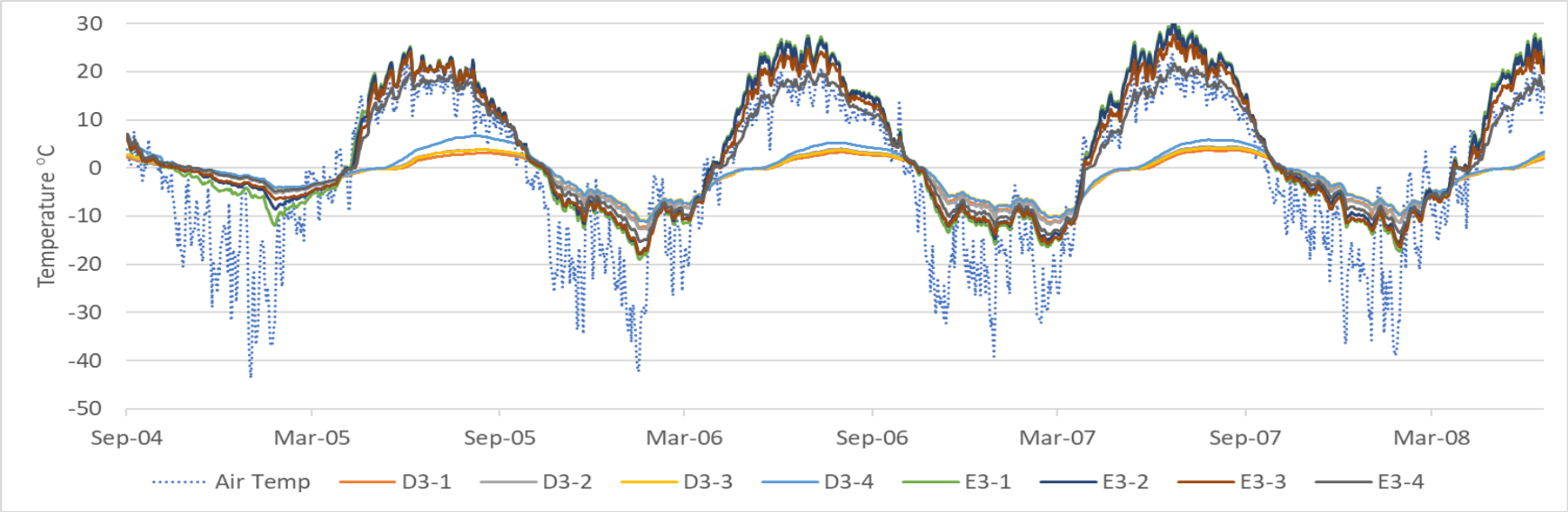

Figure 3-23 Thermosyphon Evaporator and Condenser Detailed Temperature Time Series for Test Section #3

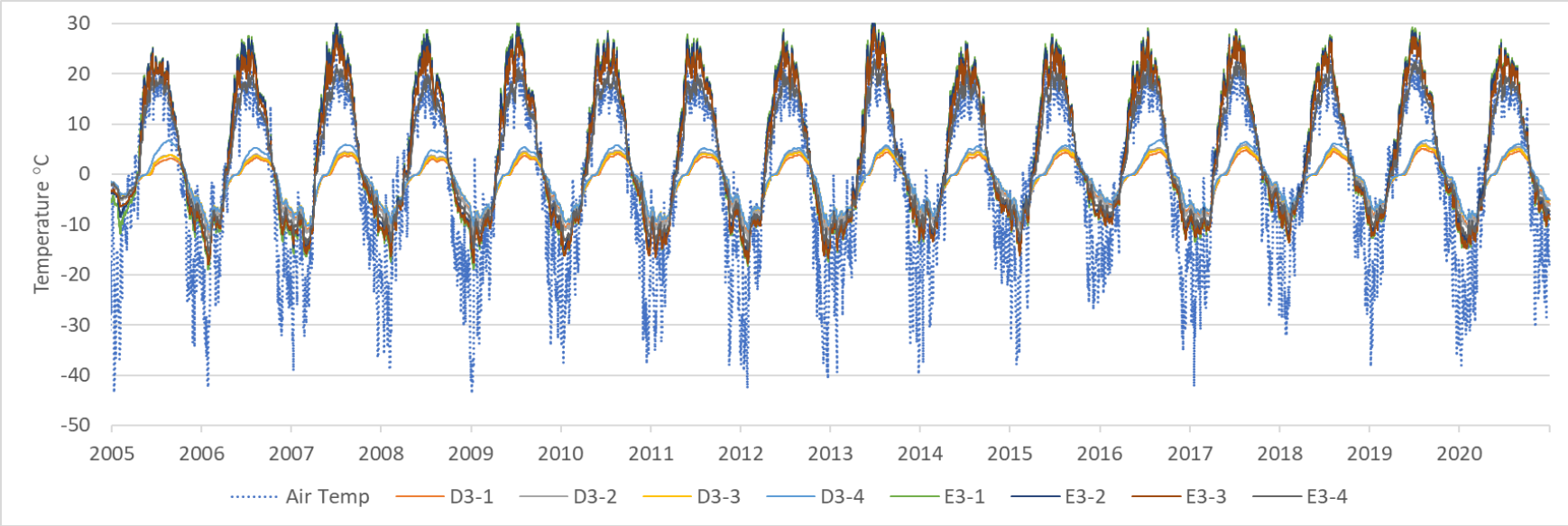

Figure 3-25 Thermosyphon Evaporator and Condenser Temperature Time Series for Test Section #3

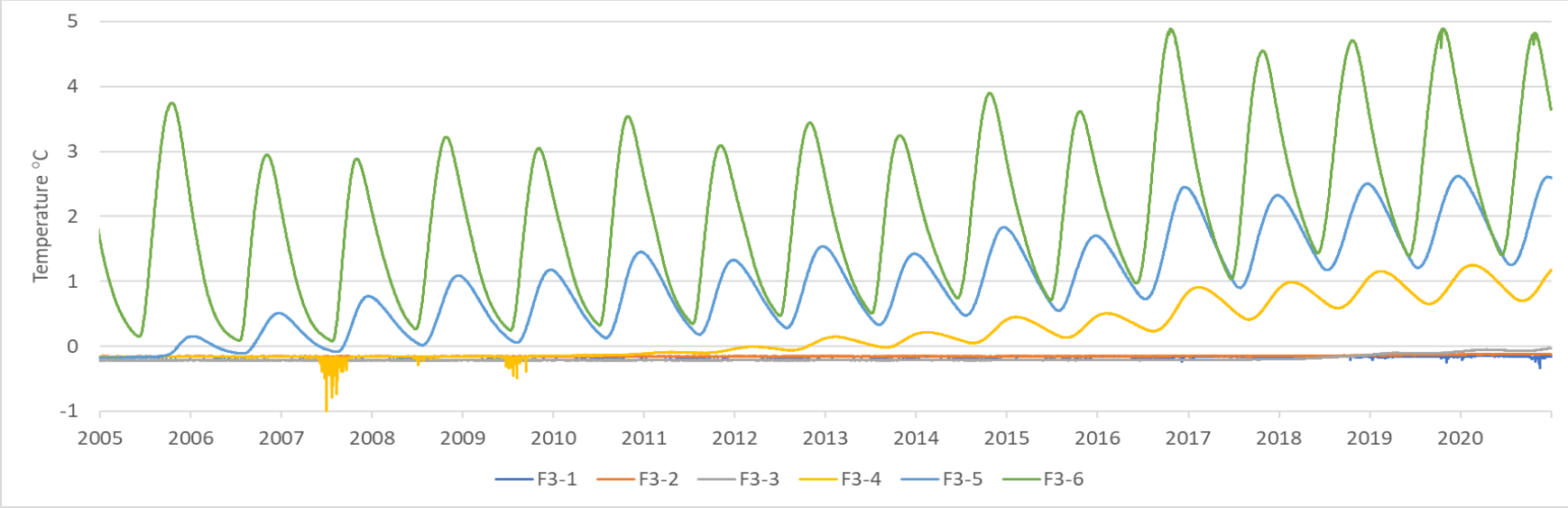

Figure 3-24 Temperature Time Series for Test Section #3, Thermistor String F

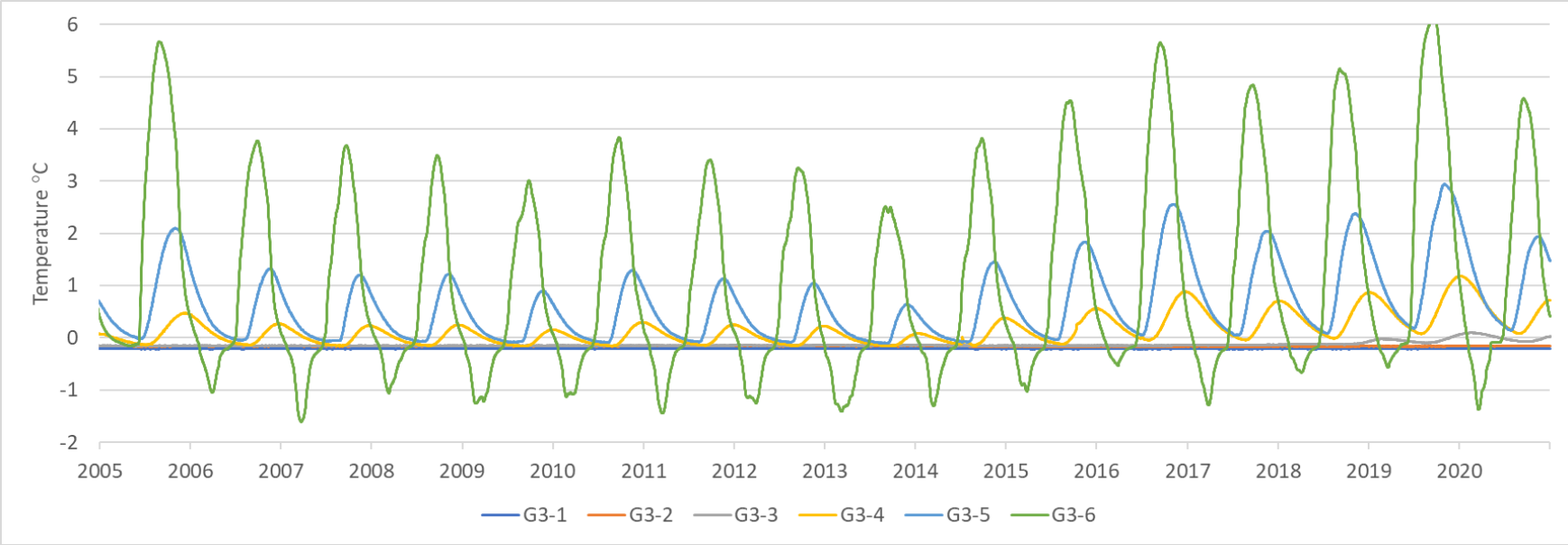

Figure 3-26 Temperature Time Series for Test Section #3, Thermistor String G

3.2. Alaska Highway – Dot Lake Experimental Results

In an effort to better understand application of ACE features to reconstruction of an existing roadway, an experimental feature was included in reconstruction of a section of the Alaska Highway near Dot Lake in the area of Milepost 1362. This portion of the highway had been experiencing embankment deformation and thaw settlement problems for many years and had been resurfaced numerous times prior to the start of reconstruction. Thus, the permafrost layer beneath the site had experienced a significant amount of thermal degradation prior to the reconstruction using ACE layers. Reconstruction was completed in 2017 and a photo of the completed project can be seen in Figure 3-27. The project included three instrumented test sections which utilized Beaded Stream temperature acquisition cables and data logging stations. The three data logging stations can be seen in Figure 3-27 with the data loggers mounted on posts adjacent to the embankment toe. The goal of the project was to investigate how well an ACE embankment could re-freeze previously degraded permafrost beneath a roadway and to determine if there were differences in thermal performance when using rounded versus angular (crushed) rock for ACE construction.

This report contains a preliminary analysis of data obtained from the site over a three-year period starting on June 1, 2017. Additional detailed information is available in Billings and Berggren [3].

Figure 3-27 Alaska Highway Dot Lake Test Section, Looking North

3.2.1. Instrumentation and Test Section Configuration

The three test sections were located at stations 4132+0, 4137+50, and 4138+50 of the project. These test sections made use of either rounded (alluvial) or angular (crushed) ACE aggregate in two size

ranges. Class I material had a gradation specification of 3”-5” aggregate, whereas class III material had a 5”-8” gradation specification.

Station 4132+00 included an ACE shoulder (ventilated shoulder) on project left and four inches of insulation board located beneath the driving surface as shown in Figure 3-28. The ventilated shoulder was constructed of rounded class III material with a thin upper layer of rounded class I material, as shown in the figure. It also included three temperature acquisition cables, one running from the left toe of the embankment just beneath the surface all the way across the embankment to the right toe, a second running beneath the base of the ventilated shoulder and then across the embankment structure beneath the insulation layer, and, finally a third vertical string located just to the left of the driving surface and extending downward roughly 25 feet below original grade (see Figure 3-28 for details). The three temperature acquisition cables contained a total of 101 temperature measurement points with temperature values collected four times per day.

Stations 4137+50 and 4138+50 had the same basic configuration with ventilated shoulders on both sides of the embankment and a five-foot-high horizontal ACE layer stretching all the way across the embankment beneath the driving surface. The configuration for these two test sections is shown in Figure 3-29. For these two test sections, class I material was used for the shoulder regions and the horizontal ACE layer, however, station 4137+50 utilized angular ACE material while station 4138+50 utilized rounded ACE material. Both of these test sections had the same layout for the temperature acquisition cables with one running just beneath the surface from toe to toe, one running at the base of the ventilated shoulders and beneath the horizontal ace layer, and a third, vertical string located just to the right of the driving surface and extending downward to a depth of roughly 25 feet below original grade. Station 4173+50 contained a total of 87 temperature sensors, and station 4138+50 contained 85. As for station 4132+00, temperatures were collected four times per day.

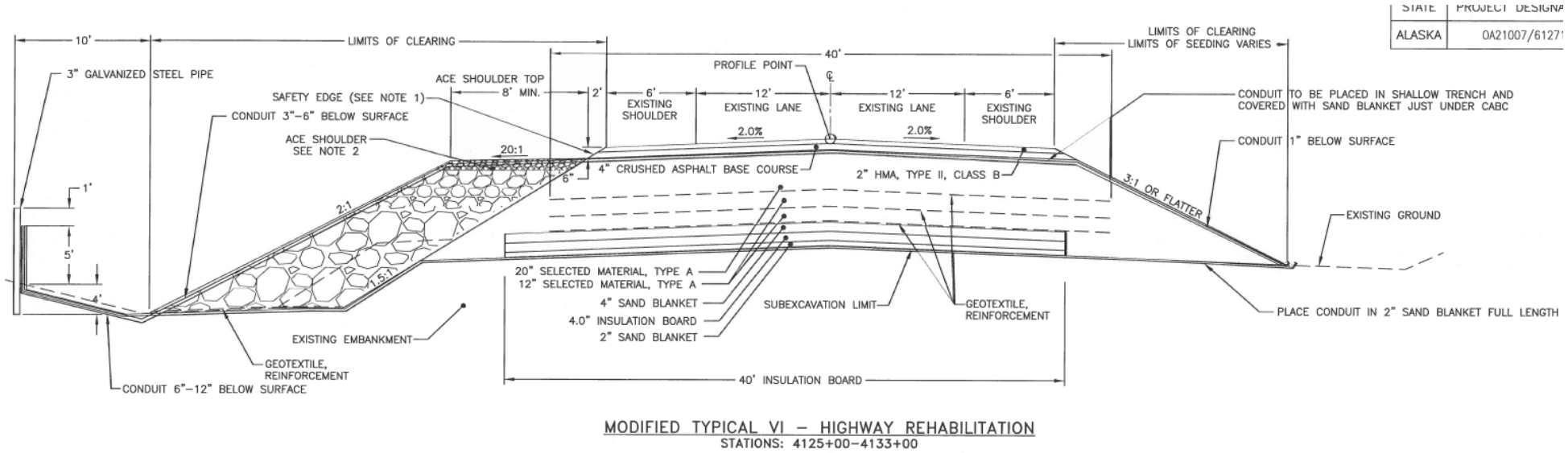

MODIFIED TYPICAL VI – HIGHWAY REHABILITATION
STATIONS: 4125+00–4133+00

Figure 3-28 Alaska Highway Dot Lake Test Section, Station 4132+00 Configuration

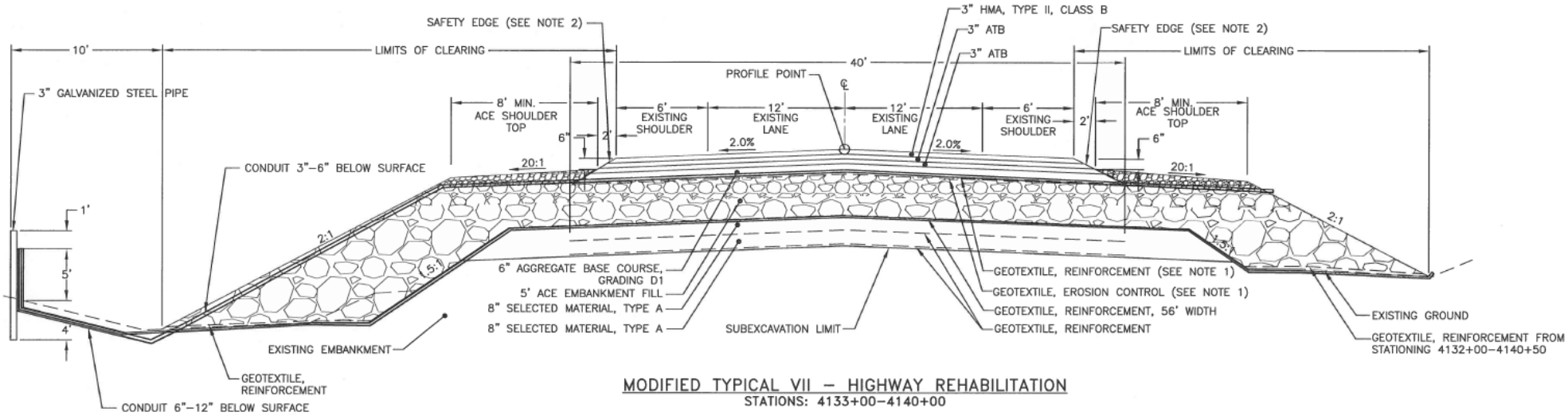

MODIFIED TYPICAL VII – HIGHWAY REHABILITATION
STATIONS: 4133+00–4140+00

Figure 3-29 Alaska Highway Dot Lake Test Section, Station 4137+50 - and Station 4138+50 Configuration

3.2.2. Alaska Highway Dot Lake Mean Annual Temperatures

Temperatures from the Alaska Highway Dot Lake test site were used to calculate mean average temperature values at locations throughout the test sections as was done for the Thompson Drive data discussed in Section 3.1.3. Given the beginning and end dates of the data collection contract with Beaded Stream, the three annual periods utilized were 6/1/2017 – 5/31/2018, 6/1/2018 – 5/31/2019, and 6/1/2019 – 5/31/2020. In addition to the embankment temperature sensors, each of the three test sections also included an air temperature sensor. Mean annual temperature values were calculated for each measurement point as well as for the air temperature values at each test section by simply averaging the individual measurements obtained throughout the appropriate annual cycle. The Environmental Atlas of Alaska [14] indicates a mean annual air temperature of 25°F for this region of Alaska, however, temperatures measured at the test sites were generally warmer than that by several degrees Fahrenheit. It is likely that the temperatures in this region were also impacted by the relatively high PDO index during these years, as shown in Figure 3-9 for Thompson Drive, perhaps explaining some of the warming influence. However, some of the warming has undoubtedly been the result of climatic change since the original environmental atlas data was collected in the 1960's and 1970's. Interestingly, these average air temperatures varied significantly from site-to-site, even though all three sites were at essentially the same elevation and within a few hundred feet of one another.

Table 3-5 shows mean annual temperature values for each station for each of the three annual periods. The data in the table shows a roughly 0.5°F average temperature variation from station to station during any given year with Station 4132+00 showing the warmest values and Station 4137+50 indicating the coldest. There is also significant interannual temperature variation with the period 6/1/2018 – 5/31/2019 averaging the warmest value of about 31.6°F (for all three stations) and the period 6/1/2019 – 5/31/2020 averaging the coldest value of 27.8°F. As noted above, all of these values are significantly warmer than those shown in the Environmental Atlas of Alaska for this area of Alaska.

Table 3-5 Average Annual Air Temperatures for the Alaska Highway Test Sections (°F)

Annual Period	Station 4132+00	Station 4137+50	Station 4138+50
6/1/2017 – 5/31/2018	30.1	29.6	29.8
6/1/2018 – 5/31/2019	31.8	31.3	31.6
6/1/2019 – 5/31/2020	28.0	27.6	27.8

Figure 3-28 through Figure 3-30 show mean annual temperature values for test Station 4132+00 for each of the three annual periods. The most striking feature of these figures is the relatively cold temperatures indicated for the base of the ventilated shoulder. Mean annual temperatures in this region are generally in the range of 26°F to 29°F, cool enough to protect and enhance the permafrost layer beneath the shoulder region. Temperatures beneath the driving surface and the unprotected shoulder on project right are much warmer, in the range of 34°F to 40°F, particularly during the first and third years of data collection. Even beneath the insulation layer that underlies the driving surface, temperatures are warm, with mean values of roughly 33°F to 35°F during the three-year measurement period. This implies that permafrost thaw beneath the road centerline may continue in the future, but given the relatively short record of data recording it is likely not possible to know the long-term influence of the cooling provided by the ventilated shoulder on project left. Closer examination of these

three figures also reveals that warming at the centerline is exacerbated during the first two years, likely due to the warmer air temperatures experienced. This is illustrated by the relatively warmer average temperatures at the upper surface of the embankment compared to those just beneath the insulation layer. To the contrary, during the third year of data collection, cooler air temperatures resulted in much closer average temperature values between the upper temperature string and the one located beneath the insulation, as shown in Figure 3-32, indicating a more neutral heat transfer situation. Note that an insulation layer will not typically support a long-term temperature difference across its thickness without allowing heat to move from the warm to the cold side of the layer, thus the situation indicated in Figure 3-30 and Figure 3-31 tends to indicate heat movement from the relatively warm driving surface to the embankment materials beneath the insulation sheet.

Examining the average temperatures for the vertical measurement string beneath Station 4132+00 shows a pre-existing talik extending down to about 15 ft. below original grade. This is no doubt a result of prior thawing due to the original roadway embankment which had been located in this area for many years. As Figure 3-30 through Figure 3-32 indicate, there is very little temperature variation in the deeper portion of the vertical measurement string over the three-year period of data collection. This is not surprising since changes at the surface, such as those produced by the cooling influence of the ventilated shoulder, will likely take a decade or more to propagate into the region of vertical temperature measurements, thus it is difficult to predict the long-term impact of the ventilated shoulder on the deeper foundation soil temperatures closer to the roadway centerline.

Figure 3-33 through Figure 3-35 show mean annual temperatures for Station 4137+50 for each of the three annual periods. As described above, this test section used angular class I ACE material for both shoulders and the horizontal ACE layer beneath the driving surface. As for Station 4132+00, a striking feature of these figures is that the regions at the base of each ventilated shoulder tend to be quite a bit colder on average than other portions of the test section. As before, this is due to the prevailing cold air circulation pattern in the winter which consists of the influx of cold ambient air at the base of the ventilated shoulder and outflow of air at the top of the shoulder. Note that the temperature depressions shown at the base of the shoulder in these three figures are not as extreme as those shown for Station 4132+00. This is likely due to the influence of both ventilated shoulder geometry and the differences between class I and class III material. Station 4132+00 has both a larger height and is constructed of the larger class III material, both of which tend to promote stronger convective cooling. Even so, the mean annual temperatures at the base of the ventilated shoulders at Station 4137+50 are still fairly cool, in the range of 29°F to 31°F, with the results for the 6/18 - 5/19 period showing slightly colder values. While not as strong as the cooling influence beneath the ventilated shoulder of Station 4132+00, these values still indicate a relatively strong permafrost preservation capability.

Figure 3-33 and Figure 3-34 show that the average temperatures at the top and bottom of the horizontal ACE layer are all above freezing, however, the temperatures at the base of the layer are significantly cooler than those at the upper surface, in the range of 32°F to 33°F as opposed to 34°F to 36°F at the upper surface. Figure 3-35 shows cooler conditions for the 6/19 – 6/20 period, with base layer temperatures mostly below freezing. In this case, the temperature difference across the layer (warmer on top and cooler on the bottom) does not necessarily indicate heat flow into the deeper embankment layers. This is due to the non-linear influence of convective air motion in the horizontal layer, which only occurs during winter. It is also interesting to note that the temperatures in the shoulder regions are significantly colder during the 6/18 – 5/19 period than for the other two years shown, even though the

mean annual air temperature is significantly warmer during this period than the other years. This may be due to the characteristics of the snow layer covering (see Billings and Berggren [3] for more discussion and analysis of this point).

Temperature data from the vertical measurement string shown in Figure 3-33 through Figure 3-35 does indicate some cooling over the three-year measurement period. Initially there is a talik indicated by the temperature measurements that extends approximately from the original grade to a depth of 15 ft. below ground surface. Cold conditions during the 6/18- - 5/19 measurement period, particularly in the zone of the right-hand shoulder, show a cooling of the upper measurement points along the vertical string. During the final measurement period (6/19 – 5/20) this cooling appears to propagate deeper beneath the embankment resulting in re-freezing of nearly 10 ft. of foundation soil, as shown in Figure 3-35.

Figure 3-36 through Figure 3-38 show mean annual temperature values for Station 4138+50. Station 4138+50 has essentially the same geometry as Station 4137+50 described above, but used rounded class I ACE material instead of angular material. The temperatures shown by these figures are very similar to the patterns illustrated in Figure 3-33 through Figure 3-35 for Station 4137+50, indicating seemingly minimal performance differences between angular and rounded ACE material. One would expect that rounded material would produce somewhat better cooling results due to the decrease in tortuosity of the pore space geometry and consequent improvement in air permeability, however this potential improvement in convective cooling is not apparent when comparing the thermal behavior of Station 4137+50 and Station 4138+50 as shown in these figures.

As was the case for Station 4137+50, the data for Station 4138+50 shows cooler temperatures at the base of both ventilated shoulders and the base of the horizontal ACE layer beneath the driving surface. There is also some indication of cooling at the base of the vertical temperature string, although this cooling does not seem to be as pronounced as it was for Station 4137+50.

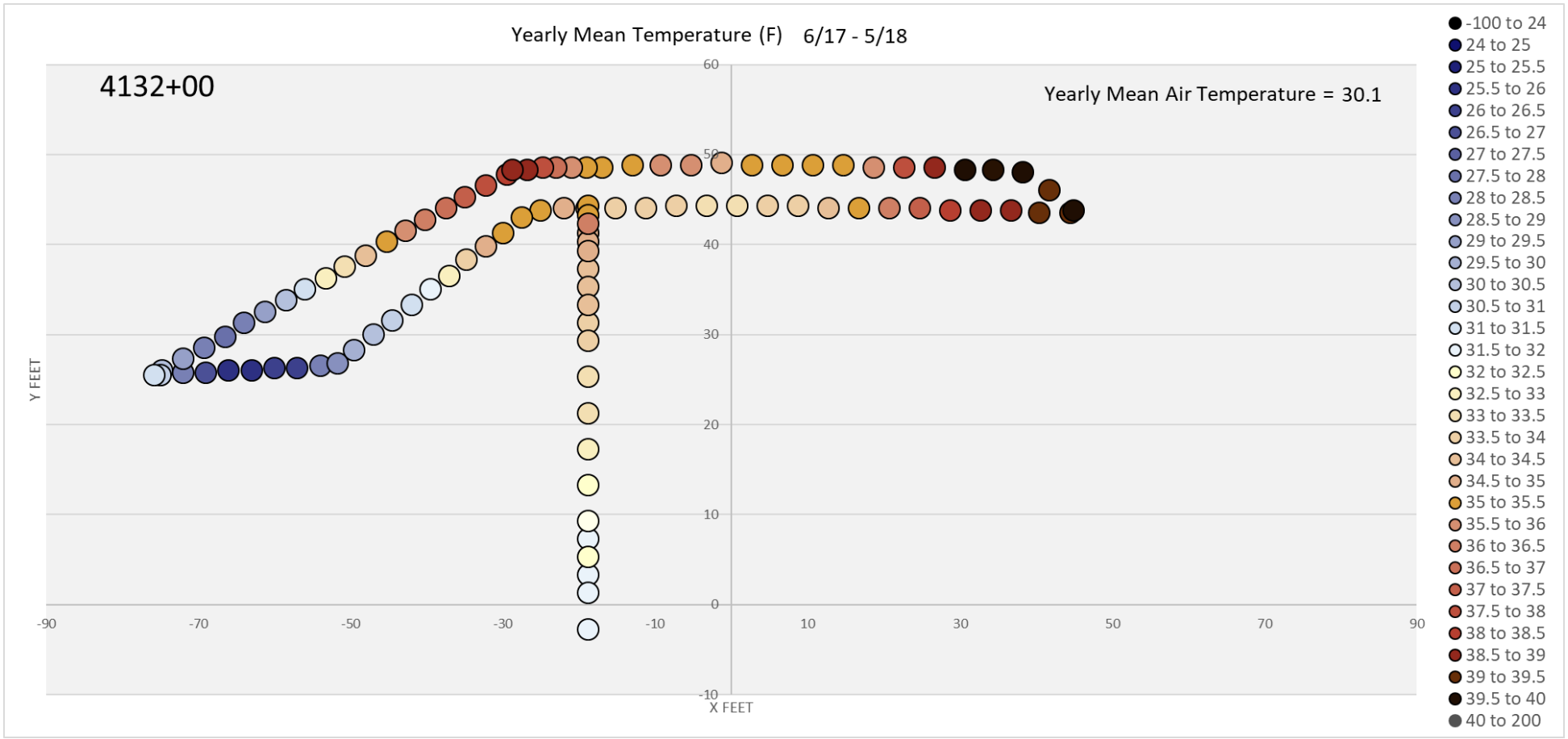

Figure 3-30 Mean Annual Temperatures for Section 4132+00 for the Period June 2017 through May 2018

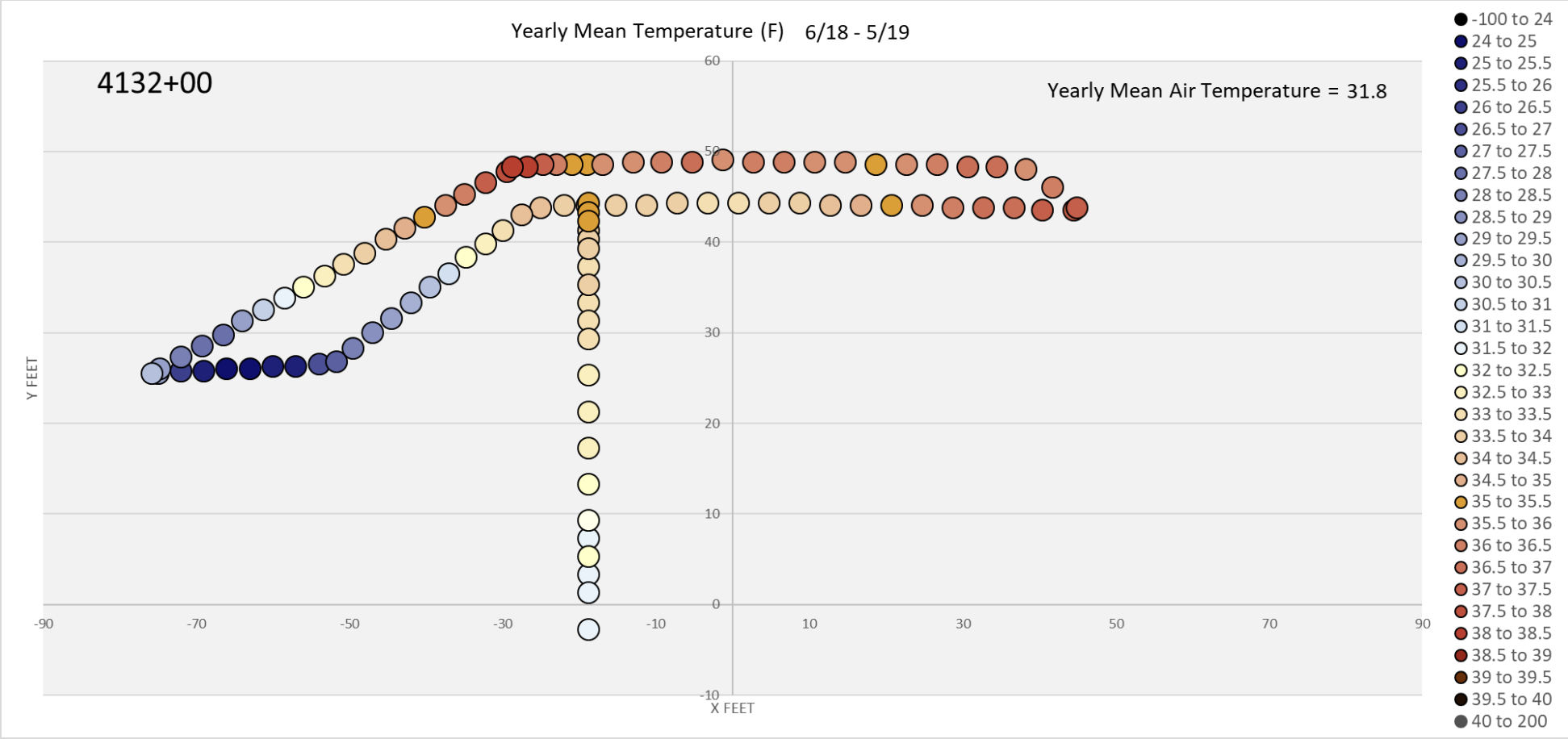

Figure 3-31 Mean Annual Temperatures for Section 4132+00 for the Period June 2018 through May 2019

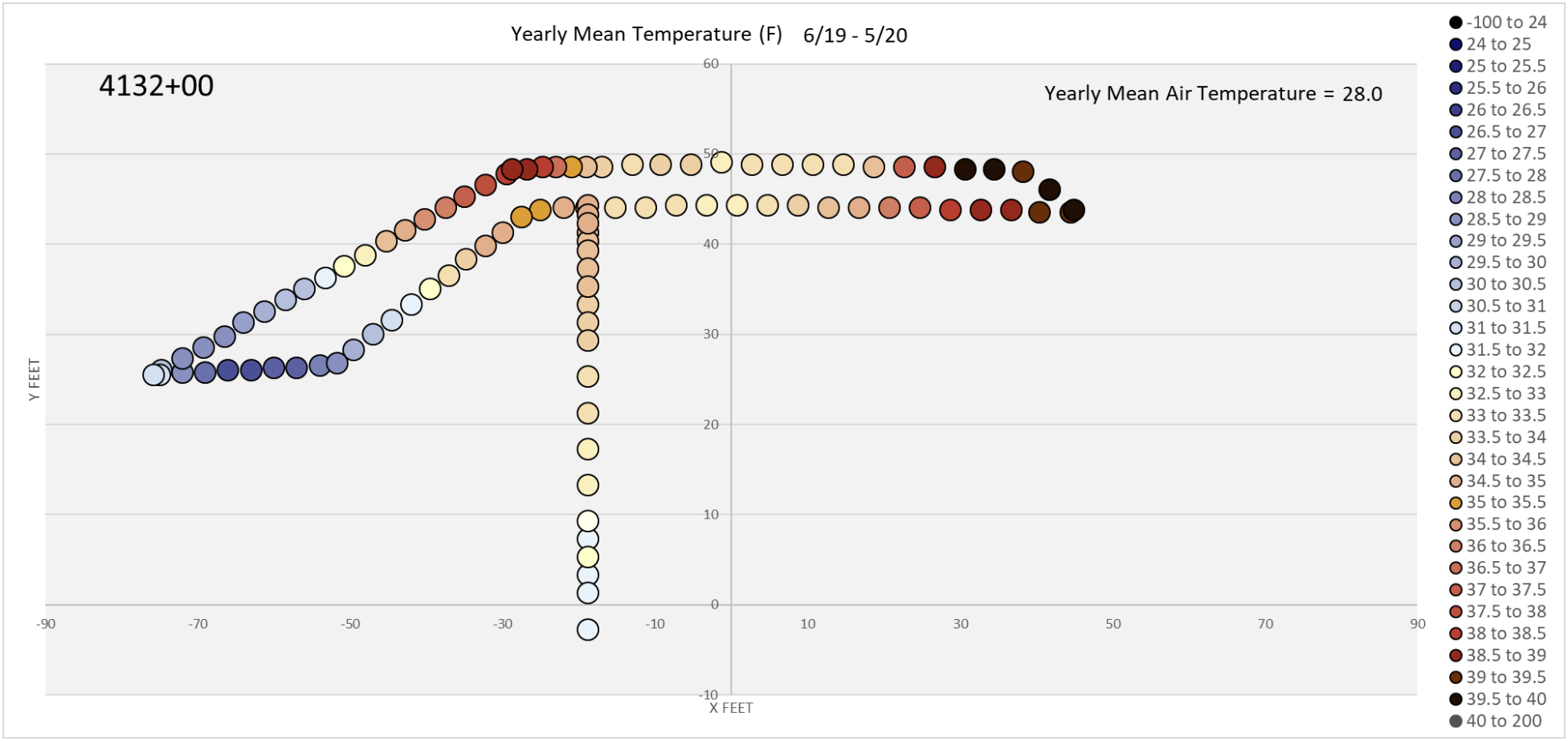

Figure 3-32 Mean Annual Temperatures for Section 4132+00 for the Period June 2019 through May 2020

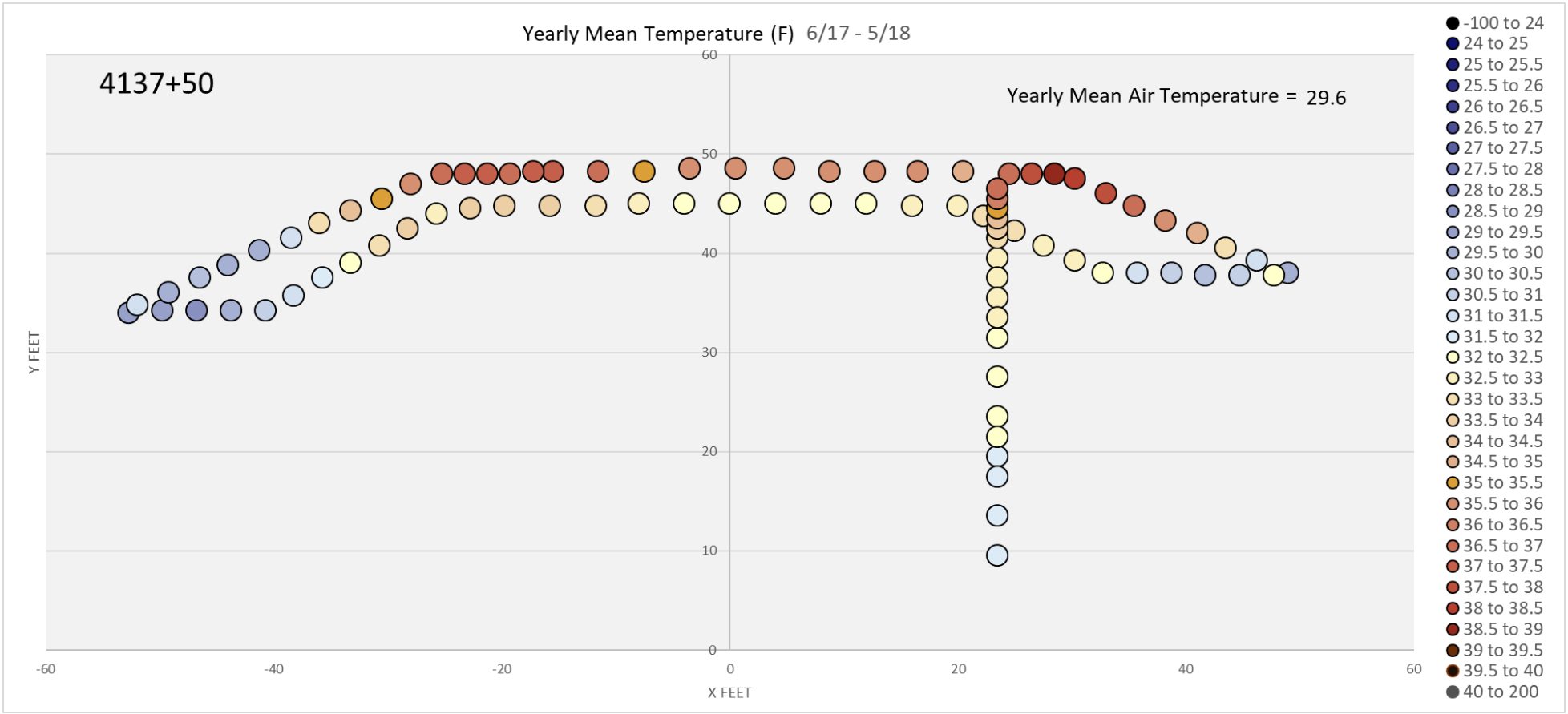

Figure 3-33 Mean Annual Temperatures for Section 4137+50 for the Period June 2017 through May 2018

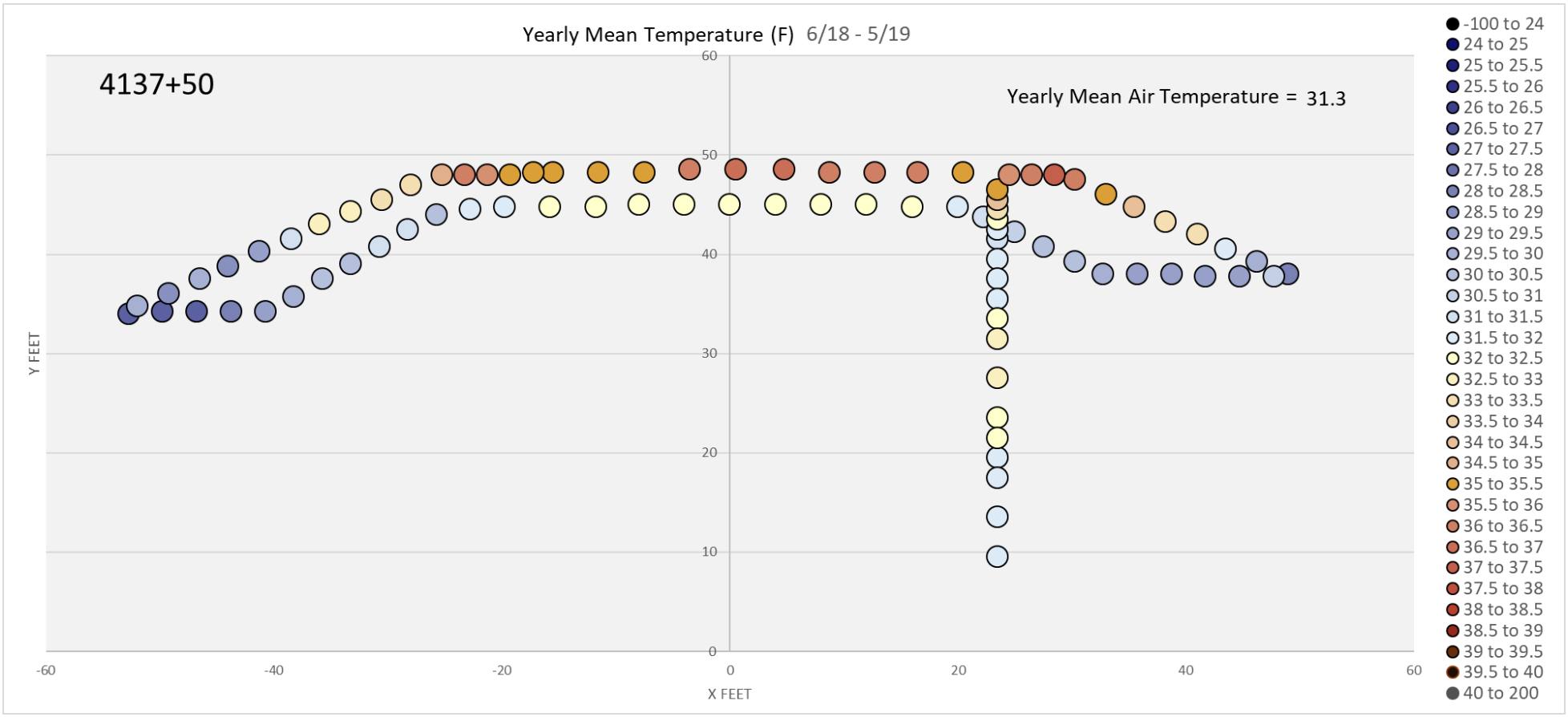

Figure 3-34 Mean Annual Temperatures for Section 4137+50 for the Period June 2018 through May 2019

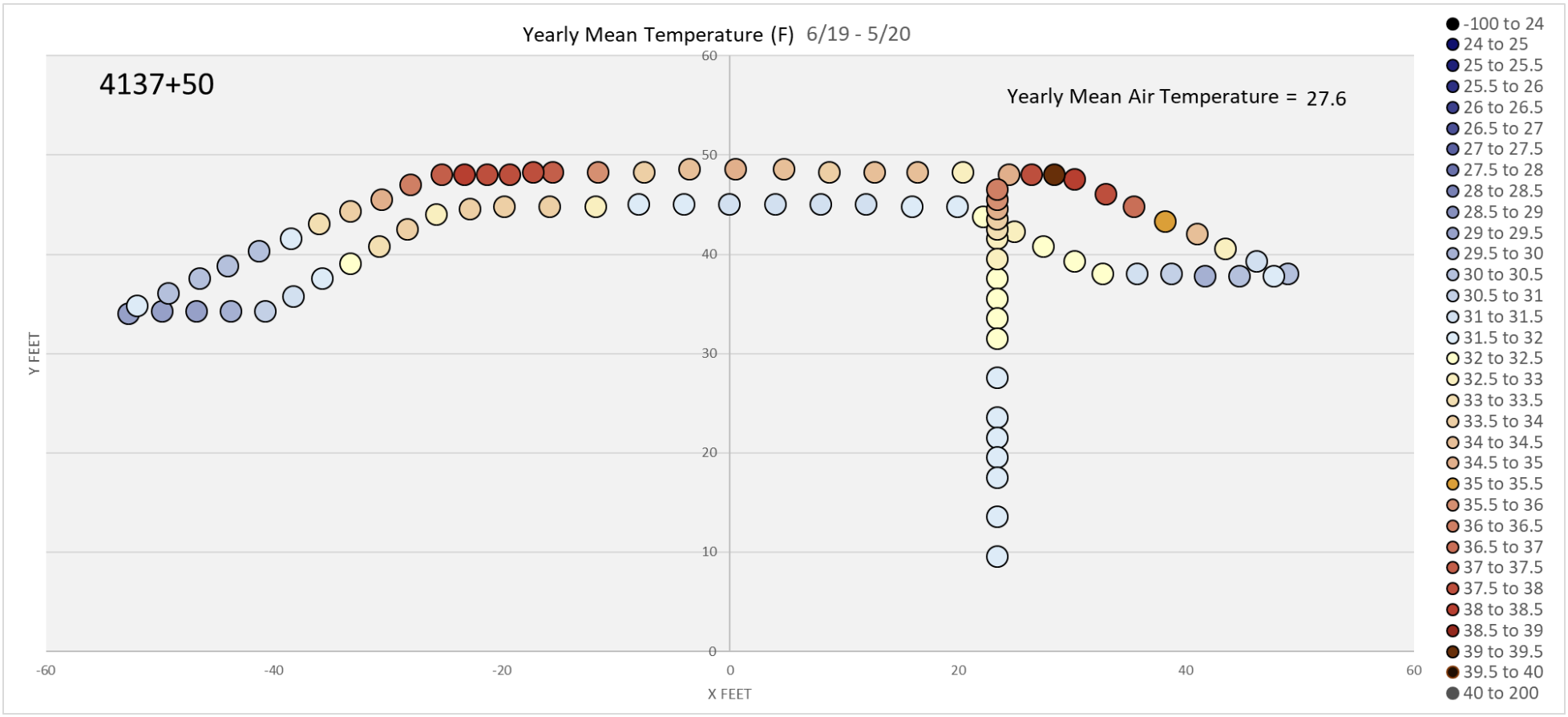

Figure 3-35 Mean Annual Temperatures for Section 4137+50 for the Period June 2019 through May 2020

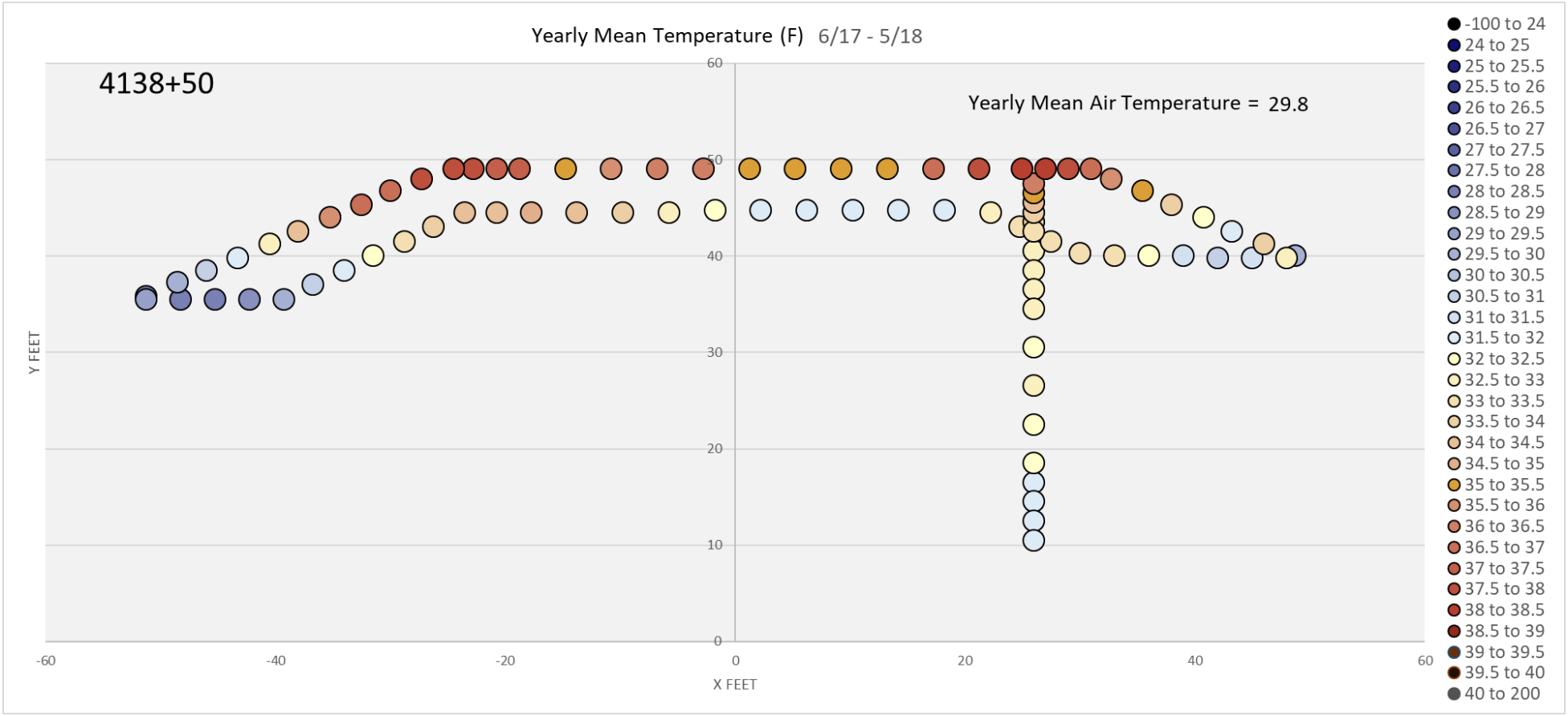

Figure 3-36 Mean Annual Temperatures for Section 4138+50 for the Period June 2017 through May 2018

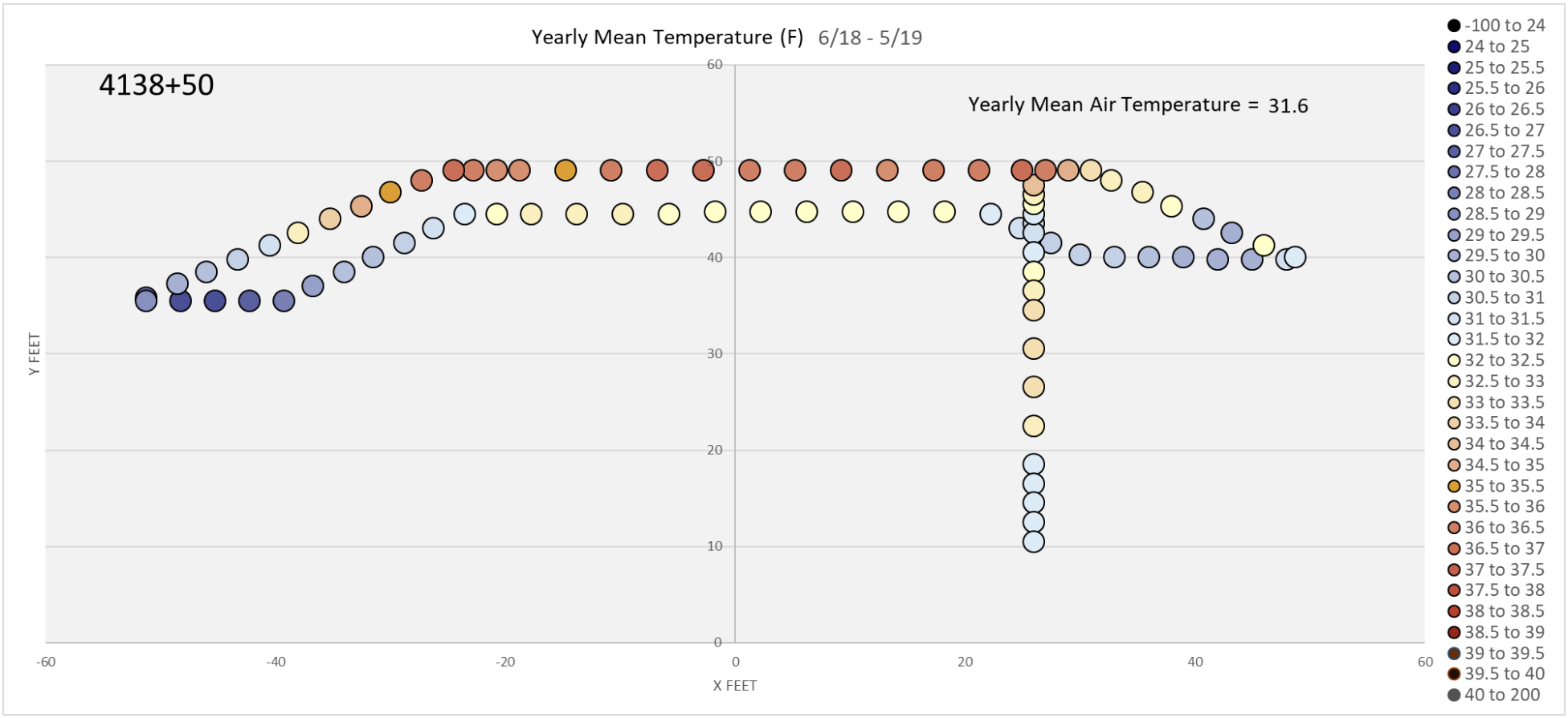

Figure 3-37 Mean Annual Temperatures for Section 4138+50 for the Period June 2018 through May 2019

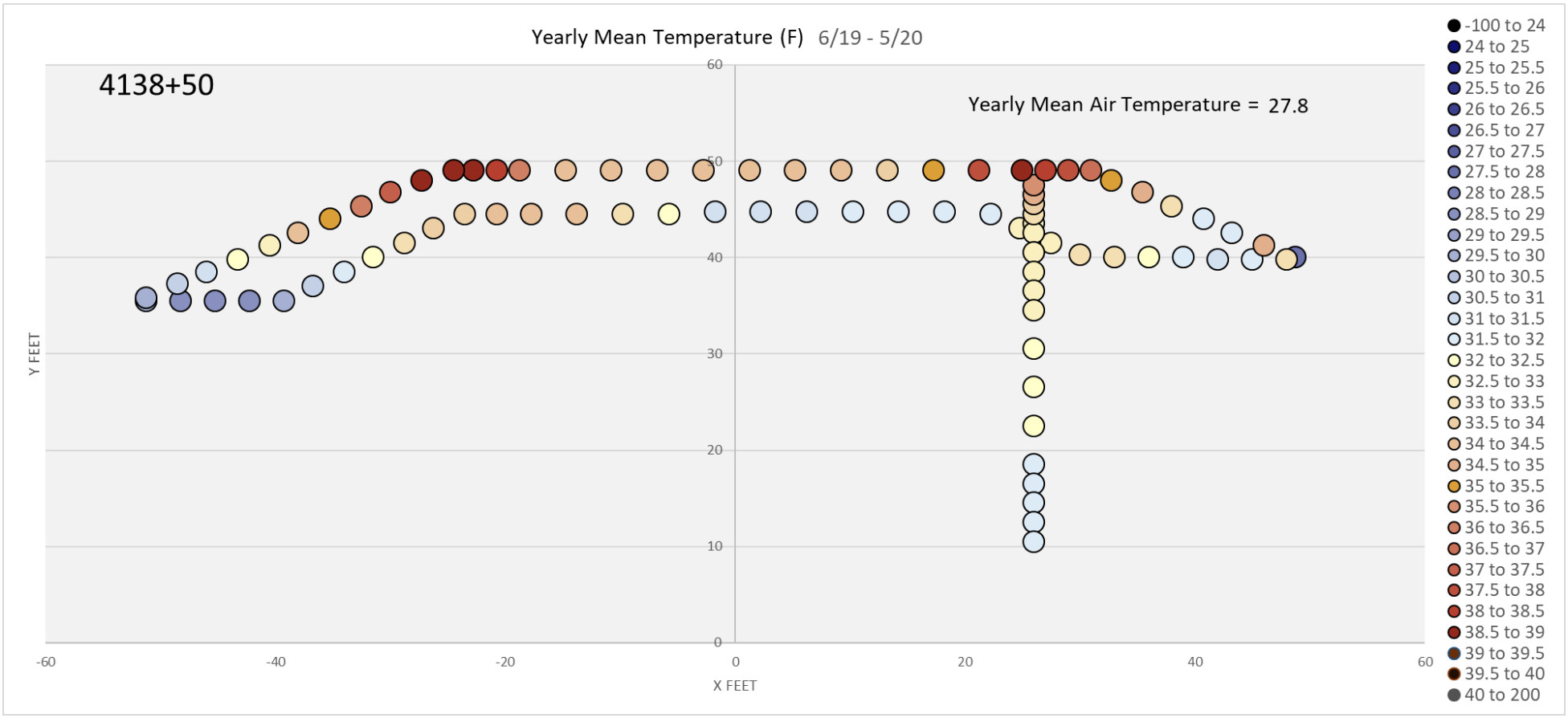

Figure 3-38 Mean Annual Temperatures for Section 4138+50 for the Period June 2019 through May 2020

CHAPTER 4. NUMERICAL SIMULATION OF EMBANKMENT PERFORMANCE

4.1. Introduction

The final portion of this project involved the application of numerical methods to simulate ACE and Ventilated Shoulder thermal performance. The goal of this work was to validate the results produced via numerical simulation against the experimental results obtained at Thompson Drive. The Thompson Drive results are well-suited for this task because of the large number and geometrical spacing of the temperature measurements. The geometrically spaced measurements allow a more direct comparison between the experimental results and the spatial temperature patterns produced by the numerical models. The overall goal of this portion of the work was to validate the numerical methods against the experimental data such that they can be used with a greater level of confidence for future designs.

In an effort to determine the best numerical approach available, two modeling packages have been evaluated. These included the SoilVision SVHeat simulation package and the GeoStudio Temp/W simulation package. The GeoStudio software has been used extensively in the past by both AKDOT and UAF personnel to simulate embankment performance, including the performance of ACE and Ventilated Shoulder systems. On the other hand, the SoilVision package has received less attention and, to the author's knowledge, has only been utilized by a few of the geotechnical engineering firms in Anchorage. As a result, in conjunction with the technical advisory committee for this project, it was decided to evaluate the SoilVision SVHeat package to determine its ability to accurately simulate the ACE and Ventilated Shoulder cooling systems that are of interest in this study.

In the sections that follow the preliminary testing of SVHeat is discussed, followed by a discussion of the more extensive testing and verification that was conducted using Geostudio Temp/W.

4.2. SoilVision SVHeat

The SoilVision SVHeat package is a product of Bentley Systems, Inc. The author had known of this simulation package for some time because of conversations with geotechnical consulting firms that were attempting to model ACE embankment performance. In an effort to evaluate the effectiveness of the package, Bentley Systems was contacted in the summer of 2020 and a software evaluation license was obtained for both UAF and AKDOT. The package was then evaluated during November and December of 2020 by the author and by Matt Billings with AKDOT.

The SVHeat code consists of two separate parts (which actually required separate licenses). The first is the core interface of SVHeat that supports the input of problem parameters, including geometry, material properties, thermal boundary conditions, etc. The SVHeat core then produces an input file for the actual finite element solver, FlexPDE, which is a product of PDE Solutions. Bentley and PDE Solutions collaborate on licensing but the two packages are separate. Once the model geometry, materials, and boundary conditions are set up in SVHeat, the input file is passed to FlexPDE for the solution process. As solution time steps proceed, FlexPDE automatically monitors the solution to ensure numerical convergence and accuracy. FlexPDE automatically determines the characteristics of the finite element grid that is used to obtain the solution, including the number, shape, and density of elements throughout the model domain. Interestingly, FlexPDE will automatically refine the finite element grid as needed as the complexity of the solution demands. This approach ensures that accurate, converged

results are obtained with a minimum of computational effort. This is a very nice feature and something that is not available in the Geoslope product.

SVHeat has been used to solve a number of cold-regions embankment problems. Fredlund and Zhang [6] discuss the use of SVHeat in solving cold regions embankment problems, including comparing their results to those of Goering [12] for a model of an ACE roadway embankment. Their results showed that SVheat was able to reproduce the complex convective flow patterns and overall airflow velocity magnitudes that had been predicted in Goering [12].

Evaluation of the SVHeat package took place in November and December of 2020. Both the author of this report and Matt Billings, AKDOT were able to run test problems. Testing indicated that the SVHeat package was relatively easy to use and that it provided very stable and accurate solutions to test problems consisting of ACE embankment configurations. The experience with the code was not flawless as a bug was identified in one of the boundary condition routines. While the bug did slow down the evaluation process, the Bentley technicians were supportive and were able to address the problem reasonably quickly. Overall the testing and, particularly, the robustness of the FlexPDE solver, led us to the conclusion that SVHeat would probably be a superior modeling package compared to the Geoslope Temp/W simulation package that both UAF and AKDOT already had access to. As a result, the decision was made to pursue purchase of the Soilvision SVHeat modeling package from Bentley Systems. However, the decision was reached at the very end of calendar year 2020 and purchasing became complicated because of year-end issues and the fact that Bentley Systems decided to withdraw the package from the market starting in 2021. As a result, in the end, we were not able to acquire the SVHeat package.

4.3. Geostudio TEMP/W

Following the evaluation work with SVHeat, attention was re-focused on the use of the GeoStudio Temp/W, Air/W modeling package. Temp/W calculates temperature profiles, while Air/W utilizes the temperature profiles to predict air motion which then feeds back into the Temp/W heat transfer model. Both UAF and AKDOT have current licenses for GeoStudio and have a relative wealth of experience using this numerical model. The overall goal of this part of the work was to utilize a coupled Temp/W – Air/W model to predict the behavior of the ventilated shoulder that is incorporated into test section #1 of Thompson Drive. See Figure 3-6 for the details of the test section and

Figure 4-1 for a schematic of the Temp/W finite element grid that was used for the numerical modeling. Note that the hairpin thermosyphon that is present at test section #1 was not included in the model. Temp/W does have provisions for modeling thermosyphons, but not for thermosyphons like the hairpin arrangement in Thompson Drive where both the evaporator and condenser are contained within the embankment. Exclusion of the thermosyphon was not deemed a significant issue since the focus of this modeling is simulating the convective airflow through the ventilated shoulder and the impact that airflow has on the temperature profiles beneath the shoulder region. These aspects of embankment performance are not impacted significantly by the presence of the thermosyphon.

As Figure 4-1 shows, the model domain extends from the embankment centerline out beyond the toe of the embankment. In the figure, the gray region consists of Selected Material A (Borrow A), the brown material is ACE rock, the yellow strip just visible in the embankment prism is a four inch thick XPS insulation layer, and the lavender material in the lower portion of the grid represents the silt foundation

soils. The grid extends 20 m below the original grade, horizontally 25 m from the embankment centerline to the toe of the ventilated shoulder, and another 15 m from the edge of the toe to the righthand boundary of the model domain. The height of the embankment at the centerline is 5.5 m and

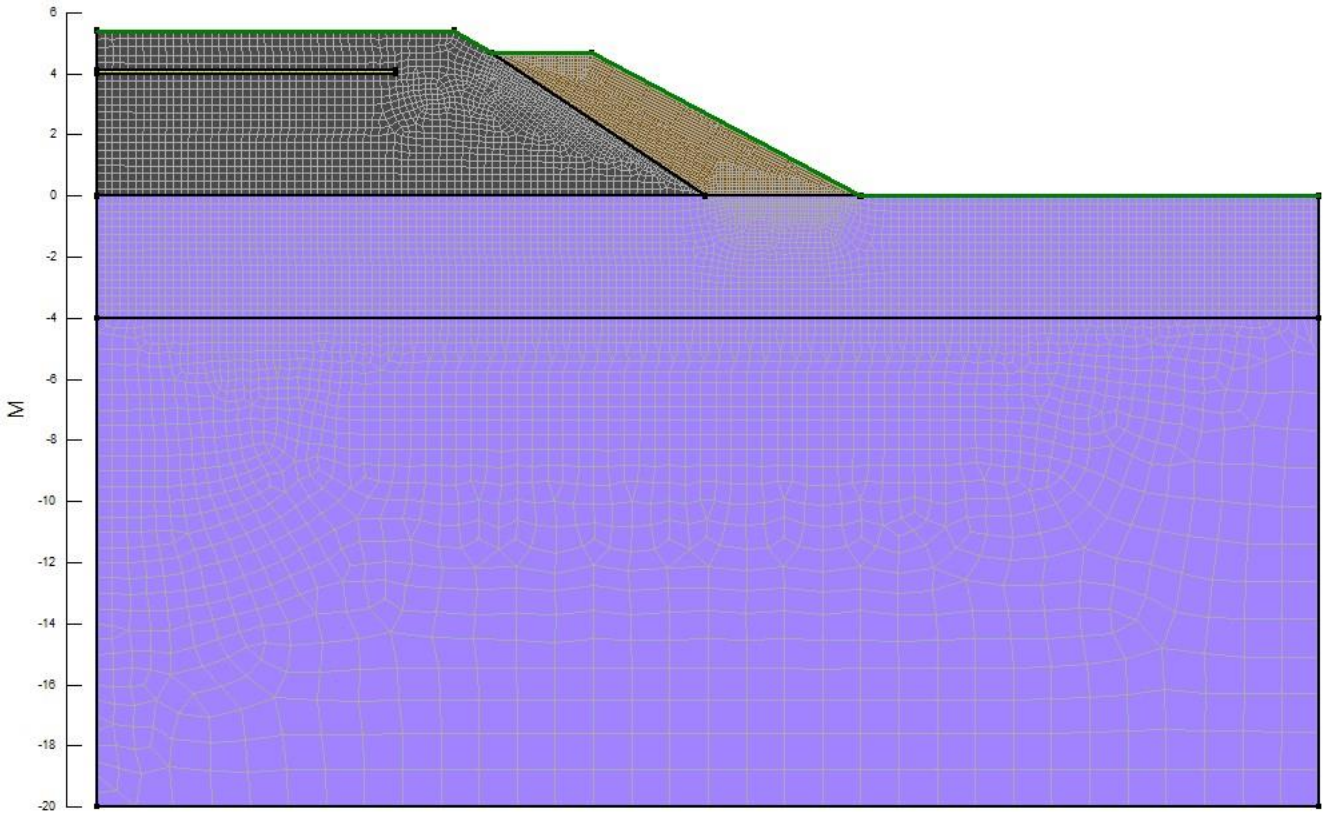

the height of the upper surface of the ventilated shoulder is 4.7 m. These dimensions closely approximate those of the actual test section shown in Figure 3-6.

Figure 4-1 Temp/W Finite Element Grid Used for Thompson Drive Simulation.

4.3.1. Material Properties

In order to carry out the Thompson Drive modeling study, material property estimates were needed. These include thermal properties for the Borrow A embankment fill, silt foundation soils, ACE shoulder material and insulation, as well as air permeability for the ACE layer. Material properties were based on the original Thompson Drive design work (Goering, 2001) which, in turn was based on sampling of the foundation soils and design specifications for the Select Material Type A (Borrow A). Volumetric water contents were assumed to be 11% for the Borrow A, 32% for the silt, and essentially zero for the ACE rock shoulder material and insulation. Given these assumptions, the thermal properties used for frozen and unfrozen thermal conductivity (k_u and k_f), volumetric heat capacity (C_u and C_f), volumetric latent heat (L) , and air permeability (K) are given for each material in Table 4-1.

Table 4-1 Material Properties used for Thompson Drive Simulation

Material	k_u (W/m °C)	k_f (W/m °C)	C_u(kJ/m^3 °C)	C_f (kJ/m^3 °C)	L (kJ/m^3)	K (m^2)
Borrow A	1.88	1.92	2,321	2,087	36,875	~0
Silt Foundation	1.39	1.87	2,816	2,141	106,784	~0

ACE Material	0.347	0.347	1300	1300	~0	6.3e-7
Insulation	0.033	0.033	10	10	~0	~0

Note that the air permeability used in these simulations is based on an average particle size of approximately 5 cm, which is smaller than the actual material used in the Thompson Drive ACE shoulder. However, material degradation and fracturing during handling and placement likely reduced air permeability somewhat so this smaller value of K=6.3e-7 m^2 was used as a conservative estimate. Also note that the intrinsic permeability can be calculated using the Fair and Hatch correlation, see Goering et al. [10] for further details.

4.3.2. Boundary and Initial Conditions

In order to conduct the numerical simulation, values were needed for the initial temperature of the foundation soil and embankment material as well as thermal and hydraulic boundary conditions at the edges of the simulation domain. Based on field measurements, the initial temperature of the foundation soil was assumed to be just below freezing at -0.2 °C. This initial temperature was also used for the embankment materials, including the gravel and ACE shoulder rock. Since the numerical simulation was started at Julian day 90 (about the end of March), the -0.2 °C temperature setting was probably reasonable, but in any case, the impact of the initial embankment temperatures diminished over the first few years of the simulation.

Thermal boundary conditions are needed along each edge of the simulation domain, including the upper asphalt surface, the surface of the embankment side slope, the natural surface to the right of the embankment toe, the centerline and righthand boundaries, and at the lower boundary of the simulation domain. At the lower boundary the geothermal heat flux of 0.06 w/m^2 was applied, while at the centerline and righthand boundaries a zero heat flux condition was used (this assumes symmetry at the embankment centerline). At the upper surfaces, all exposed to the ambient environment, air temperature data from Thompson Drive test section #1 was used to derive appropriate temperature relationships using an N-factor approach. Test section #1 air temperature data was compiled for the first ten years of project monitoring (Table 4-2) and used to determine average air freezing and thawing indices. These freezing and thawing indices were then used to construct harmonic temperature functions that represent air temperature, asphalt surface temperature, side slope surface temperature, and native ground surface temperature.

Table 4-2 Thompson Drive Test Section #1 Air Temperature Values

Yearly Averages	Ambient Air (°C)	AFI (°C-days)	ATI (°C-days)
2005	-0.42	2558	2405
2006	-2.13	2993	2215
2007	-1.05	2792	2411
2008	-2.69	3018	2033
2009	-1.40	2832	2322
2010	-0.99	2755	2392
2011	-1.35	2734	2240
2012	-3.04	3364	2253
2013	-1.11	2659	2252

2014	0.10	2128	2164
Overall Average	-1.41	2783	2269

Using the data from Table 4-2, harmonic temperature functions of the form:

$$T = T_{avg} - T_{amp}\, cos\left(\frac{2\pi(t-10)}{365}\right)$$

were generated for the upper surfaces using N-factors appropriate for each surface type. Note that this function assumes a 10-day lag from January 1 until the minimum temperature of the year is achieved based on typical time lag data for Fairbanks. The resulting parameters are shown in Table 4-3.

Table 4-3 Temperature Boundary Condition Functions

Temperature Function	Freeze N-factor	Thaw N-factor	T_{avg} (°C)	T_{amp} (°C)
Ambient Air	1	1	-1.41	21.7
Asphalt Surface	1	1.6	2.32	27.5
Side Slope Surface	0.6	1.4	4.13	20.4
Natural Surface	0.35	0.4	-0.18	8.1

In addition to the temperature boundary conditions discussed above, hydraulic (airflow) boundary conditions are also needed at the edges of the computational domain. However, these conditions only have importance for the high-permeability portions of the roadway embankment where airflow can occur. As a result, all boundaries except the upper edges of the ACE shoulder region are assumed to be impermeable. For the ACE ventilated shoulder, two different scenarios were investigated, one in which the surface of the ventilated shoulder was assumed to be impermeable (as might be the case with a layer of top soil or an extremely dense snow or ice layer covering the surface) and one in which the surface of the ventilated shoulder is assumed to be open to the surrounding ambient air mass (as might be the case with no surface covering or with a highly permeable snow layer covering the surface). No attempt was made to actually model the seasonally varying snow layer itself, although that approach may be indicated in the future.

4.3.3. Simulation Results

In an effort to model the behavior of the ventilated shoulder as seen in the Thompson Drive experimental data, and investigate the impact of different boundary condition assumptions, a number of numerical simulations were performed using Geoslope's Temp/W and Air/W modules. The simulations were broken down into five different cases depending on how the ventilated ACE shoulder and associated boundary conditions were treated. Table 4-4 describes each of the five cases, starting with the conduction-only case where the ACE shoulder material was replaced with Borrow A, eliminating any pore air convection because of the low permeability. Case 1 can be considered a base case that is comparable to a normal roadway embankment with no ACE layers or convective cooling. Cases 2 – 5 are then used to investigate the cooling effectiveness of the ACE ventilated shoulder using different combinations of hydraulic and thermal boundary conditions. Case 2 utilizes a closed shoulder surface boundary such that airflow into or out of the ventilated shoulder from the ambient air mass is not allowed. For this case the thermal boundary condition is relatively easy to specify using the normal N-

factor approach, as indicated in the table by the side slope temperature thermal boundary condition. For cases 3 – 5, the shoulder boundary was open to the ambient air mass meaning that airflow occurred from the ambient air into and out of the ventilated shoulder (through the snowpack in winter). For these conditions it is much harder to specify the thermal boundary condition because airflow through the snowpack will significantly alter the temperatures present on the shoulder surface. In areas of inflow, the shoulder boundary is likely to be close to the ambient air temperature since the snowpack itself has a very small thermal heat capacity. On the other hand, where pore air is being exhausted out of the ventilated shoulder through the snowpack, the temperature at the boundary is more likely to be determined by the temperature of the shoulder material itself, since pore air flowing toward the boundary will have a temperature close to the material temperature. These complexities make it very difficult to use an N-factor approach or a conventional snowpack model to simulate the temperature boundary conditions at the surface of the ACE shoulder. Cases 3 – 5 investigate the impact of various thermal boundary condition assumptions, even though none of them accurately mimic the actual thermal conditions expected on the surface of the ACE shoulder. Case 3 assumes that the airflow does not impact surface temperatures and simply uses the N-factor based side slope thermal boundary condition. Case 4 assumes that the airflow through the snowpack results in equilibration between the ambient air temperature and the temperatures on the surface of the side slope. This is probably reasonably accurate where ambient air is flowing into the shoulder. Finally, case 5 treats the surface of the shoulder the same as the asphalt surface. This could also be considered to make sense in areas where ambient air is flowing into the shoulder (the freeze N-factor for the asphalt boundary is 1, indicating that it is at the same temperature as the ambient air during winter). During summer, the asphalt surface warms appreciably due to incoming solar radiation. Solar radiation also impacts the side slope surface during summer, so using an asphalt temperature boundary condition at the side slope surface may also make sense during the warm portion of the annual cycle. While it is likely that none of these boundary condition assumptions are good approximations of the actual conditions at the surface of the ACE ventilated shoulder, it is likely that they bracket the true conditions, so some indication of the real world cooling effectiveness and impact of these boundary condition assumptions can be obtained by comparing the results from the cases listed in Table 4-4.

Table 4-4 Case descriptions for numerical simulations

Case #	Description	Shoulder Material	Thermal BC	Hydraulic BC
1	Conduction-only	Borrow A	Side slope temp	Impermeable
2	Closed boundary	ACE rock	Side slope temp	Impermeable
3	Open boundary	ACE rock	Side slope temp	Open to ambient
4	Open boundary w/air temp	ACE rock	Air temp	Open to ambient
5	Open boundary w/asphalt temp	ACE rock	Asphalt temp	Open to ambient

For each case shown in Table 4-4 a Temp/W simulation was run for a total of 12 annual cycles starting on April 1 of the first simulation year with an initial temperature set to -0.2°C for both the foundation soil and the embankment. The impact of the initial temperature assumption quickly dissipates within the embankment but persists much longer in the foundation soils. As noted above, the -0.2°C initial

condition was based on actual temperature measurements from Thompson Drive. Results were saved at regular intervals throughout the 12-year simulation period but then were also saved for Jan. 15, Feb. 15, March 15, April 15, May 15, June 15, July 15, Aug. 15, Sept. 15, Oct. 15, Nov. 15, and Dec. 15 of the final year of simulation for more detailed comparison to the field results from Thompson Drive.

4.3.4. Case 1 Results

As indicated in Table 4-4, Case 1 is an examination of the thermal behavior of the embankment assuming that the shoulder region is constructed of Borrow A instead of ACE rock. For this case the embankment acts more like a conventional roadway embankment with no special cooling measures. In this case it would be expected that thaw and talik formation would gradually occur beneath the shoulder region due to the relatively warm thermal boundary conditions indicated in Table 4-3 for the shoulder surface (T_{ave} = +4.13°C for the shoulder surface). Some thaw and talik formation could also be expected beneath the centerline of the roadway, except that the warming would be retarded somewhat by the presence of the insulation layer in that area.

Figure 4-2 through Figure 4-4 show the results of the Case 1 simulation on January 1 of the 1st, 6th, and 12th year of simulation. These figures show that a thawed region develops beneath the roadway and grows over time, achieving maximum depth of thaw in the region beneath the shoulder of the embankment. After twelve years the maximum depth of the thaw zone extends down nearly six meters below the original grade. In a real-world situation where the embankment is located on permafrost with excess ice content, we would expect that this thaw behavior would cause significant deformation of the embankment and outward rotation of the shoulders due to the exacerbated thaw beneath the toe.

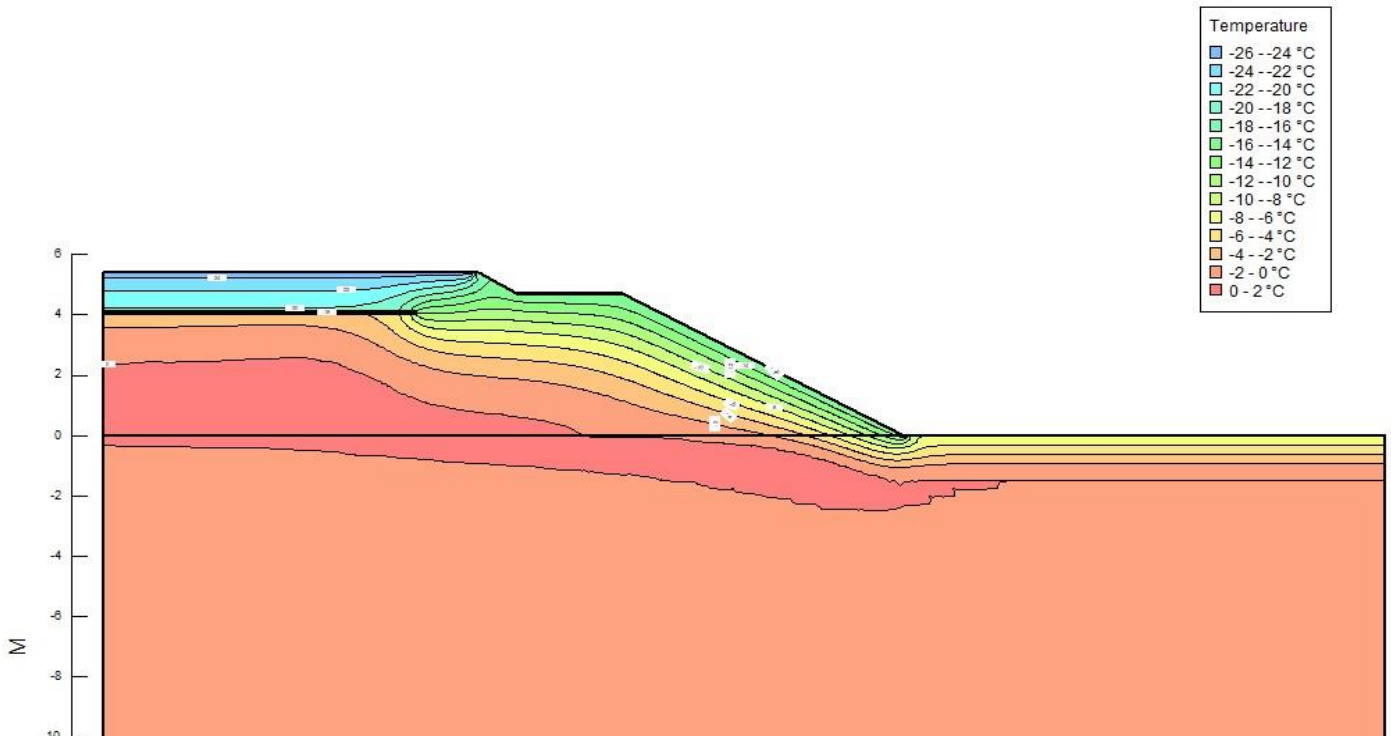

Figure 4-2 Simulation Results for Case 1 for January 1 of Year 1

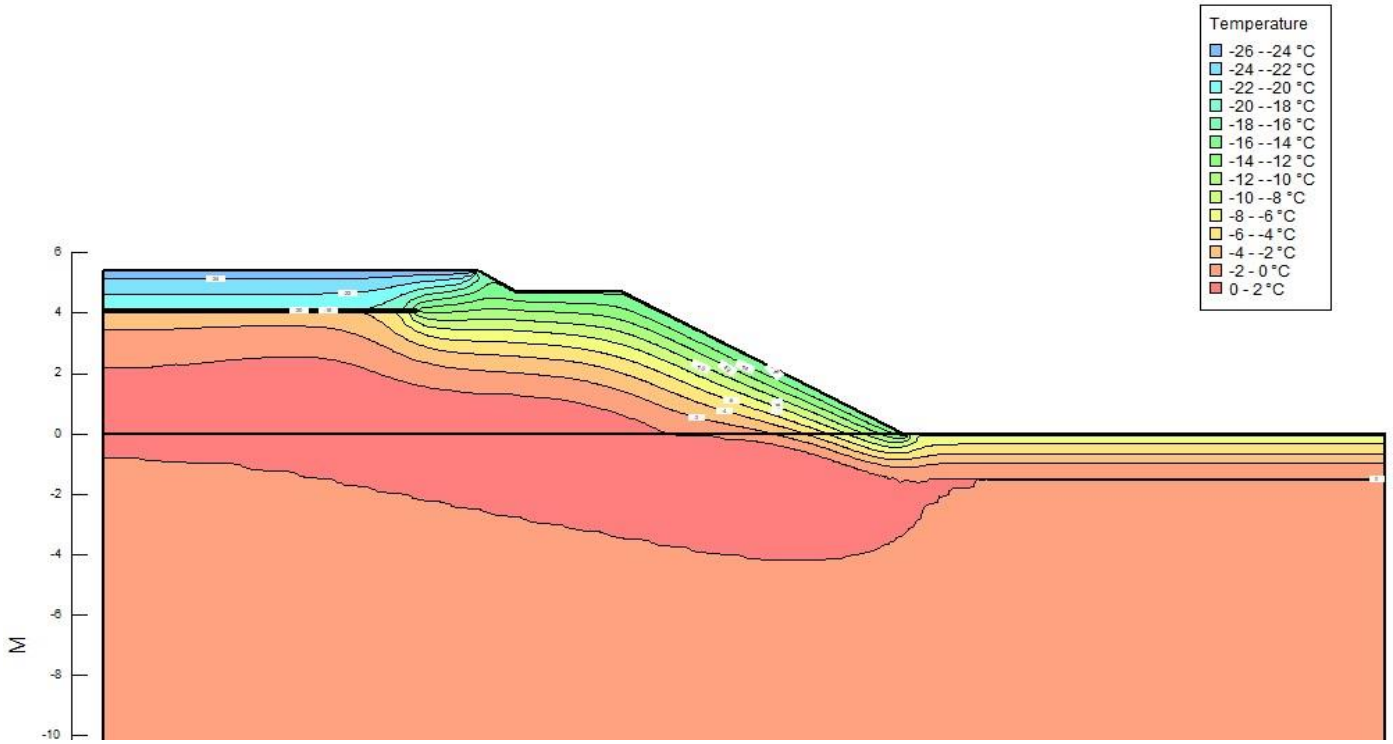

Figure 4-3 Simulation Results for Case 1 for January 1 of Year 6

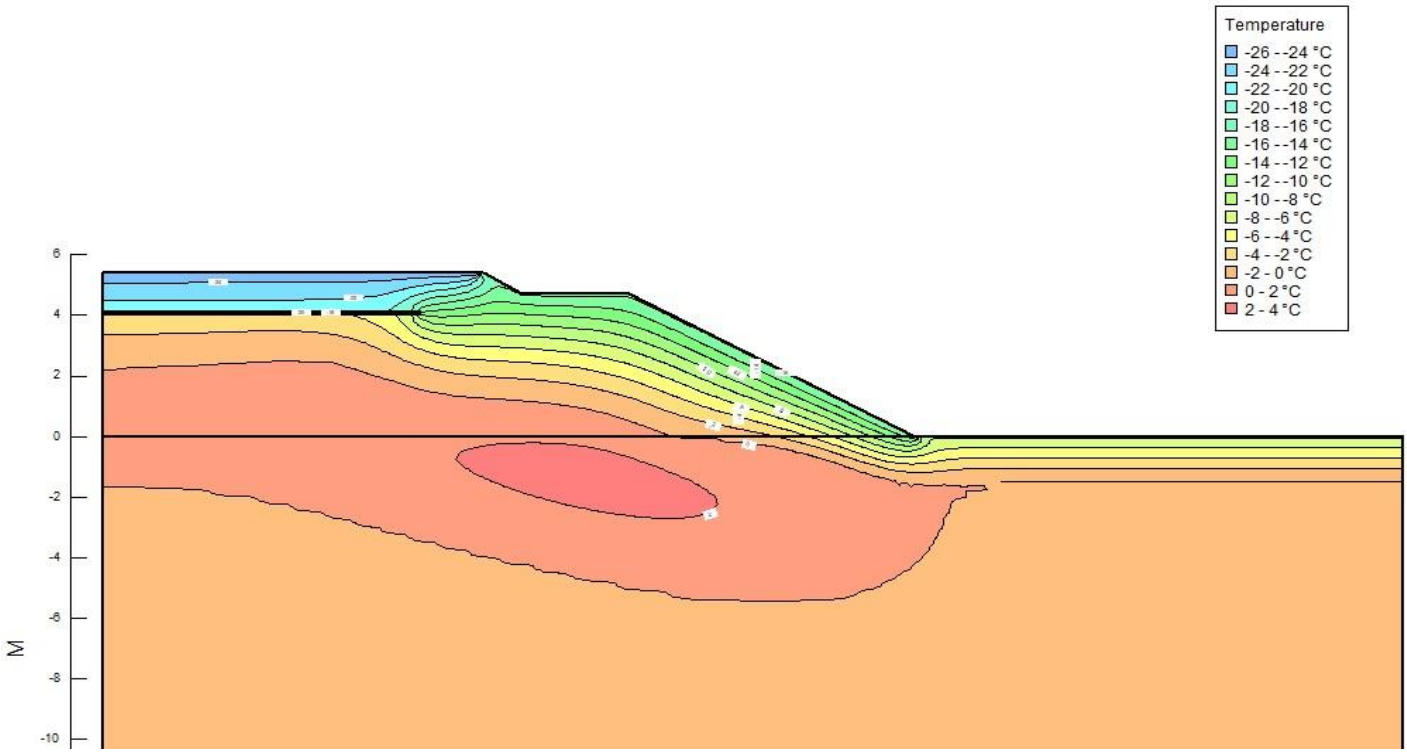

Figure 4-4 Simulation Results for Case 1 for January 1 of Year 12

The type of thermal behavior indicated in Figs. 4-2 to 4-4 is typical of roadway behavior in warm discontinuous permafrost zones. Warm asphalt and side-slope surfaces cause gradual thaw of the pre-existing permafrost layer beneath the embankment. However, thawing takes time and occurs somewhat gradually over the years with the thaw bulb only slowly expanding beneath the shoulder and centerline. As a result, any thaw-induced settlement will continue year after year, causing periodic maintenance problems that are likely to last throughout the lifetime of the project.

The Case 1 results shown above bear little resemblance to the experimental results obtained from test section #1 on Thompson Drive, illustrating that the conduction-only analysis is not capable of simulating the type of behavior observed in the field. This is not a surprise since it is clear from the experimental results that air convection in the ventilated shoulder, which is not included in the Case 1 simulation, does have a large impact on the thermal performance and foundation soil temperatures.

4.3.5. Case 2 Results

For the Case 2 simulations, the material in the ventilated shoulder region shown in Figure 4-1 and in Figure 3-6 consisted of ACE rock as in the actual Thompson Drive configuration. For this case, pore air convection does take place in the ventilated shoulder, but the upper boundaries of the shoulder region are treated as closed, impermeable boundaries, thus eliminating airflow from the ambient air mass into and out of the shoulder. Also note, as indicated in Table 4-4, that the warm side-slope boundary condition is used for the temperature at the surface of the shoulder. While this case represents one step closer to field behavior as compared to Case 1, it still simplifies the situation by disallowing airflow across the shoulder boundary. Ample evidence from the Thompson Drive site suggests that airflow does indeed occur into and out of the shoulder region, even in the presence of a snow layer. Thus, while the expectation is that Case 2 would produce simulation results that are closer to the results observed in the field, there will still likely be significant differences.

Unlike for the Case 1 results, the simulation for Case 2 shows very active pore air convection in the ventilated shoulder, particularly during winter. Figure 4-5 shows the pore airflow pattern for January 1 during the twelfth year of the simulation. As shown in the figure there is a very vigorous circulation of pore air within the shoulder region as evidenced by the airflow vectors shown in the figure and the distorted temperature isotherms which are impacted by the air convection. Given that the outer boundaries of the shoulder are impermeable, all of the circulation occurs within internal circulation cells that are not directly connected to the external ambient air mass. Since much of the circulatory flow indicated in the figure is occurring in directions nearly perpendicular to the shoulder boundaries, this circulation helps to promote increased heat transfer between the outer surface of the shoulder and the core of the embankment, particularly during winter. As a result, there is an enhanced cooling influence during the winter season.

Figure 4-6 shows the airflow patterns within the ventilated shoulder for July 1. While there is still notable airflow within the shoulder, the characteristics of the flow pattern are completely different than those observed during winter conditions. As before, the airflow is confined to the shoulder zone with no inflow or outflow, and no direct connection to the external ambient air mass. Airflow occurs in one large circulation cell with upward flow along the outer surface and downward flow along the inner boundary that abuts the conventional borrow embankment. This airflow is gentler than that experienced during winter conditions and does not have much impact on the temperature isotherms as

evidenced in the figure. As a result, the convective airflow is less effective at enhancing summer warming of the embankment core and foundation soils.

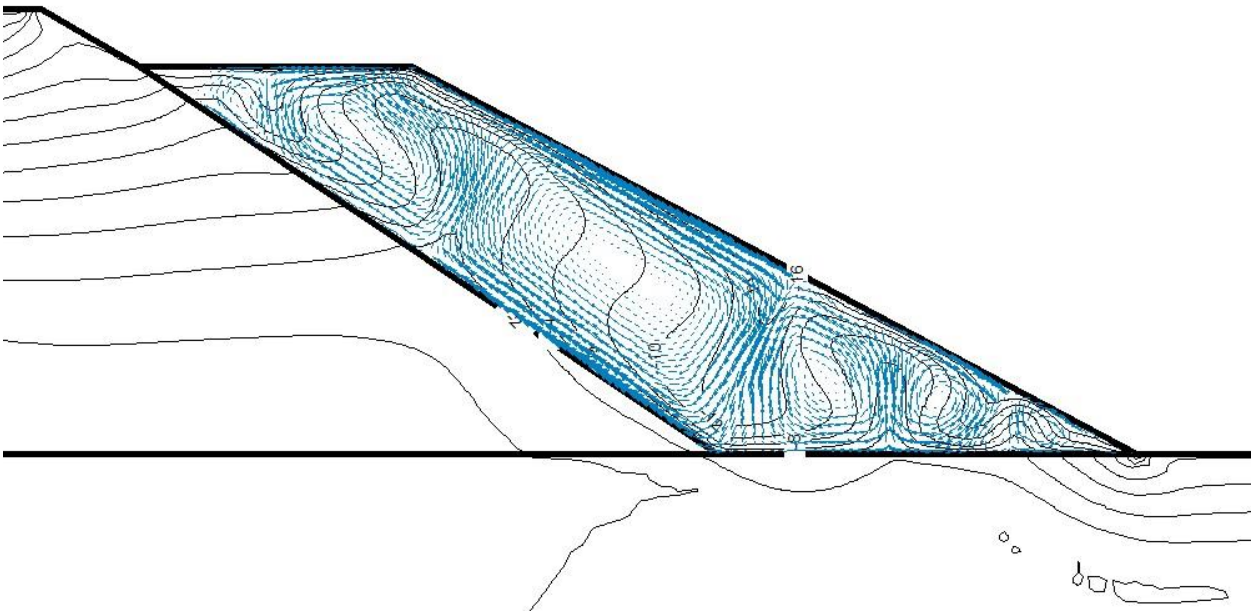

Figure 4-5 Convective Airflow Pattern in the Ventilated Shoulder on January 1 for Case 2

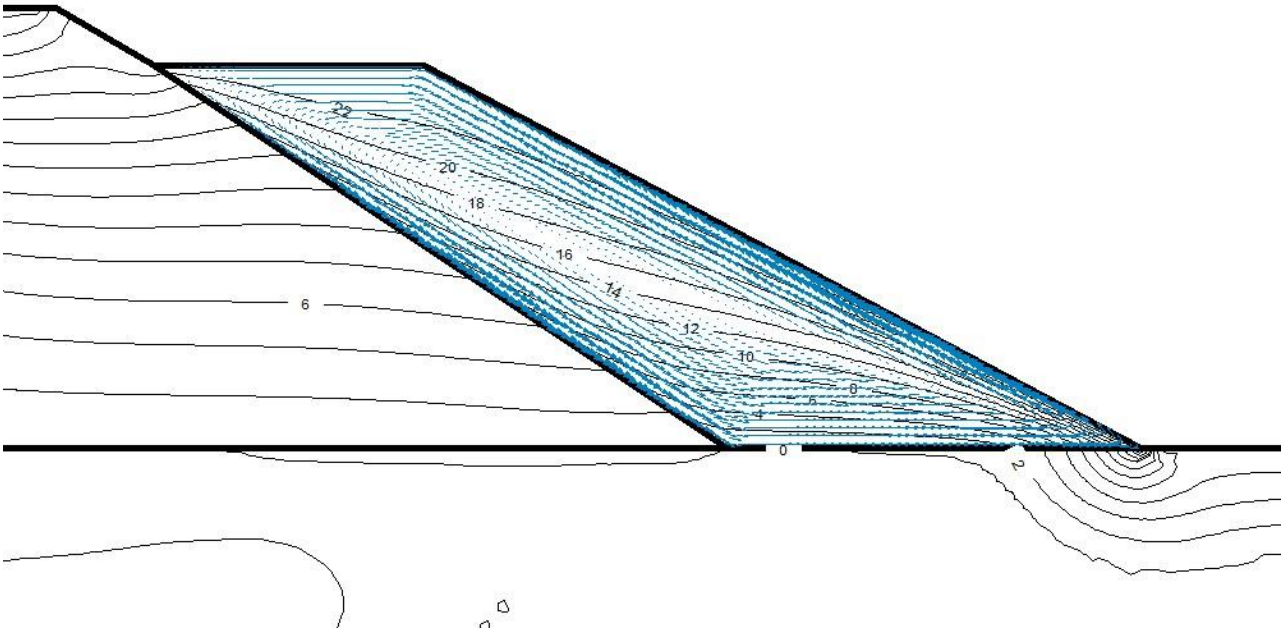

Figure 4-6 Convective Airflow Pattern in the Ventilated Shoulder on July 1 for Case 2

Figure 4-7 through Figure 4-9 show temperature isotherms for the Case 2 simulation on January 1 of the 1st, 6th, and 12th year of simulation. As for Case 1, the results show a developing thaw zone beneath the core of the embankment which gradually expands during the first twelve years of simulation. However, the zone of thawed material beneath the shoulder is much more limited than for Case 1, indicating that the internal flow in the ventilated shoulder is capable of providing a significant cooling effect. This is evidenced by the fact that there is no thawed material immediately beneath the base of the shoulder even after the full twelve years of simulation (see Figure 4-9). This is despite the fact that the mean annual temperature of the shoulder surface is set to +4.13°C, well above the freezing point.

Figure 4-10 shows simulation results for Case 2 for May 12 of the 12th year of simulation. As seen in the figure there is a large talik remaining beneath the embankment at the end of the winter season, although the foundation soil beneath the shoulder is frozen. Figure 4-11 shows results for September 15, at the end of the summer season and indicates that the talik remains although it has changed shape somewhat. Also, even after the warm summer season, the foundation soil just beneath the base of the ventilated shoulder remains frozen.

As was the case for Case 1, these results for Case 2 do not bear a strong resemblance to the field data for test section #1 on Thompson Drive, although they are closer to field observations than those for Case 1. In particular, it appears that the air convection in the shoulder is able to counteract the warm thermal boundary condition at the surface of the shoulder and maintain frozen conditions at least in the foundation soil immediately below the base of the shoulder.

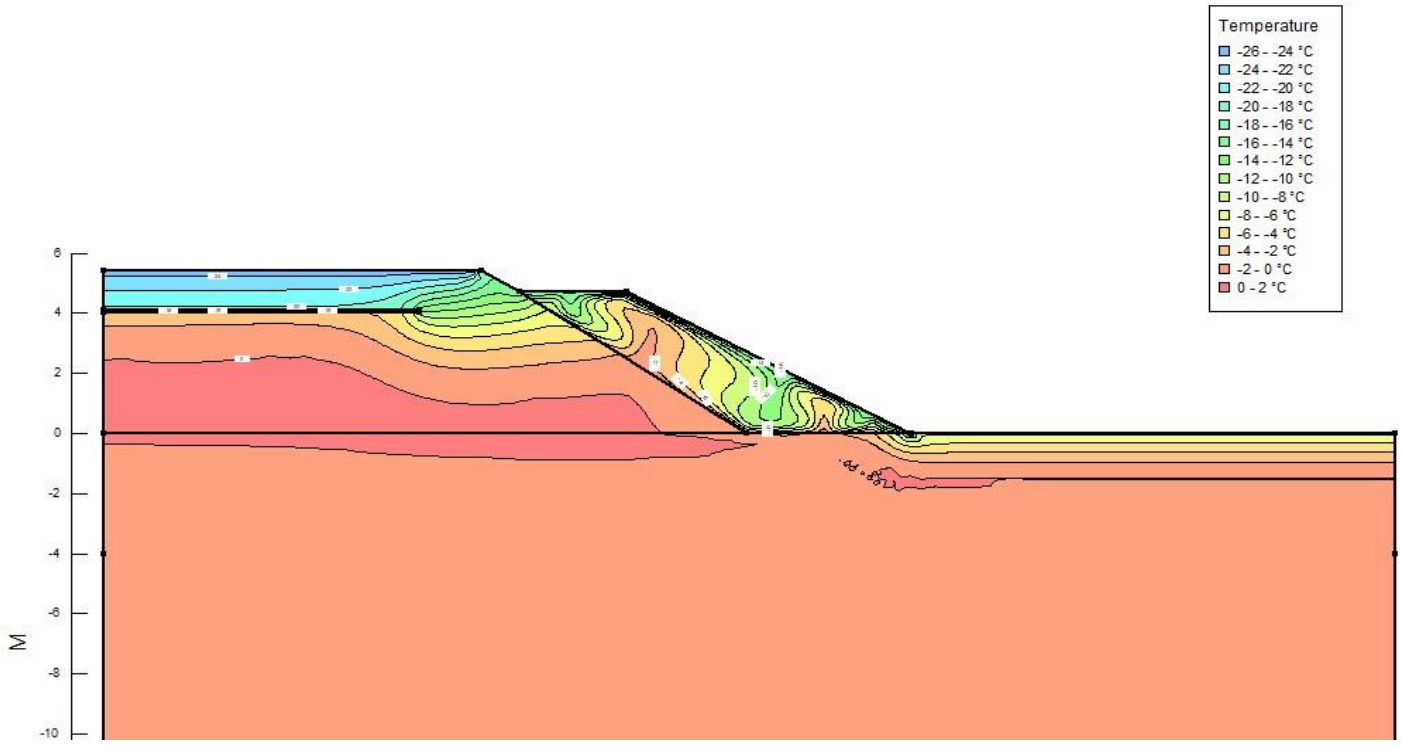

Figure 4-7 Simulation Results for Case 2 for January 1 of Year 1

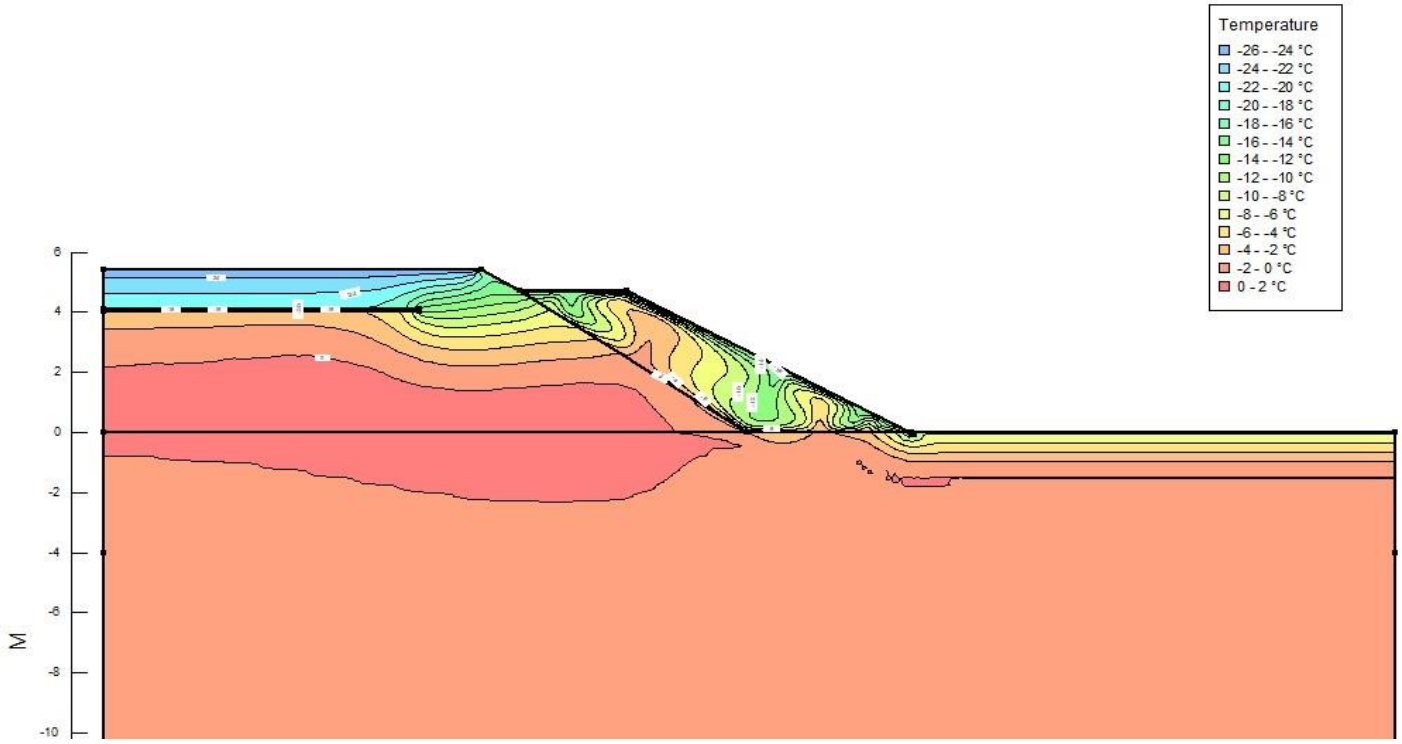

Figure 4-8 Simulation Results for Case 2 for January 1 of Year 6

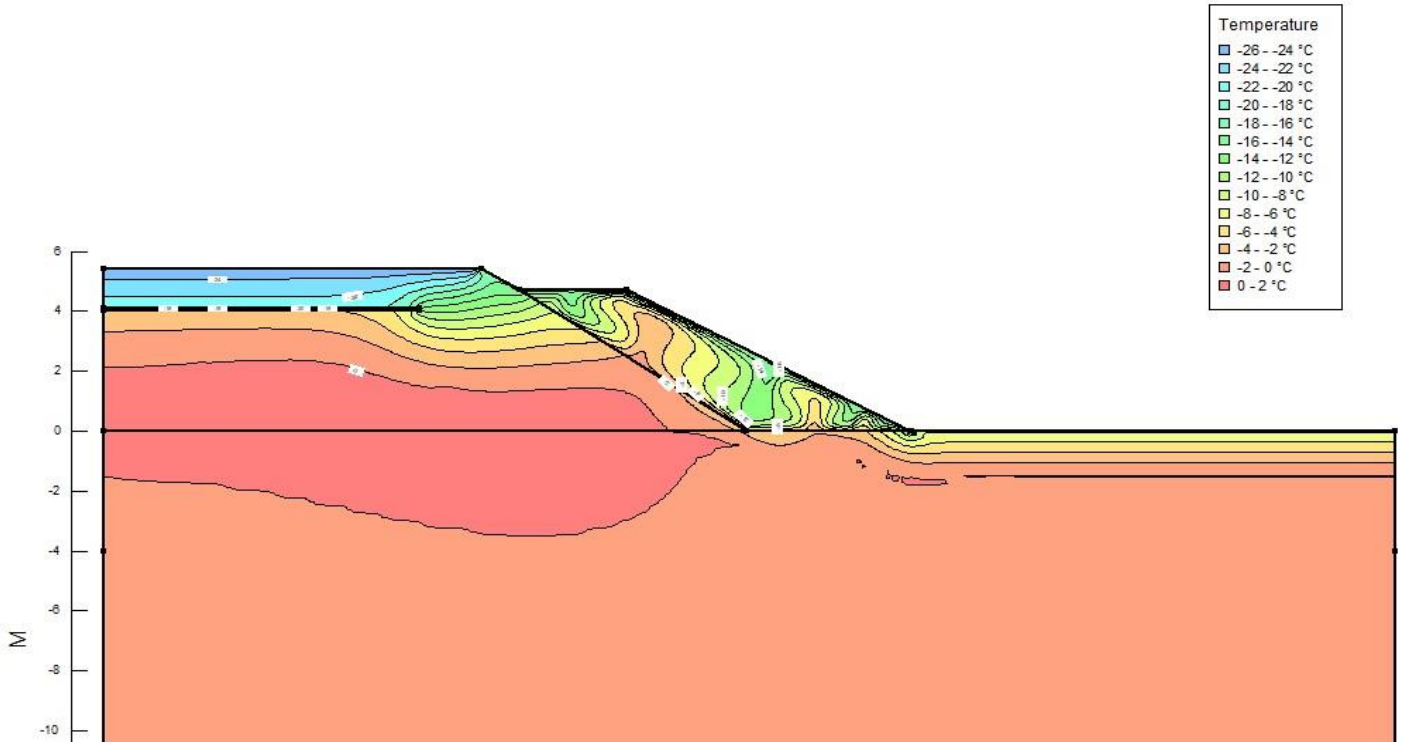

Figure 4-9 Simulation Results for Case 2 for January 1 of Year 12

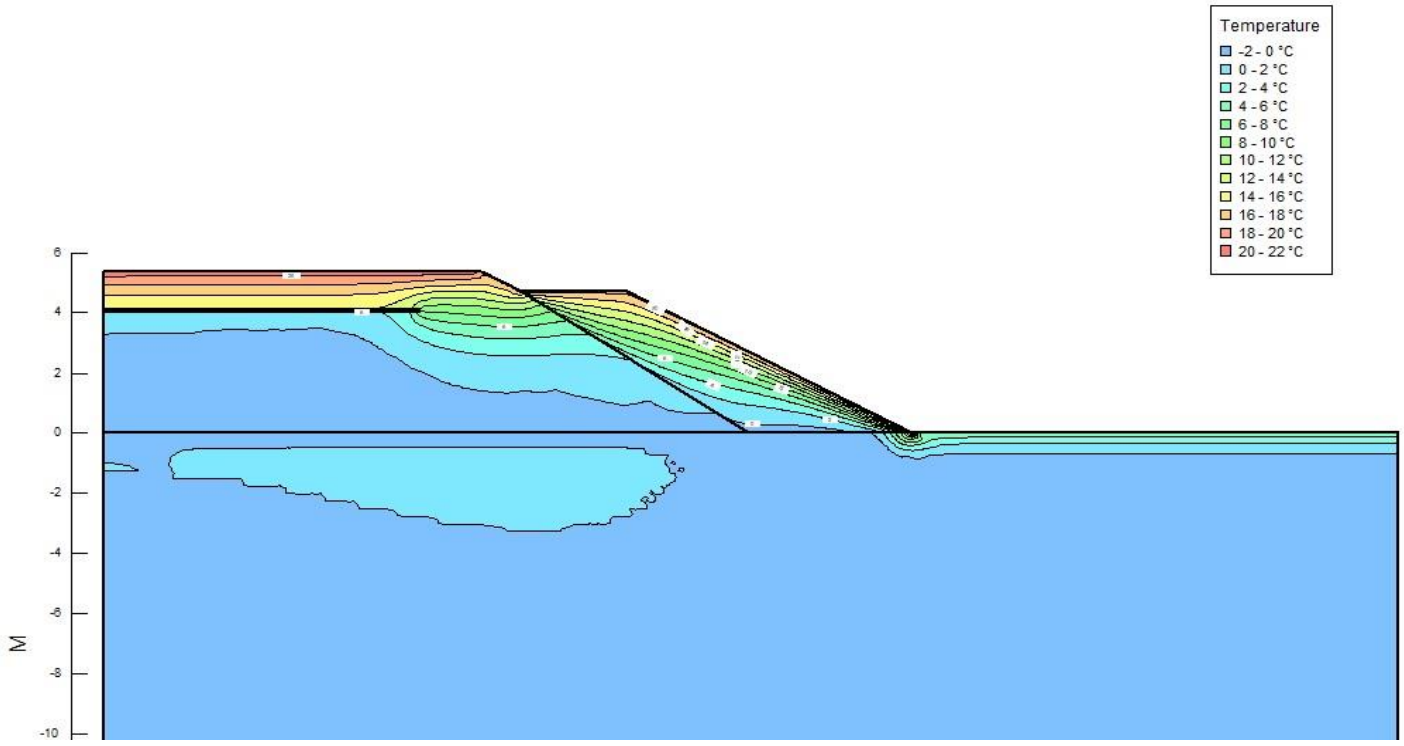

Figure 4-10 Simulation Results for Case 2 for May 15 of Year 12

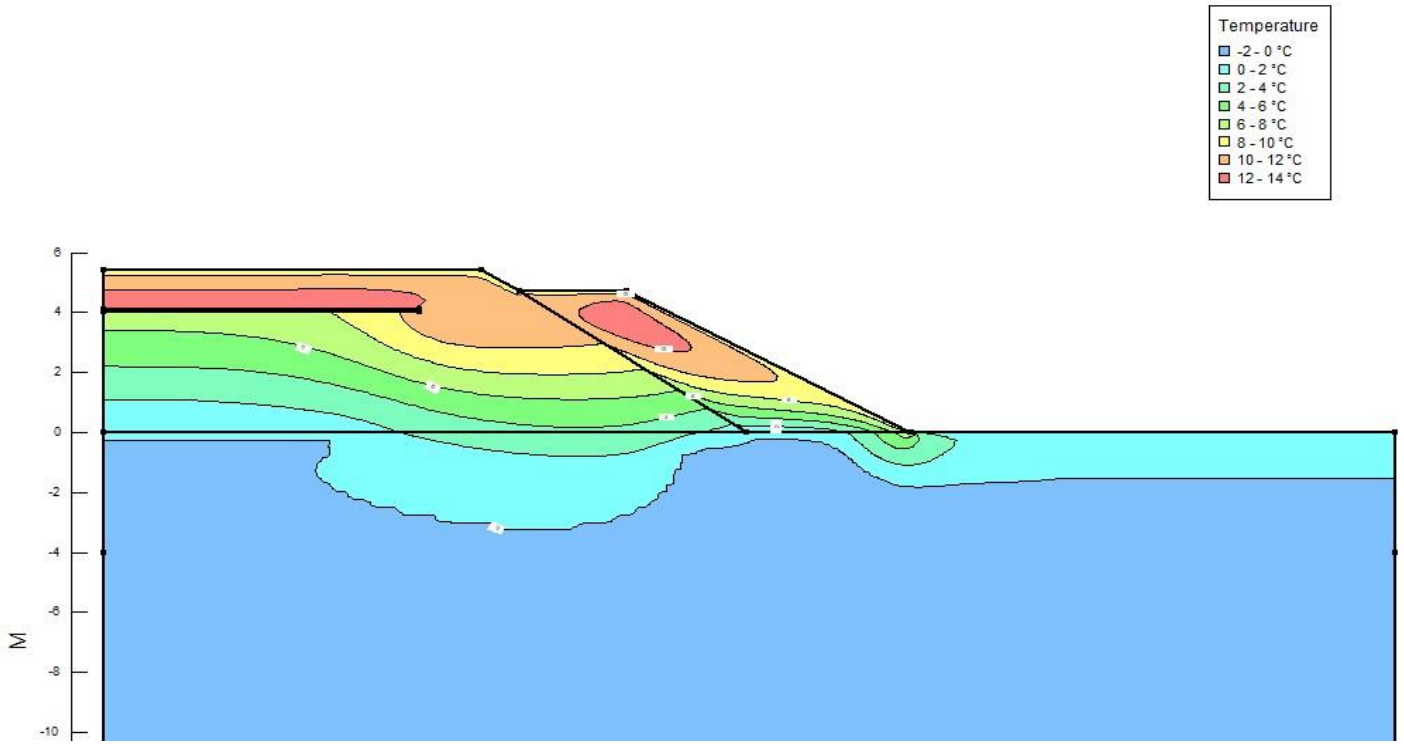

Figure 4-11 Simulation Results for Case 2 for September 15 of Year 12

4.3.6. Case 3 Results

The Case 3 simulation was identical to the Case 2 simulation except that the upper boundaries of the ventilated shoulder were treated as open boundaries and airflow was allowed to occur into and out of the shoulder surface. Thus, the airflow through the shoulder zone was directly connected to the ambient air mass. The airflow is assumed to occur regardless of the presence of snow on the upper surface of the shoulder during winter. Given the relatively high permeability of snow, this assumption is more reasonable than utilizing the impermeable no-flow condition that was imposed in Case 2. However, Case 3, similar to Case 2, uses the side slope thermal boundary condition listed in Table 4-3, which is likely inaccurate for this case, particularly during winter. The N-factors shown in Table 4-3 for the side slope surface come from the literature and are based on typical conditions for a gravel surface covered by snow. Normally the snow layer provides a substantial insulating effect during winter which results in the relatively low freezing N-factor of 0.6 as listed in Table 4-3 for the side slope boundary. However, in this case airflow is occurring through the snow layer and typically enters the ventilated shoulder by flowing through the snow layer in the region of the shoulder toe. As this airflow occurs, it transports cold ambient air directly through the snow layer, thus fundamentally changing the type of heat transfer occurring in the snow and effectively eliminating the insulation effect. Thus, while considering the ventilated shoulder boundaries as open boundaries represents a more realistic condition from the perspective of airflow, the thermal boundary condition is still likely not representative of actual conditions in the field.

As shown in Figure 4-12, the open boundary fundamentally alters the type of airflow through the shoulder zone during winter. Rather than a collection of internal circulation cells as seen in Figure 4-5 for Case 2, in this case airflow enters the ventilated shoulder along the lower portion of the outer boundary and flows upward through the ACE rock, eventually leaving the shoulder by flowing out of the upper surface. This has the effect of putting the pore air within the ventilated shoulder structure in direct communication with the ambient air and directly exposed to the relatively rapid changes in ambient air temperatures.

Figure 4-13 shows the pattern of pore air flow during the summer months and is fairly similar to that observed for Case 2 as shown in Figure 4-6 with airflow moving upward along the outer boundary and downward along the inner boundary of the ventilated shoulder zone. Close examination of the airflow patterns reveals that there is some influx of ambient air downward from the upper horizontal surface of the ventilated shoulder. This air moves downward along the inner boundary and then some of it exits the ventilated shoulder at the toe. Along the outer boundary there is an upward airflow with some ambient air entering the ventilated shoulder along the sloped boundary and exiting at the upper corner. However, summer airflow patterns have only a modest impact on temperature isotherms.

Figure 4-14 through Figure 4-16 show temperature isotherm profiles for the Case 3 simulation after one, six, and twelve years. The patterns shown in these figures are very similar to those shown for Case 2 although Figure 4-16 tends to indicate slightly warmer conditions than for Case 2 with a small zone of foundation soil that is warmer than +2°C. This warm zone did not appear in the Case 2 simulation. However, as was true for Case 2, the foundation soil immediately beneath the ventilated shoulder remains frozen in the Case 3 simulation.

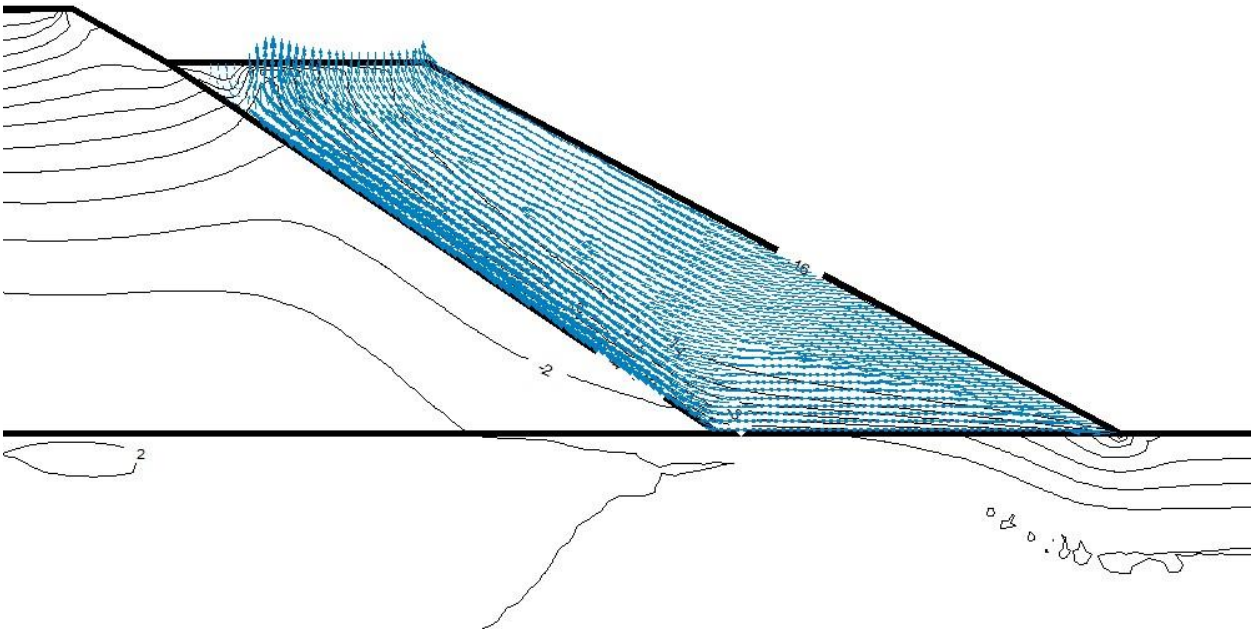

Figure 4-12 Convective Airflow Pattern in the Ventilated Shoulder on January 1 for Case 3

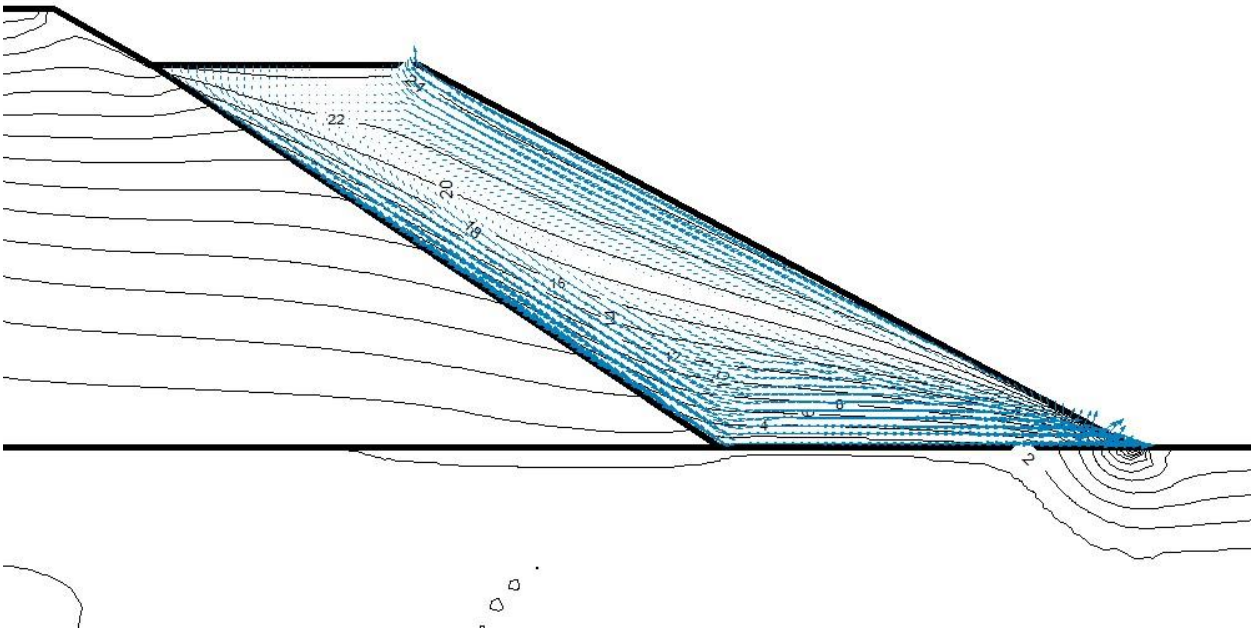

Figure 4-13 Convective Airflow Pattern in the Ventilated Shoulder on July 1 for Case 3

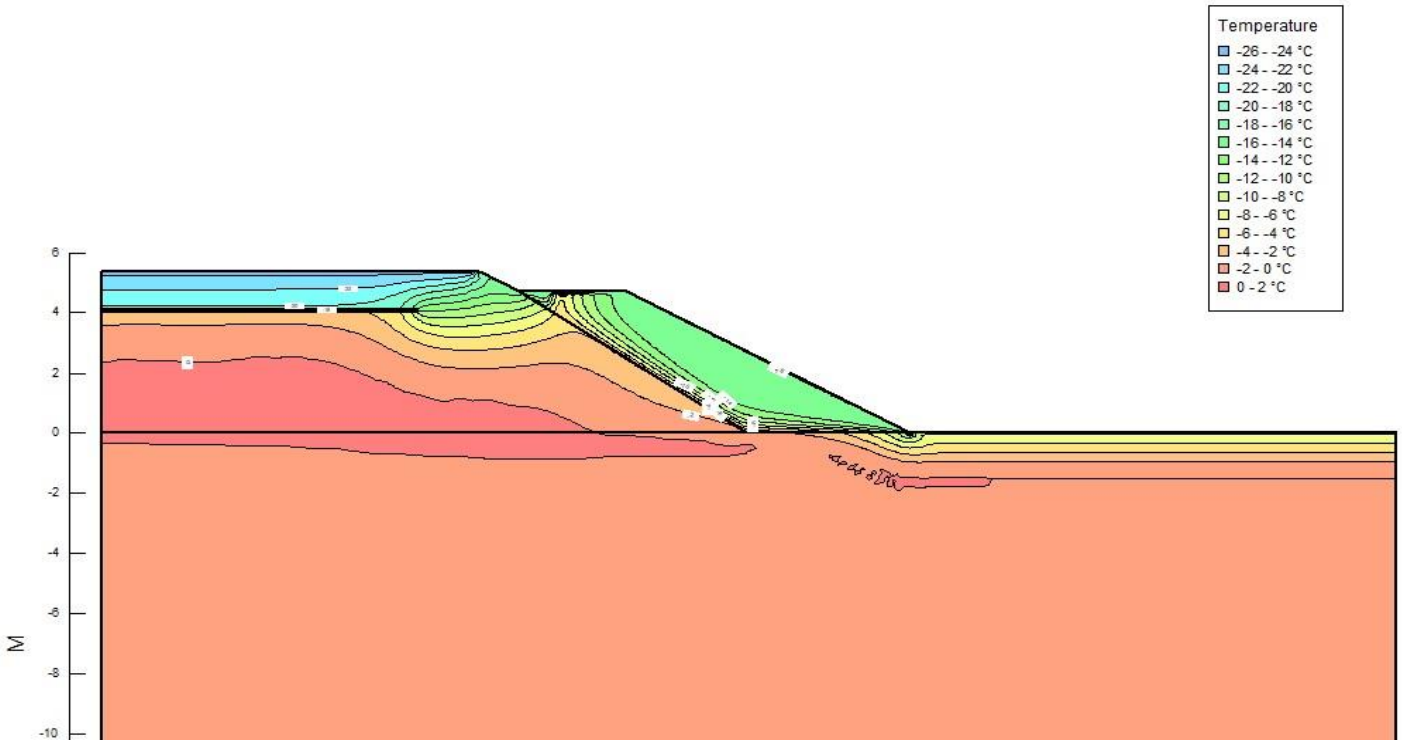

Figure 4-14 Simulation Results for Case 3 for January of Year 1

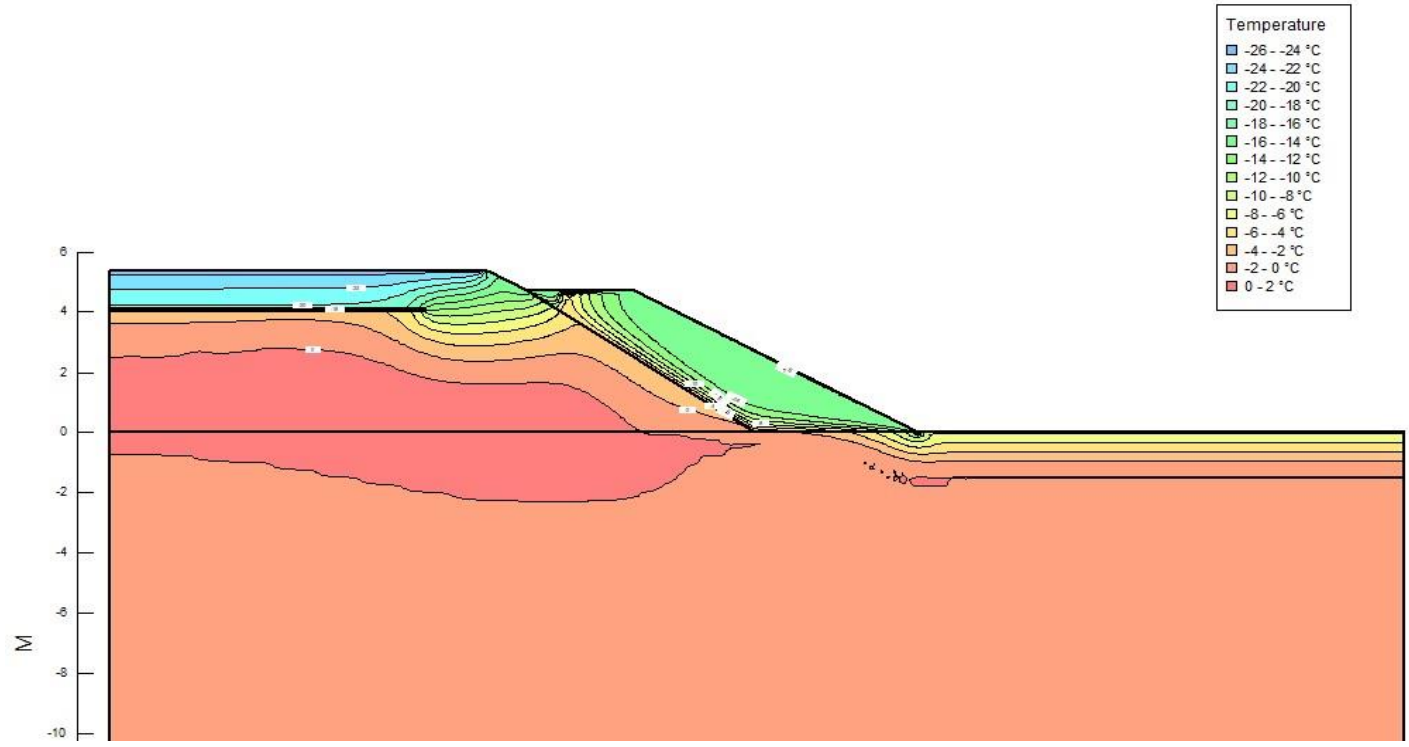

Figure 4-15 Simulation Results for Case 3 for January of Year 6

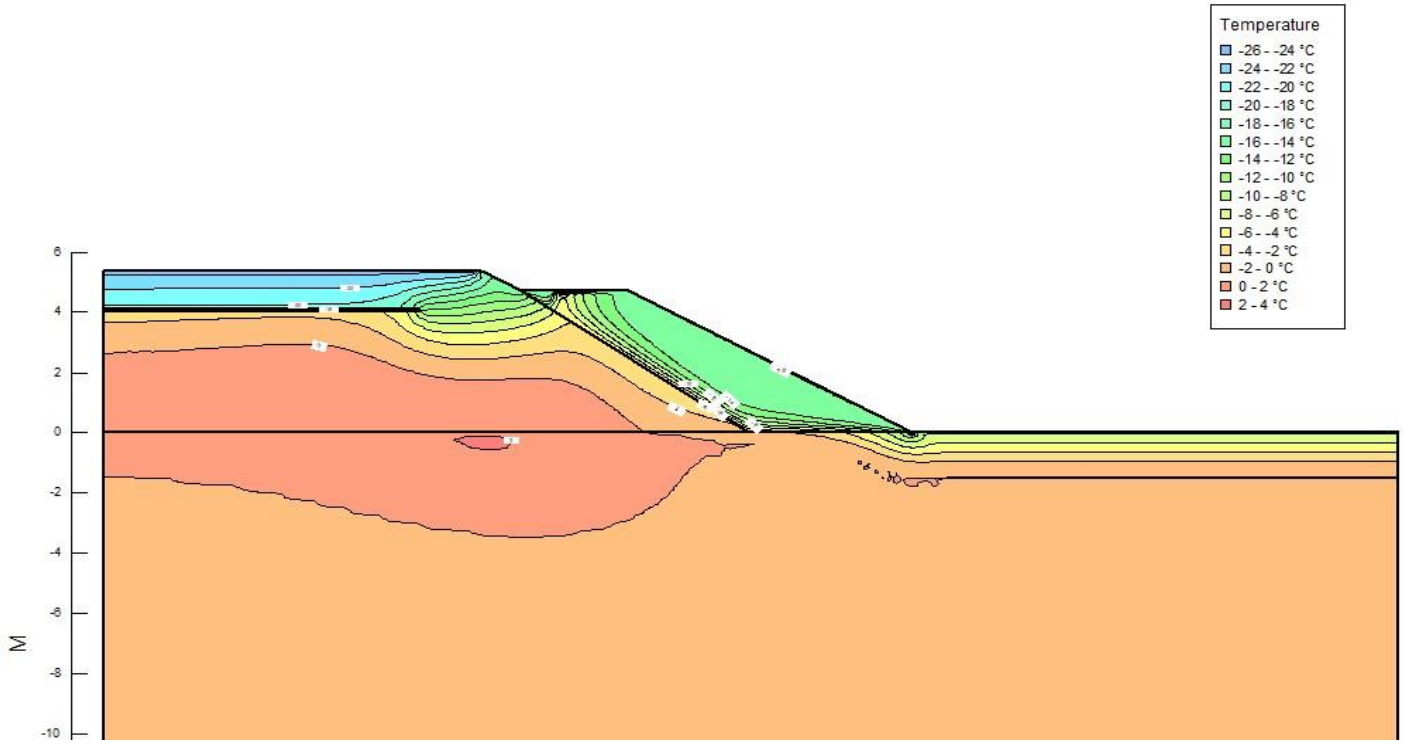

Figure 4-16 Simulation Results for Case 3 for January of Year 12

Figure 4-17 and Figure 4-18 show temperature isotherms for Case 3 on May 15 and September 15, respectively, of the twelfth year of simulation. The temperature patterns shown in these figures are very similar to those obtained for the Case 2 simulations with a slightly larger thaw zone on May 15 and a somewhat smaller thaw zone on September 15 as compared to the Case 2 results. Figure 4-18 also shows less heat accumulation in the upper portion of the ventilated shoulder during summer as compared to the Case 2 results, likely a result of the open boundary and the incoming airflow at the upper boundary during summer as shown in Figure 4-13.

Similar to the Case 2 results, these results for Case 3 are not very representative of the field data obtained from test section #1 of Thompson Drive. In particular, the Thompson Drive results show a stronger cooling influence in the foundation soil beneath and just to the left of the ventilated shoulder.

4.3.7. Case 4 Results

The Case 4 simulation was similar to Case 3 with the exception that the thermal boundary condition along the side slope surface was changed to the ambient air temperature, effectively using freezing and thawing N-factors of 1. As for Case 3, the upper surfaces of the ventilated shoulder were open to inflow and outflow from the ambient air mass. This case was run to investigate the impact of the thermal boundary condition that is utilized for the side slope. As discussed above, it is likely unrealistic to use typical N-factors for a snow-covered gravel side slope surface since airflow through the snow pack will significantly alter the ability of the snow to insulate the surface. This case essentially assumes that the snow is completely ineffective at insulating the side slope or restricting airflow during winter and imposes the ambient air temperature directly on the side slope boundary.

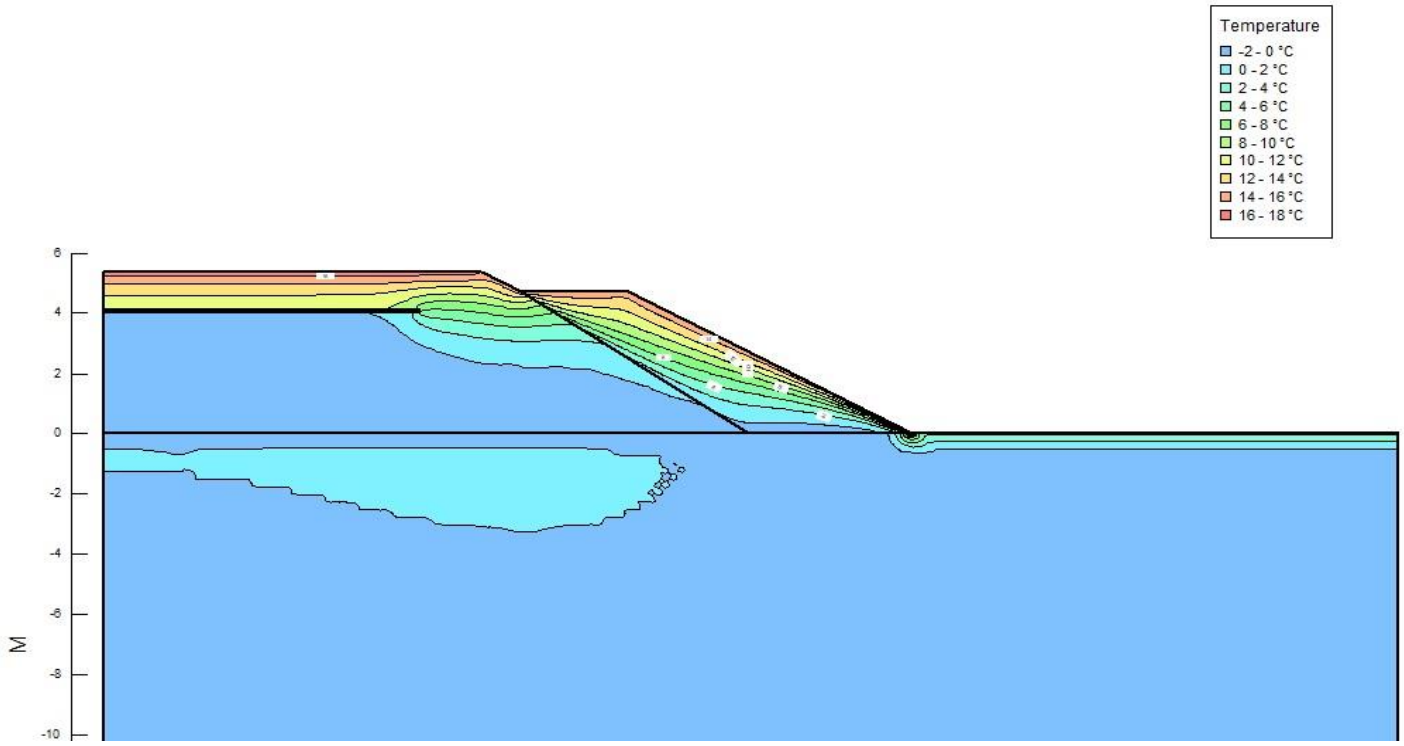

Figure 4-17 Simulation Results for Case 3 for May 15 of Year 12

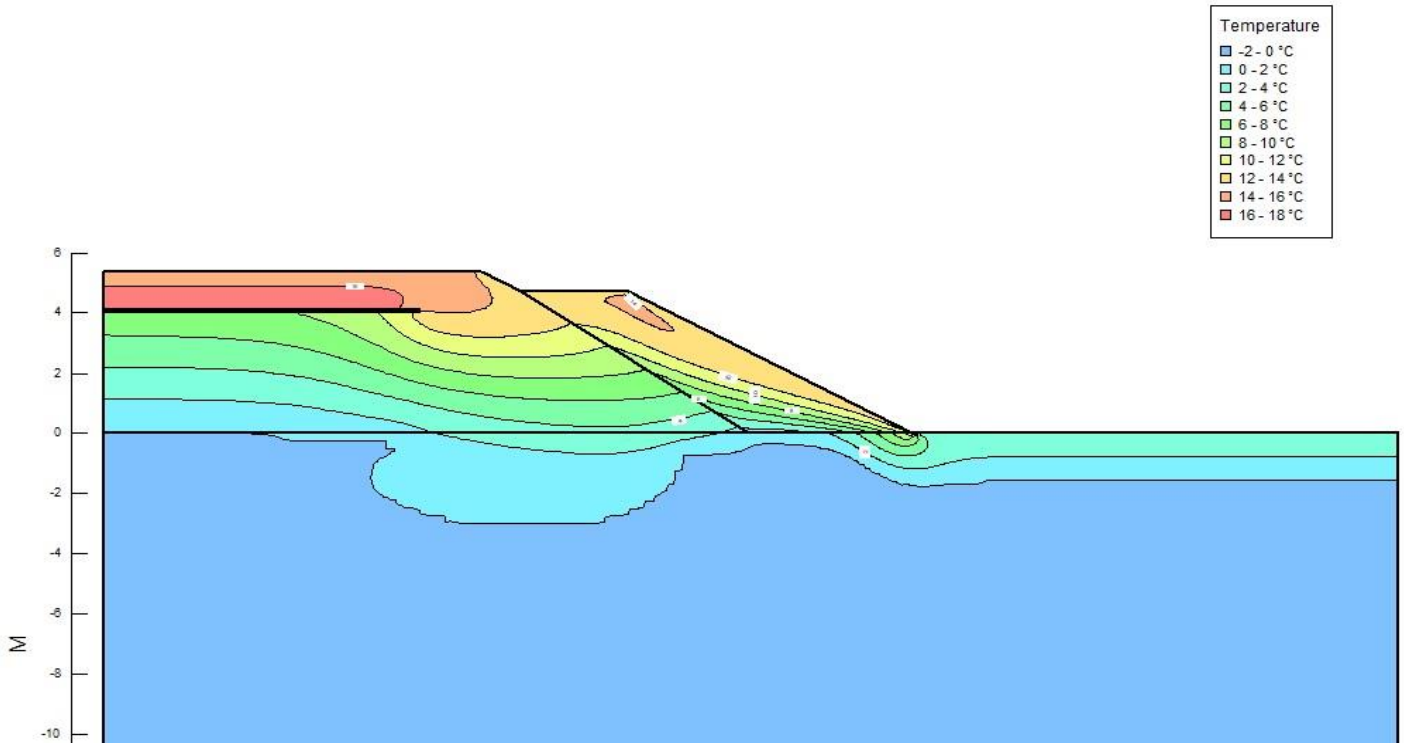

Figure 4-18 Simulation Results for Case 3 for September 15 of Year 12

Interestingly, the convective airflow patterns shown in Figure 4-19 for Case 4 on January 1 display characteristics that could be considered a mixture of the airflow patterns observed for Case 2 and Case 3. On the one hand, it is clear that ambient air is entering and exiting the embankment surface at multiple locations as was the situation for Case 3, however, the internal airflow is organized into a series of circulatory patterns similar to that observed for Case 2. These circulation cells result in five or more sections of the upper ventilated shoulder boundary where airflow is entering or leaving the shoulder surface. This type of behavior was also seen in the numerical simulations performed during the design phase of the Thompson Drive project, Goering [11]. The more complex airflow patterns shown in the figure for January are likely the result of stronger temperature gradients in the shoulder region due to the imposition of ambient air temperatures directly on the upper boundary of the shoulder.

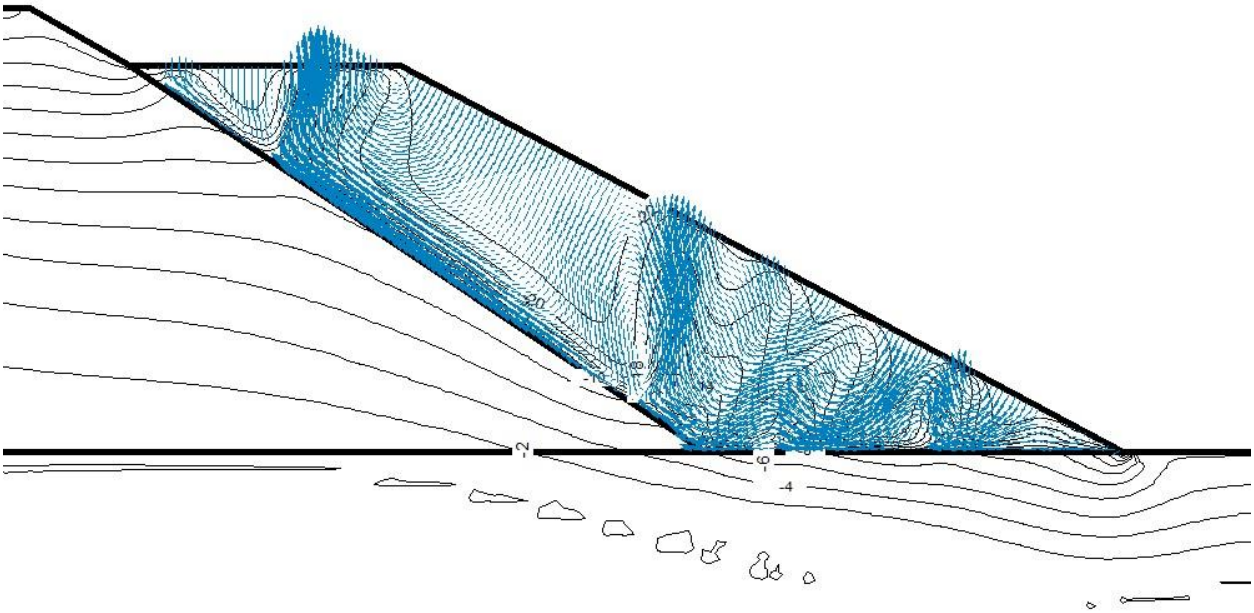

Figure 4-19 Convective Airflow Pattern in the Ventilated Shoulder on January 1 for Case 4

Figure 4-20 shows airflow patterns for Case 4 on July 1. The airflow shown in this figure also differs substantially from the patterns shown for Case 2 and Case 3 in that the circulation pattern consists of a single large flow cell with airflow entering the lower portion of the shoulder boundary and traveling all the way in to the Borrow A boundary as it flows upward and out of the upper surface. This is fundamentally different than the July 1 airflow patterns observed for Case 2 and Case 3. In those prior simulations, July airflow in the ventilated shoulder is more cellular in nature, with upward airflow along the upper surface of the ventilated shoulder and then downward airflow along the Borrow A boundary, see Figure 4-6 and Figure 4-13. These different flow patterns result in significant differences in summer heat transfer in the ventilated shoulder and foundation soil immediately beneath it. For Case 4 the inward warm airflow at the base of the ventilated shoulder transfers much more heat to the foundation soil than does the cellular flow pattern for Cases 2 and 3. As a result, summertime heating of the foundation soil beneath the ventilated shoulder is much greater for Case 4 than it is for Case 2 or 3. This is an interesting result since the summer surface temperature at the upper edge of the ventilated

shoulder is much cooler for Case 4 than it is for Case 2 or 3. This is a result of the thermal boundary condition used for Case 4 which imposes ambient air temperature on the shoulder boundary as opposed to cases 2 and 3 which use the side-slope boundary condition that has a thawing N-factor of 1.4. The rather surprising result is that Case 4 produces greater summer heating of the foundation soil beneath the shoulder even though it has a colder boundary temperature than Case 2 or 3. This is an example of the effectiveness of convective heat transfer in that the airflow pattern has more influence on the temperatures beneath the side-slope than the actual surface boundary temperature.

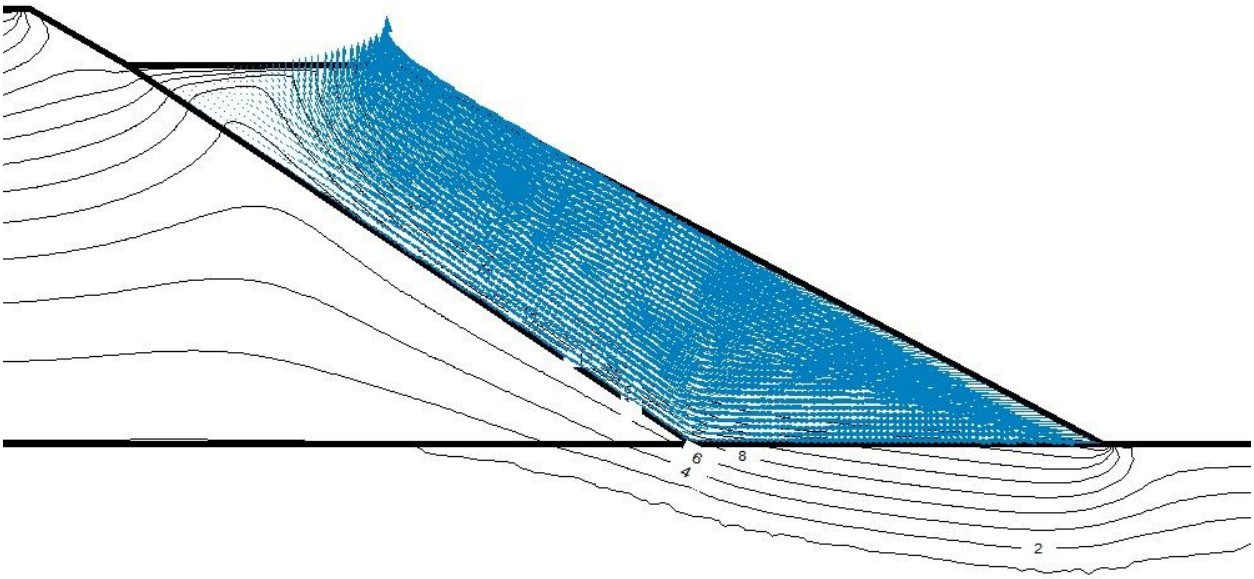

Figure 4-20 Convective Airflow Pattern in the Ventilated Shoulder on July 1 for Case 4

Figure 4-21 through Figure 4-23 show temperature isotherm profiles for the Case 4 simulation after one, six, and twelve years. The isotherm patterns displayed in these figures show significantly improved cooling as compared to any of the earlier results. This is, no doubt, due to the influence of the relatively colder thermal boundary condition used at the surface of the ventilated shoulder for this case (i.e. freezing N-factor of 1 rather than 0.6 as used for Cases 1, 2, and 3). These figures show a thawed zone beneath the center of the embankment, but the foundation soil beneath the side-slope and the shoulder region is nearly completely re-frozen by January 1. The size of the thawed region is significantly smaller than in any of the prior cases and is limited to the region of the embankment beneath the insulation sheet. Also note that the depth of the thawed material beneath the embankment extends to a depth of only about 1.5 m beneath the original ground surface, roughly the same depth as the original active layer beneath the undisturbed surface. As such, it is unlikely that the thaw zone shown in these figures would result in any thaw settlement of the embankment.

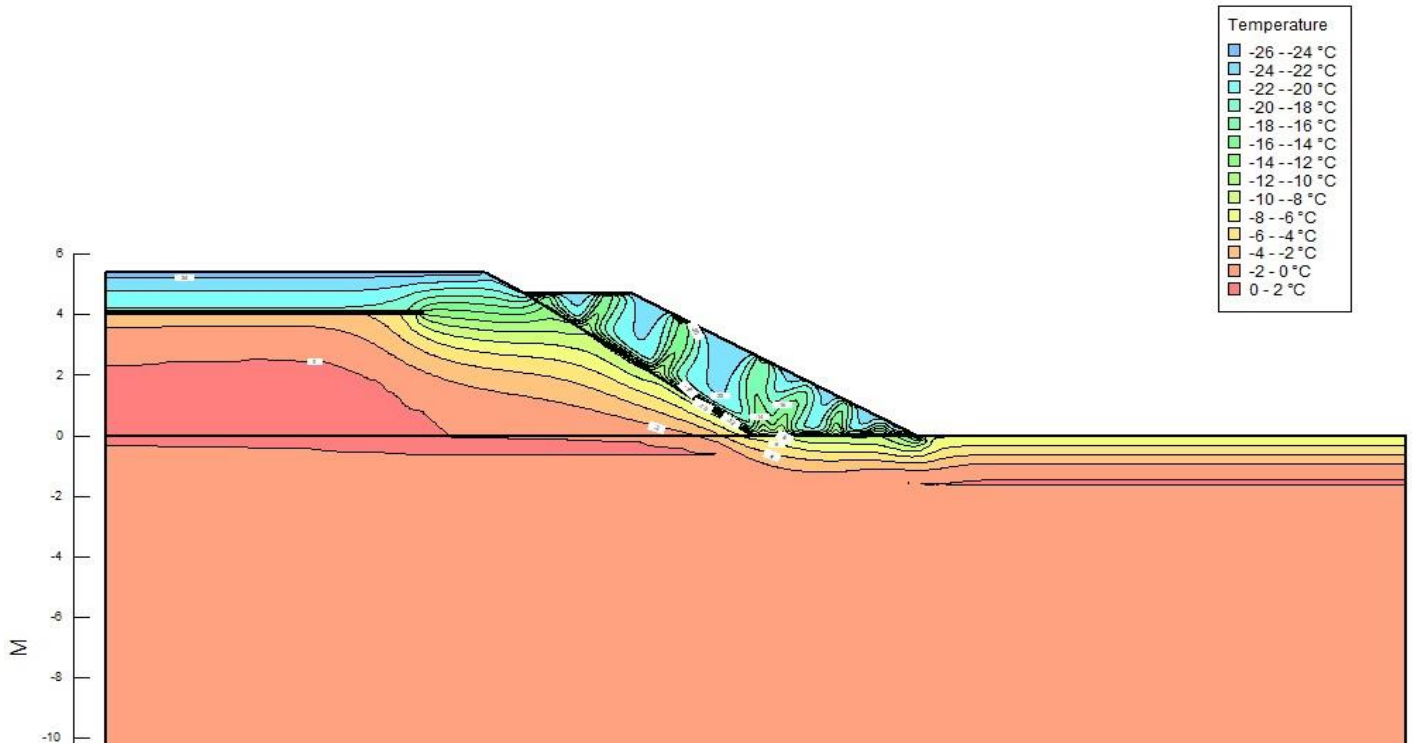

Figure 4-21 Simulation Results for Case 4 for January of Year 1

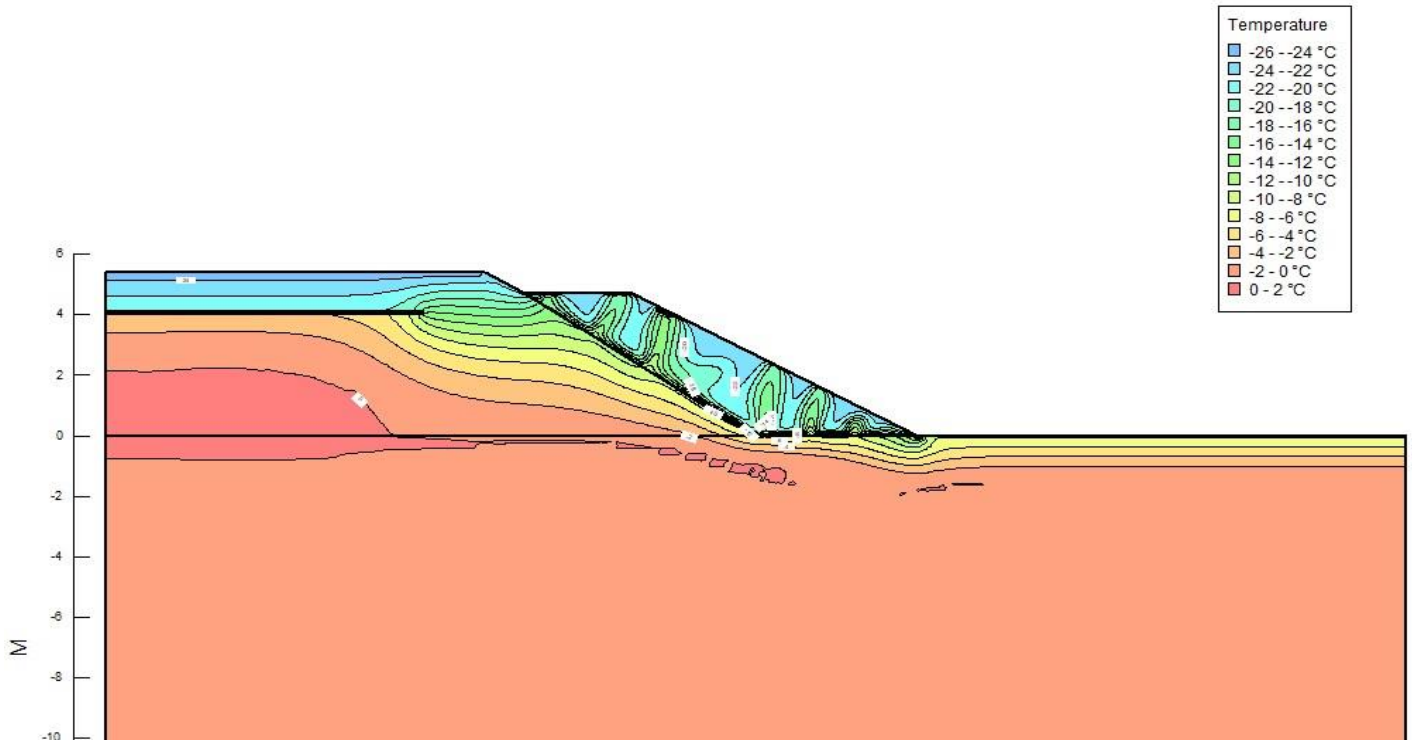

Figure 4-22 Simulation Results for Case 4 for January of Year 6

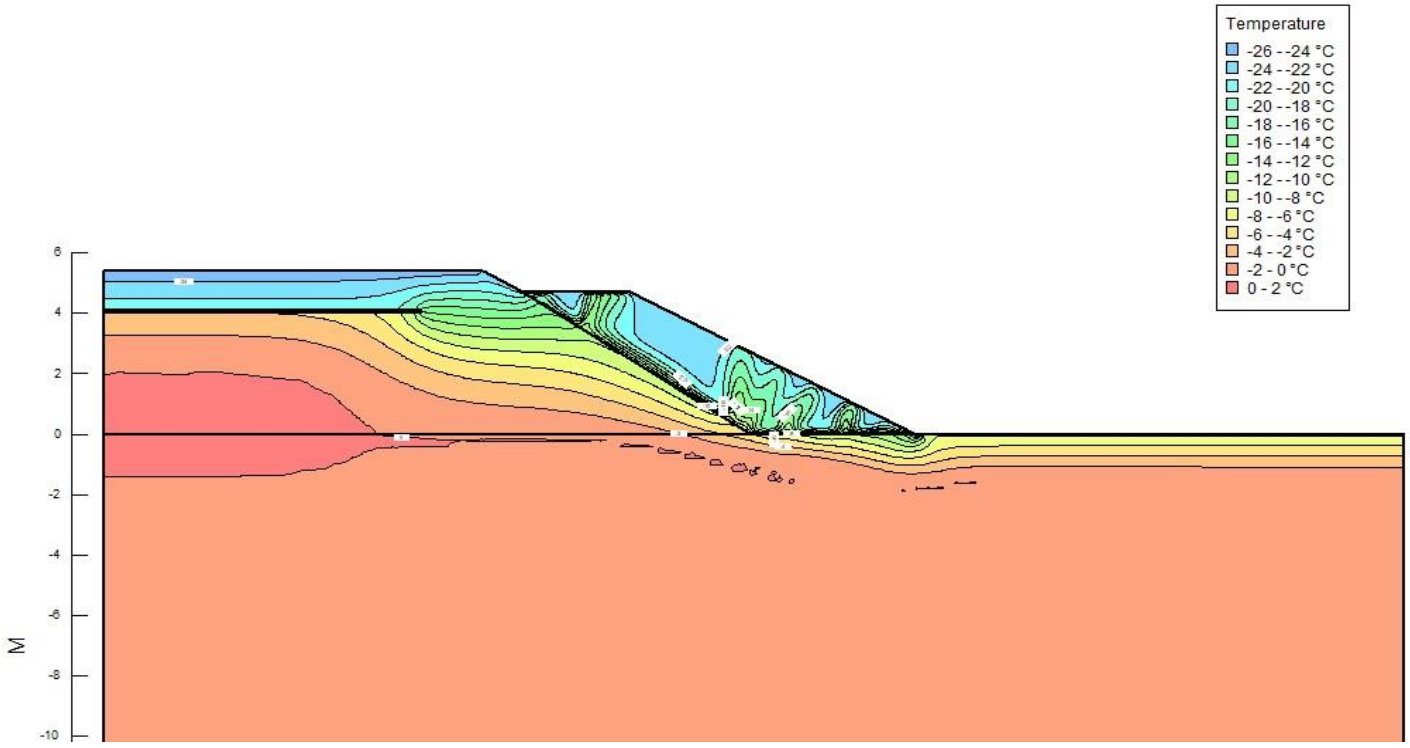

Figure 4-23 Simulation Results for Case 4 for January of Year 12

Figure 4-24 and Figure 4-25 show temperature isotherms for Case 4 on May 15 and September 15, respectively, of the twelfth year of simulation. The temperature patterns shown in these figures also show generally colder conditions than for any of the prior cases. In particular, note that there is no penetration of the thaw beneath the embankment and the May 15 isotherms show a chilled section of the Borrow A material adjacent to the ventilated shoulder. Figure 4-25 does show a slightly enhanced thaw zone beneath the ventilated shoulder. This is due to the altered summer flow pattern in the ventilated shoulder as described above.

4.3.8. Case 5 Results

Case 5 represents yet another experiment with the boundary conditions that are applied at the surface of the ventilated shoulder. For this case, thermal boundary conditions equivalent to those used for the asphalt surface were applied at the surface of the ventilated shoulder. The rational for this test was simply that winter air circulation through the snow layer effectively eliminates the snow insulation effect, just as is the case for an asphalt surface with no snow present. Also, this case mimics the summer heating due to solar input that is present on both the asphalt and rock side-slope surface.

Figure 4-26 and Figure 4-27 show the airflow patterns for Case 5 on January 1 and July 1, respectively. Not surprisingly the January 1 airflow pattern is nearly identical to that obtained for the Case 4 simulation as shown in Figure 4-19. This makes sense since the winter boundary condition at the surface of the ventilated shoulder is the same for Case 4 and Case 5. However, the summer airflow pattern shown in Figure 4-27 is much more similar to the cellular flow pattern obtained for Case 2 and Case 3, as opposed to that obtained for Case 4. As a result, summer heating of the foundation soil beneath the ventilated shoulder is reduced for Case 5 as compared to Case 4.

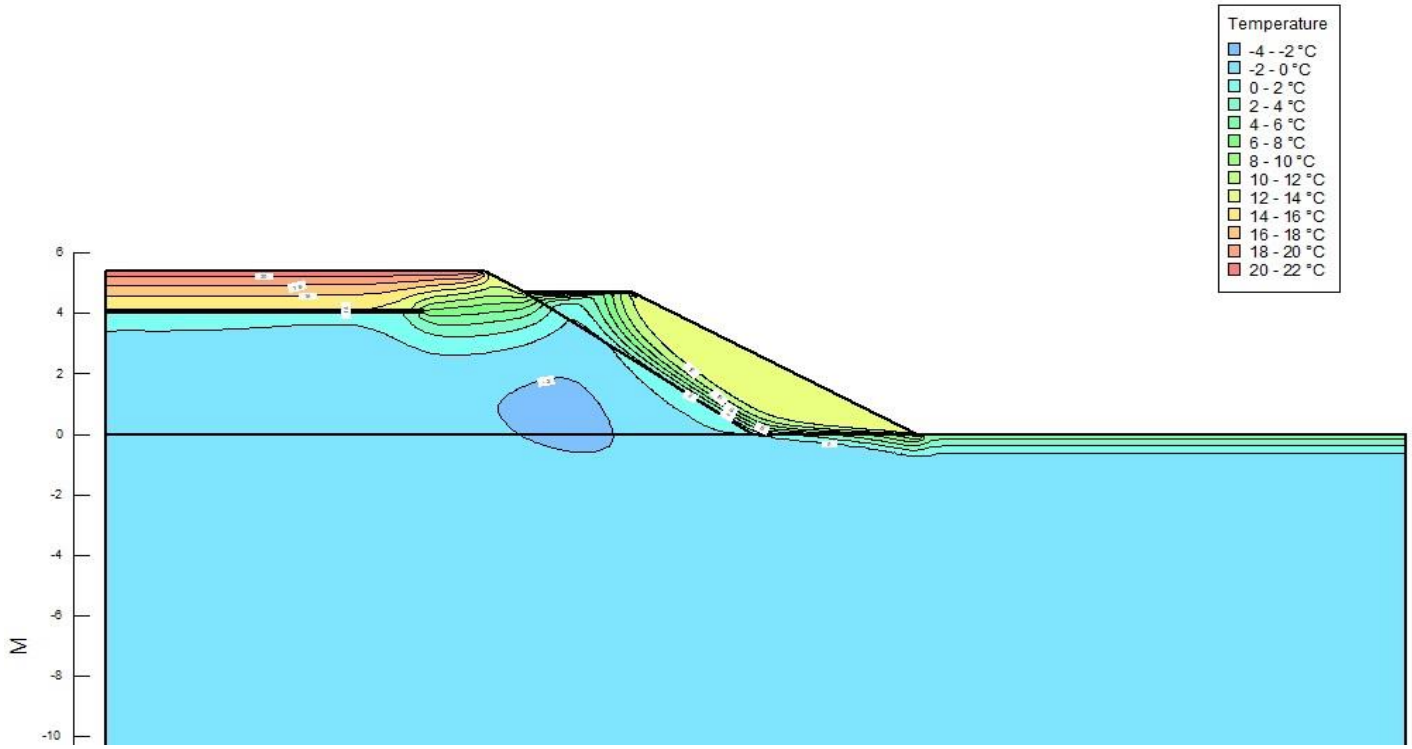

Figure 4-24 Simulation Results for Case 4 for May 15 of Year 12

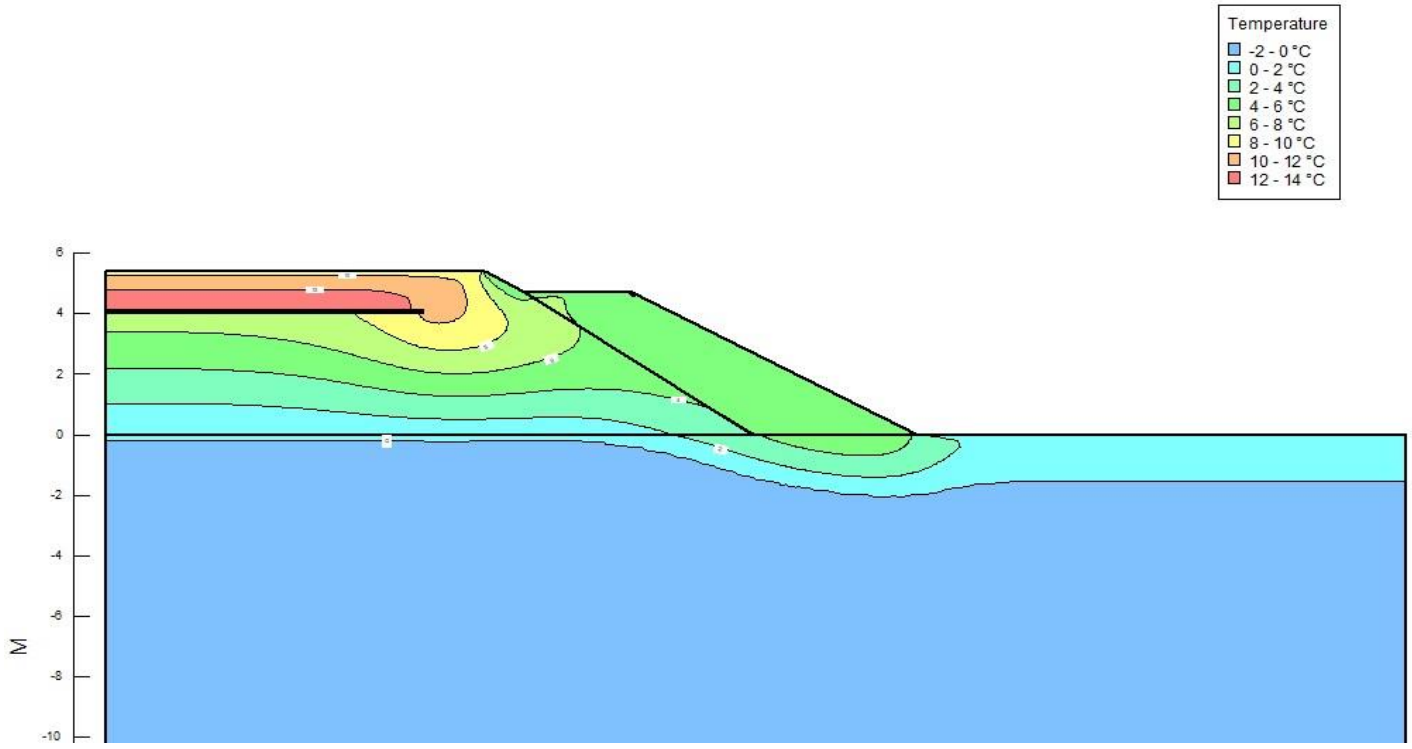

Figure 4-25 Simulation Results for Case 4 for September 15 of Year 12

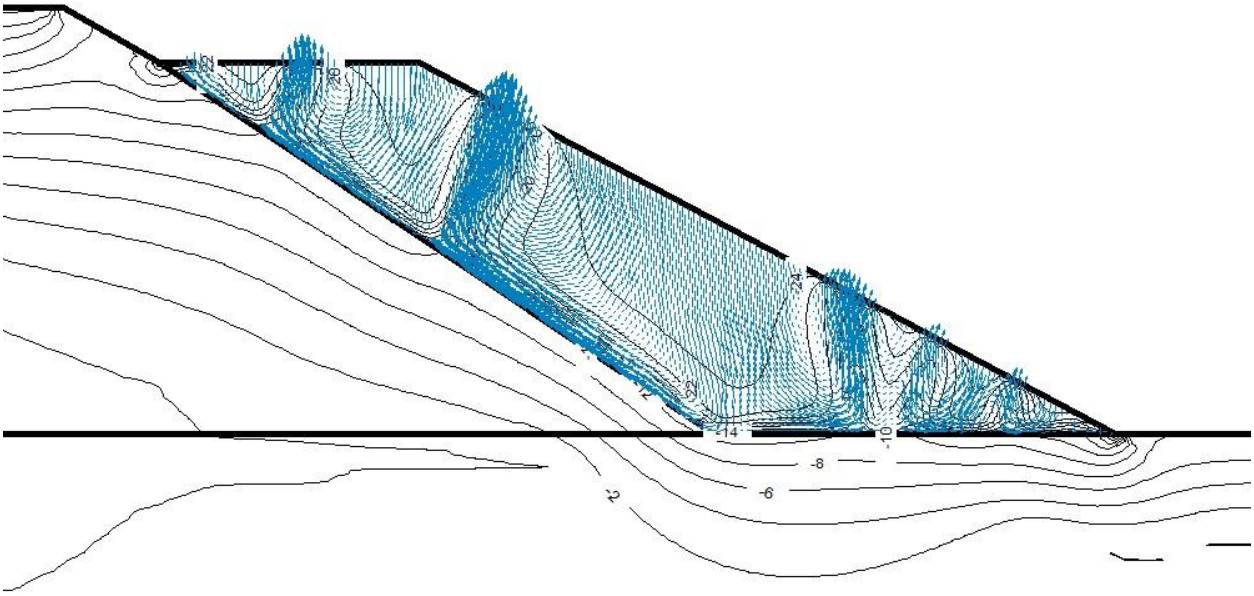

Figure 4-26 Convective Airflow Pattern in the Ventilated Shoulder on January 1 for Case 5

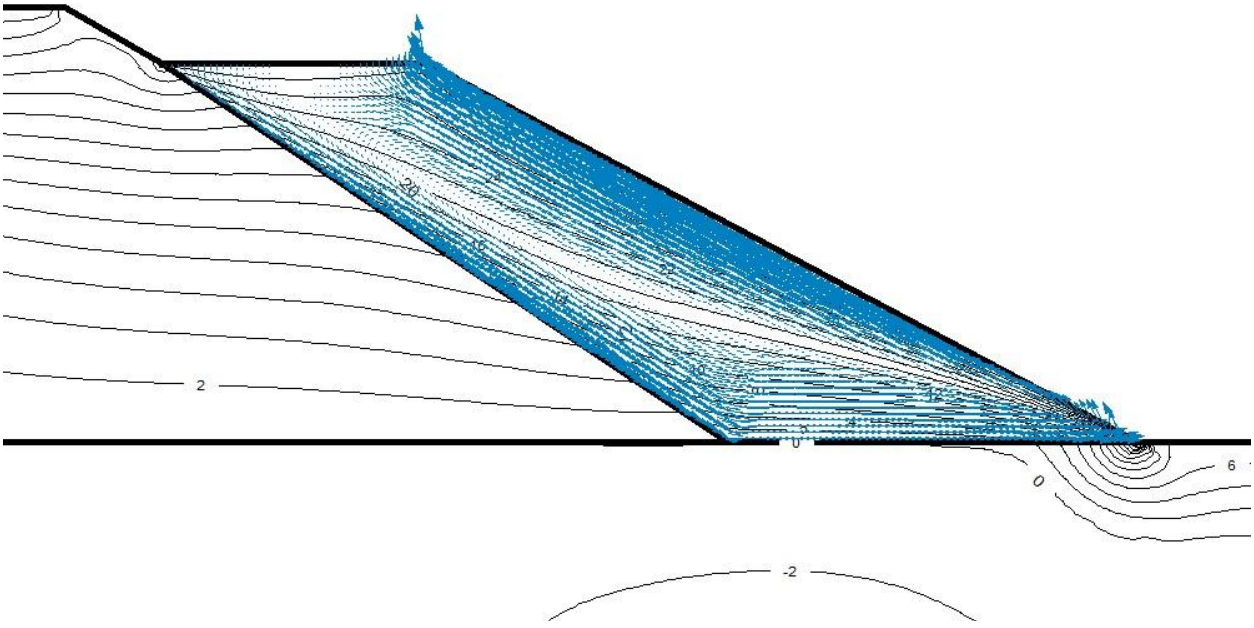

Figure 4-27 Convective Airflow Pattern in the Ventilated Shoulder for July 1 for Case 5

Figure 4-28 through Figure 4-30 show temperature isotherm profiles for the Case 5 simulation after one, six, and twelve years, respectively. These figures show isotherm patterns that are similar to those obtained for Case 4, with the exception that there is a somewhat larger thaw zone remaining in the Borrow A material. In particular, the warm "finger" that extends from the embankment core toward the ventilated shoulder is a bit more robust in this case compared to what was observed for Case 4. On the other hand, temperatures beneath the ventilated shoulder are colder than those for Case 4 and do not show any remaining spots of thawed material as was the situation for Case 4. This is likely mostly a consequence of the different airflow pattern generated by the Case 5 simulation during summer where airflow occurs upward along the outer boundary of the ventilated shoulder but in the downward direction along the inner Borrow A boundary. This results in significantly less summer heating of the foundation soil immediately beneath the base of the shoulder and allows for more effective cooling of that area once the winter convection pattern sets in.

Figure 4-31 and Figure 4-32 show temperature isotherms for Case 5 on May 15 and September 15, respectively, of the twelfth year of simulation. Figure 4-31 shows that the thawed zone indicated in Figure 4-30 is essentially completely refrozen by May 15 and also shows a zone of very cold temperatures centered beneath the ventilated shoulder. The pattern of chilled foundation soil shown in this figure is generally in good agreement with the experimental results obtained from Thompson Drive and, from that perspective, the Case 5 simulation bears the strongest resemblance to the experimental results (see discussion in the next section of the report). Similarly, Figure 4-32 shows results that are also in better agreement with experimental observations than the prior cases. Note that thaw penetration beneath the shoulder is quite limited, unlike the situation that was observed for Case 4.

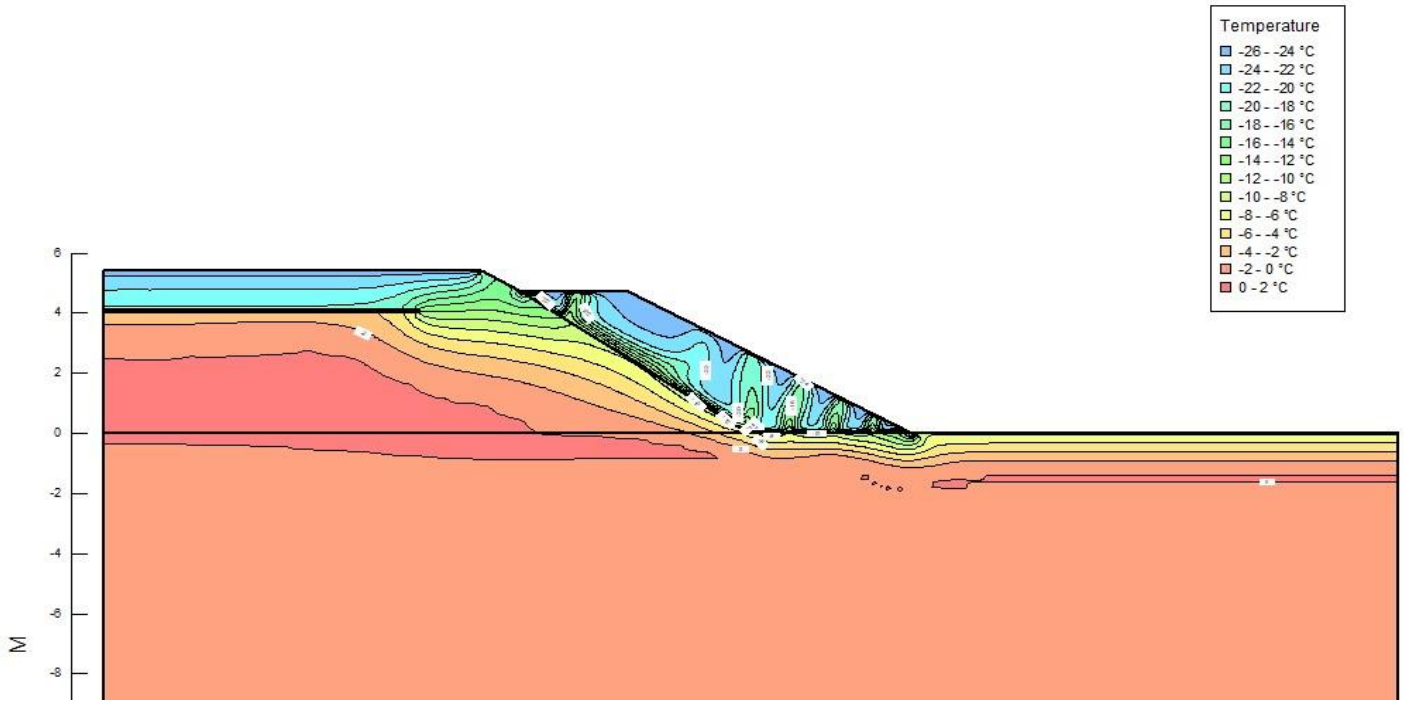

Figure 4-28 Simulation Results for Case 5 for January 1 of Year 1

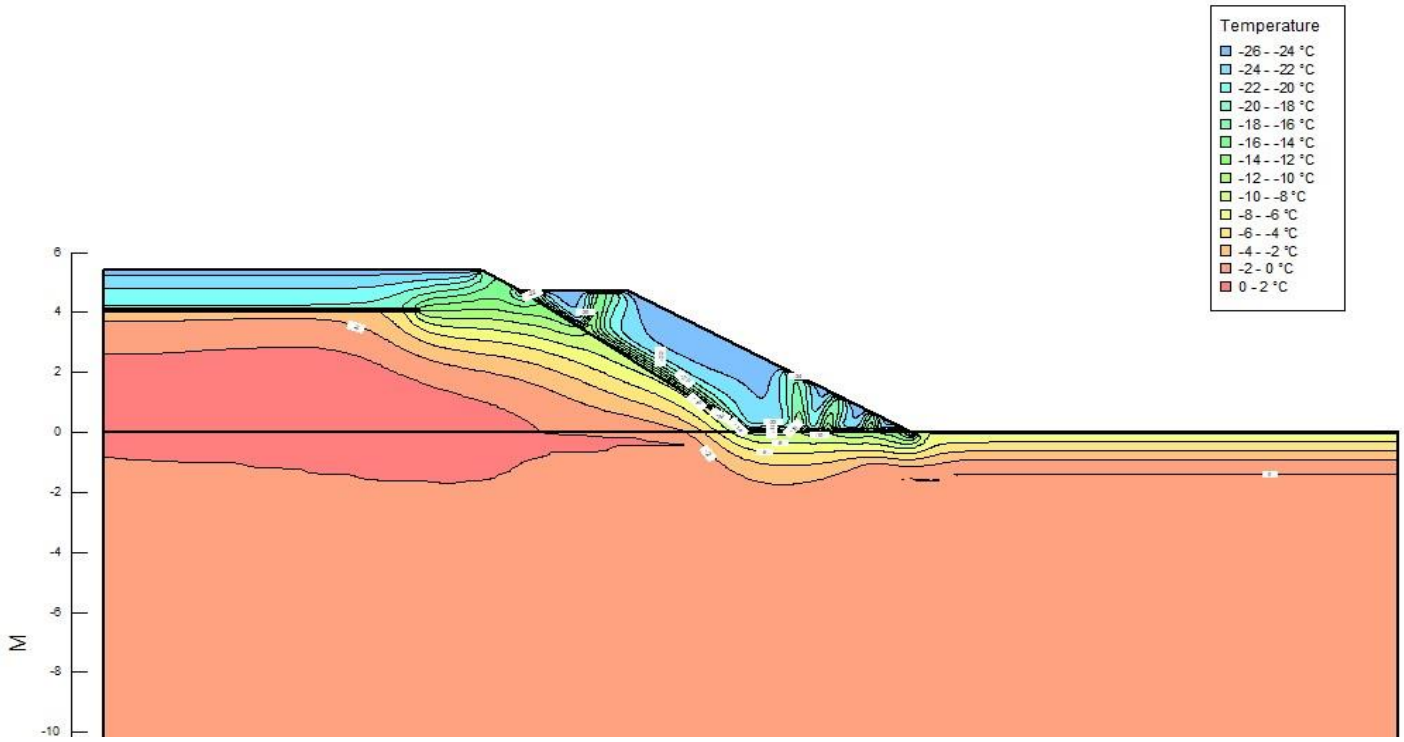

Figure 4-29 Simulation Results for Case 5 for January 1 of Year 6

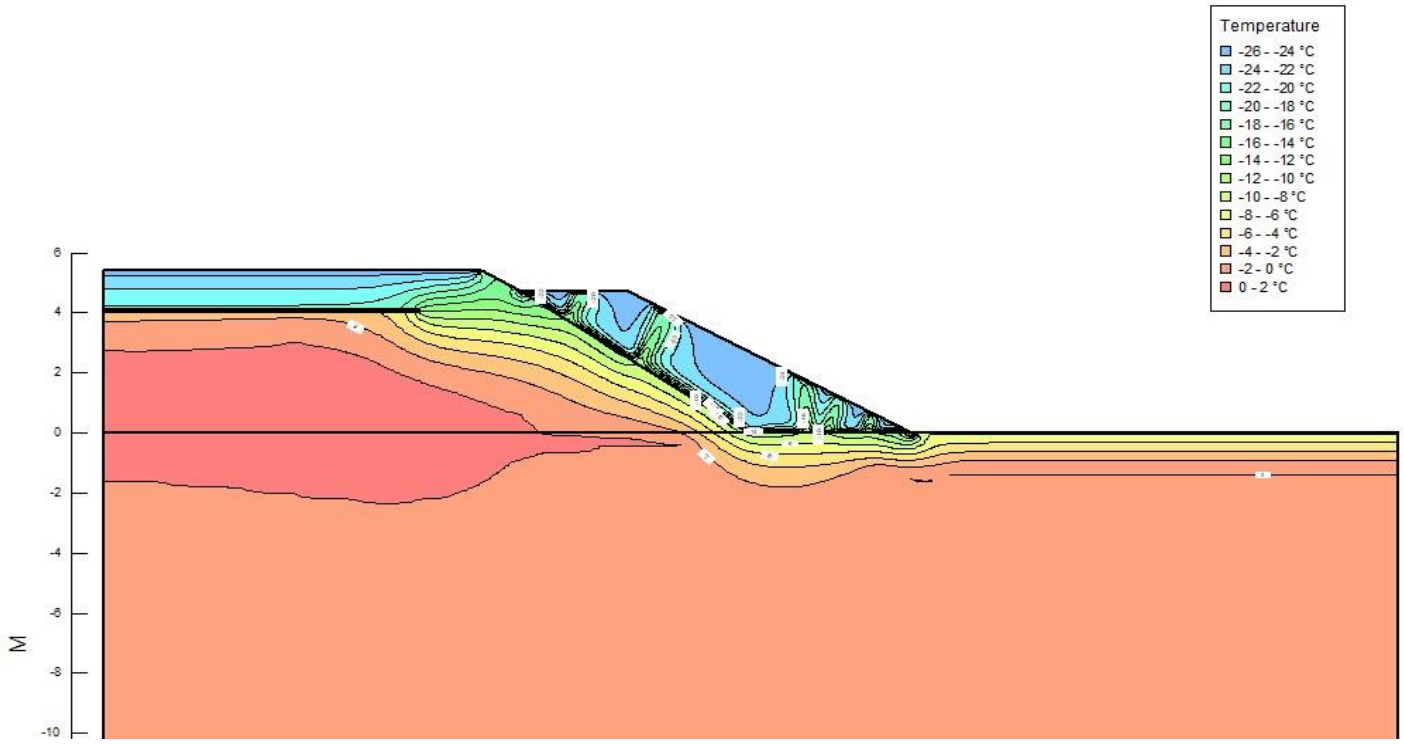

Figure 4-30 Simulation Results for Case 5 for January 1 of Year 12

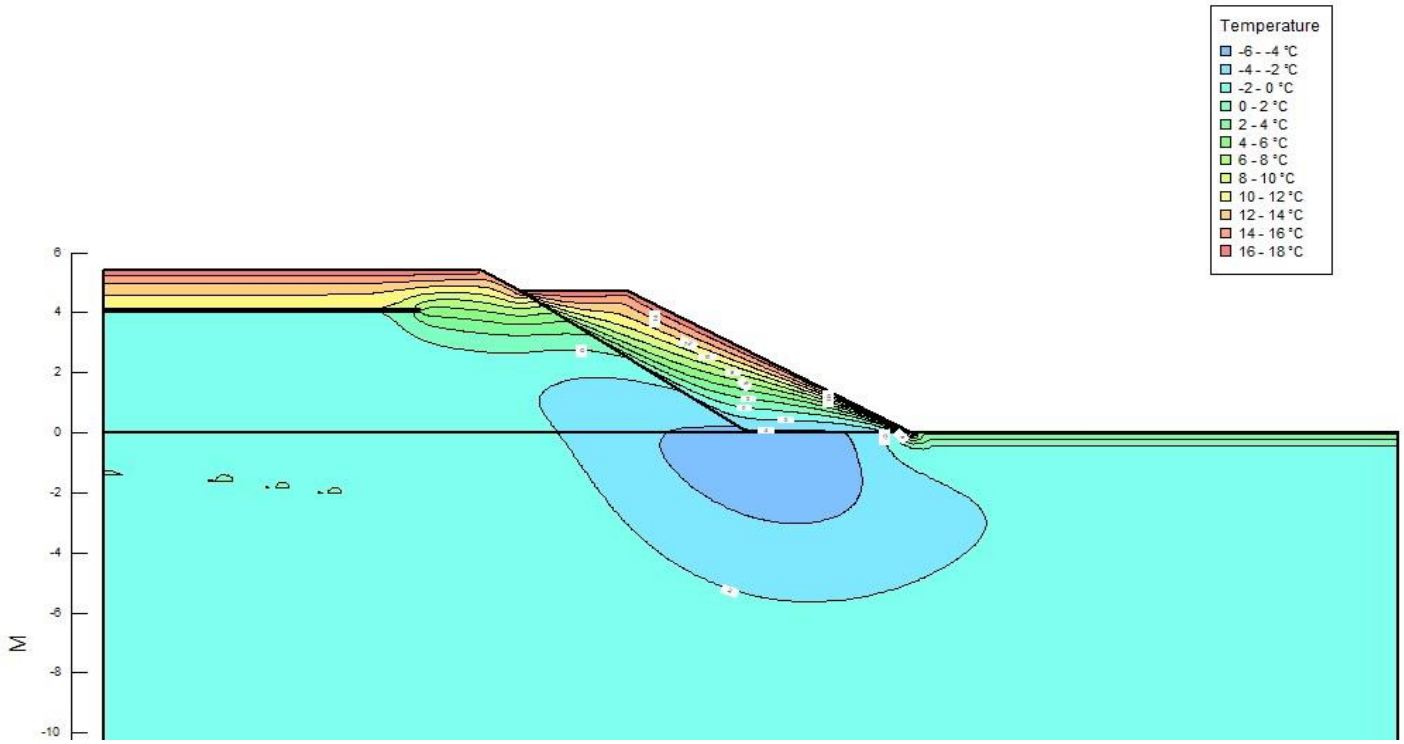

Figure 4-31 Simulation Results for Case 5 for May 15 of Year 12

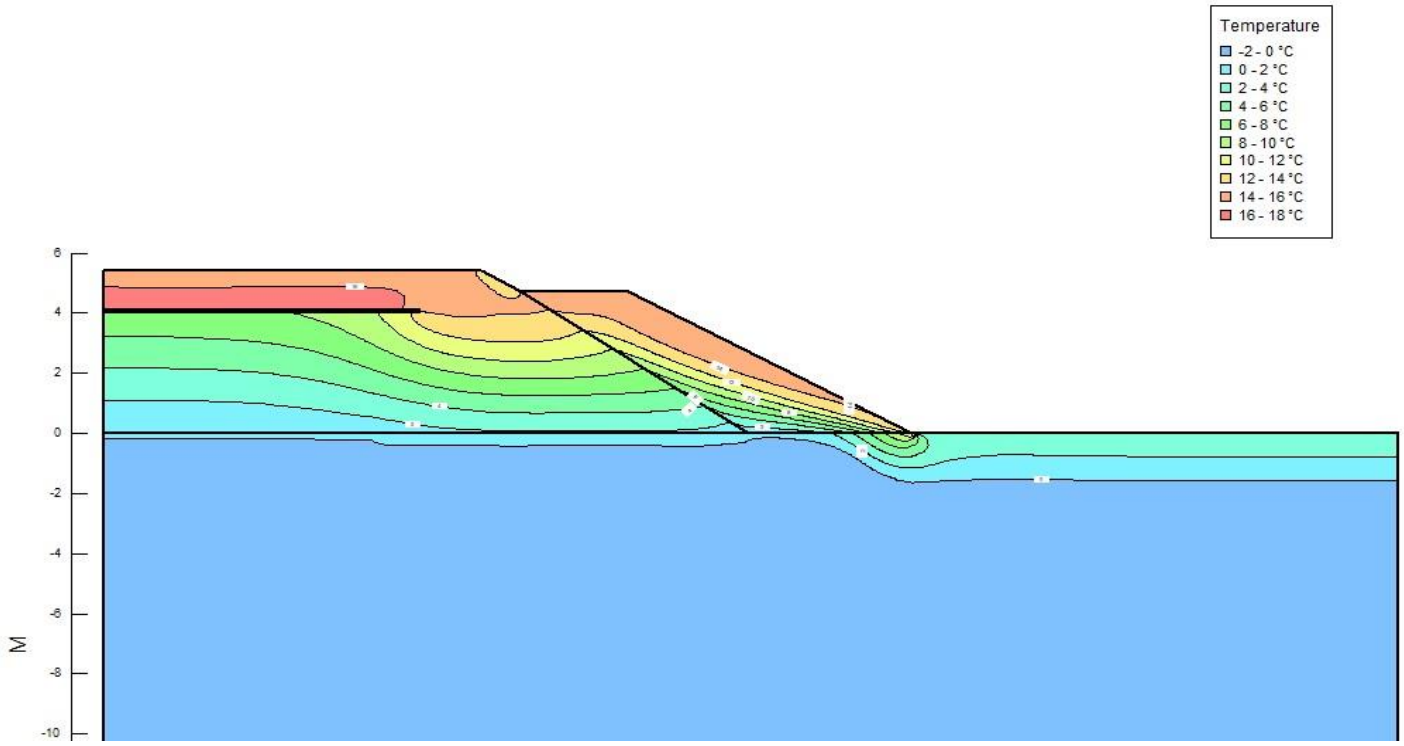

Figure 4-32 Simulation Results for Case 5 for September 15 of Year 12

4.3.9. Comparison of Numerical Simulations to Thompson Drive Field Data

In this section a more detailed comparison between the numerical simulations and the field data obtained from Thompson Drive is presented. As discussed above, of all the simulations conducted, the Case 5 results bear the strongest resemblance to the actual field data obtained from Thompson Drive test section #1. In particular, the May 15 temperature profiles shown in Figure 4-31 for the Case 5 simulation show a region of subcooling that is centered directly beneath the ventilated shoulder. This temperature pattern most closely matched that observed in the field data and, as such, the comparison presented in this section is focused on the Case 5 results.

Field data from Thompson Drive test section #1 is shown in Figure 4-33 for May 15, 2015, roughly ten years after construction of Thompson Drive. As shown in this figure, the field data shows a zone of reduced temperature centered beneath the ventilated shoulder. The data indicates a minimum temperature of somewhat less than -2.5°C at the center of the cooled area, substantially colder than any other portion of the foundation soil layers.

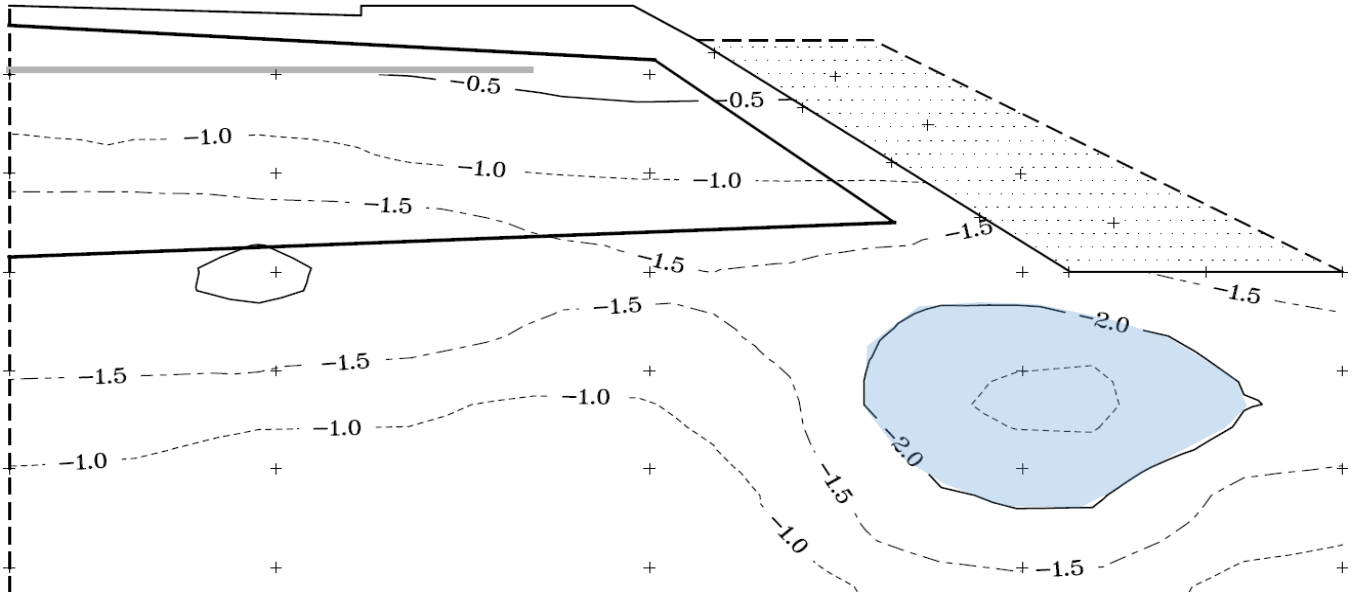

Figure 4-33 Temperature Contours for Thompson Drive Test Section #1 on May 15, 2015

The shape and position of the low temperature zone shown in Figure 4-33 matches quite well with the results from the Case 5 numerical simulation which are repeated in greater detail in Figure 4-34. As shown in this figure the size and position of the chilled foundation soil zone matches well with the field data, although the minimum temperature achieved at the center of the zone was somewhat colder than -4°C, roughly 1.5°C colder than observed in the Thompson Drive data. Despite this mis-match is temperature magnitude, other aspects of the numerical simulation results match the field data quite well and this match is taken as an indication that the boundary conditions used for the Case 5 simulation were likely the best match for the actual thermal behavior in the field. Note that there are some discrepancies in the position of the -1°C isotherm when comparing the two figures, but this is likely due to the fact that the simulation did not include the hairpin thermosyphon which was effective at cooling the Borrow A material closer to the embankment centerline, thus the cooler temperatures shown in the field data.

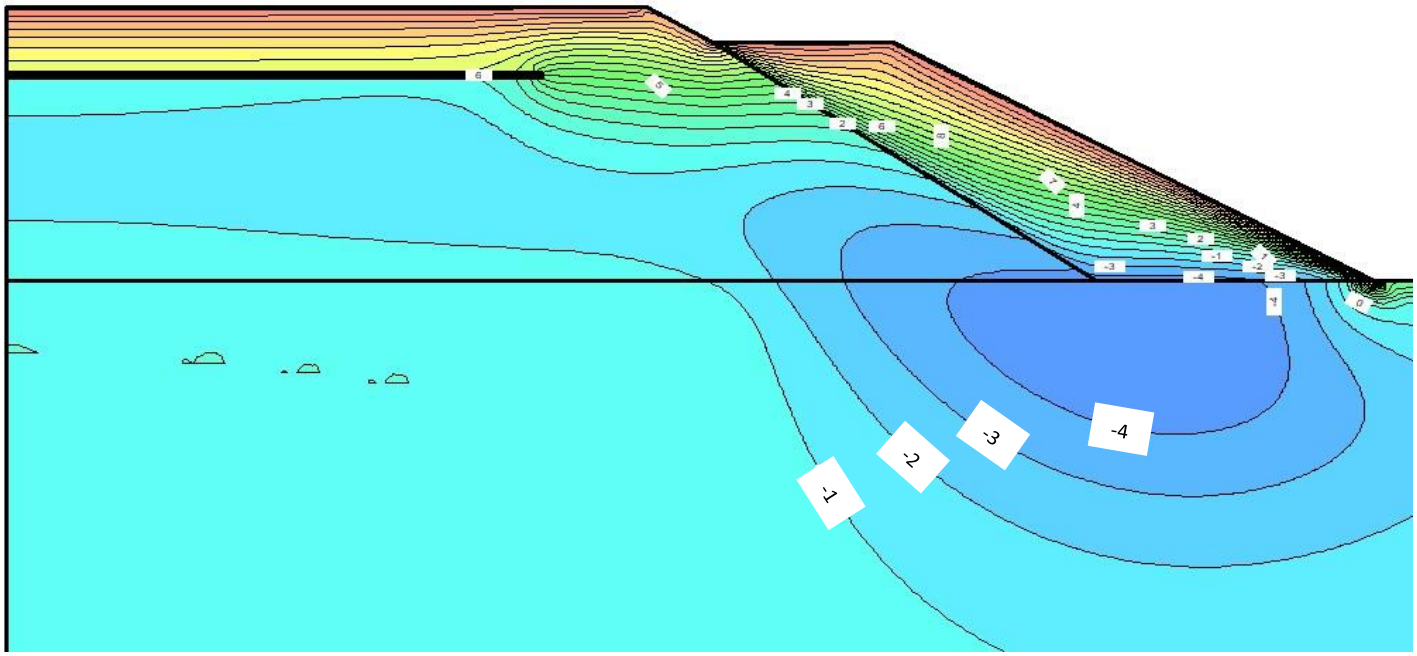

Figure 4-34 Detailed Simulation Results for Case 5 for May 15 of Year 12

Figure 4-35 shows filed data from Thompson Drive test section #1 for September 15, 2015. The data in this figure indicates that the chilled zone of foundation soil persists beneath the ventilated shoulder even after the summer season. As shown in the figure a zone of sub-cooled foundation soil remains in the same area as that shown for the May 15 results, although its temperature has increased by roughly 1.5°C over the summer months with a minimum temperature value of between -1°C and -2°C. Also note that the thaw has penetrated the foundation soil to a depth of about 0.5 m below the original ground surface.

The corresponding Case 5 numerical results are shown in Figure 4-36 for September 15. Comparing the two figures illustrates quite good agreement between the numerical simulation and the field results. In particular, the remaining chilled zone is found roughly in the same position in both the field data and numerical simulation and the temperature depressions indicated are nearly identical. The zone shown for the numerical results appears slightly larger than the field measurements, but despite that, the agreement is quite good. Examining the position of the -1°C, 0°C, 1°C, 2°C, 6°C, and 8°C isotherms also indicates a very high level of agreement between the field data and simulation results. Note that the agreement of the isotherm shapes near the center of the embankment for these end-of-summer results is not that surprising since the hairpin thermosyphons are not active in summer and, thus, likely have less of an impact on the late summer isotherm shapes.

While the aspects of these comparisons between the field results and the Case 5 simulation are quite good, the comparison is clearly not perfect. Remaining discrepancies are likely resulting from material property assumptions used in the simulations as compared to the actual field values, as well as remaining uncertainty in the thermal and hydraulic boundary condition used at the surface of the ventilated shoulder.

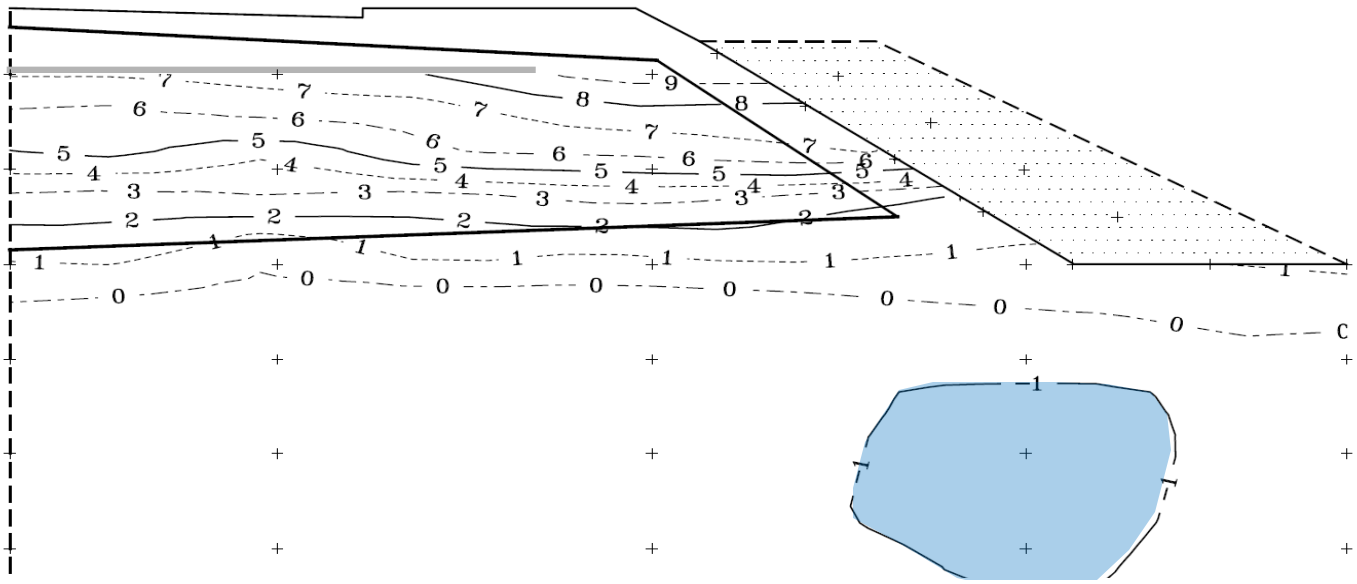

Figure 4-35 Temperature Contours for Thompson Drive Test Section #1 on September 15, 2015

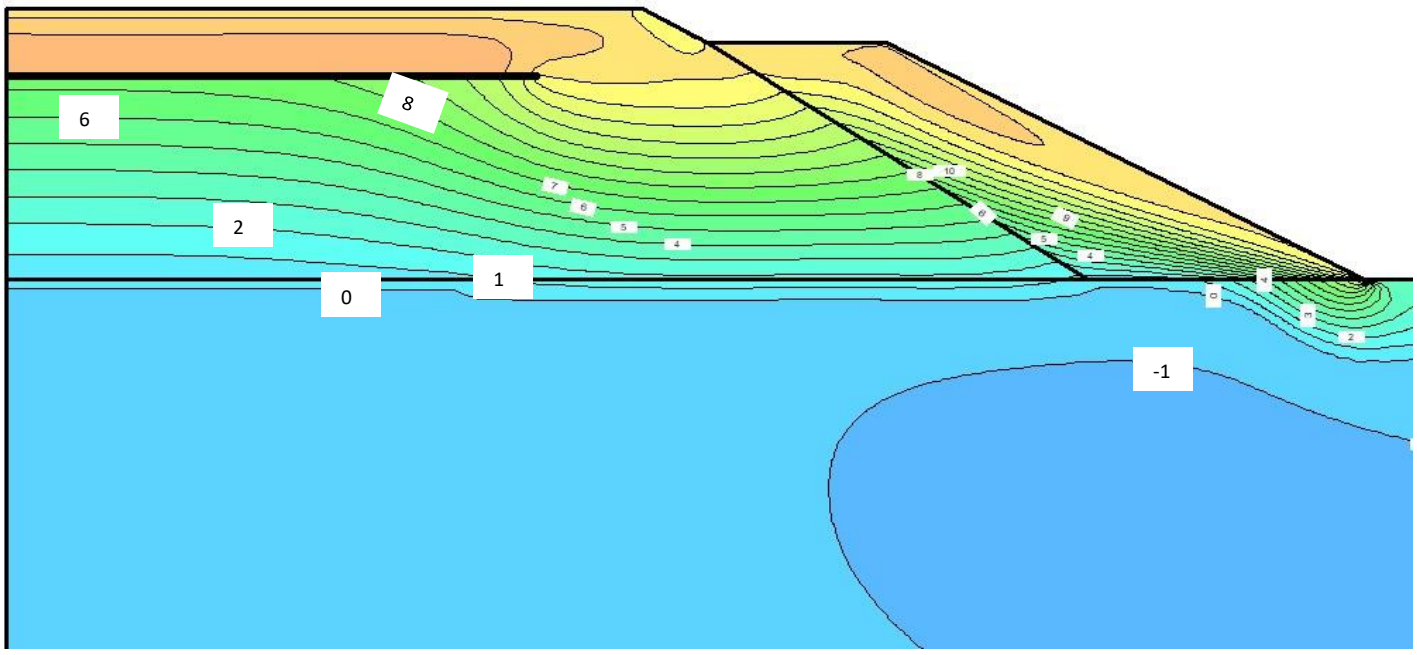

Figure 4-36 Detailed Simulation Results for Case 5 for September 15 of Year 12

CHAPTER 5. CONCLUSIONS

5.1. Field Data

The field data presented in this report, particularly for Thompson Drive, represents a very valuable data set that provides much insight into how ACE and ventilated shoulder systems actually perform in the field. The data not only demonstrate the effectiveness of the cooling systems used in Thompson Drive and at the Alaska Highway test site, but they also provide an important set of benchmarks for future design and numerical simulation efforts. As shown in the previous chapter, the detailed temperature isotherm shapes provided by the Thompson Drive field data is very valuable for verifying the performance of numerical models. Due to the complexity of the convective cooling behavior of ACE and ventilated shoulder installations, numerical simulation will continue to provide the most accurate design tool, and, thus, verification of the accuracy of numerical simulations is key to being able to accurately design these features in the future.

In addition to providing information for verification of numerical models, the field data presented in this report has also gone a long way in proving the effectiveness of these cooling systems when applied in the field. In general, the data from all three test sections on Thompson Drive has shown that the cooling systems employed there (ACE, ventilated shoulder, and hairpin thermosyphons) have all been effective at cooling the foundation soils beneath the embankment and maintaining frozen conditions throughout the 15-year life of the project. This was true even during the string of extremely warm annual temperatures that were encountered in Fairbanks during the 2014-2019 time period. The three-year data record from the Alaska Highway test site has, likewise, demonstrated that both the ventilated shoulder installations and the horizontal ACE layers included in that rehabilitation project provided a significant cooling effect that should counteract future thawing and, over time, begin to re-freeze the foundation soil beneath the rebuilt embankment.

Results from both Thompson Drive and the Alaska Highway test site tend to indicate that the most effective cooling systems included in these projects were the ventilated shoulder structures. Cooling at the base of the ventilated shoulders, both on Thompson Drive and the Alaska Highway, was very pronounced and in both cases lowered mean annual temperatures beneath the shoulder area by several degrees Celsius. As a result, it appears that ventilated shoulders should be able to provide several important advantages for roadways constructed on warm permafrost. First of all, the cooling provided at the base of the shoulder region will be very effective at eliminating the shoulder rotation problem which effects many of Alaska's highways. Secondly, with an insulation layer placed beneath the driving surface, it may be possible for the cooling influence of a ventilated shoulder to provide an adequate cooling effect that reaches all the way to the embankment centerline, thus protecting the entire roadway embankment from thaw settlement. On the other hand, the results from both projects also demonstrate that horizontal ACE layers are also effective at providing cooling and maintaining frozen conditions, so both ACE layers and ventilated shoulders can be considered effective design alternatives for embankment design on warm permafrost.

5.2. Numerical Simulation of ACE/Ventilated Shoulder Performance

CHAPTER 4 describes an in-depth attempt to simulate the field results obtained from Thompson Drive test section #1. As stated above, numerical simulation provides the most accurate design tool for ACE and ventilated shoulder installations since the convective flow present in these structures leads to

complicated heat transfer patterns that are not easy to model with approximate methods. Having said that, however, it is also true that accurate numerical modeling depends on knowledge of material properties and boundary conditions. In general, material properties can be obtained via field sampling combined with empirical models that can predict both thermal and hydraulic properties based on measurements of dry densities, mineral content, porosity, and moisture content. Often the challenge is that these material properties may be highly variable in the foundation soils, and moisture content may change seasonally.

In terms of boundary conditions, the most challenging boundary to deal with is the upper surface of the embankment and shoulder region that is in contact with the atmospheric air. Traditionally N-factors are often used to help calculate effective surface temperatures (needed for the model boundary conditions) based on air temperature trends. This approach is useful for modeling since air temperatures are typically more available for a given location and, in any case, are relatively easy to measure with a standard meteorological station. N-factor data is available in the literature for a wide range of surface types and can be used reliably for simple non-snow-covered surfaces such as the asphalt or gravel driving surface. For snow-covered surfaces the N-factor data is more limited and is generally more suspect in nature since the connection between surface temperature and ambient air temperature becomes even more complicated due to the impact of an ever-changing snow pack during winter. One solution to this problem is to perform a full surface energy balance that utilizes snow pack depth as a function of time. Such an approach is available in Temp/W. However, the surface energy balance model, such as the one included in Temp/W, assumes that heat is transferred through the snowpack by heat conduction. This is a viable assumption for most situations but is not applicable to the upper surface of a ventilated shoulder. As shown in the simulation results included in CHAPTER 4 a ventilated shoulder allows “breathing” of ambient air into and out of the shoulder surface. During winter, this airflow occurs through the snowpack, thus fundamentally changing the nature of the heat transfer through the snow layer. This, essentially, invalidates the existing N-factor data in the literature for snow-covered surfaces. As shown in Section 4.3, the type of hydraulic and thermal boundary condition used at the surface of the ventilated shoulder has a significant impact on the numerical results. Based on the numerical data presented there, it appears that the Case 5 simulation results most closely matched with the field data from Thompson Drive, but that simulation was based on a simplified assumption that the winter snowpack did not interfere with airflow into the embankment and did not provide any “insulation” between the surface and the ambient air. In reality this is an oversimplification of the problem and a more accurate technique would be to somehow include the impact of airflow through the snowpack in the model. Such an approach may be possible utilizing the Temp/W modeling package in combination with the Software Development Toolkit that is provided by Geostudio for programming custom modeling extensions.

5.3. Recommendations for Further Research

The experimental data contained in this report goes a long way to illustrate the cooling effectiveness of air convection embankments and ventilated shoulders. However, further work is needed to optimize these installations in order to strike a balance between cooling effectiveness and cost. Both thermosyphons and the open-graded coarse rock needed for ACE and VS layers are expensive, and may add unneeded costs to construction projects if their use is not optimized. As an example, the ventilated shoulder structures used in the Thompson Drive project were very thick (on the order of 2 meters), and

required a large volume of rock to construct. This was also true for the Alaska Highway experimental feature. It is likely that much thinner layers that require much less rock would also have produced sufficient cooling to maintain underlying permafrost. Some of these questions are currently being evaluated at a newer experimental feature installation on the Dalton Highway that uses several different layer thicknesses for a set of experimental ventilated shoulder structures. Further investigation of required layer thicknesses could probably be done via numerical simulation which would be much more cost effective than building lots of different test sites. Future use of ACE and VS cooling systems would benefit from additional research work aimed at optimizing these systems.

In addition to ACE and VS system optimization, another area where further research would be useful is in the area of numerical simulation of these systems. In particular, as explained in CHAPTER 4, ventilated shoulder installations are difficult for existing numerical models to simulate accurately due to the way that ambient airflow interacts with the surface snow layer. Even though models such as GeoSlope Temp/W do include routines to simulate the existence of a snow layer on the surface of the ground or embankment, these routines are not able to take air convection into account. As a result, they cannot simulate the behavior of VS structures accurately. As shown in CHAPTER 4, different combinations of boundary conditions were able to come close to mimicking the behavior of the Thompson Drive ventilated shoulder, but none of them accurately capture the physics of the snowpack airflow. Thus, additional research and development work in the area of numerical simulation of ventilated shoulder structures would be very helpful for future design efforts.

REFERENCES

1. AKDOT (1996). Parks/Chena Ridge Interchange, project No. NH-I-OA4-5(7)/63538.
2. AKDOT (2002). Proposed highway projects STP-MGE-MGS-0002(90)/60395 UAF/New Geist Road access.
3. Billings, M. & Berggren, M. (2021). Construction of an air convection embankment (ACE) with non-angular ACE aggregate, Alaska Highway MP 1354-1364 rehabilitation project. AKDOT Project No. OA21007/61271.
4. Chen, L., Yu, W., Yi, X., Hu, D., & Liu, W. (2018). Numerical simulation of heat transfer of the crushed-rock interlayer embankment of Qinghai-Tibet Railway affected by aeolian sand clogging and climate change. *Cold Regions Science and Technology*, *155*, 1-10.
5. Côté, J., Fillion, M. H., & Konrad, J. M. (2011). Intrinsic permeability of materials ranging from sand to rock-fill using natural air convection tests. *Canadian Geotechnical Journal*, *48*(5), 679-690.
6. Darrow, M. M., & Jensen, D. D. (2016). Modeling the performance of an air convection embankment (ACE) with thermal berm over ice-rich permafrost, Lost Chicken Creek, Alaska. *Cold Regions Science and Technology*, *130*, 43-58.

7. Doré, G., Niu, F., & Brooks, H. (2016). Adaptation methods for transportation infrastructure built on degrading permafrost. *Permafrost and Periglacial Processes*, *27*(4), 352-364.

8. Fillion, M. H., Côté, J., & Konrad, J. M. (2011). Thermal radiation and conduction properties of materials ranging from sand to rock-fill. *Canadian Geotechnical Journal*, *48*(4), 532-542.

9. Fredlund, M., & Zhang, J. (2012). Benchmarks for solving coupled thermal, hydraulic, and air (THA) numerical models in roadways in cold regions. 15th International Conf. on Cold Regions Engineering, Quebec, CA, August.

10. Goering, D.J., Instanes, A., & Knudsen, S (2000). Convective Heat Transfer in Railway Embankment Ballast. Ground Freezing 2000, A. A. Balkema, Rotterdam, 31-36.

11. Goering, D. J. (2001). ACE and thermosyphon design features Loftus Road extension project. Federal Highway Admin. FHWA-AK-RD-02-01.

12. Goering, D. J. (2003). Passively cooled railway embankments for use in permafrost areas. J. of Cold Regions Engineering, 17(3), 119-133.

13. Goering, D. J. (2005). Loftus Road extension project – final report. Federal Highway Admin. FHWA-AK-RD-05-01.

14. Hartman, C. & Johnson, P. (1978). Environmental Atlas of Alaska. University of Alaska, Fairbanks, AK. 2nd Edition.

15. Jørgensen, A. S., Doré, G., Voyer, É., Chataigner, Y., & Gosselin, L. (2008). Assessment of the effectiveness of two heat removal techniques for permafrost protection. *Cold Regions Science and Technology*, *53*(2), 179-192.

16. Kong, X., Doré, G., & Calmels, F. (2019). Thermal modeling of heat balance through embankments in permafrost regions. *Cold Regions Science and Technology*, *158*, 117-127.

17. Kong, X., Doré, G., Calmels, F., & Lemieux, C. (2019). Development of Design Tools for Convective Mitigation Techniques to Stabilize Embankments Built on Thaw Sensitive Permafrost. Cold Regions Engineering 2019, 607-615.

18. Lebeau, M., & Konrad, J. M. (2009). Natural convection of compressible and incompressible gases in undeformable porous media under cold climate conditions. Computers and Geotechnics, 36(3), 435-445.

19. Lebeau, M., & Konrad, J. M. (2016). Non-Darcy flow and thermal radiation in convective embankment modeling. Computers and Geotechnics, 73, 91-99.

20. Lepage, J. M., Doré, G., & Fortier, F. (2016). Experimentation of mitigation techniques to reduce the effects of permafrost degradation on transportation infrastructures at Beaver Creek Experimental Road Site, Alaska Highway, Yukon (Doctoral dissertation, Université Laval).

21. Liu, M., Ma, W., Niu, F., Luo, J., & Yin, G. (2018). Thermal performance of a novel crushed-rock embankment structure for expressway in permafrost regions. *Int. J. of Heat and Mass Transfer*, 127, 1178-1188.

22. Liu, M., Niu, F., Ma, W., Fang, J., Lin, Z., & Luo, J. (2017). Experimental investigation on the enhanced cooling performance of a new crushed-rock revetment embankment in warm permafrost regions. *Applied Thermal Engineering*, *120*, 121-129.

23. Luo, J., Niu, F., Liu, M., Lin, Z., & Yin, G. (2018). Field experimental study on long-term cooling and deformation characteristics of crushed-rock revetment embankment at the Qinghai–Tibet Railway. *Applied Thermal Engineering*, *139*, 256-263.

24. Ma, W., Feng, G., Wu, Q., & Wu, J. (2008). Analyses of temperature fields under the embankment with crushed-rock structures along the Qinghai–Tibet Railway. *Cold Regions Science and Technology*, *53*(3), 259-270.

25. Mu, Y., Ma, W., Niu, F., Liu, Y., Fortier, R., & Mao, Y. (2018). Long-Term Thermal Effects of Air Convection Embankments in Permafrost Zones: Case Study of the Qinghai–Tibet Railway, China. *Journal of Cold Regions Engineering*, *32*(4), 05018004.

26. Papineau, J. M., (2001). Wintertime temperature anomalies in Alaska correlated with ENSO and PDO. *Int. J. of Climatology,* 1577-1592.

27. Pei, W., Zhang, M., Li, S., Lai, Y., & Jin, L. (2017). Enhancement of convective cooling of the porous crushed-rock layer in cold regions based on experimental investigations. International Communications in Heat and Mass Transfer, 87, 14-21.

28. Qin, Y., Tan, K., Liang, J., Li, Y., & Li, F. (2016). Experimental study on the solar reflectance of crushed rock layer with different sizes. Environmental Earth Sciences, 75(9), 817.

29. Rieksts, K., Hoff, I., Kuznetsova, E., & Côté, J. (2017). Laboratory investigations of thermal properties of crushed rock materials. In Tenth International Conference on the Bearing Capacity of Roads, Railways and Airfields.

30. Rieksts, K., Hoff, I., Kuznetsova, E., & Côté, J. (2017). Laboratory investigations on heat transfer of coarse crushed rock materials. In 70th Canadian Geotechnical Conference., GeoOttawa, Ottawa, Canada, October (pp. 1-3).

31. Rieksts, K., Hoff, I., Scibilia, E., & Côté, J. (2019). Laboratory investigations into convective heat transfer in road construction materials. Canadian Geotechnical Journal, (ja).

32. Rieksts, K., Hoff, I., Scibilia, E., & Côté, J. (2019). Modelling the Nu-Ra relationship to establish the intrinsic permeability of coarse open-graded materials from natural air convection tests in a 1 m3 cell. International Journal of Heat and Mass Transfer, 135, 925-934.

33. Yu, W., Liu, W., Chen, L., Yi, X., Han, F., & Hu, D. (2016). Evaluation of cooling effects of crushed rock under sand-filling and climate warming scenarios on the Tibet Plateau. *Applied Thermal Engineering*, *92*, 130-136.

34. Zhao, H., Wu, Q., & Zhang, Z. (2019). Long-term cooling effect of the crushed rock structure embankments of the Qinghai–Tibet Railway. *Cold Regions Science and Technology*, *160*, 21-30.

35. Zhizhong, S., Wei, M., & Dongqing, L. (2005). In situ test on cooling effectiveness of air convection embankment with crushed rock slope protection in permafrost regions. *Journal of Cold Regions Engineering*, *19*(2), 38-51.

APPENDIX A MEAN ANNUAL TEMPERATURES FOR THOMPSON DRIVE TEST SECTION #1

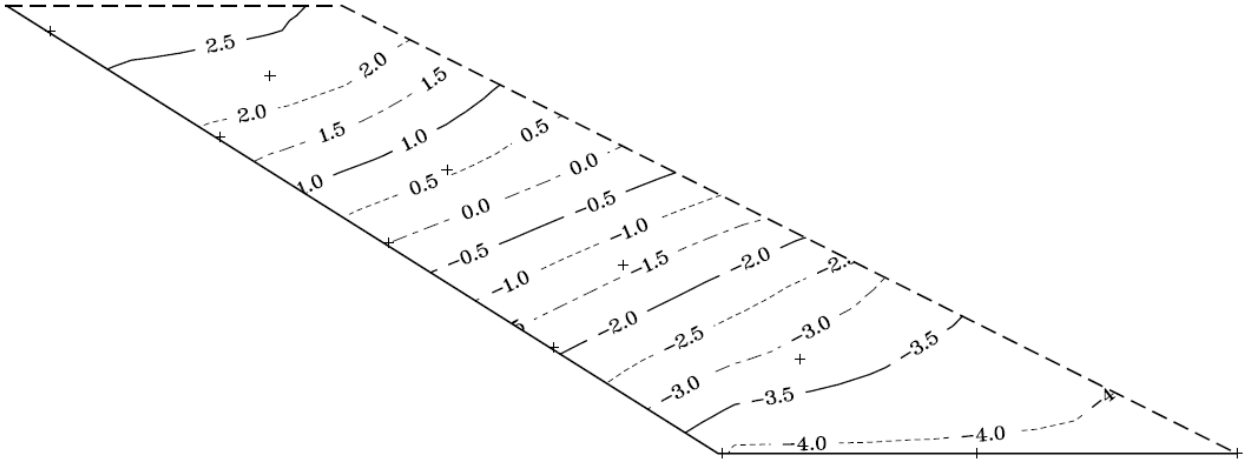

(a)

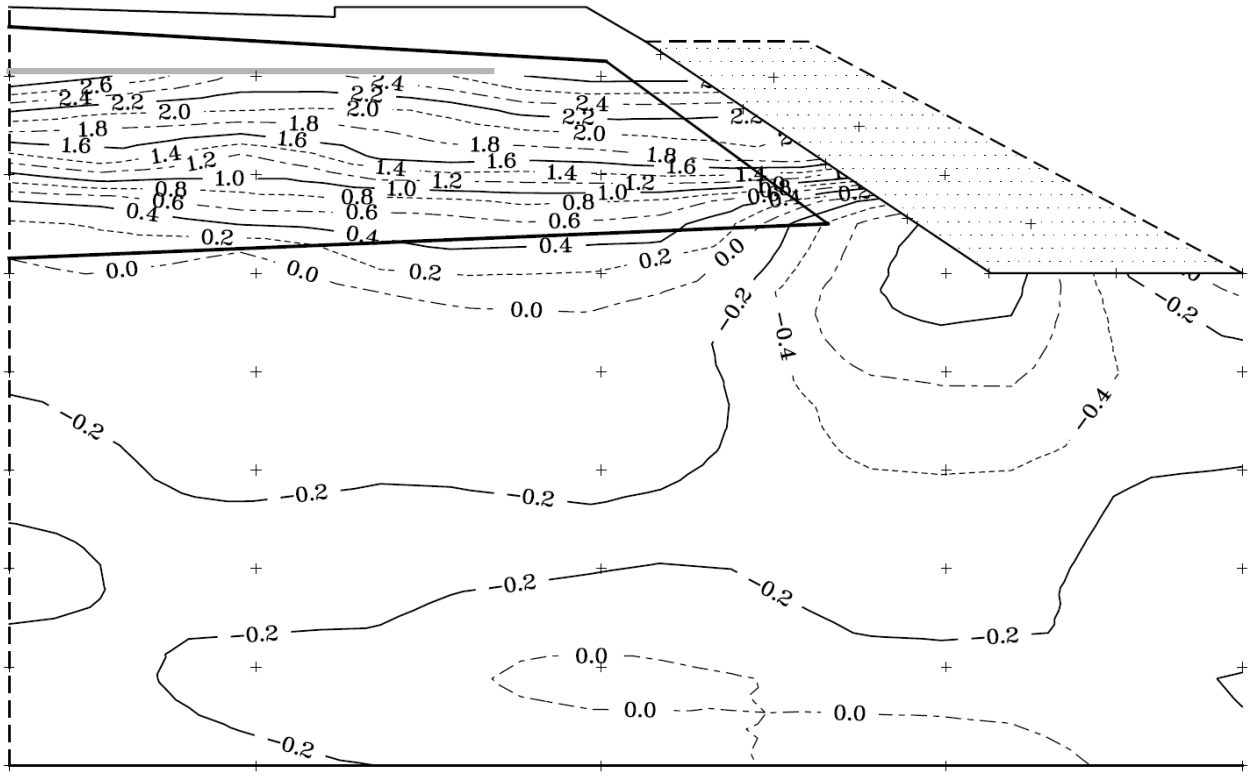

(b)

Figure A-1 Mean annual temperature contours for test section 1 in 2005, (a) ventilated shoulder, (b) embankment core and foundation soils

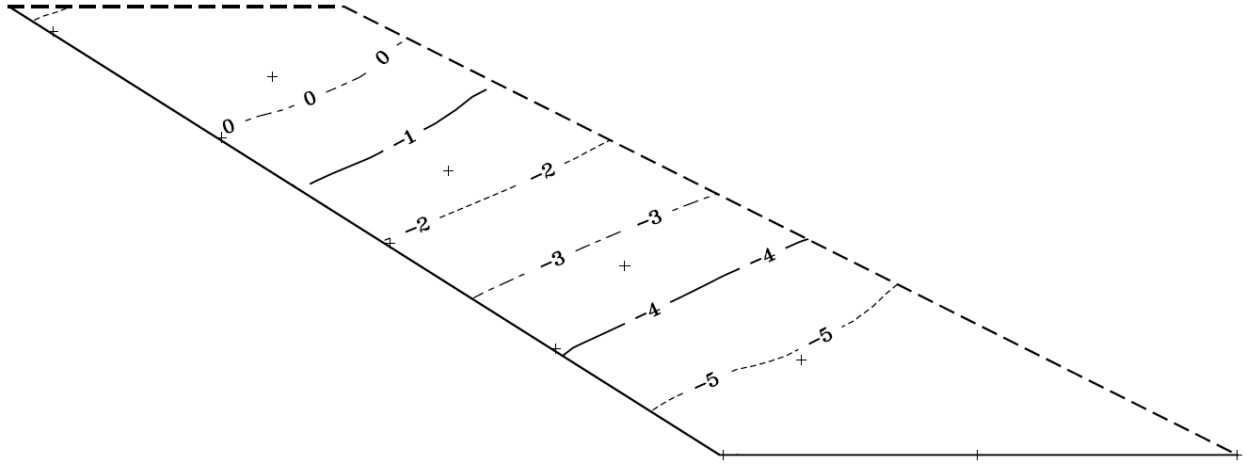

(a)

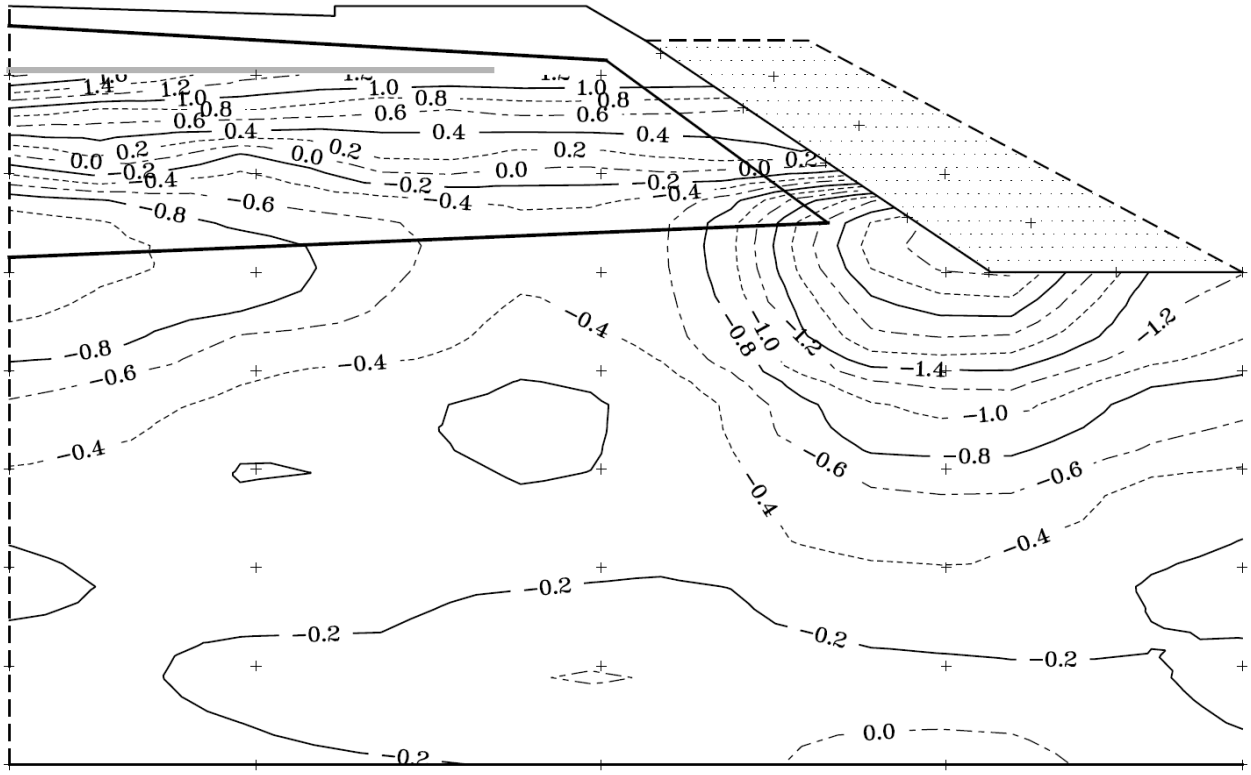

(b)

Figure A-2 Mean annual temperature contours for test section 1 in 2006, (a) ventilated shoulder, (b) embankment core and foundation soils

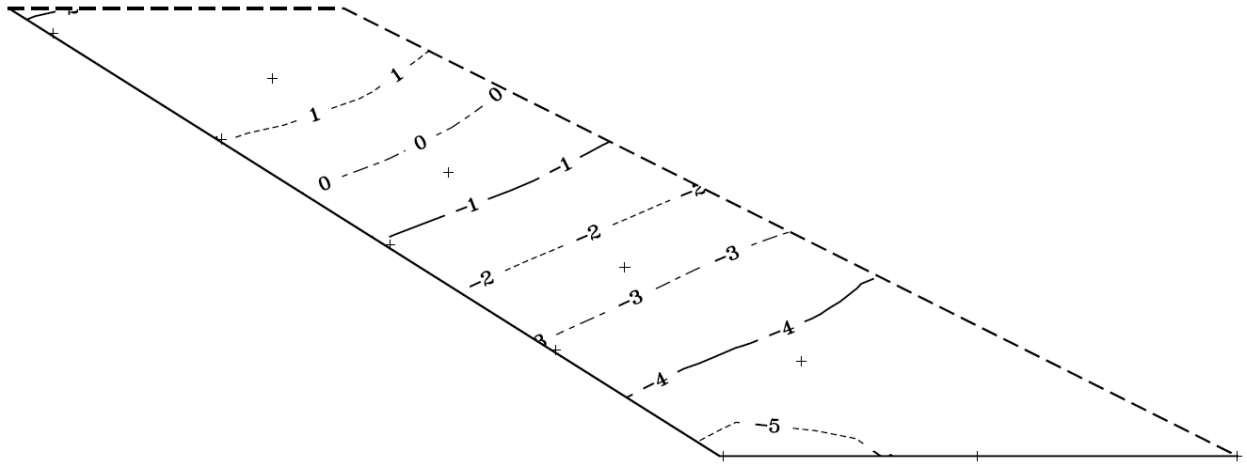

(a)

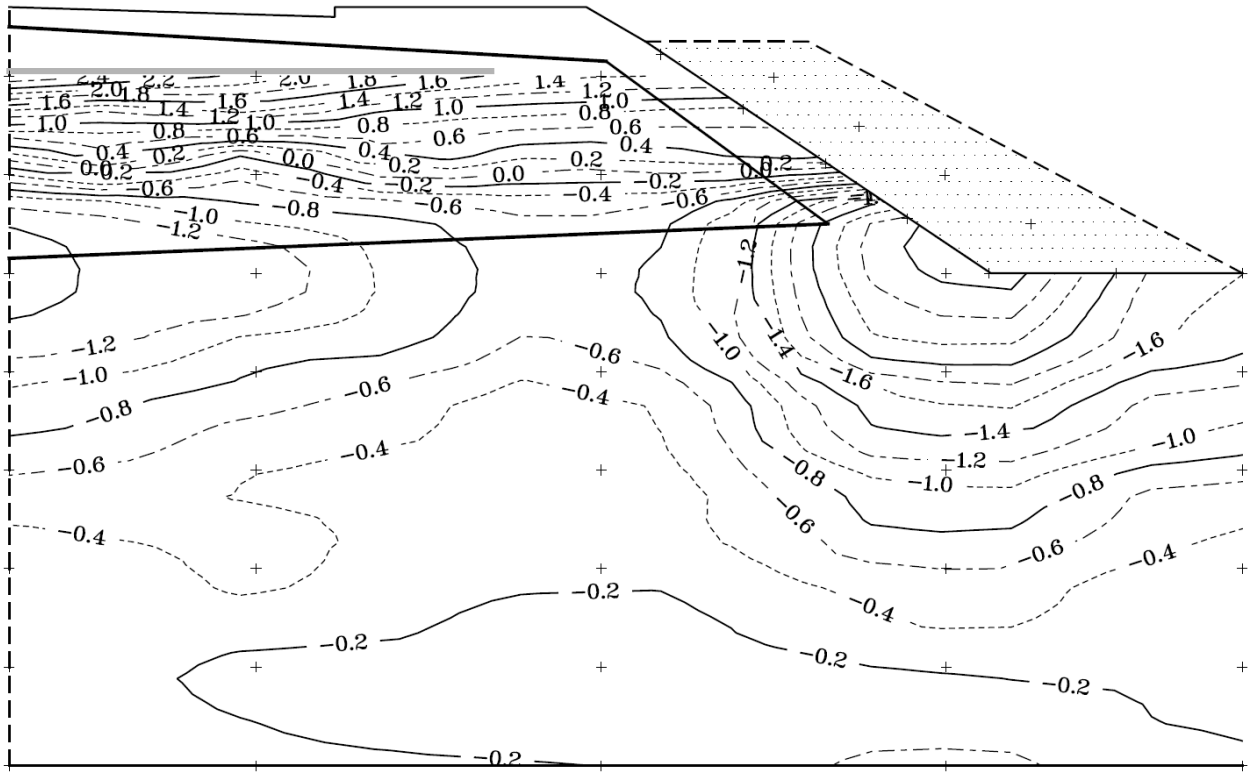

(b)

Figure A-3 Mean annual temperature contours for test section 1 in 2007, (a) ventilated shoulder, (b) embankment core and foundation soils

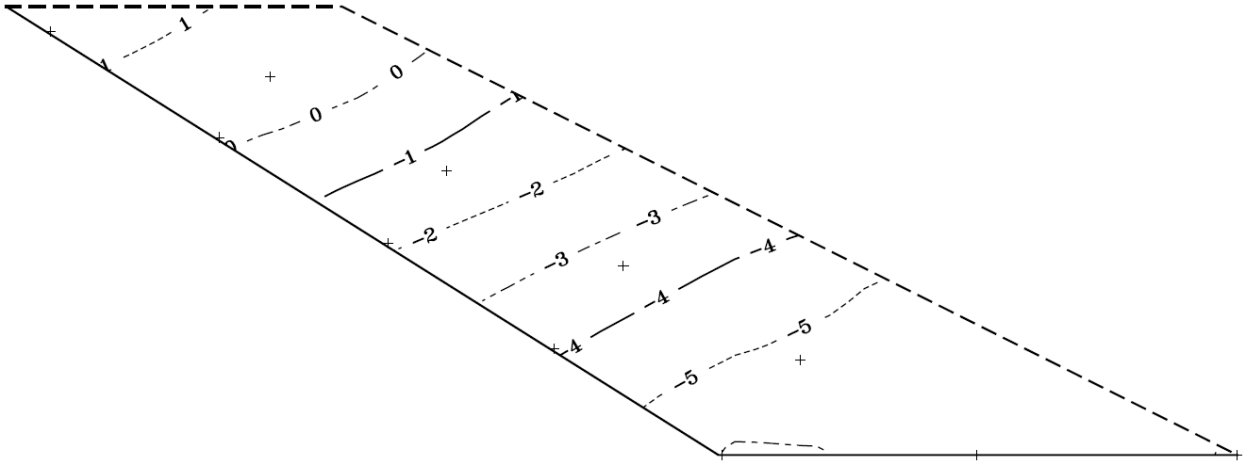

(a)

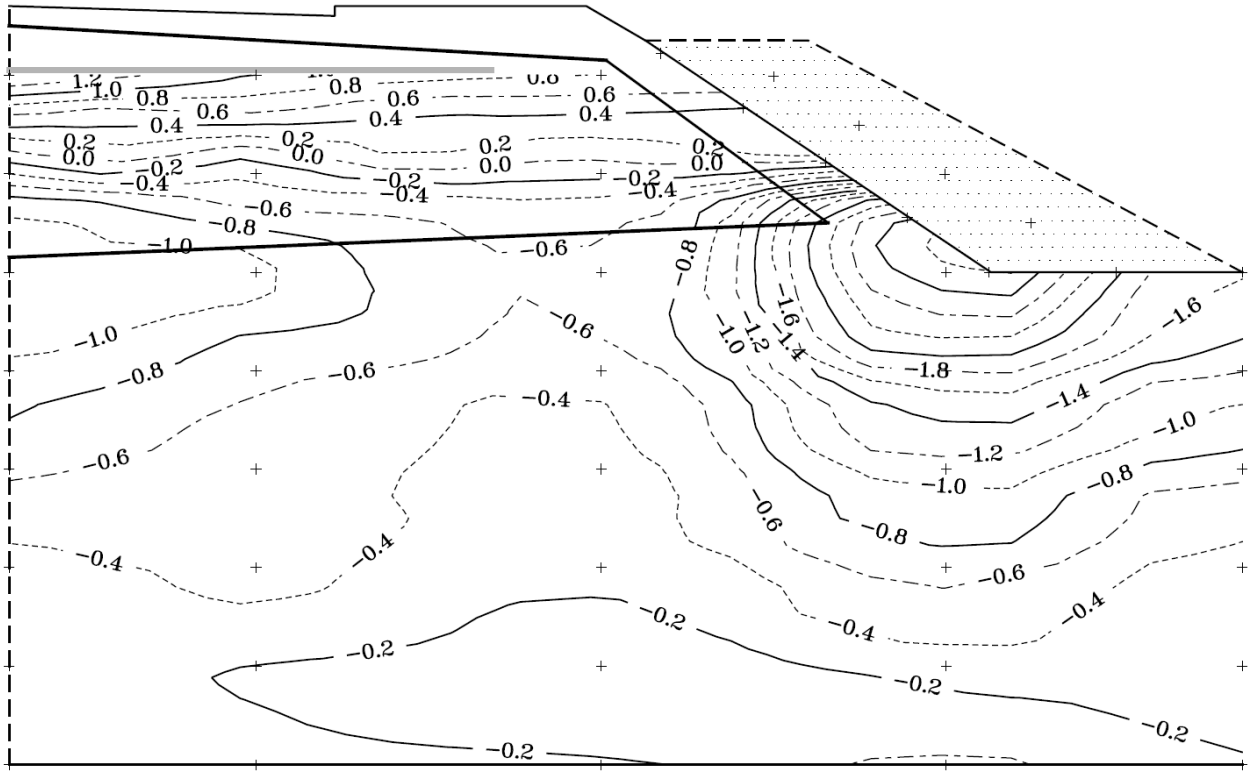

(b)

Figure A-4 Mean annual temperature contours for test section 1 in 2008, (a) ventilated shoulder, (b) embankment core and foundation soils

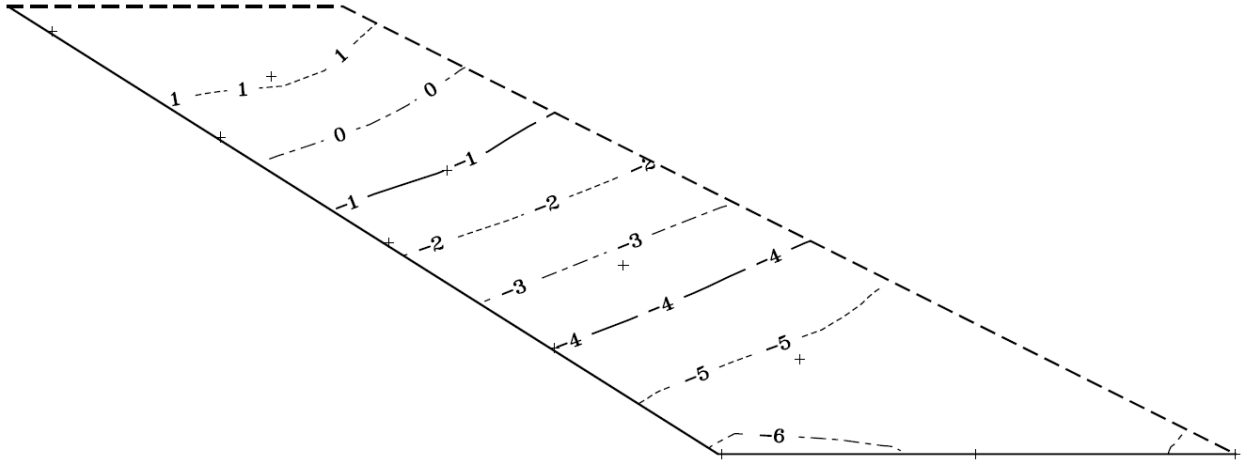

(a)

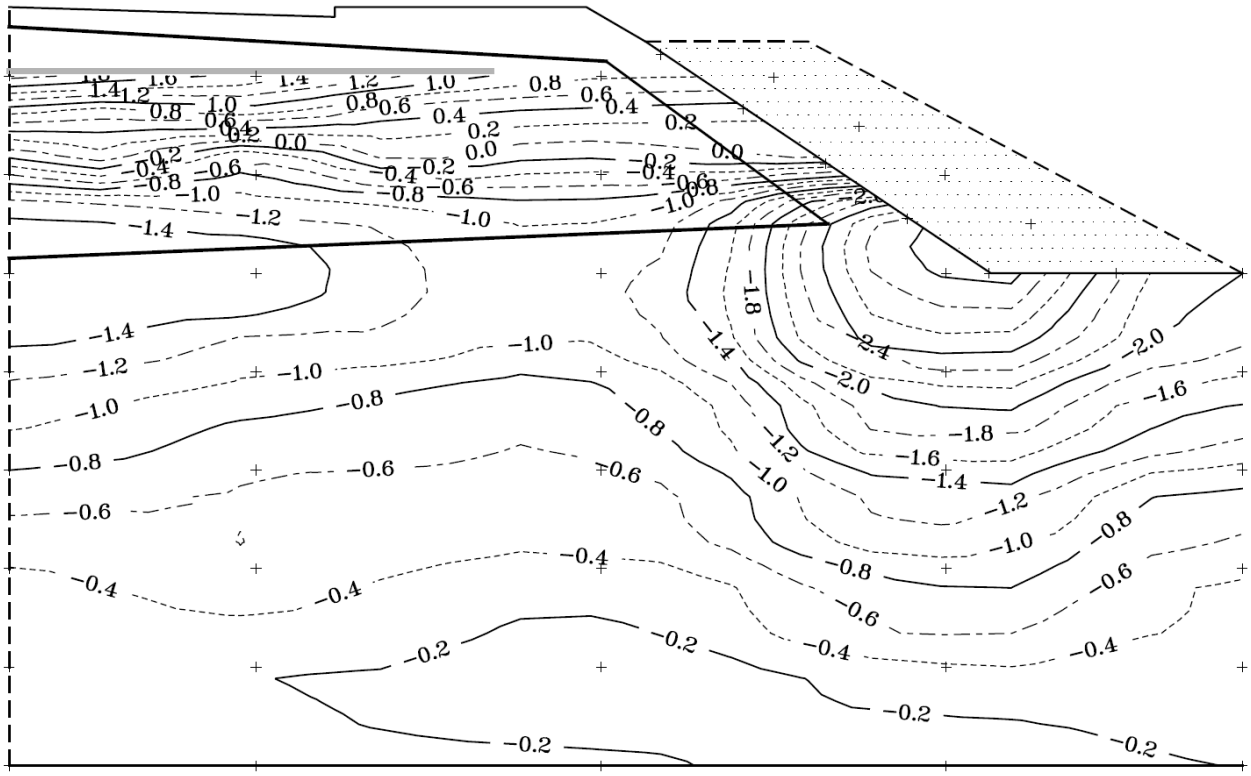

(b)

Figure A-5 Mean annual temperature contours for test section 1 in 2009, (a) ventilated shoulder, (b) embankment core and foundation soils

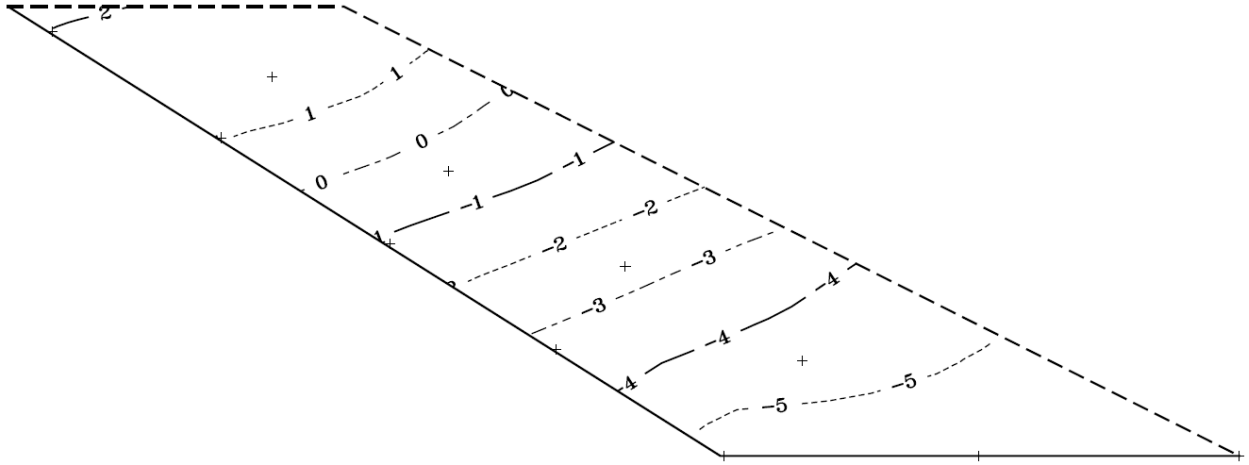

(a)

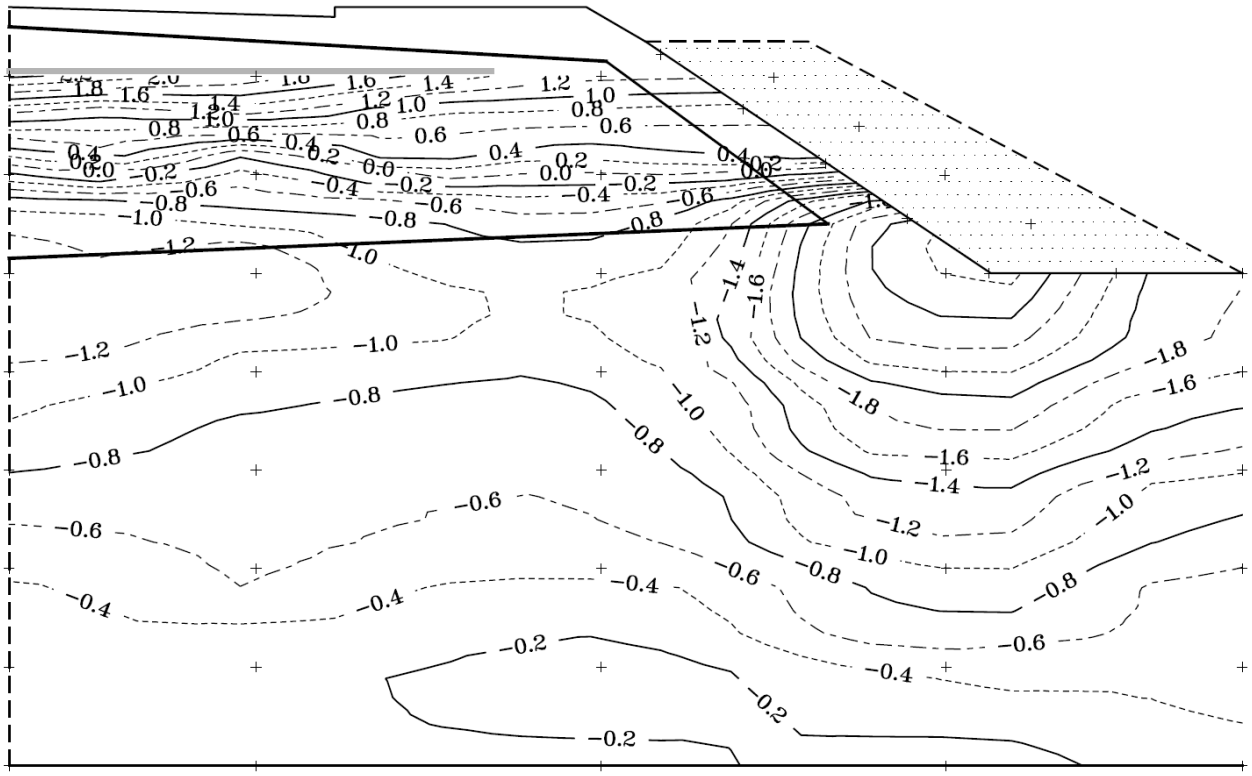

(b)

Figure A-6 Mean annual temperature contours for test section 1 in 2010, (a) ventilated shoulder, (b) embankment core and foundation soils

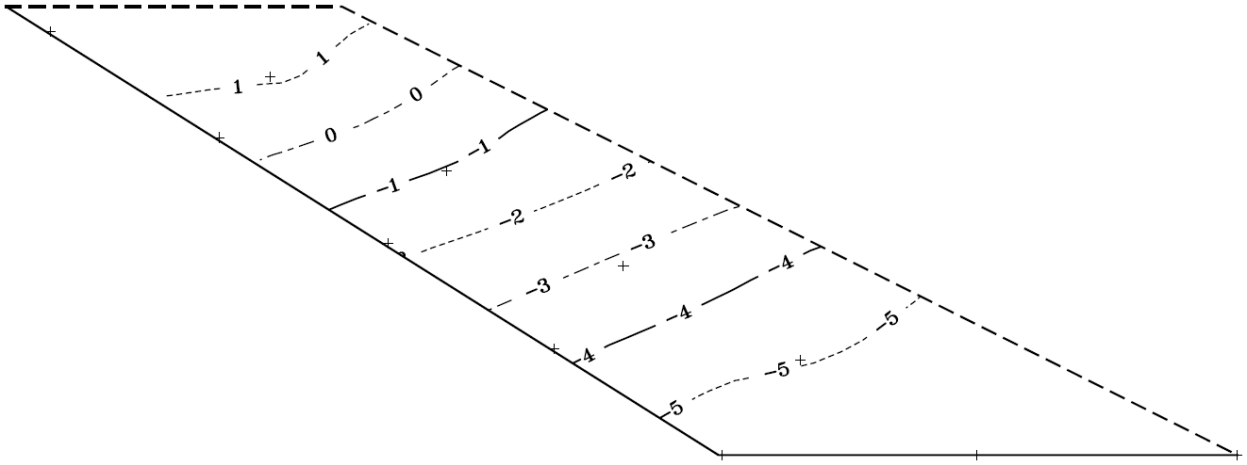

(a)

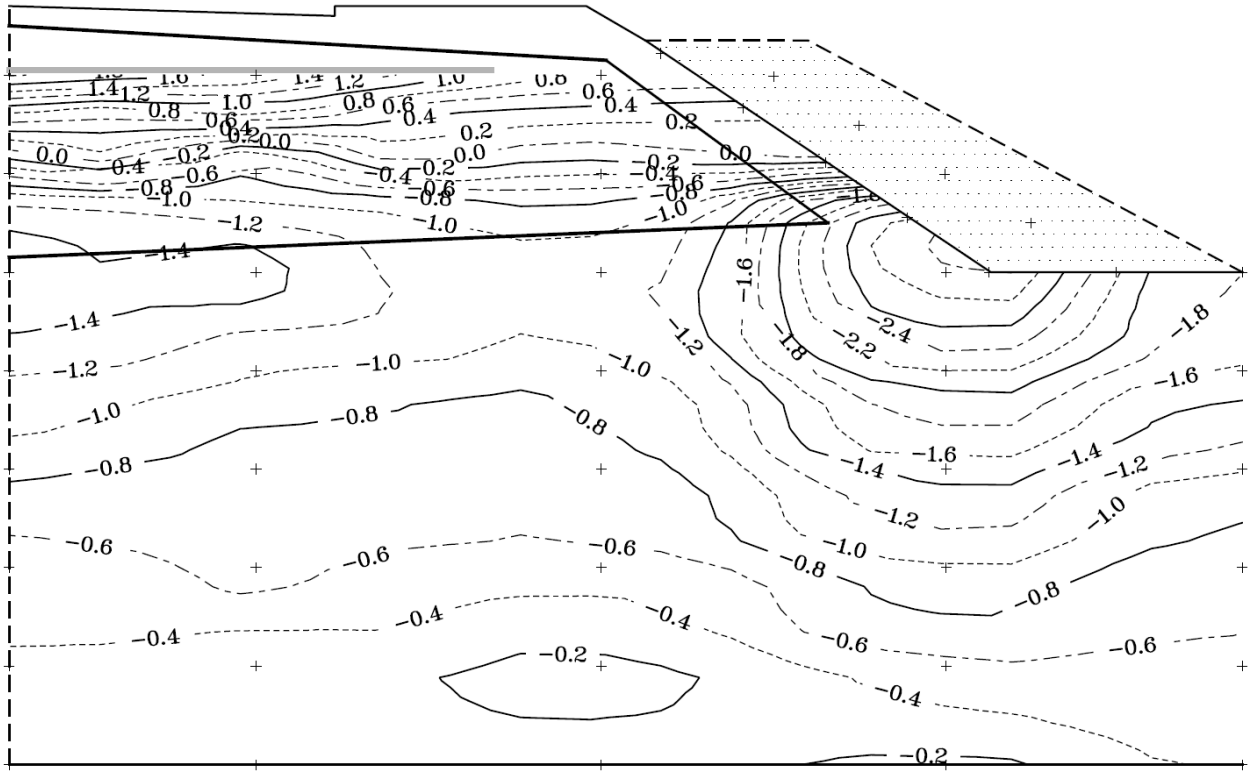

(b)

Figure A-7 Mean annual temperature contours for test section 1 in 2011, (a) ventilated shoulder, (b) embankment core and foundation soils

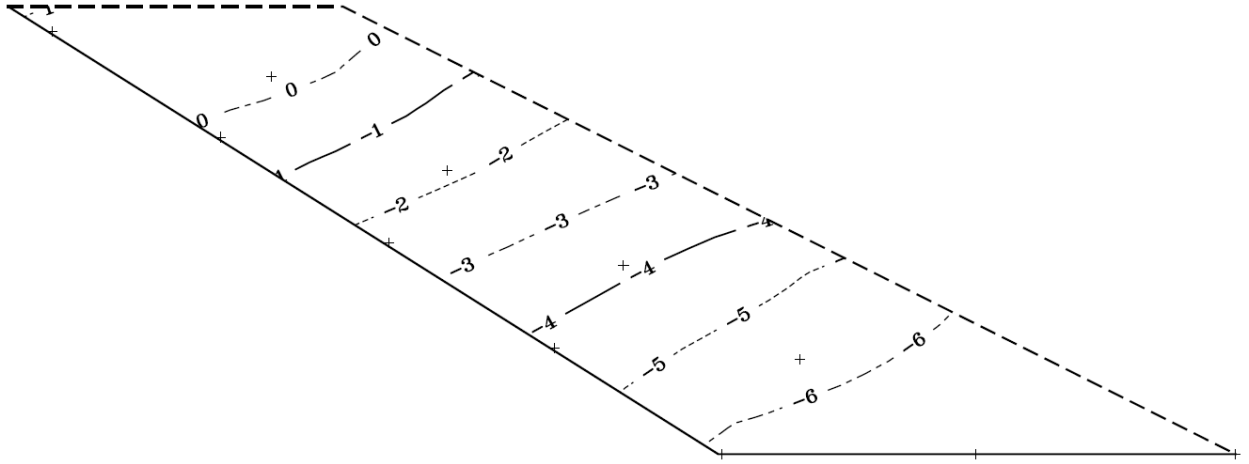

(a)

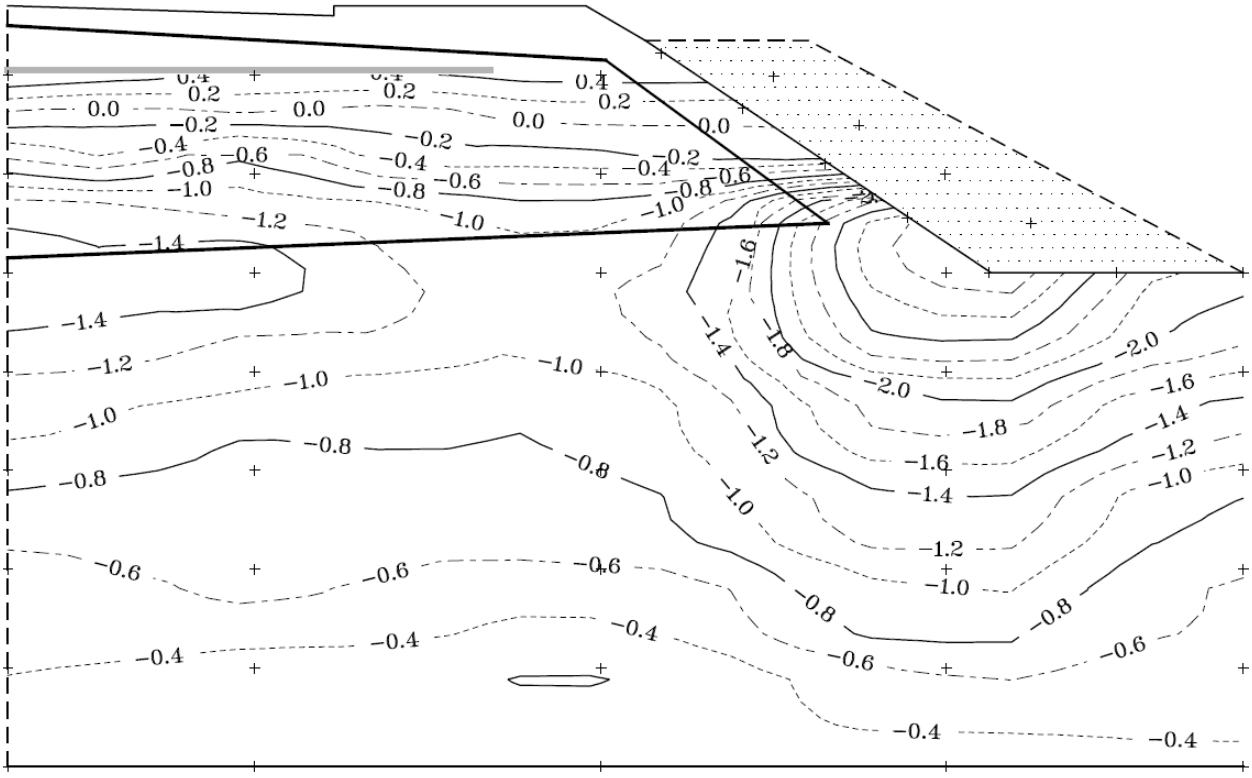

(b)

Figure A-8 Mean annual temperature contours for test section 1 in 2012, (a) ventilated shoulder, (b) embankment core and foundation soils

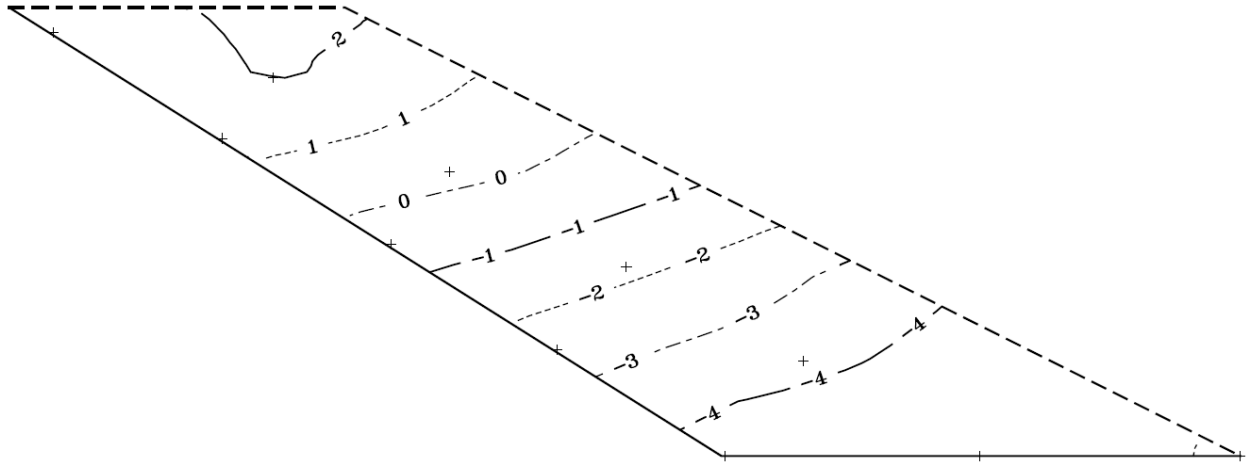

(a)

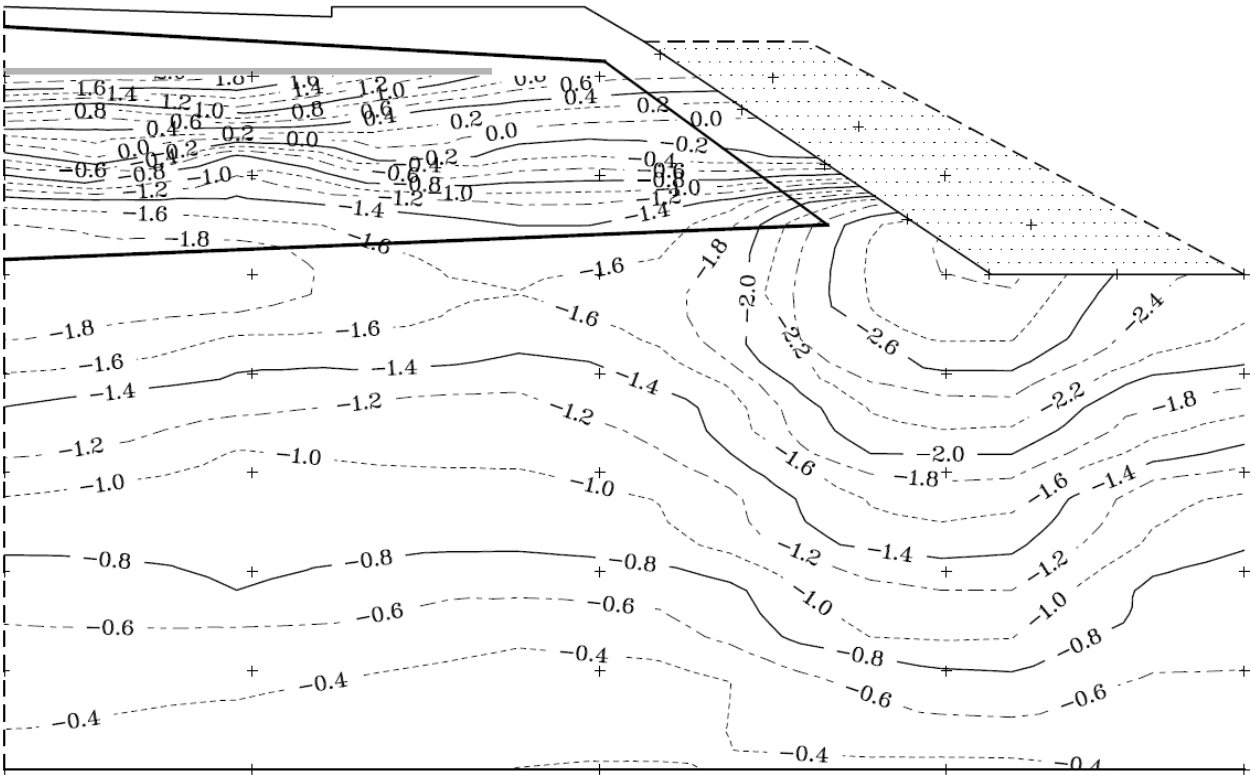

(b)

Figure A-9 Mean annual temperature contours for test section 1 in 2013, (a) ventilated shoulder, (b) embankment core and foundation soils

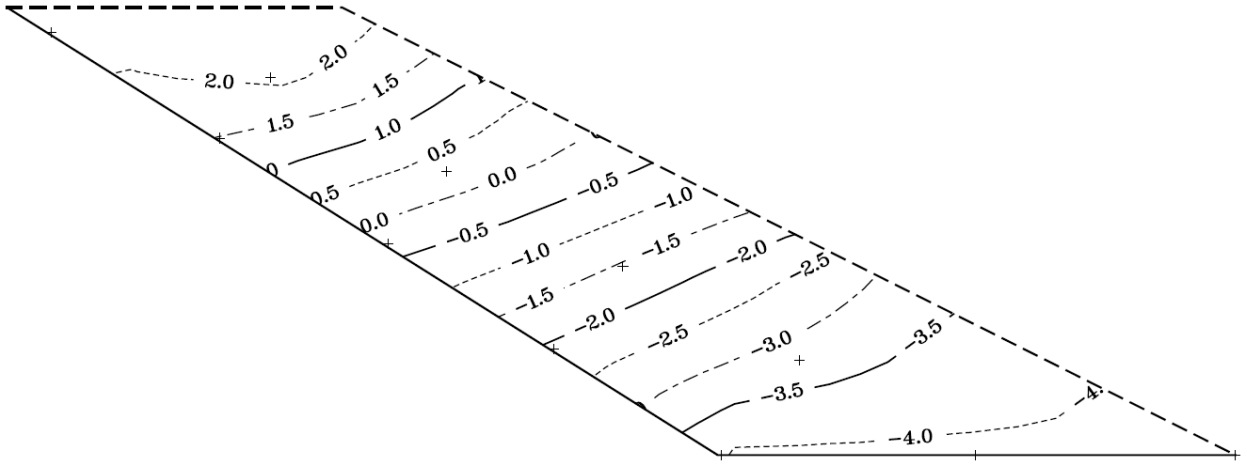

(a)

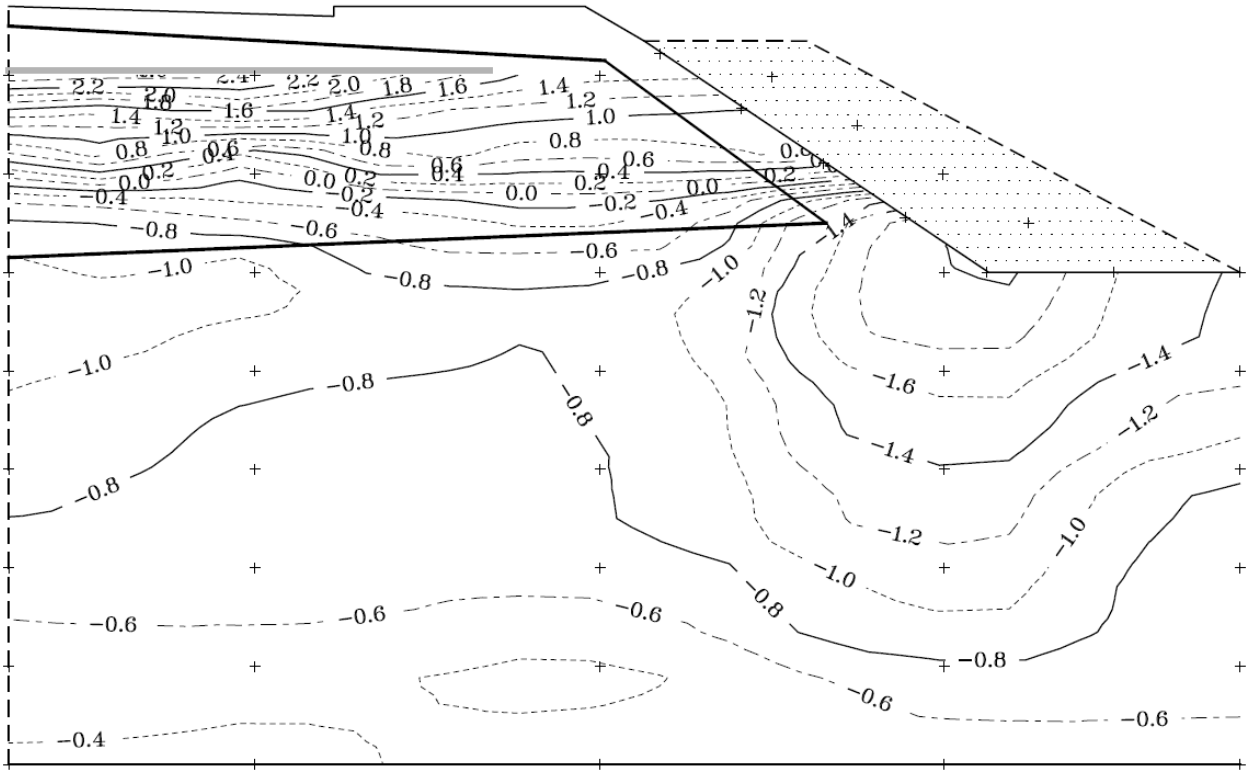

(b)

Figure A-10 Mean annual temperature contours for test section 1 in 2014, (a) ventilated shoulder, (b) embankment core and foundation soils

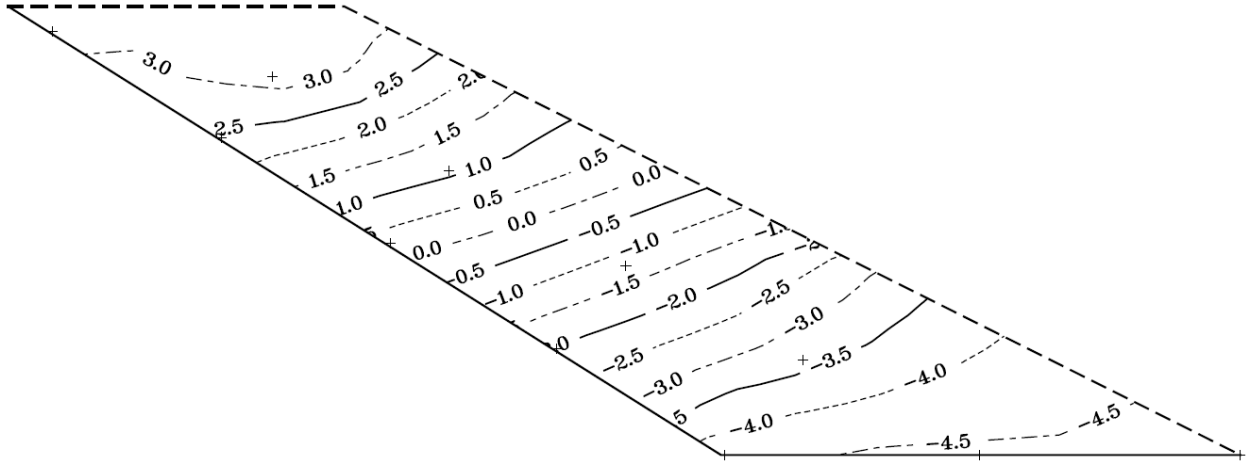

(a)

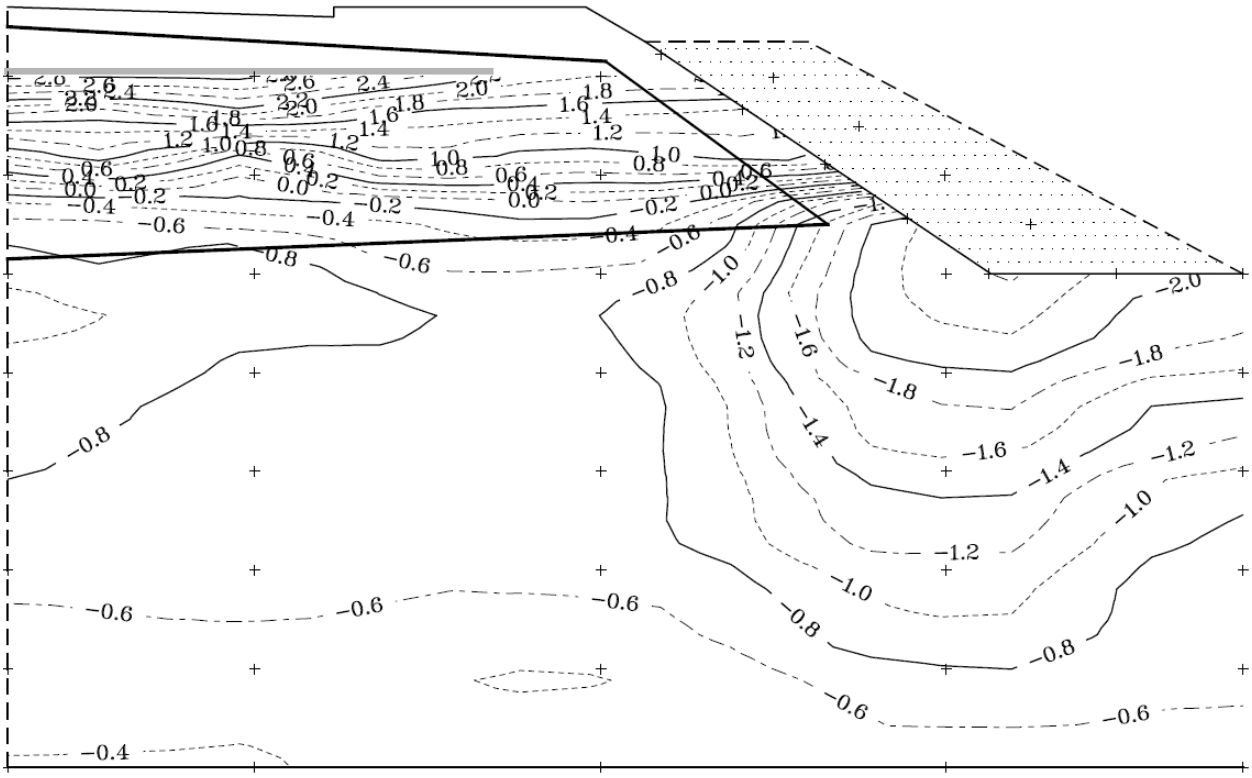

(b)

Figure A-11 Mean annual temperature contours for test section 1 in 2015, (a) ventilated shoulder, (b) embankment core and foundation soils

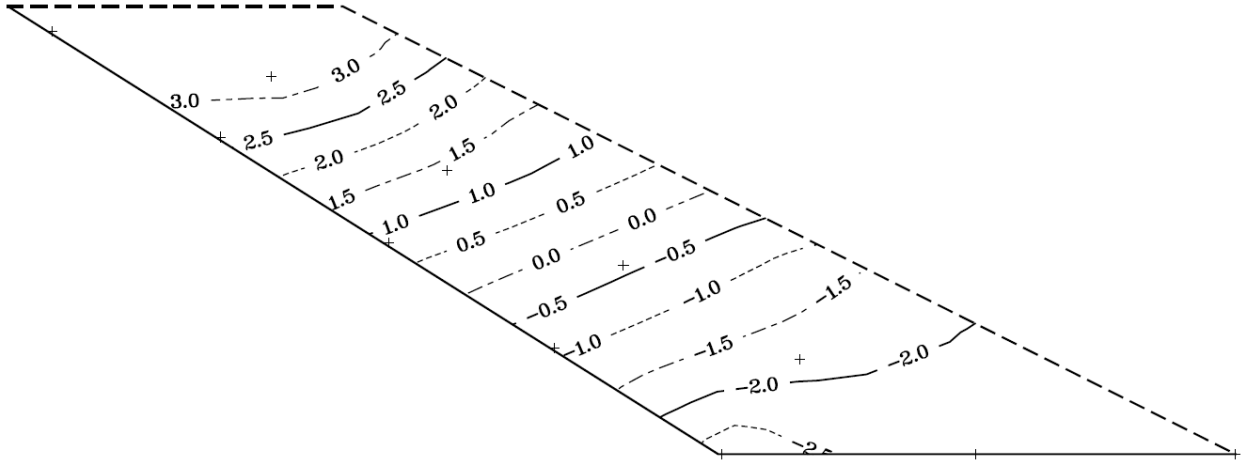

(a)

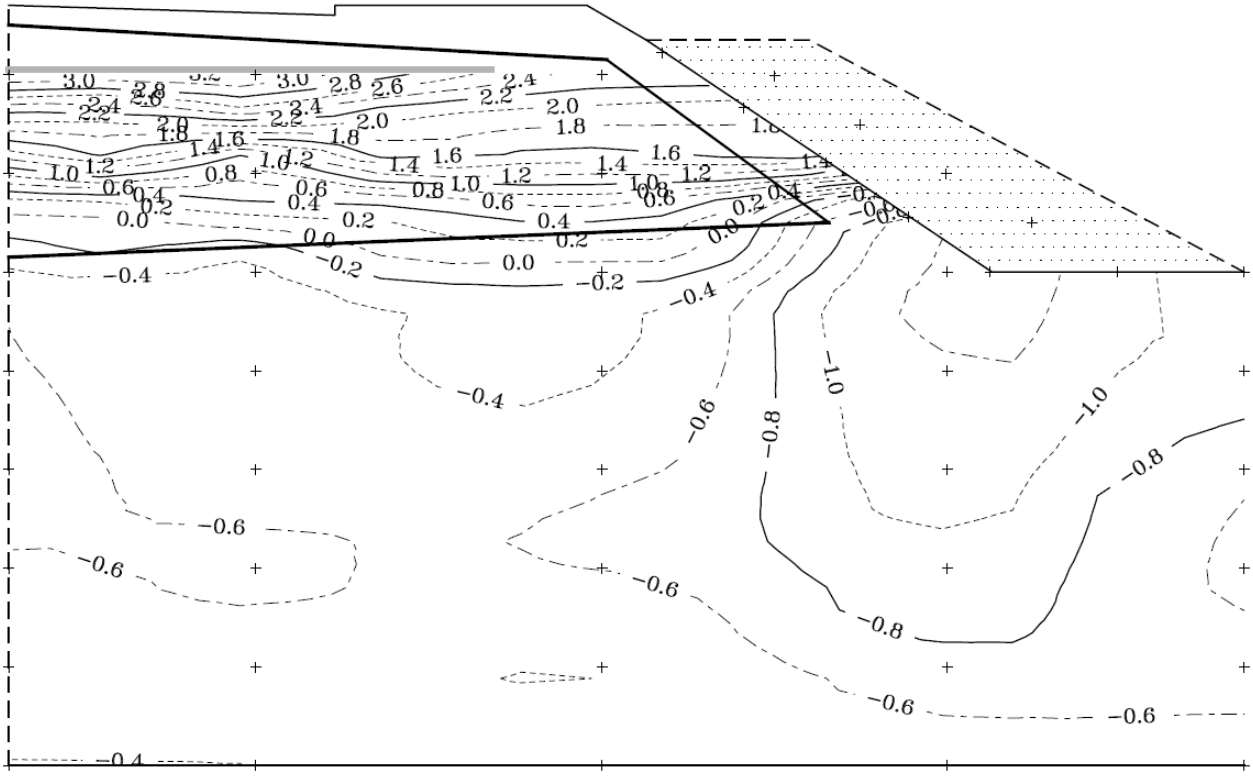

(b)

Figure A-12 Mean annual temperature contours for test section 1 in 2016, (a) ventilated shoulder, (b) embankment core and foundation soils

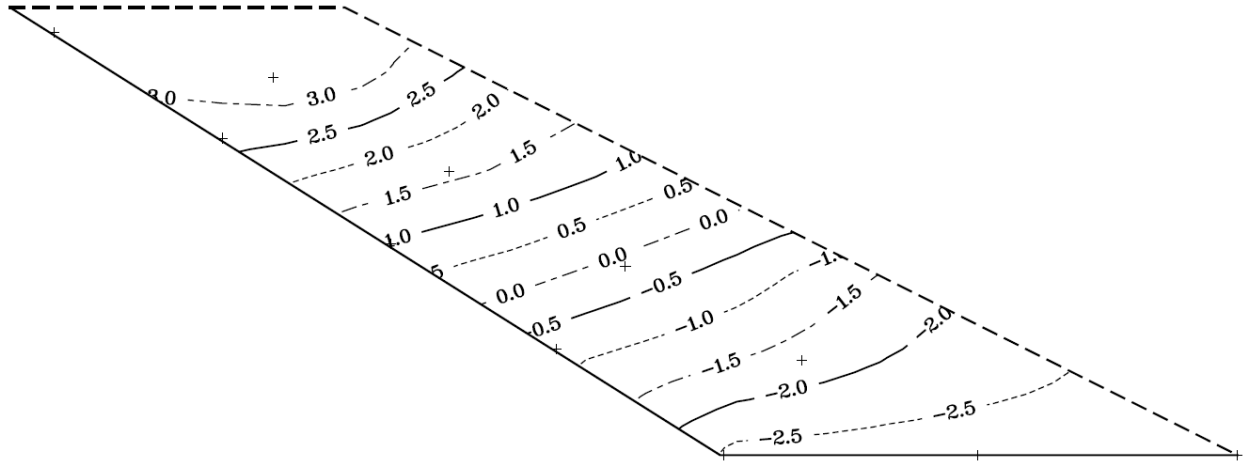

(a)

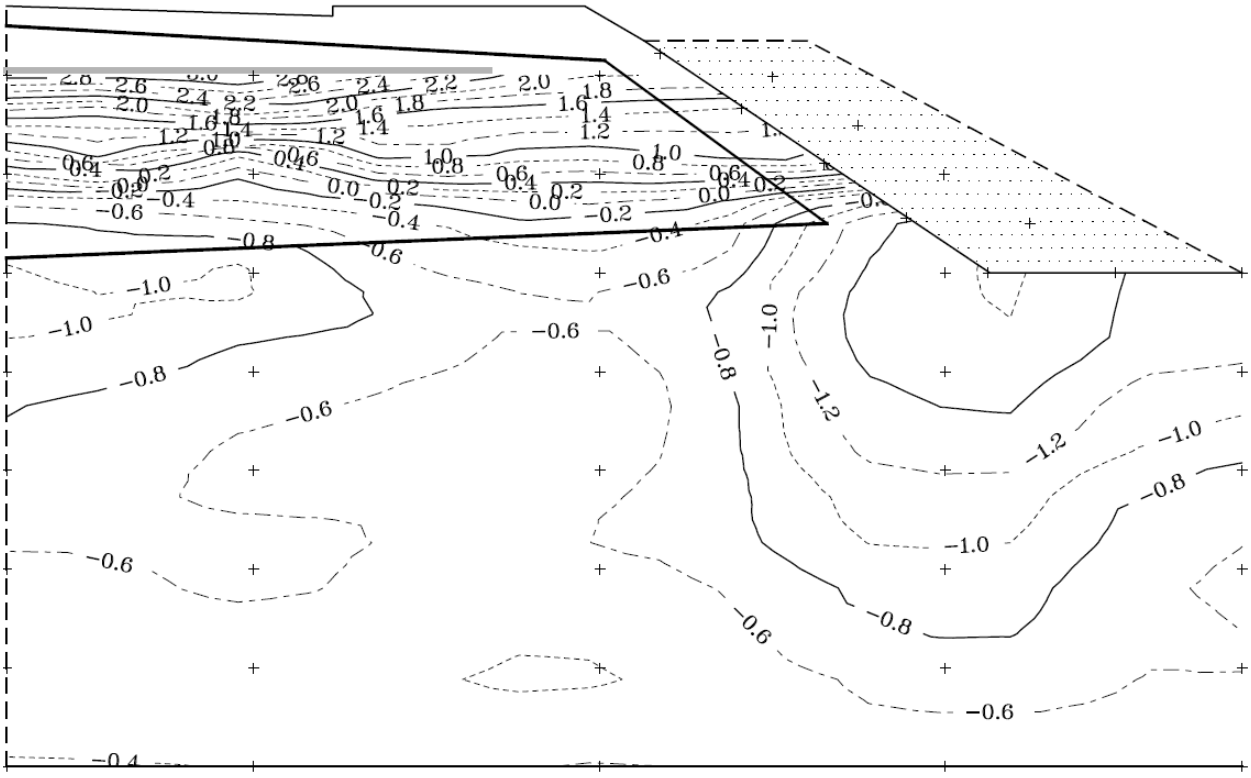

(b)

Figure A-13 Mean annual temperature contours for test section 1 in 2017, (a) ventilated shoulder, (b) embankment core and foundation soils

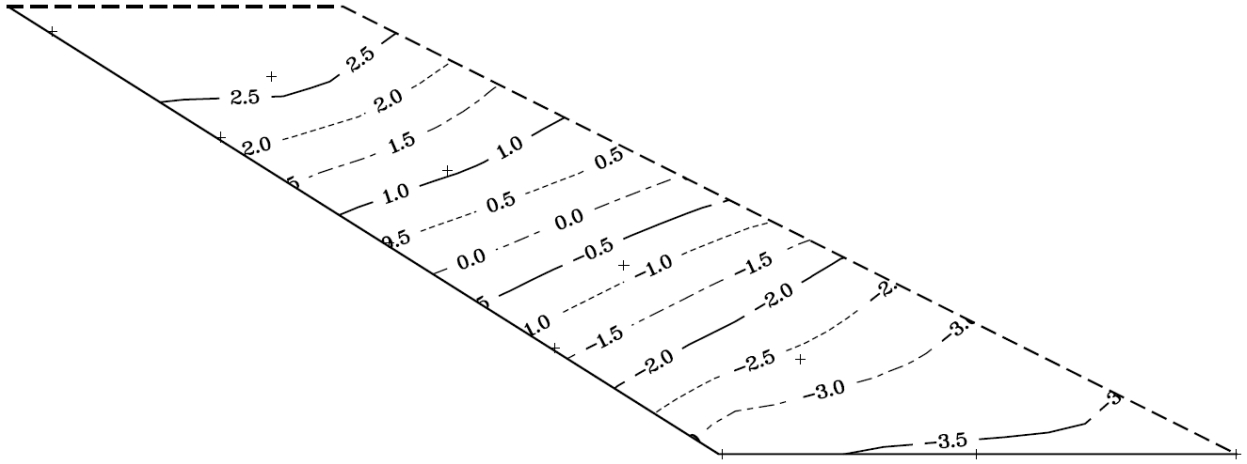

(a)

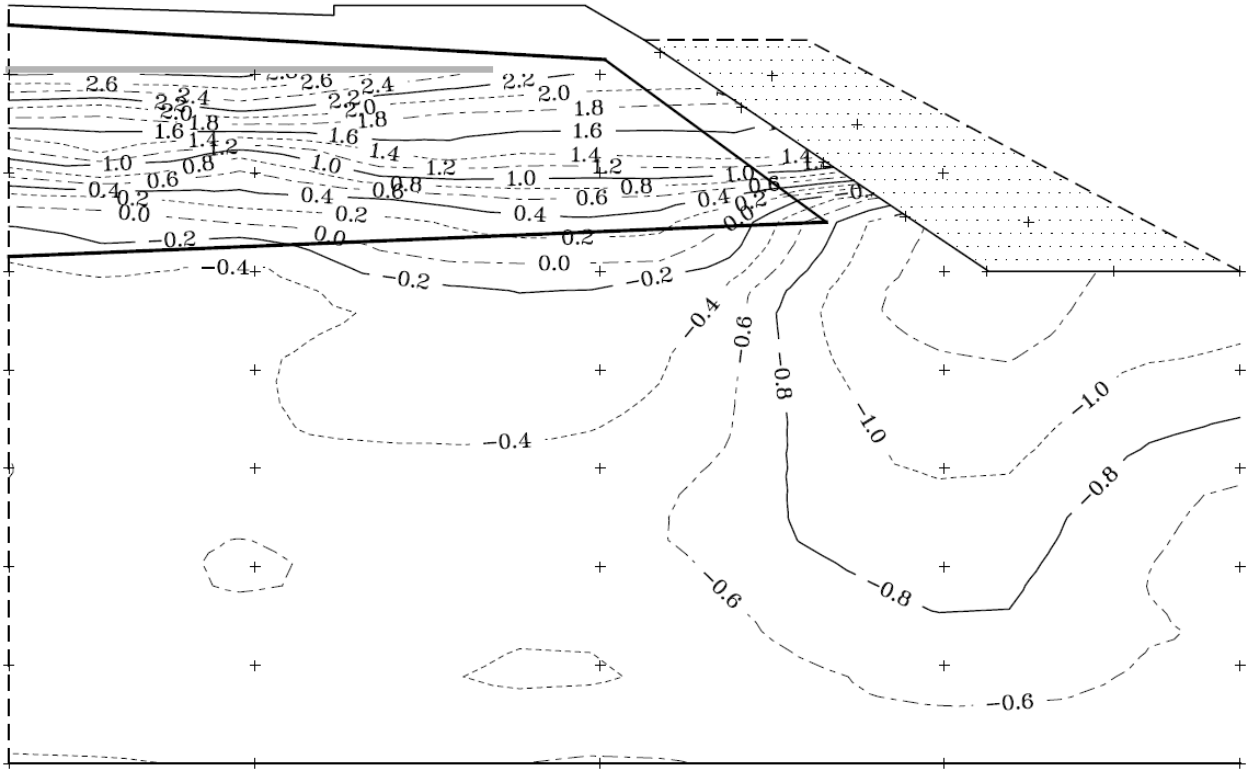

(b)

Figure A-14 Mean annual temperature contours for test section 1 in 2018, (a) ventilated shoulder, (b) embankment core and foundation soils

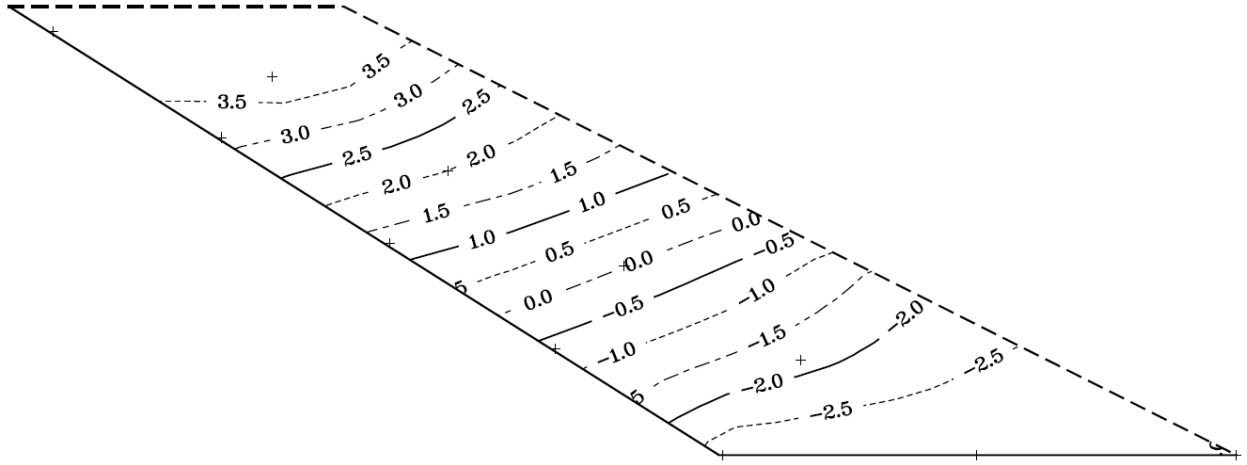

(a)

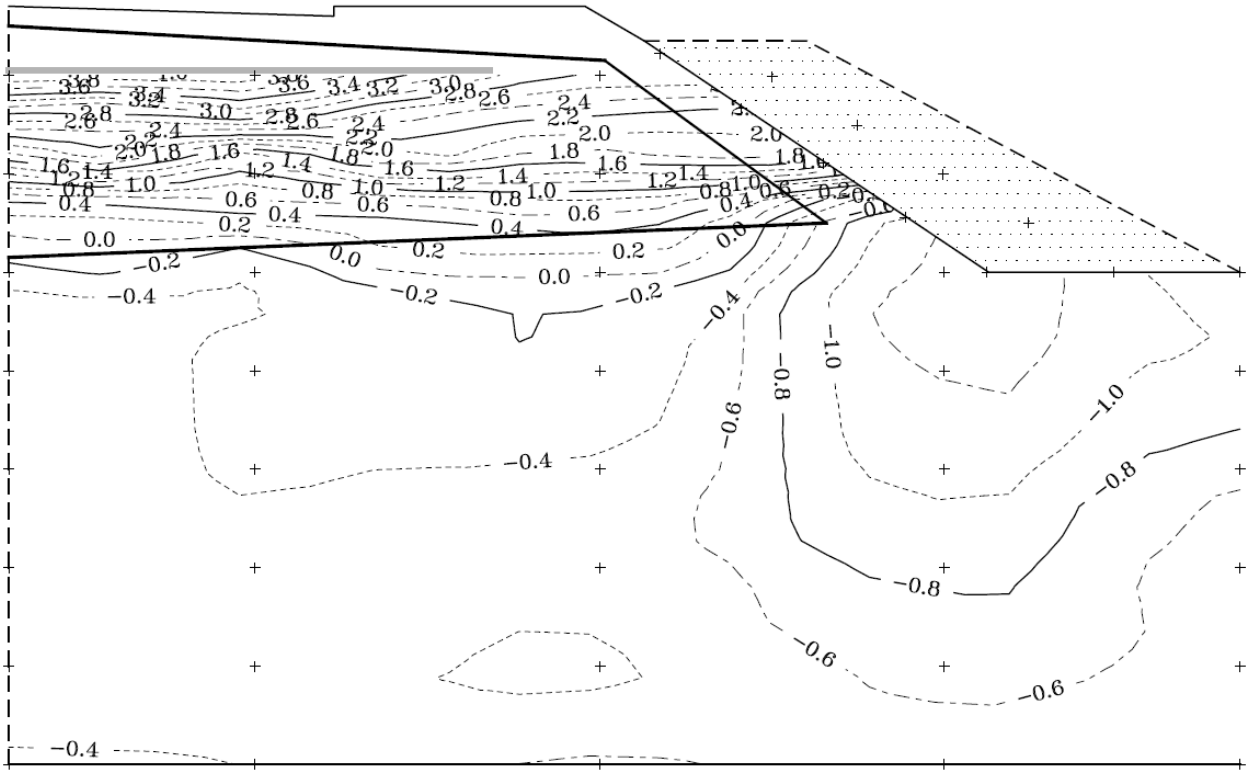

(b)

Figure A-15 Mean annual temperature contours for test section 1 in 2019, (a) ventilated shoulder, (b) embankment core and foundation soils

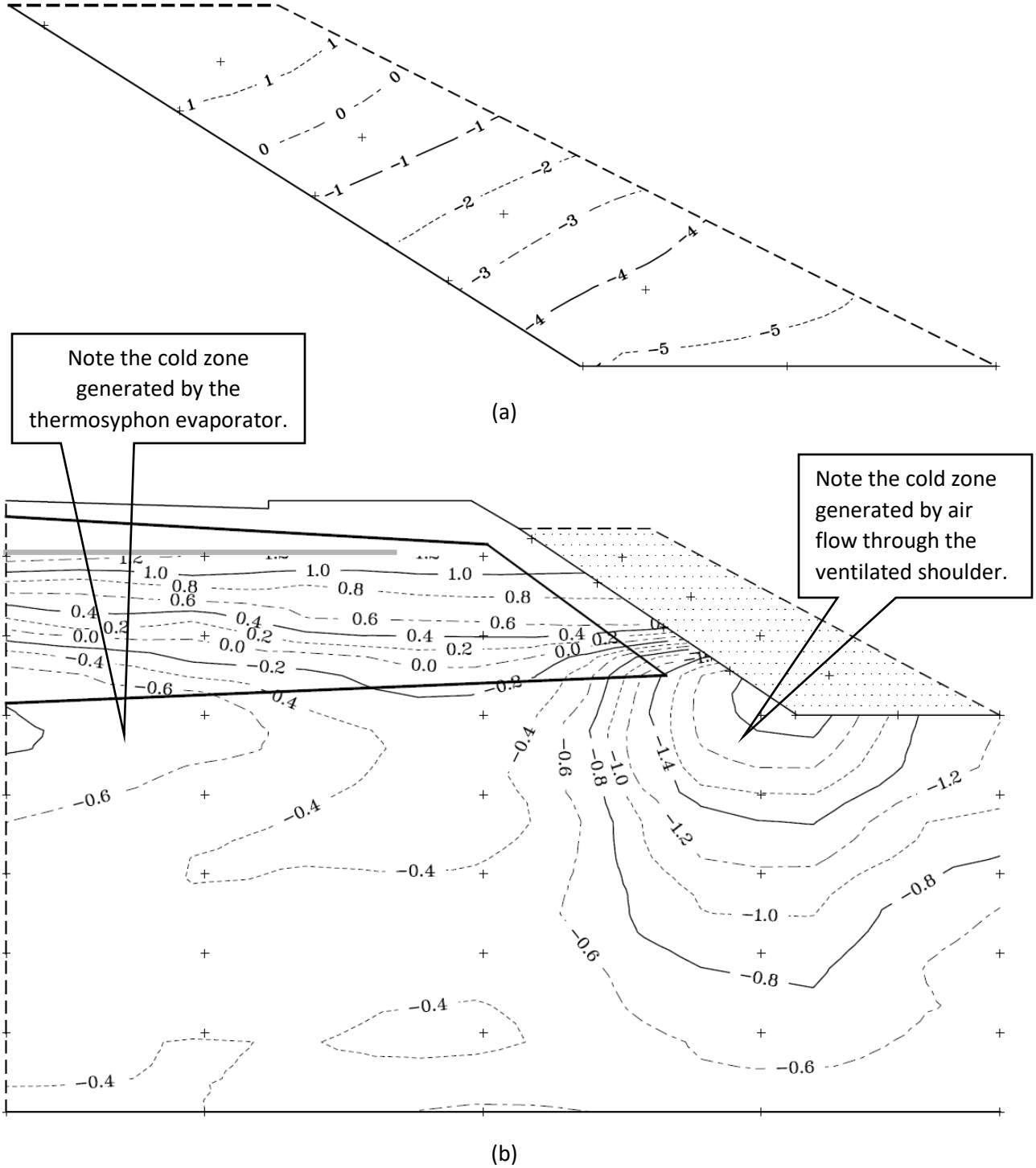

Figure A-16 Mean annual temperature contours for test section 1 in 2020, (a) ventilated shoulder, (b) embankment core and foundation soils

APPENDIX B MEAN ANNUAL TEMPERATURES FOR THOMPSON DRIVE TEST SECTION #2

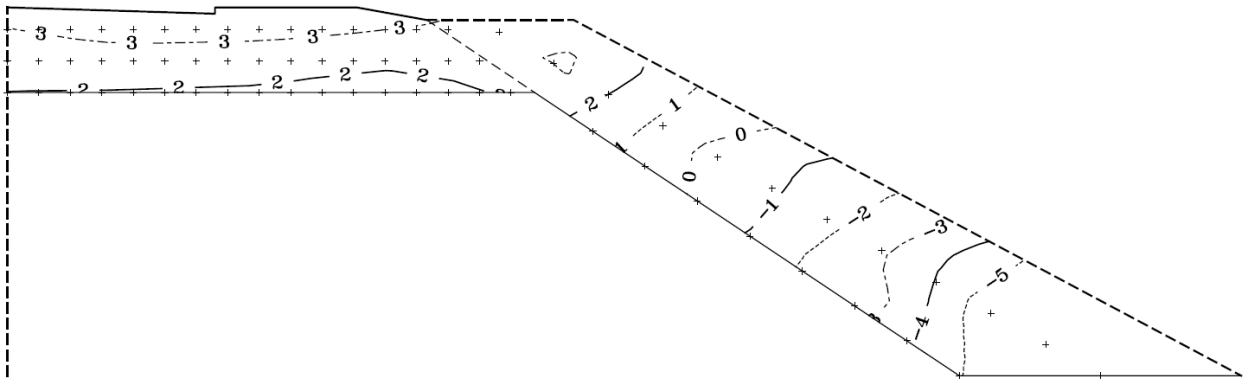

(a)

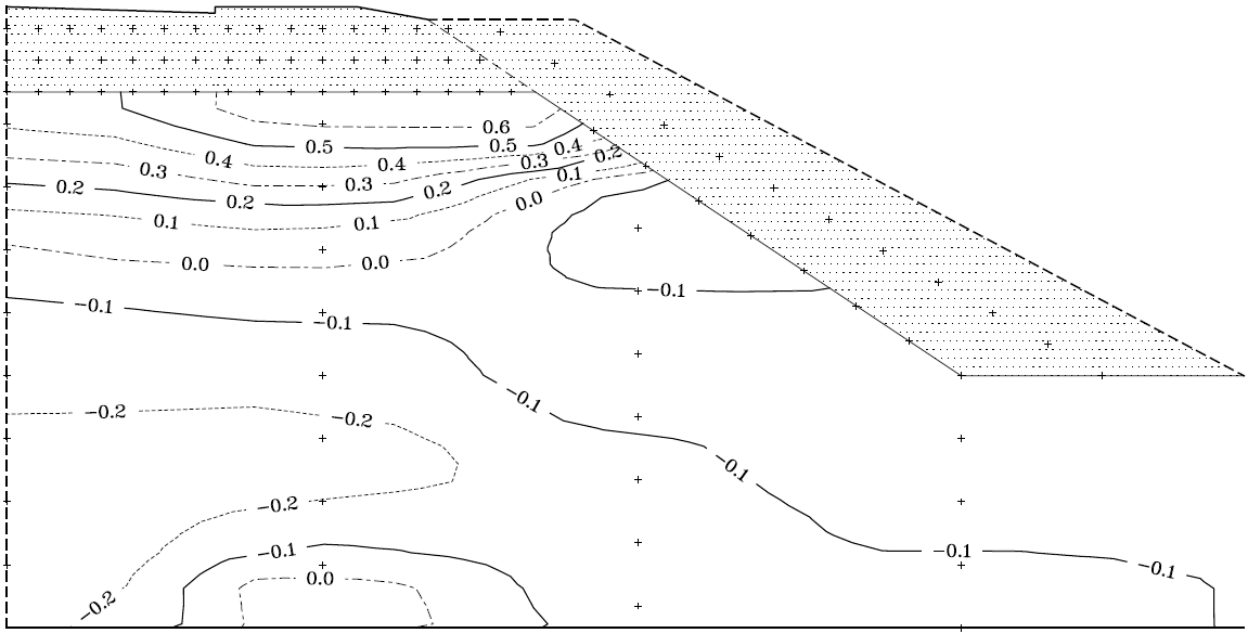

(b)

Figure B-1 Mean annual temperature contours for test section 2 in 2005, (a) ACE and ventilated shoulder layers, (b) embankment core and foundation soils

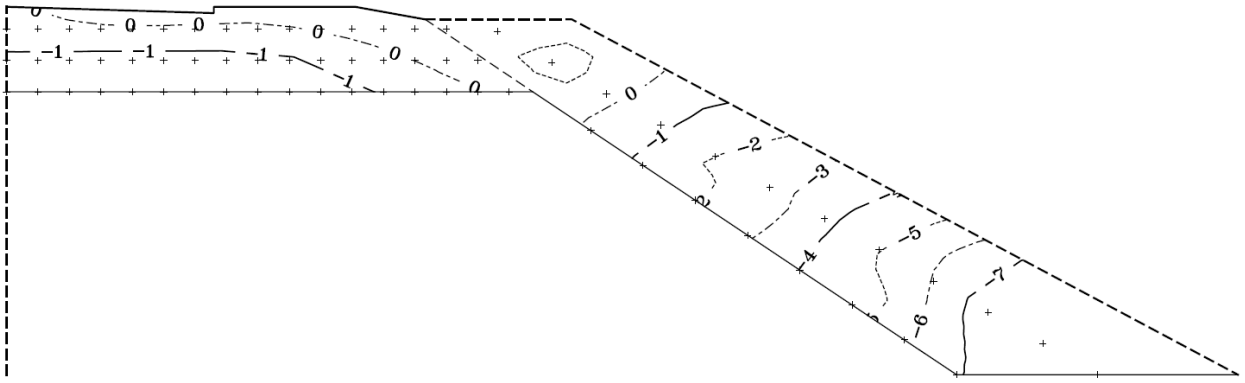

(a)

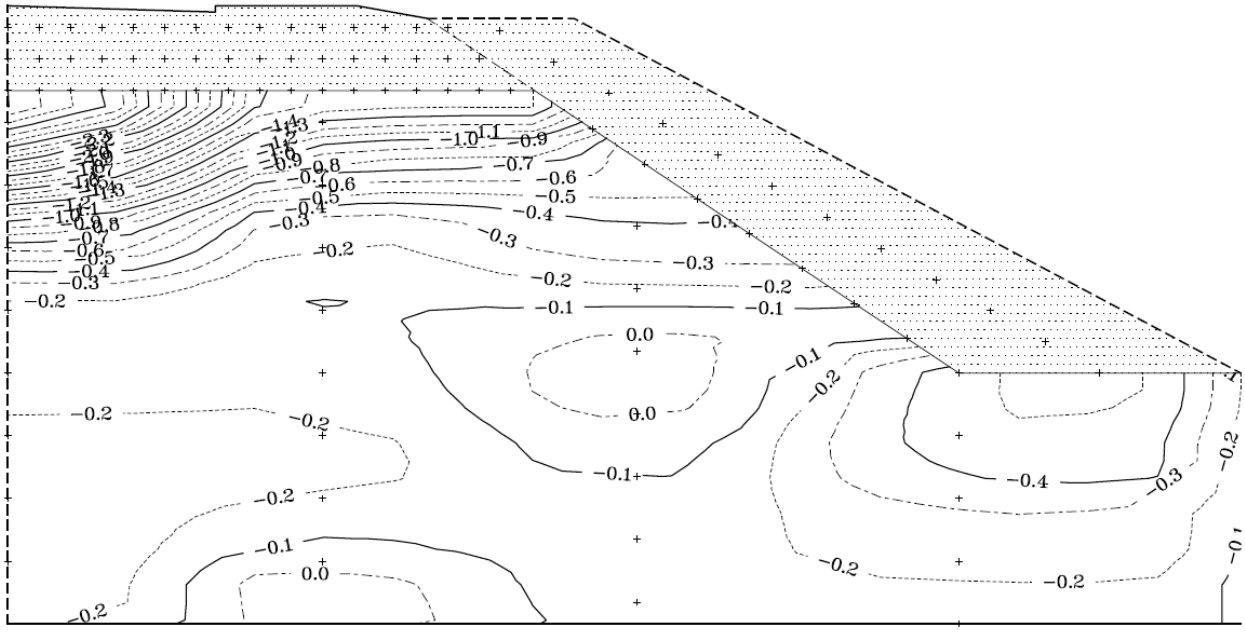

(b)

Figure B-2 Mean annual temperature contours for test section 2 in 2006, (a) ACE and ventilated shoulder layers, (b) embankment core and foundation soils

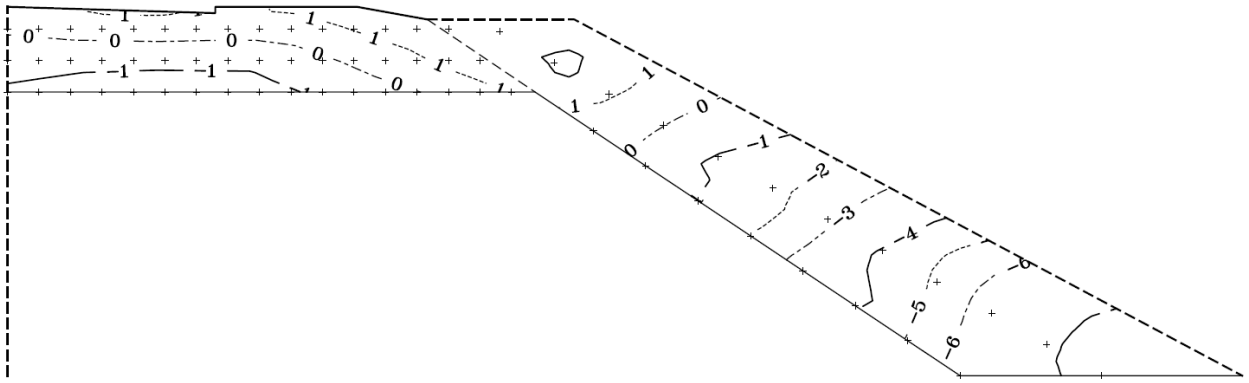

(a)

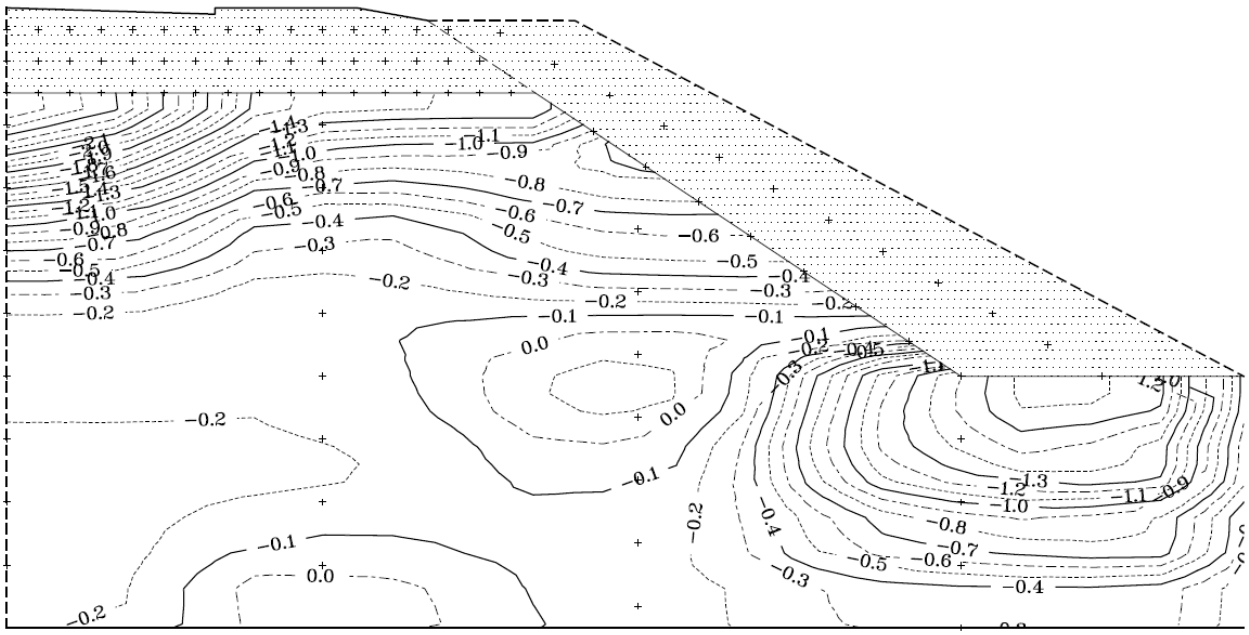

(b)

Figure B-3 Mean annual temperature contours for test section 2 in 2007, (a) ACE and ventilated shoulder layers, (b) embankment core and foundation soils

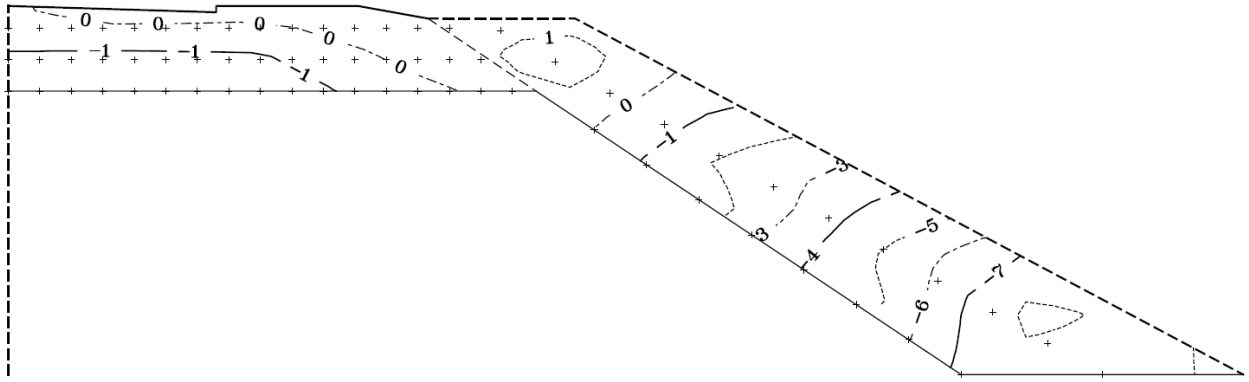

(a)

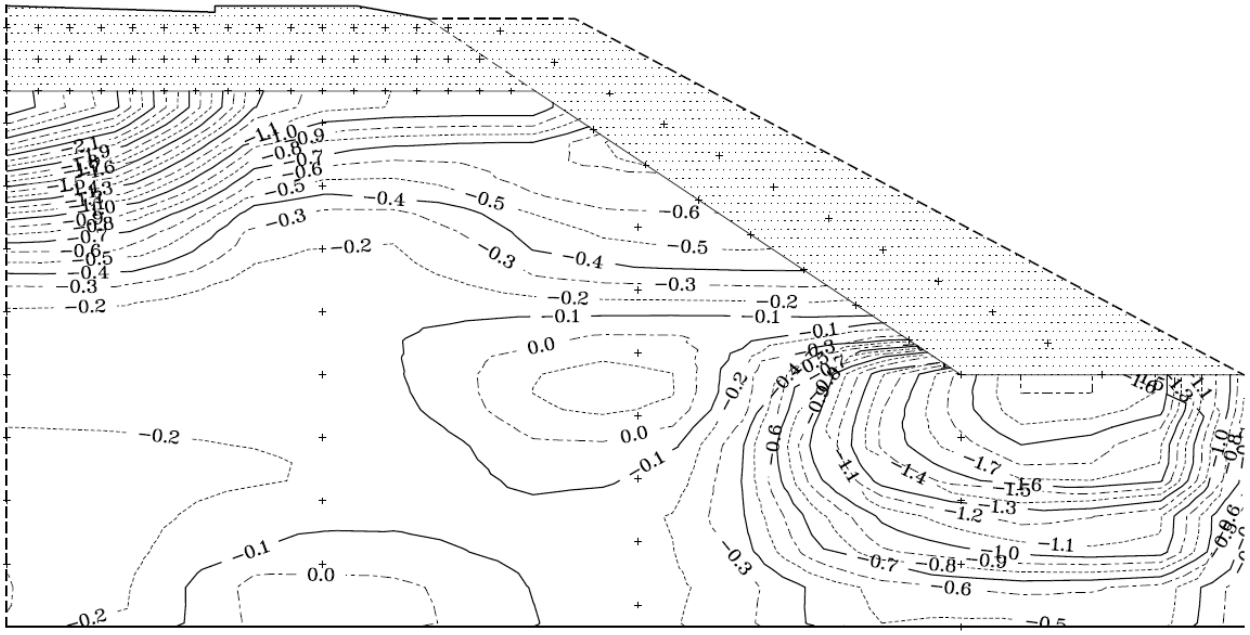

(b)

Figure B-4 Mean annual temperature contours for test section 2 in 2008, (a) ACE and ventilated shoulder layers, (b) embankment core and foundation soils

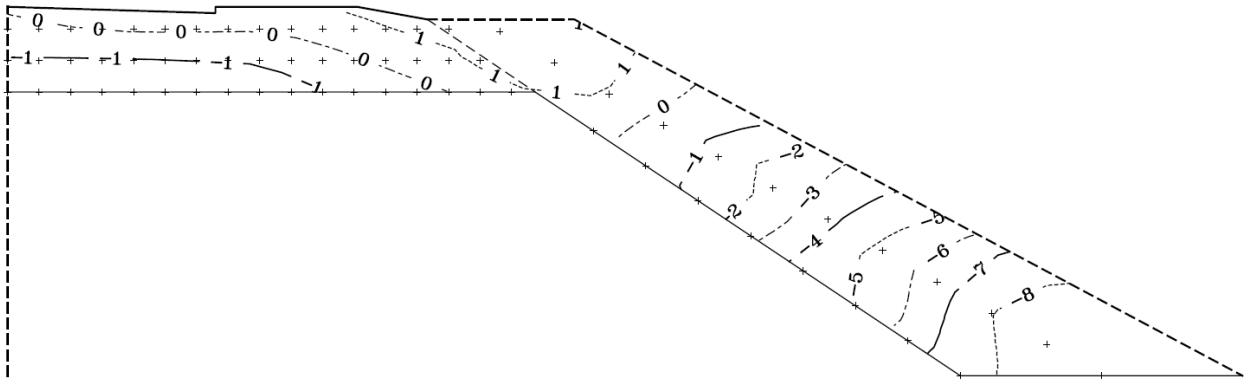

(a)

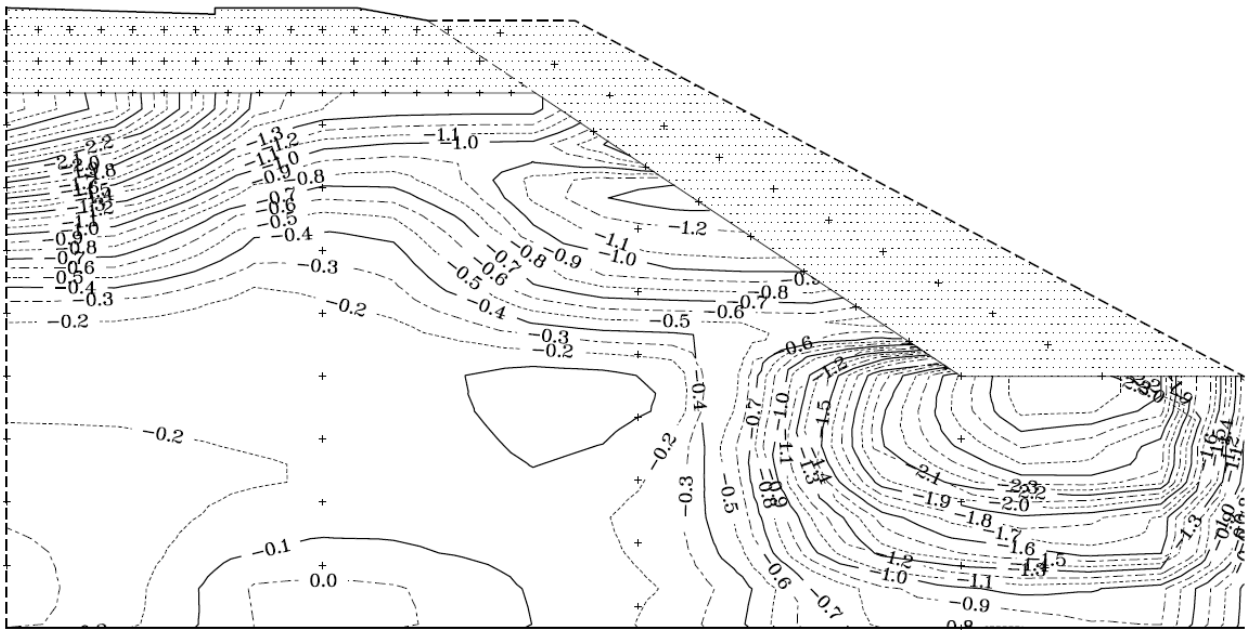

(b)

Figure B-5 Mean annual temperature contours for test section 2 in 2009, (a) ACE and ventilated shoulder layers, (b) embankment core and foundation soils

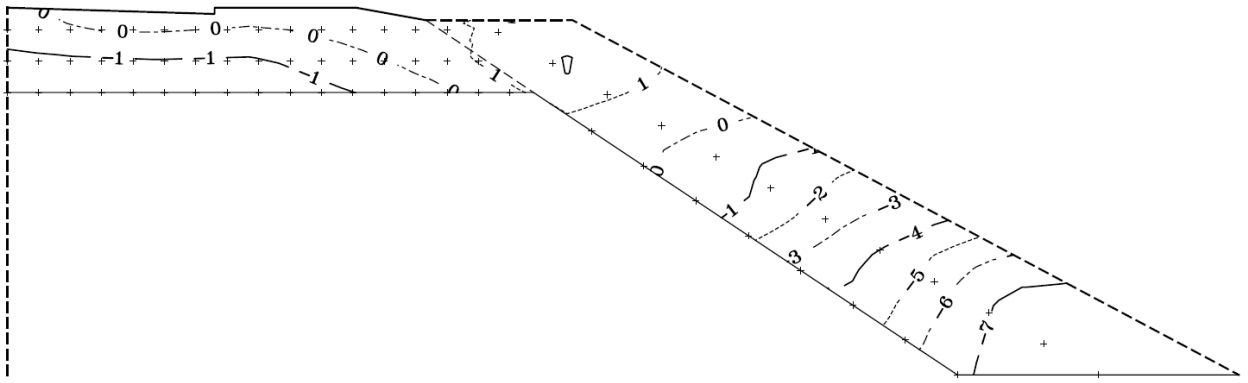

(a)

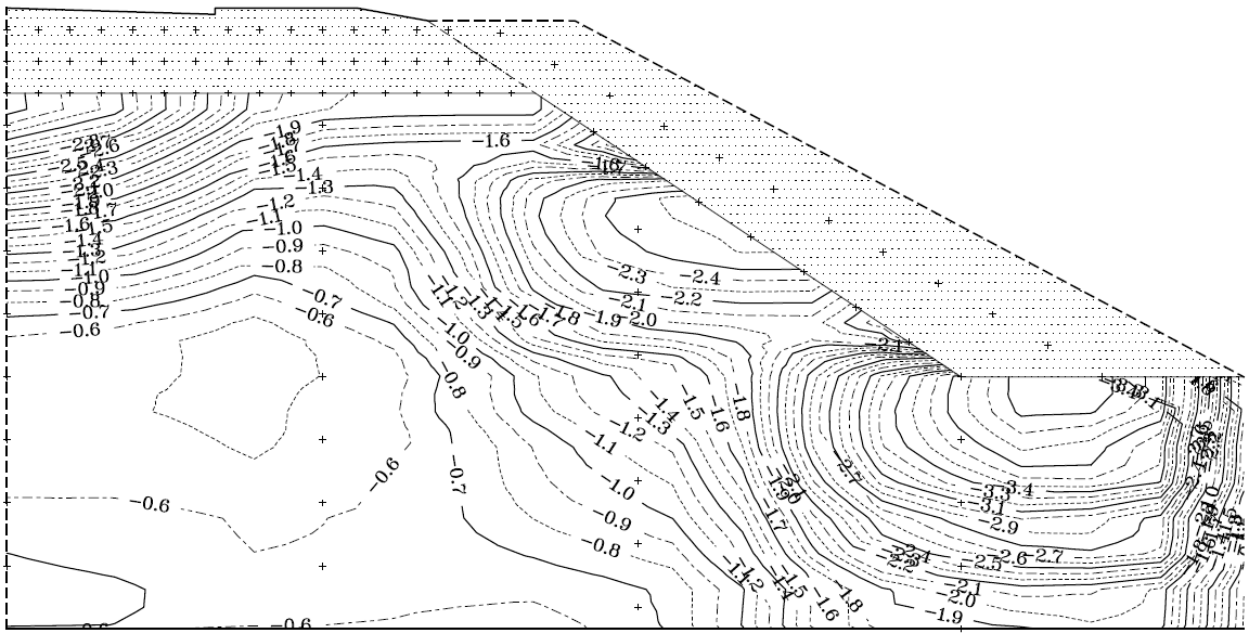

(b)

Figure B-6 Mean annual temperature contours for test section 2 in 2013, (a) ACE and ventilated shoulder layers, (b) embankment core and foundation soils

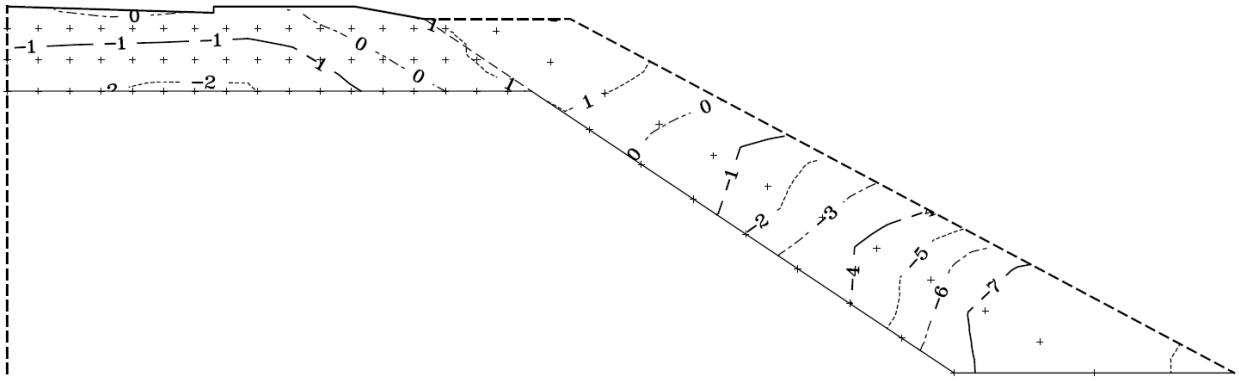

(a)

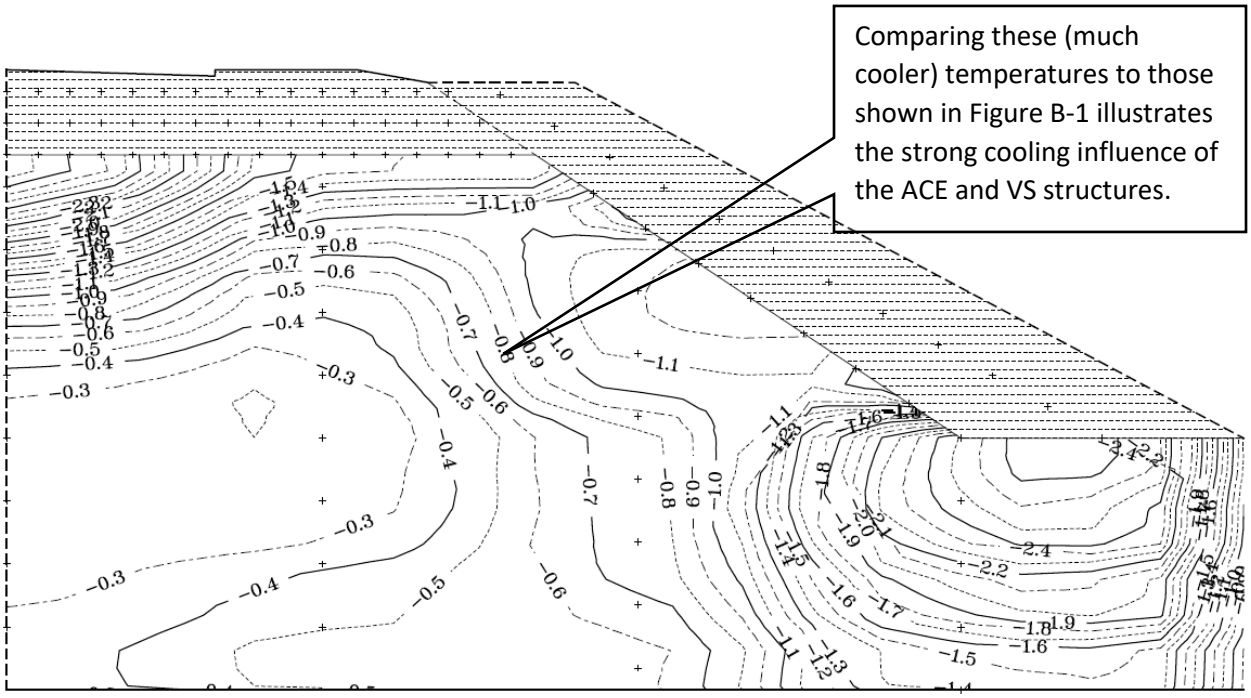

(b)

Figure B-7 Mean annual temperature contours for test section 2 in 2020, (a) ACE and ventilated shoulder layers, (b) embankment core and foundation soils

APPENDIX C MEAN ANNUAL TEMPERATURES FOR THOMPSON DRIVE TEST SECTION #3

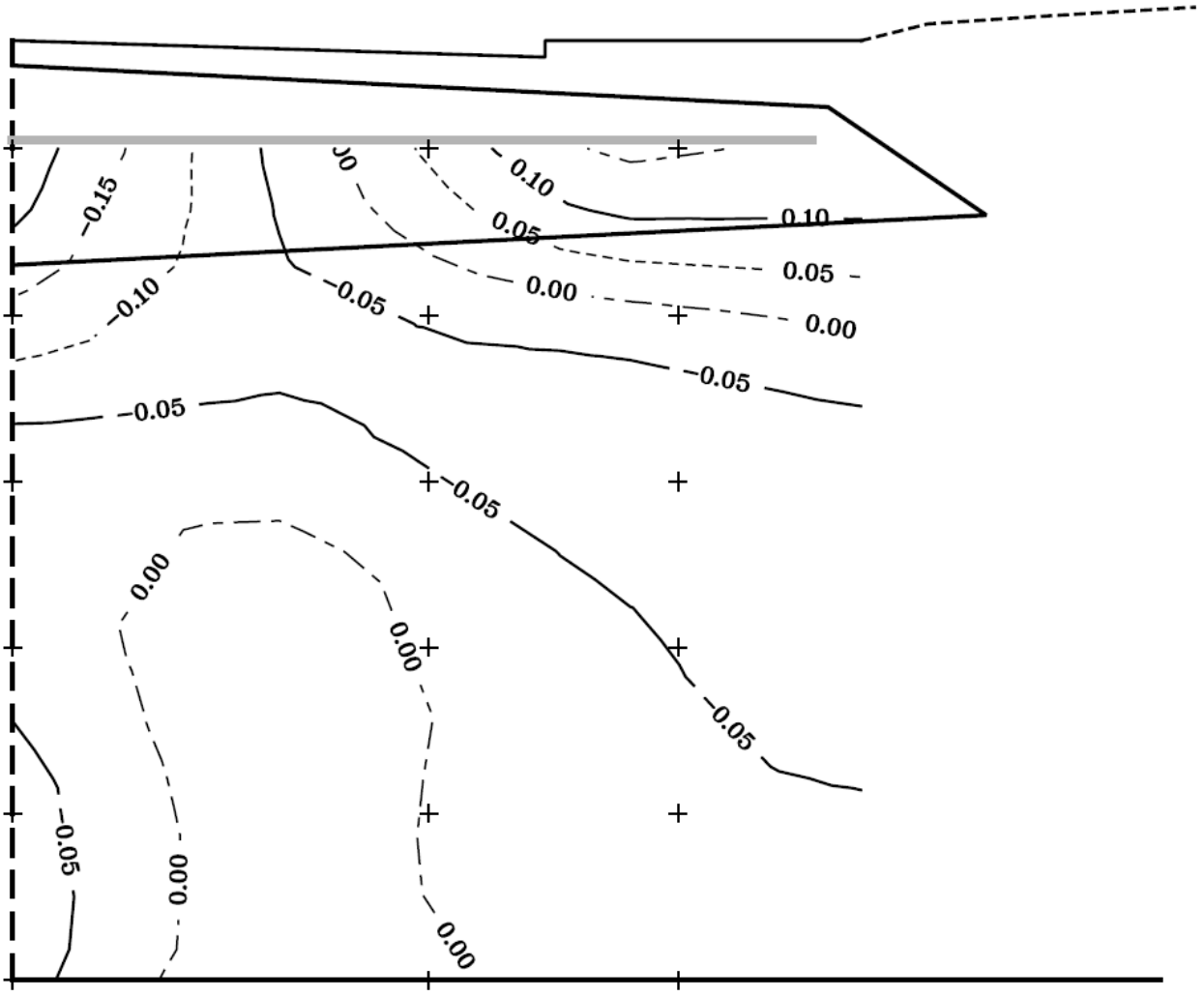

Figure C-1 Mean annual temperature contours for test section 3 in 2005

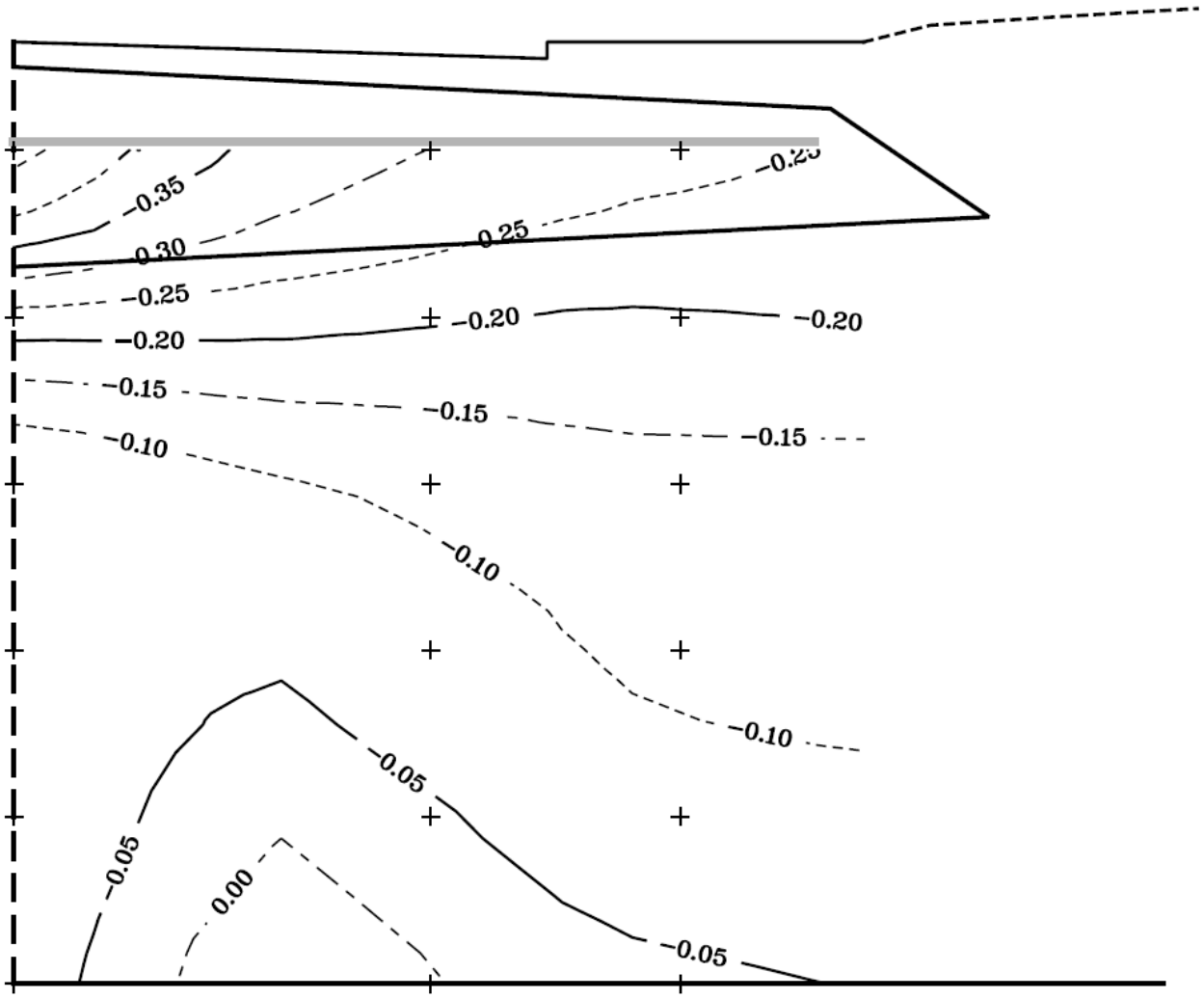

Figure C-2 Mean annual temperature contours for test section 3 in 2006

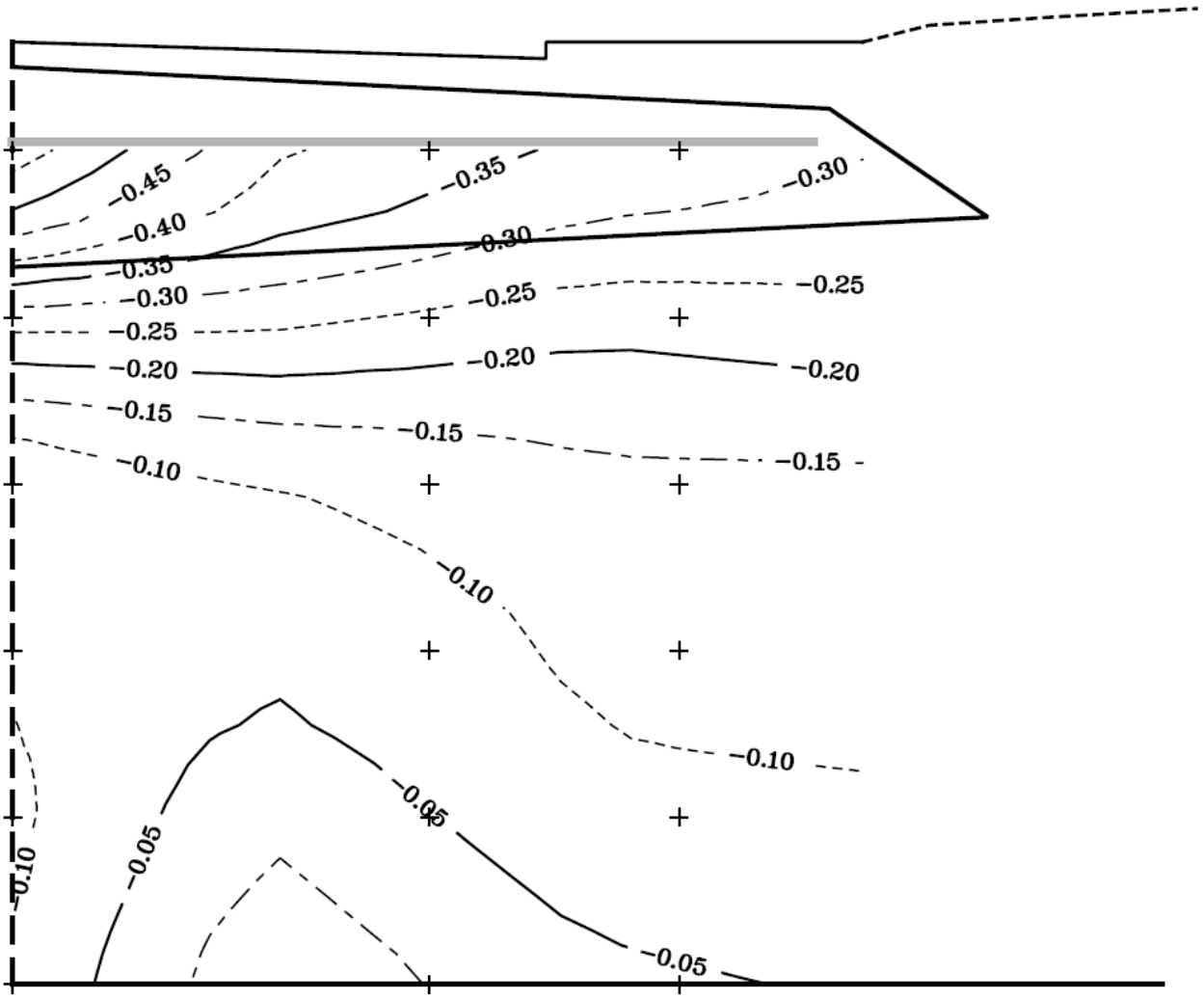

Figure C-3 Mean annual temperature contours for test section 3 in 2007

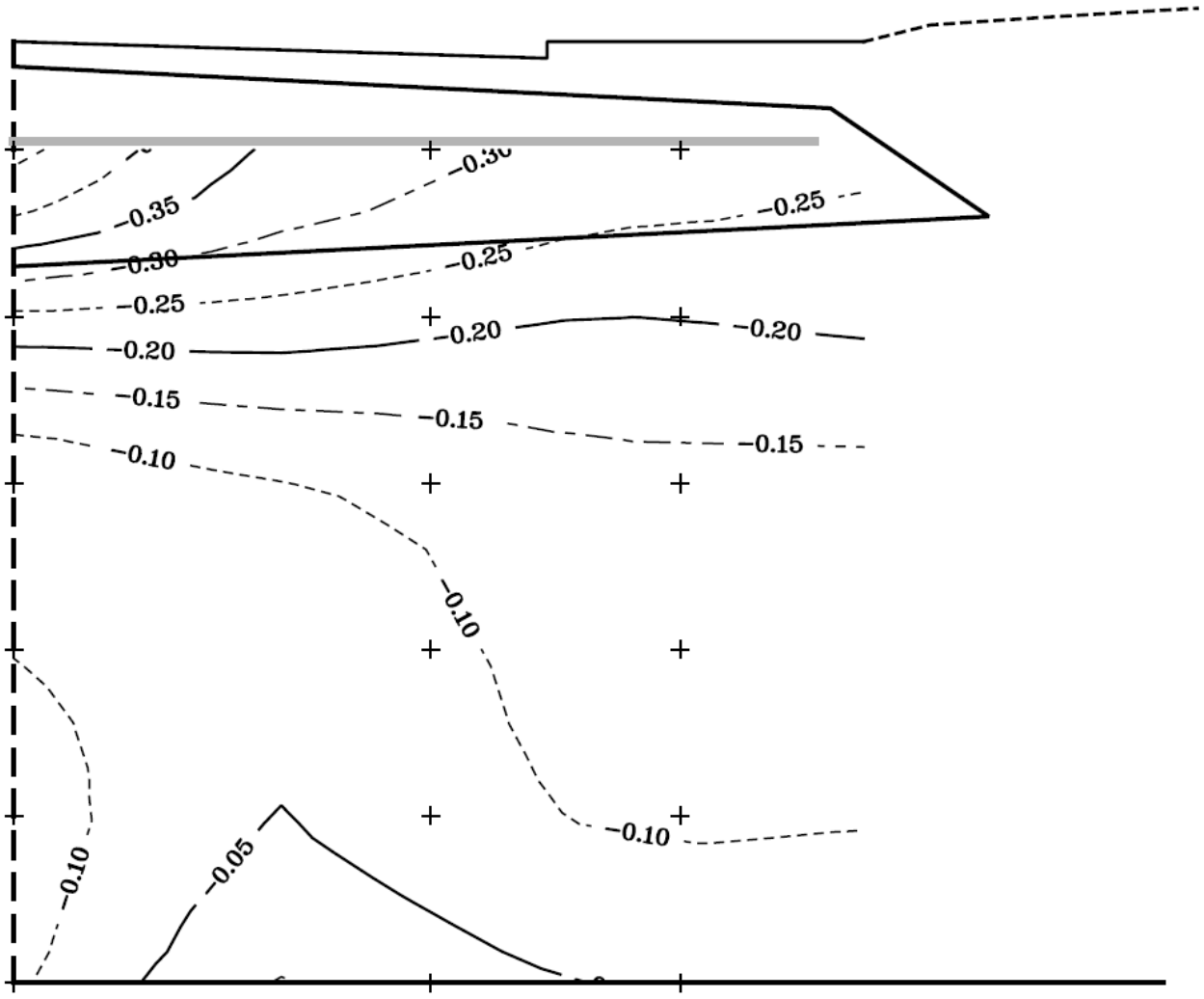

Figure C-4 Mean annual temperature contours for test section 3 in 2008

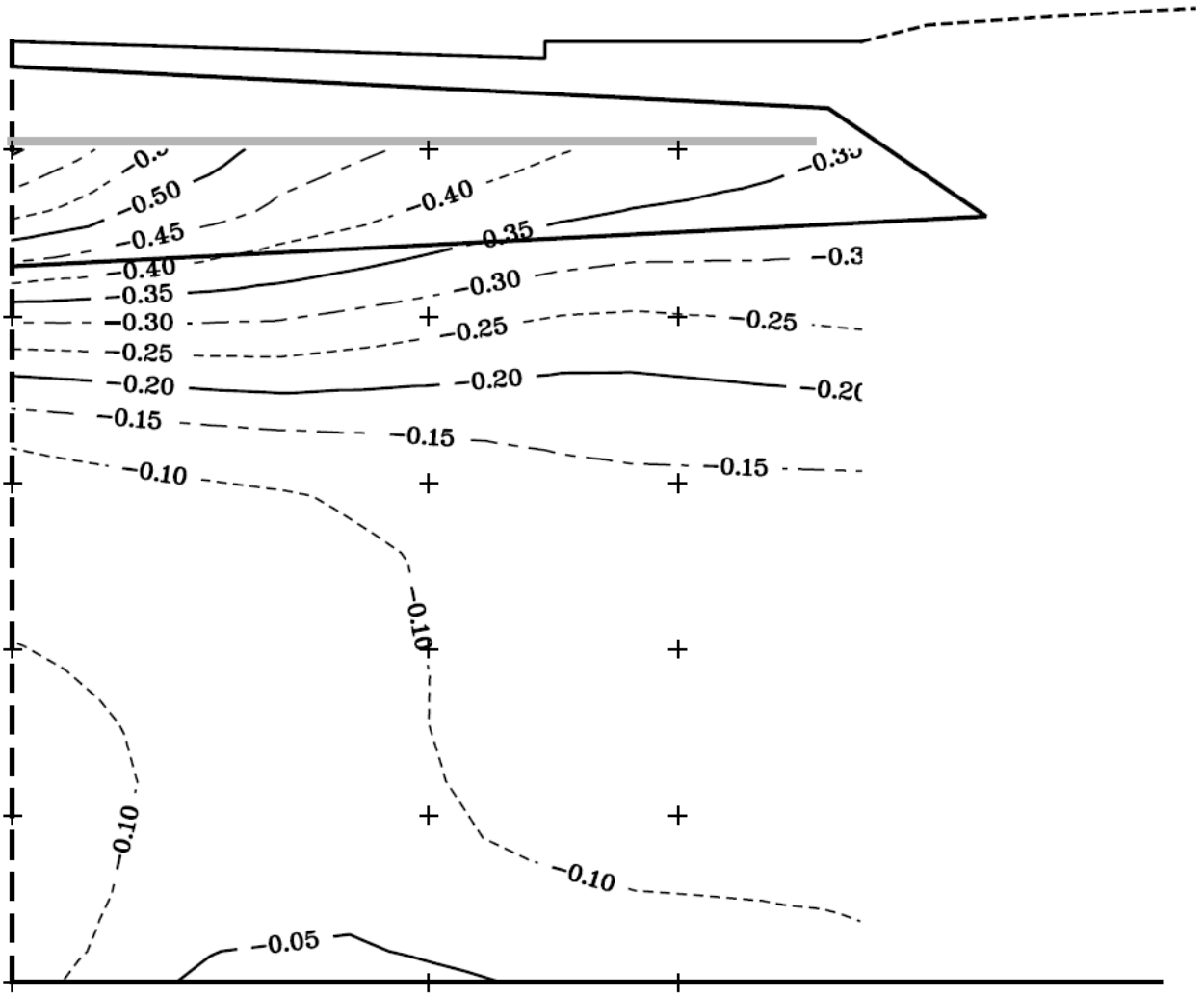

Figure C-5 Mean annual temperature contours for test section 3 in 2009

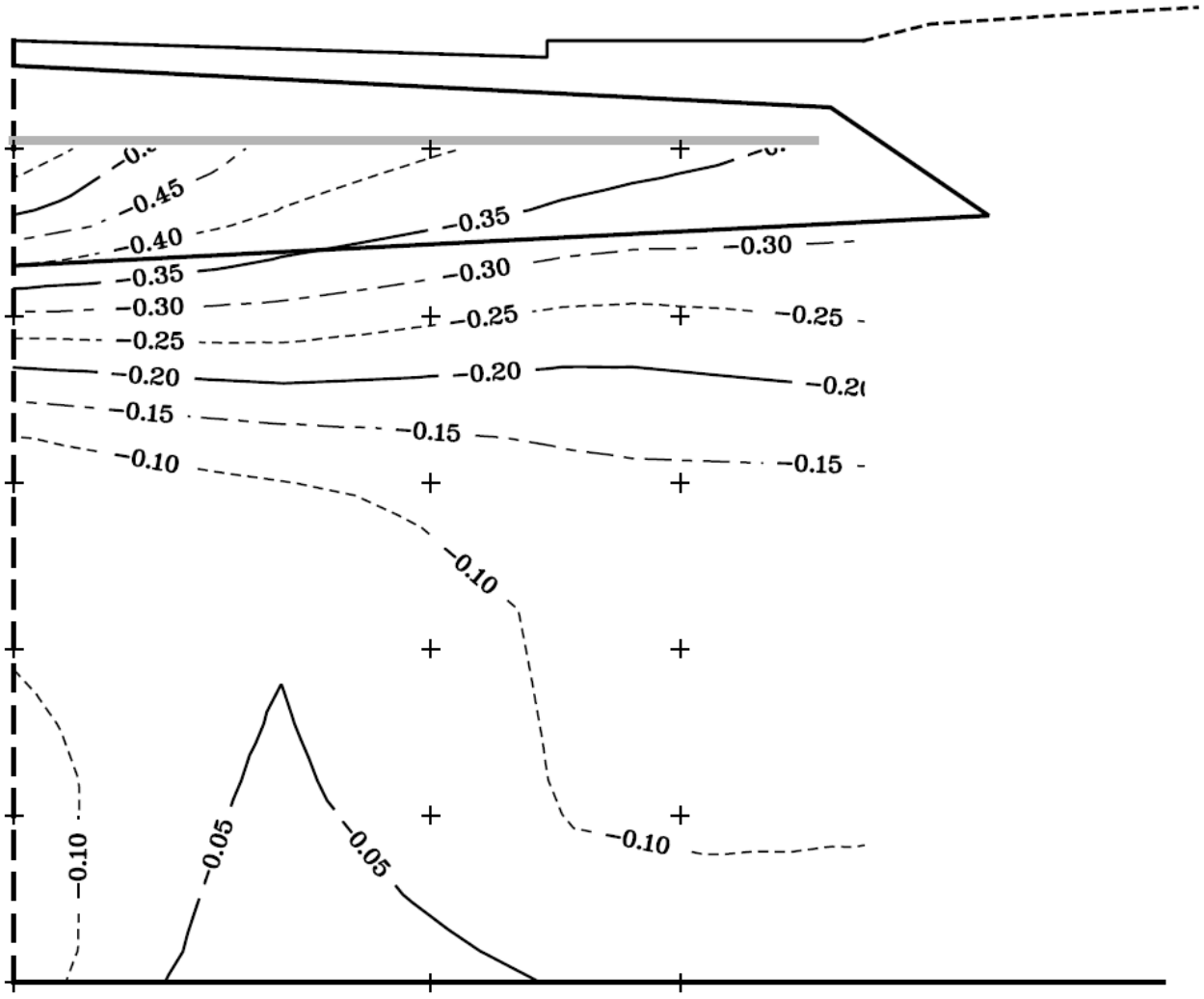

Figure C-6 Mean annual temperature contours for test section 3 in 2010

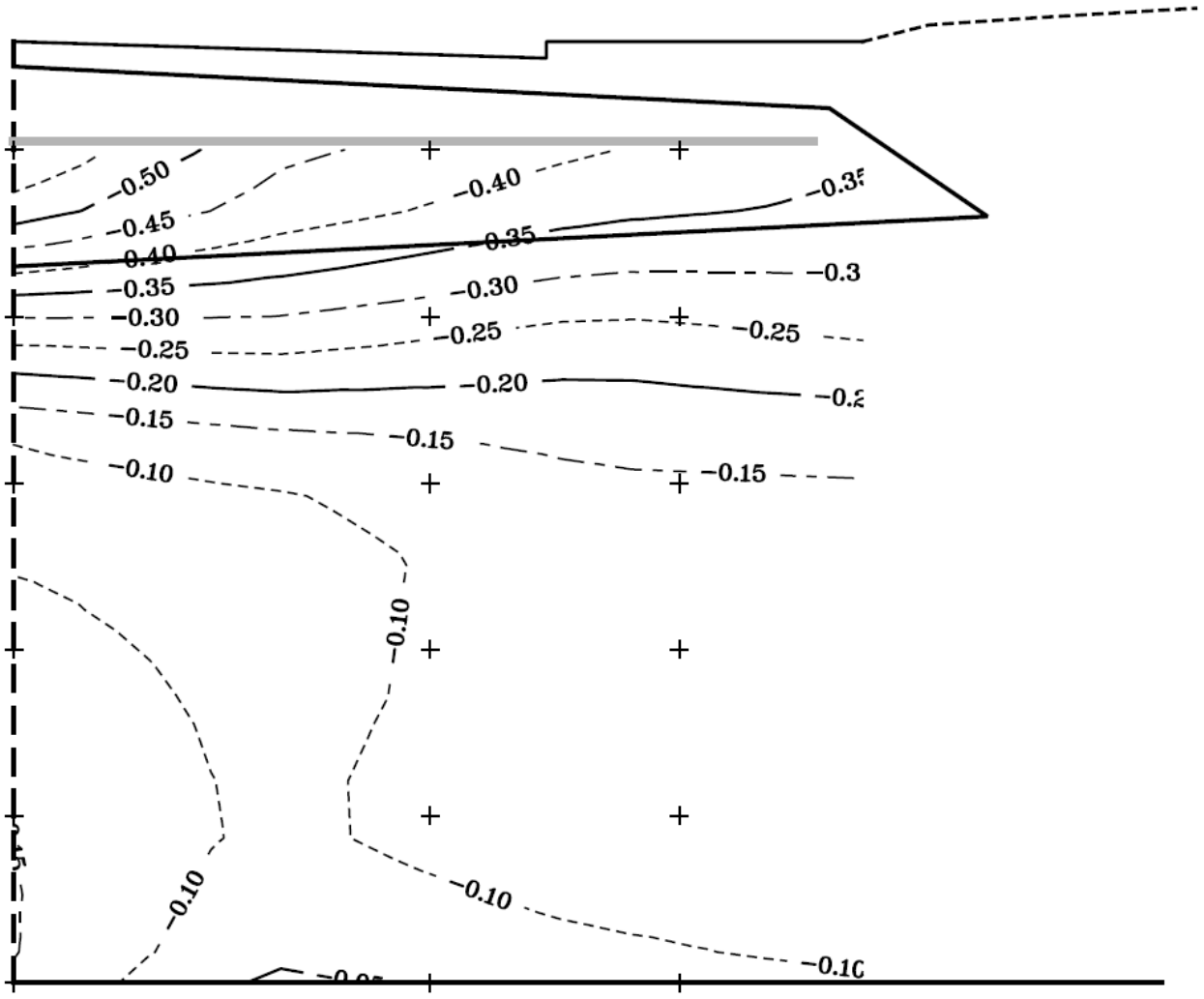

Figure C-7 Mean annual temperature contours for test section 3 in 2011

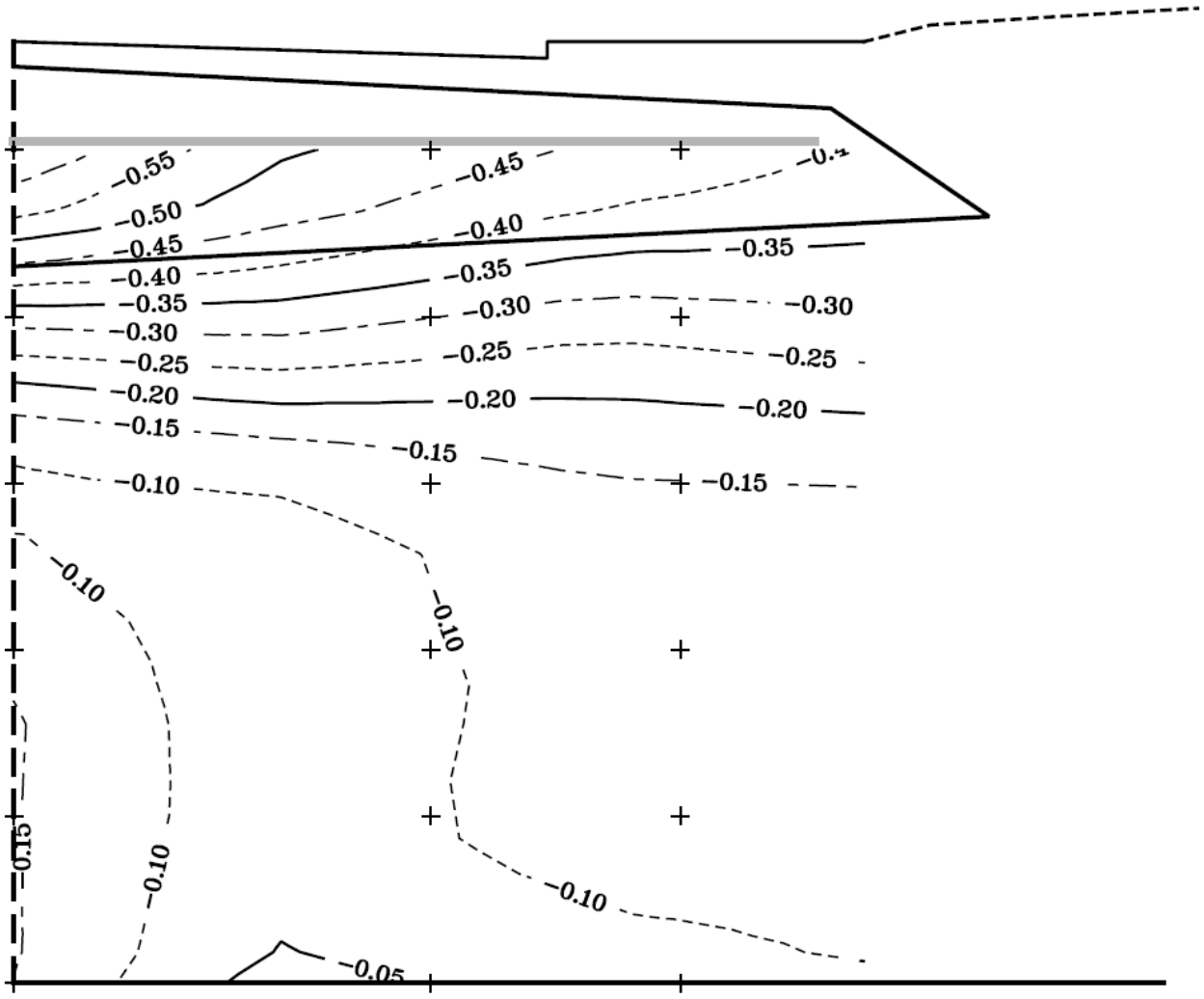

Figure C-8 Mean annual temperature contours for test section 3 in 2012

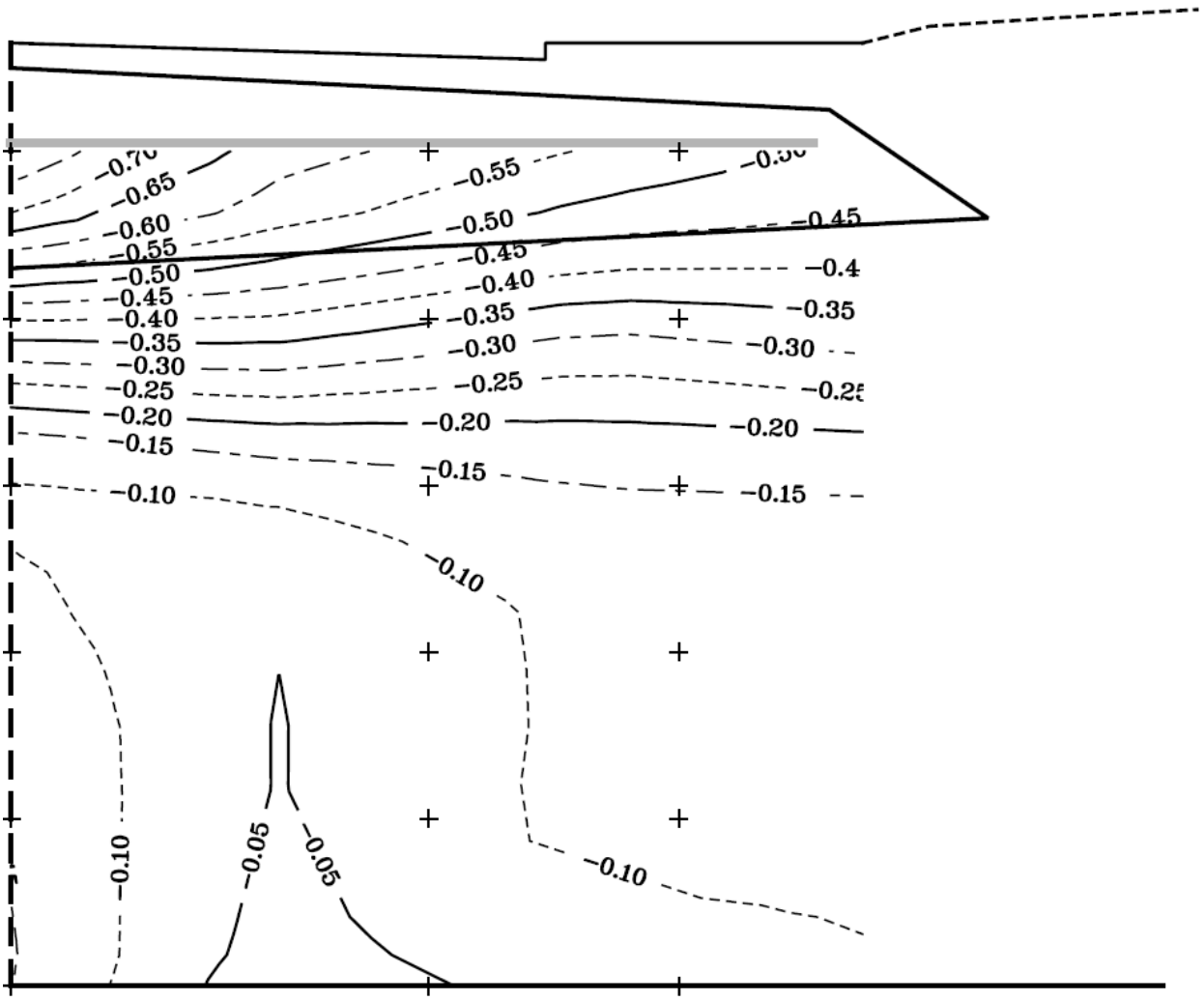

Figure C-9 Mean annual temperature contours for test section 3 in 2013

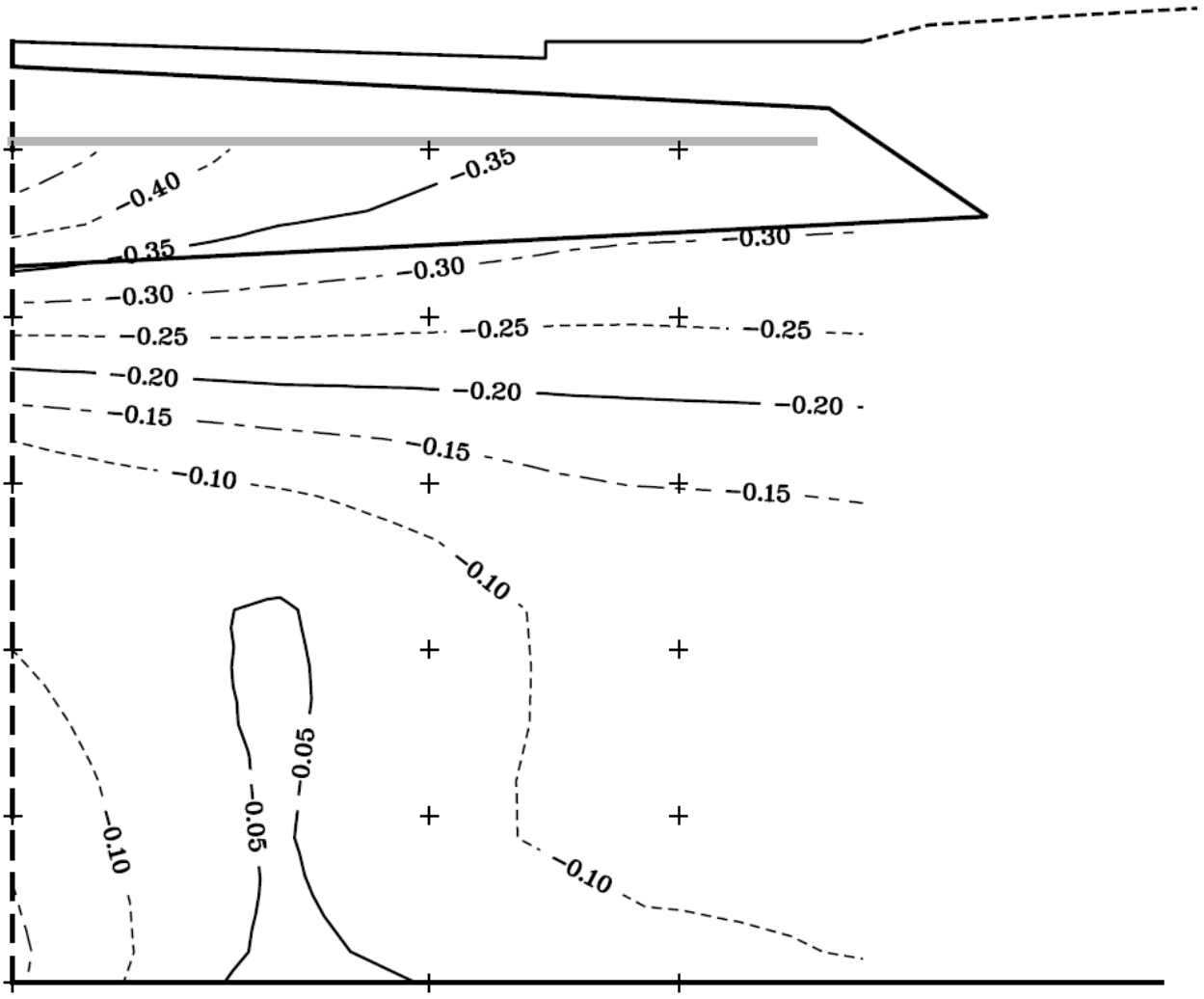

Figure C-10 Mean annual temperature contours for test section 3 in 2014

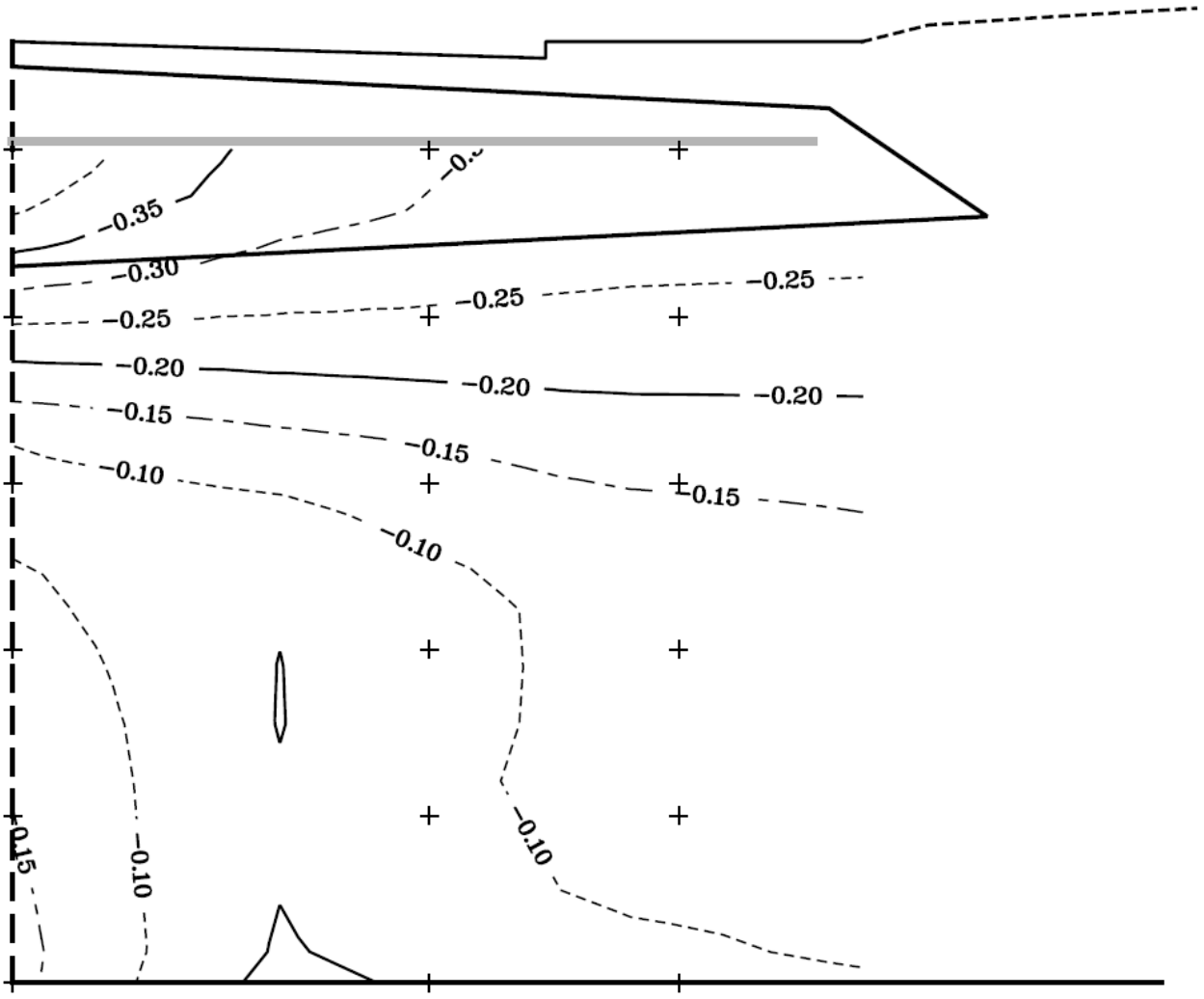

Figure C-11 Mean annual temperature contours for test section 3 in 2015

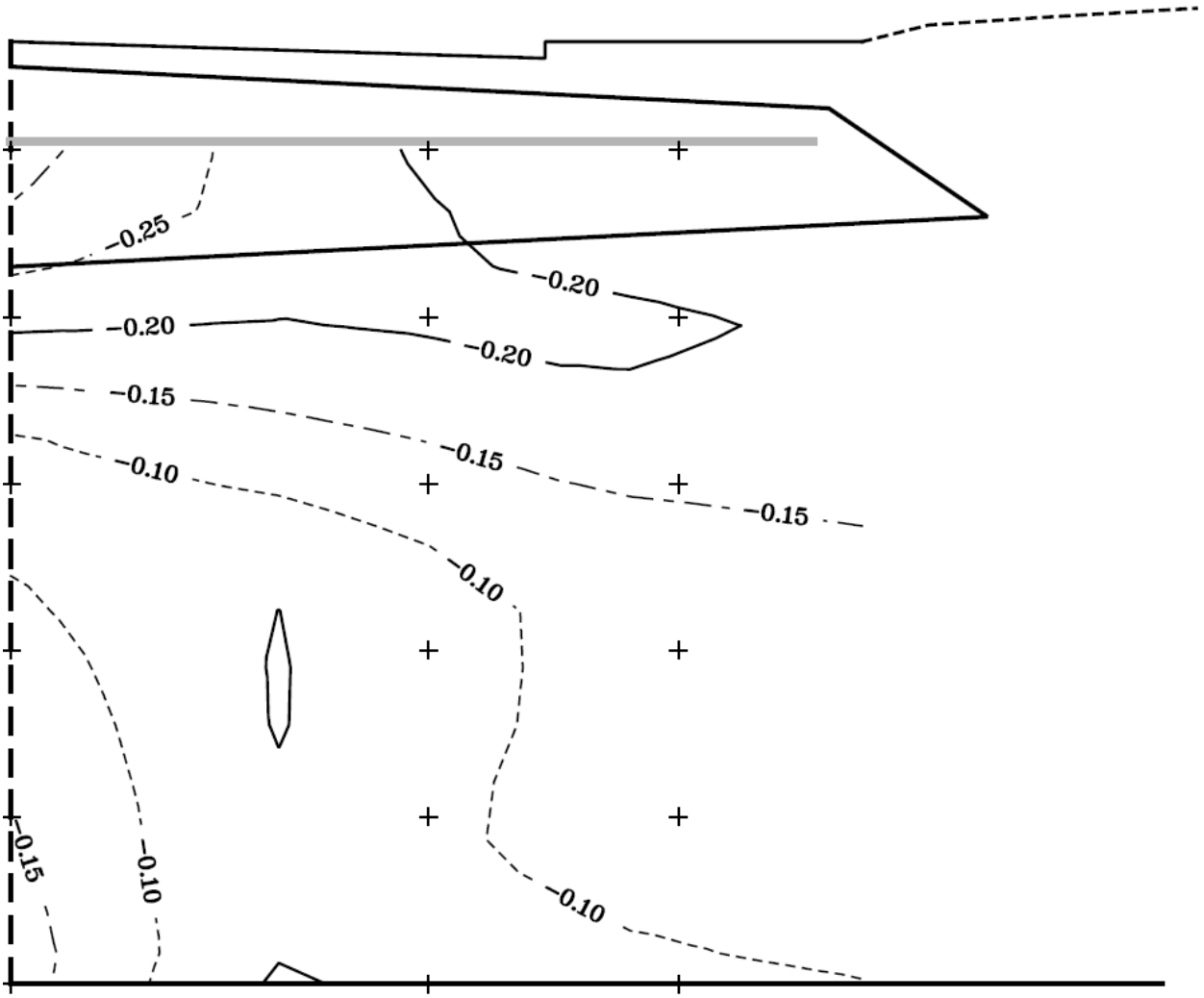

Figure C-12 Mean annual temperature contours for test section 3 in 2016

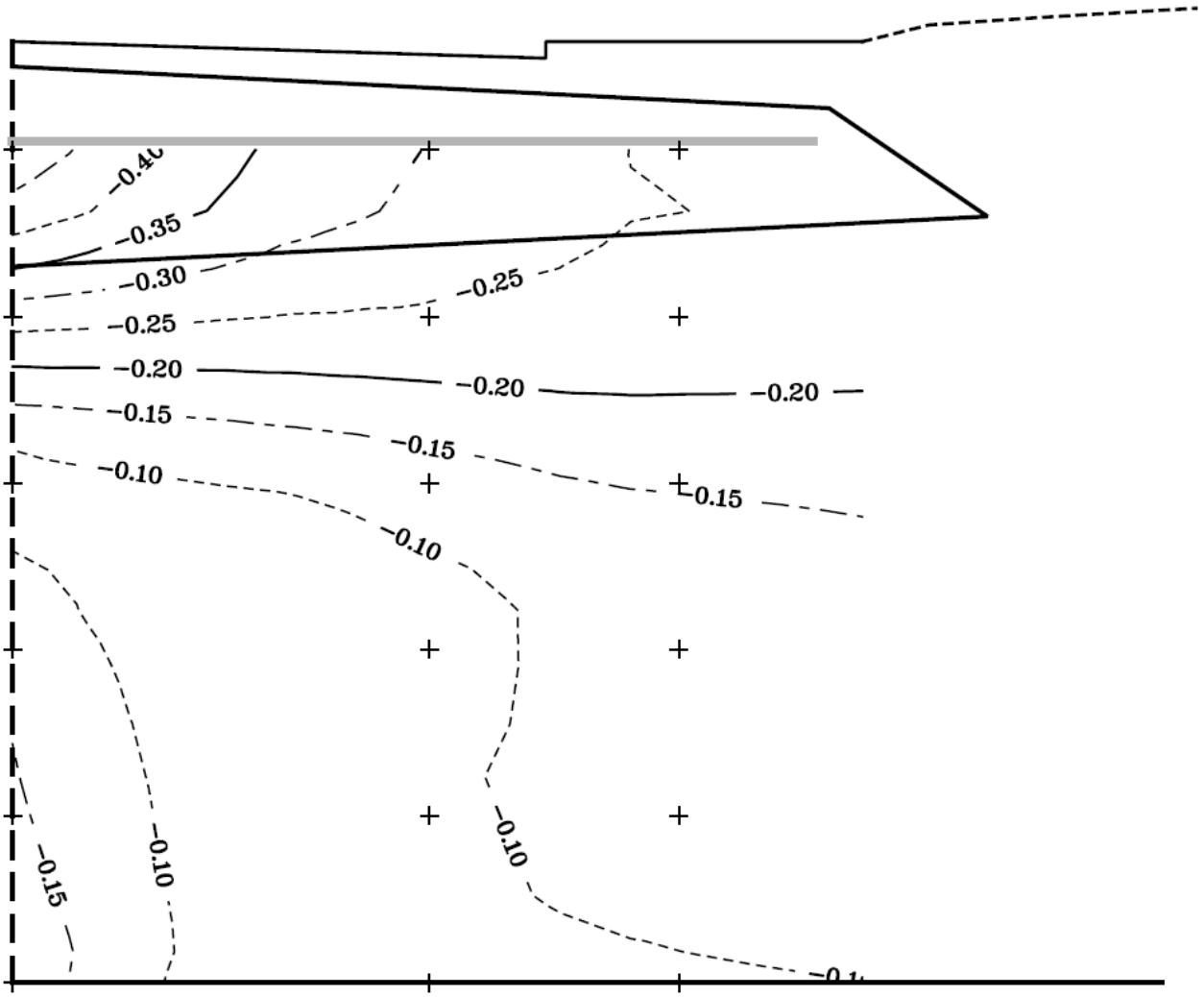

Figure C-13 Mean annual temperature contours for test section 3 in 2017

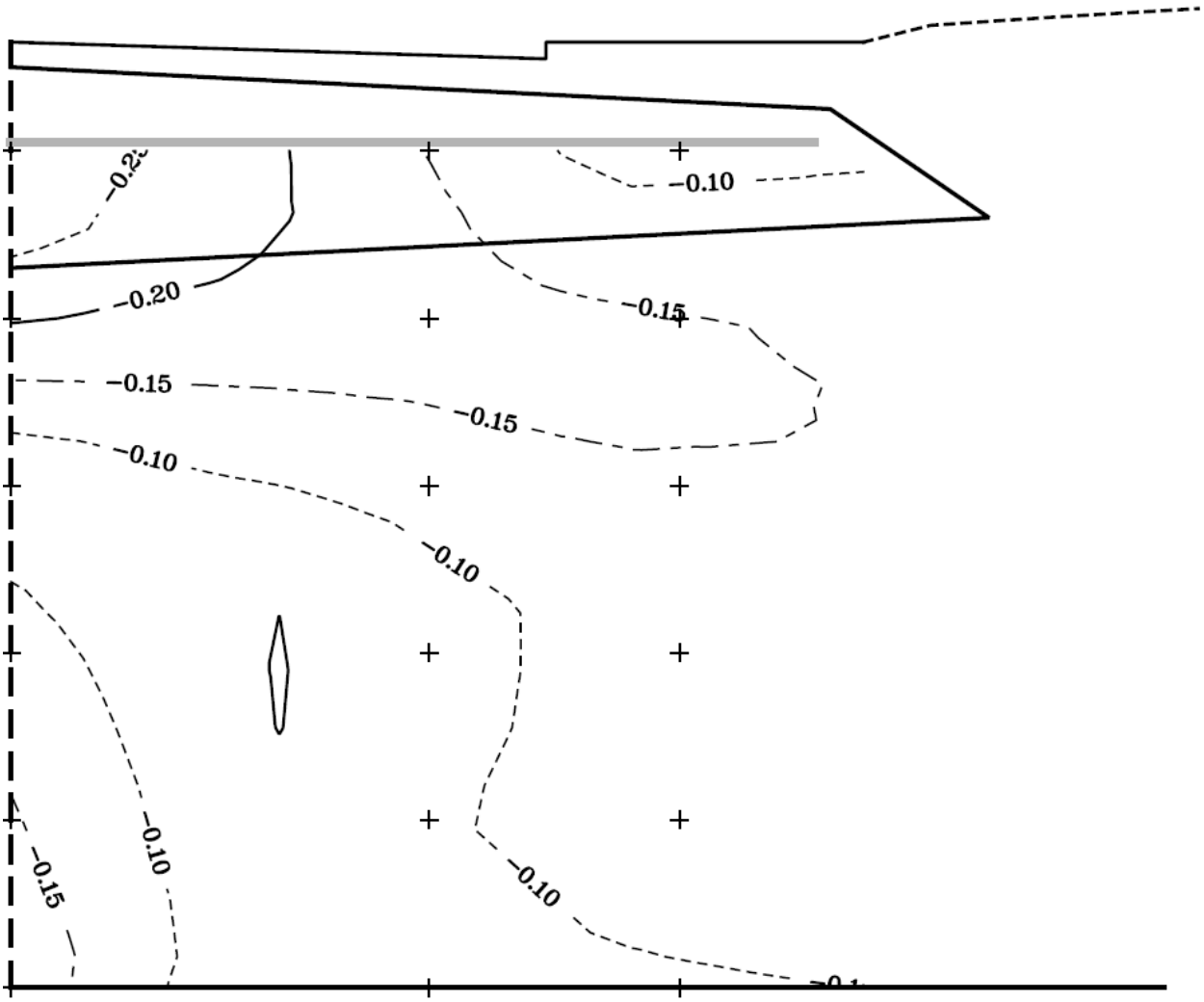

Figure C-14 Mean annual temperature contours for test section 3 in 2018

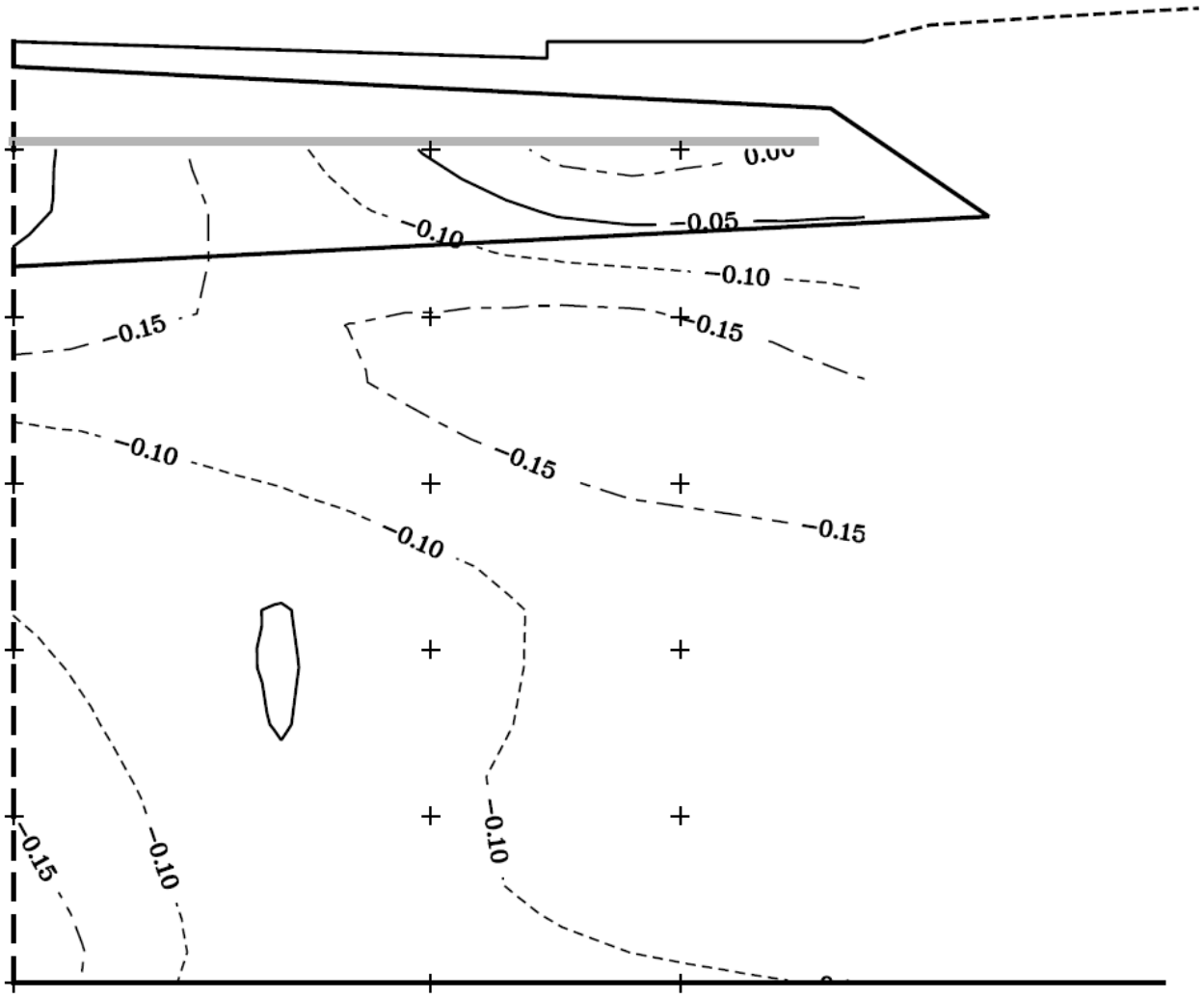

Figure C-15 Mean annual temperature contours for test section 3 in 2019

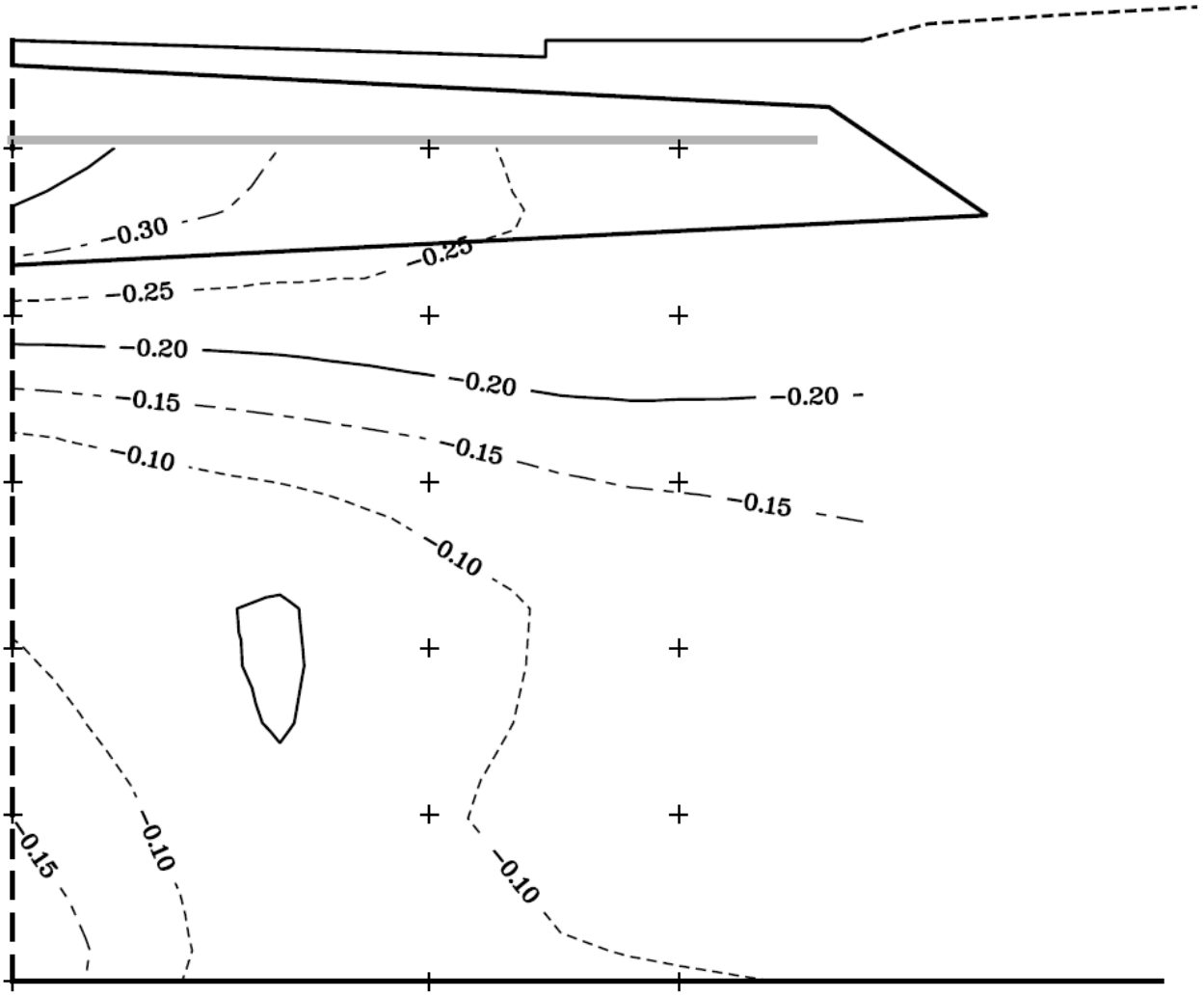

Figure C-16 Mean annual temperature contours for test section 3 in 2020